Title

The Relationship between Organ Dose and Patients Size in Multidetector Computed Tomography (MDCT) Scans Utilizing Tube Current Modulation (TCM)

Author

Khatonabadi, Maryam

Publication Date

2013

Peer reviewed|Thesis/dissertation

UNIVERSITY OF CALIFORNIA

Los Angeles

The Relationship between Organ Dose and Patients Size in Multidetector Computed Tomography (MDCT) Scans Utilizing Tube Current Modulation (TCM)

A dissertation submitted in partial satisfaction of the

requirements for the degree Doctor of Philosophy

in Biomedical Physics

by

Maryam Khatonabadi

2013

ABSTRACT OF THE DISSERTATION

The Relationship between Organ Dose and Patients Size in Multidetector Computed Tomography (MDCT) Scans Utilizing Tube Current Modulation (TCM)

By

Maryam Khatonabadi

Doctor of Philosophy in Biomedical Physics

University of California, Los Angeles, 2013

Professor Michael McNitt-Gray, Chair

Computed Tomography (CT) has been one of the leading imaging modalities in today's practice of Radiology. Since its introduction in 1970s, its unique tomographic capability has not only prevented countless number of unnecessary surgeries but also saved lives by early detection of disease. Radiation dose from CT has been estimated to contribute to almost 50% of all medical radiation exposures. Concerns about radiation-induced carcinogenesis have resulted in efforts that encourage monitoring and reporting radiation dose from CT examinations. It has been suggested that the most appropriate quantity for assessing risk of carcinogenesis from x-ray imaging procedures is the radiation dose to individual patients. Currently employed dose metrics used to report patient dose are $CTDI_{vol}$ and DLP, neither of which is patient-specific dose, let alone dose to individual organs.

$CTDI_{vol}$ is dose to a homogenous cylindrical phantom, which is defined for fixed tube current CT exams. With the implementation of Tube Current Modulation (TCM) feature in almost all clinical CT protocols as an intended means for dose reduction, while maintaining an appropriate diagnostic image quality, $CTDI_{vol}$ definition was standardized across scanners to reflect dose to CTDI phantom based on the average tube current across the entire scan length. Depending on the type of CT exam, the average tube current used to report a $CTDI_{vol}$ value may or may not represent the actual tube current at a specific table location. In addition to not taking into account variation of the tube current across a single exam, $CTDI_{vol}$ is size-independent, i.e. patients with different sizes have the same $CTDI_{vol}$ value if scanned using the same imaging parameters.

To adjust $CTDI_{vol}$ for size, AAPM Task Group 204 was established and subsequently published a report containing conversions as a function of effective diameter which can be applied to scanner-reported $CTDI_{vol}$ to adjust for patient size. However, the generated conversion factors were based on fixe tube current measurements and Monte Carlo simulations and failed to take into account TCM. Additionally, the size metric used in TG 204 was entirely based on patients' physical dimensions and does not take into account variations in composition and density among patients, let alone within a single patient; i.e. differences between chest and abdomen in terms of attenuation properties could not be explained with a simple measure of dimension such as effective diameter. Instead attenuation-based metrics need to be implemented to explain these differences.

The overall purpose of this dissertation was to improve organ dose estimation from Computed Tomography exams by: (a) taking into account the commonly used feature in CT protocols, Tube Current Modulation (TCM), (b) employing a more appropriate way of reporting CTDI for TCM

exams and (c) using a patient size descriptor capable of describing the attenuation properties of individual patients.

For this dissertation a validated Monte Carlo based MDCT model capable of simulating organ dose was utilized to estimate organ dose to voxelized patient models undergoing tube current modulated CT examinations. Both detailed TCM and z-axis-only modulation information were used in the simulations in case raw projection data was not accessible. In addition to simulated organ doses different $CTDI_{vol}$ values based on the type of patient model, abdomen versus chest, were calculated. These $CTDI_{vol}$ values included regional $CTDI_{vol,regional}$ and organ-specific $CTDI_{vol,organ}$ along with scanner-reported $CTDI_{vol}$, referred to as global $CTDI_{vol,global}$. Furthermore different size metrics, such as effective diameter and attenuation-based metrics, were calculated for every axial CT image within a series and averaged corresponding to the same regions and images used to calculated the above mentioned regional and organ-specific $CTDI_{vol}$ values.

Using an approach similar to previous efforts and AAPM Task Group 204, the estimated organ doses were normalized by CT Dose Index ($CTDI_{vol}$) values. However, for TCM scans normalized organ doses by $CTDI_{vol,global}$ were observed to not have a strong correlation with patient size. This result was quite different from that observed previously for fixed tube current exams. In contrast, when regional descriptors of scanner output ($CTDI_{vol,regional}$ and $CTDI_{vol,organ}$) were used as a modified normalization factor, the results demonstrated significantly improved correlations with patient size.

Additionally, an attenuation-based patient size metric, the water equivalent diameter (WED), was investigated in terms of its ability to describe the effects of patient size on organ dose. WED was compared to the size metric introduced in TG204, effective diameter, which is based only on

patient morphology (e.g. perimeter) and not on attenuation. Results of the comparisons demonstrated no statistically significant improvements of correlation between normalized organ doses and size metric once WED was utilized, except for normalized lung dose. Although there were no statistically significant improvements, the correlation of determination, R^2, increased for almost all organs once WED was employed. Similarly, there was no statistically significant difference between differently averaged size metrics, i.e. global average of size metrics versus regional average of size metrics, except for normalized lung dose, which showed a statistically significant improvement in R^2 once a regional WED was employed as a size metric compared to global WED.

Using improved normalization quantity and patient size metric for tube current modulated CT examinations, Generalized Linear Models were used to generate a predictive model capable of estimating dose from TCM exams using regional $CTDI_{vol}$ and WED. Different models based on scanners and organs were generated to establish the level of accuracy of each model and to determine the level of specification needed to achieve best organ dose estimates. Additionally, models with different response variables, normalized organ dose versus actual organ dose, were explored and compared.

When tested using a separate test set, investigated models with regional $CTDI_{vol}$ either as a predictor or normalization factor resulted in very similar results while models created with global $CTDI_{vol}$ as a predictor resulted in underestimation of organ dose across all organs. Additionally, it was shown that a model based on pooled data was not significantly different than scanner and organ-specific models since the pooled-data model resulted in employing significant categorical predictors such as scanners and organs. This observation confirms the fact that TCM algorithms are different across scanners and regional $CTDI_{vol}$ is not capable of eliminating these differences,

but it can eliminate differences among TCM functions across a single CT scanner. Predictive organ dose estimates using generated models resulted in a mean percent difference of less than 10% when compared to actual Monte Carlo simulated organ doses.

The improvement of the newly generated model was also compared against currently used dose metrics, $CTDI_{vol}$, SSDE, and ImPACT. While comparisons with actual Monte Carlo simulated organ doses resulted in statistically significant differences between conventional dose metrics and simulated organ doses, comparisons with organ estimates from the newly developed model resulted in no difference from Monte Carlo simulated organ doses.

This work demonstrated the feasibility of estimating organ dose from tube current modulated scans from three major CT manufacturers using an improved descriptor of tube current modulated scans as normalization quantity or predictor and a patient size metric based on patients attenuation properties.

The dissertation of Maryam Khatonabadi is approved.

Christopher Cagnon

John DeMarco

Hyun Jung Kim

Matthew Brown

Jianwei Miao

Michael McNitt-Gray, Committee Chair

University of California, Los Angeles

2013

I dedicate this dissertation to my parents Behrooz Khatonabadi and Gauhar Ansari, without whose sacrifices in life I would not have achieved my dreams of higher education.

TABLE OF CONTENTS

ACKNOWLEDGEMENTS

First of all I would like to thank the person who made this work possible, my advisor Dr. Michael McNitt-Gray. Mike has not only been supportive throughout my graduate studies, but he has also been a strong believer of my visions and ideas. He has been my advisor not only in the field of Biomedical Physics, but life in general. With Mike I knew exactly who to go to for practically any obstacle I came across. In the past five years, I had moments when I was not sure what the purpose of my work was, or how I can make sense of things I have observed. With every meeting I had with Mike came new and exciting ideas for my project. He taught me how to step back and have a general look at a problem, how to simplify problems, and only concern myself with the actual issue rather than trying to solve problems surrounding the main issue. His patience is unearthly, going over multiple revisions of my papers and abstracts. Mike always made sure I reach the perfect version I have visualized and would like to deliver. Words cannot express my gratitude to Mike; I will be thankful to him forever and blessed to have such a great, one-in-a-million person in my life.

I would like to refer to Dr. Chris Cagnon as my biggest fan. His enthusiasm has given me confidence in pursuing my ideas and has given me excitement on my work at times when I saw nothing interesting about it. Almost after each Monday meeting, his words motivated me to continue my work. His consistent reminder of the actual clinical relevance of scientific work has been the reason for me to generate relevant work which can be applied in the clinic and also improve patient care. I am very grateful for his guidance throughout the past five years and, of course, for the rest of my career and am looking forward to working closer with him.

Next, I would like to thank Dr. John DeMarco, whose work has been the fundamental tool of my research and without which I would have not been able to answer problems addressed in this dissertation. His skepticism has helped me to look at problems from a different perspective and improve my thought process. He taught me to not settle and look further to reach the best possible result. I am very thankful for his critical point of view.

Dr. Jianwei Miao, my undergrad advisor and mentor, was the person who introduced me to medical physics and gave me an opportunity to be part of his research group. I would like to

thank him for believing in me and giving me a chance to experience being part of a scientific research lab.

Next, I would like to thank Dr. Matthew Brown and his team ambitious team, especially Greg Chu and Bharath for helping me with this work. Dr. Brown's guidance and straightforward thinking has helped me to better identify my research question and strategies to validate my answers. His ongoing contribution and improvements to QIWS has simplified research and made important sections of this work possible.

I would also like to thank our statisticians, Dr. Grace Kim and Peiyun Lu, whose contribution to this work was essential. Without their help, this work would have failed statistical significance and I very much appreciate their expertise and statistical knowledge used to improve this work.

I would like to thank all the volunteers, Jessey Sandberg, Naghmeh Eshghi, Ashley, David Orio, Karen Mok, and Carlos Flores, for making this work possible. When I joined this lab we only had 20 voxelized models with Tube Current Modulation data and with the help of all of my volunteers, I was able to create and use over 200 patients in this dissertation. I will always be thankful for their great contribution and hard work.

In the past four years, I have had the opportunity to firsthand experience the flow of pharmaceutical clinical trials and the importance of imaging lab core through MedQIA staff and my work as a QC physicist for credentialing sites and phantom studies. I would like to thank Dr. Jonathon Goldin for this once in life time opportunity and his great team of project managers, especially Laura Guzman, who has been very patient and considerate, and all the lab techs who have helped me with various tasks and supported me throughout the last four years.

Having an administrative staff that you can count on and will always provide you with the most up-to-date information on any academic procedure is a blessing. I can't thank Terry Moore and Reth Tech Im enough for making graduate life easier on me by being there for me to figure out any academic question I had. Their support has been made this experience much easier and pleasant for me.

Being able to expand our ideas to different CT manufacturers and not be limited by just Siemens alone, required collaborations with extraordinary people such as Dr. Dianna Cody, Dr. Bruce Greenberg, and Dr. Gary Arbique, who have made it possible for us to go beyond what we had available to us at UCLA. Their contribution to this work was essential and made this work worthwhile.

Next, I would like to thank my family for their support and believe in me as a scientist. When my parents moved from Iran to seek a better life in Europe and then the States, they were actually seeking this better life for my siblings and I since they had it much easier in their motherland and were established and successful citizens. Their futuristic minds have improved my life and the lives of my siblings and I will never forget their sacrifices to give us something better. I will always be grateful for my parents because I am who I am because of them and their hard work. Maman baba dusetoon daram.

At last I would like to thank my husband for simply being there for me the last years. No matter how hard it was at times, being frustrated with data or just feeing like I was not good enough, he was there to make me realize that life is not about graduate school, writing papers, or convincing people of your ideas. He has helped me see beyond my studies, and that life is also about love…

I would like to acknowledge the following grants and fellowship for funding portion of this work:

- UCLA Eugene V. Cota-Robles Fellowship (2008-2009) and (2011-2012)
- National Institute of Biomedical Imaging and Bioengineering - R01 EB004898 (2007-2010)
- Siemens Medical Solutions Master Research Agreement

The following are chapter-specific acknowledgments:

- Chapter 6 is based on research accepted as an oral presentation at 55th annual meeting of American Association of Physicists in Medicine (AAPM) 2013

Khatonabadi M, Mueller J, McMillan K, Flores C, Cody D, Cagnon C, DeMarco J, McNitt-Gray M: The Accuracy of Monte Carlo Based Dose Estimates Compared to In-Vivo Dose Measurements. Oral presentation, 55th Annual Meeting of American Association of Physicists in Medicine (AAPM); Indianapolis, Indiana. 2013

McMillan K, Khatonabadi M, McNitt-Gray M: A Classification of Validation Tasks for Monte Carlo Simulations of CT Scanners: From Simple to Complex Source Models and Geometries. Oral presentation, 55th Annual Meeting of American Association of Physicists in Medicine (AAPM); Indianapolis, Indiana. 2013

- Chapter 7 is based on research published in the journal Medical Physics and presented in 98th annual meeting of Radiological Society of North America (RSNA) 2010

Khatonabadi M, Zhang D, Mathieu K, Kim HJ, Lu P, Cody D, Demarco JJ, Cagnon CH, McNitt-Gray MF. The Accuracy of Organ Doses Estimated from Monte Carlo CT Simulations Utilizing Approximations to the Tube Current Modulation. Med. Phys. 39, 5212 (2012), DOI:10.1118/1.4736807

Khatonabadi M, Angel E, DeMarco J, Turner A, Zhang D, McNitt-Gray M, Cagnon C: The Accuracy of Organ Doses Estimated from Monte Carlo CT Simulations Utilizing Approximations to the Tube Current Modulation Function. Oral presentation, 96th Scientific Assembly and Annual Meeting of the Radiological Society of North America (RSNA); Chicago, Illinois. 2010

- Chapter 8 is based on research published in the journal Medical Physics and presented in 98th annual meeting of Radiological Society of North America (RSNA) 2010

Khatonabadi M, Kim HJ, Lu P, McMillan KL, Cagnon CH, Demarco JJ, McNitt-Gray MF. The feasibility of regional CTDIvol to estimate organ dose from tube current modulated CT exams. Med. Phys. 40, 051903 (2013), DOI:10.1118/1.4798561

Khatonabadi M, McNitt-Gray M: Linear Relationship between Average (global) and Regional Average Tube Current (mA) in Tube Current Modulated CT Scans. Oral Presentation, American Association of Physicists in Medicine (AAPM) 54th Annual Meeting; Charlotte, NC. AAPM 2012.

Khatonabadi M, Turner A, Zhang D, DeMarco J, Cagnon C , McNitt-Gray M: Linear Relationship between Organ Specific CTDIvol-Normalized Organ Dose and Patient Perimeter for Tube Current-modulated CT Scans. Oral Presentation, 97th Scientific Assembly and Annual Meeting of the Radiological Society of North America (RSNA); Chicago, Illinois. 2011

- Chapter 9 is based on research presented at the 59th annual meeting of of American Association of Physicists in Medicine (AAPM)

Khatonabadi M, Zhang D, Cagnon CH, Demarco JJ, McNitt-Gray MF: Water Equivalent Diameter (Dw) As a Patient Size Metric for Estimating Organ Dose to Patients Undergoing CT Exams. Oral Presentation, 98th Scientific Assembly and Annual Meeting of the Radiological Society of North America (RSNA); Chicago, Illinois. 2012

Khatonabadi M, Zhang D, Banola A, Doria D, DeMarco JJ, Cagnon CC, McNitt-Gray MF: Organ dose correlation with an attenuation based patient size Metric. Oral Presentation, European Congress of Radiology (ECR) 2012 Annual Meeting, Vienna, Austria, March 2012.

- Chapter 10 is based on research presented at the 98th annual meeting of Radiological Society of North America (RSNA) 2010

Khatonabadi M, Chu G, Oria D, Cagnon C, DeMarco J, McNitt-Gray M: Estimating Organ Dose From CT Scans Performed with Tube Current Modulated ScansOral presentation, 55th Annual Meeting of American Association of Physicists in Medicine (AAPM); Indianapolis, Indiana. 2013

- Chapter 11 is based on research presented at the 98th annual meeting of Radiological Society of North America (RSNA) 2010

Khatonabadi M, Zhang D, Kim G, Lu P, McMillan K, Cagnon CH, DeMarco JJ, McNitt-Gray MF: CT Dose Estimates: How closely do they approximate detailed Monte Carlo based organ dose estimates? Oral Presentation, 98th Scientific Assembly and Annual Meeting of the Radiological Society of North America (RSNA); Chicago, Illinois. 2012

VITA

December 30, 1982	Born, Esfahan, Iran
2007 – 2008	Rudnick-Abelmann Undergraduate Scholarship in Physics University of California, Los Angeles Los Angeles, California
2008	B.S., Physics University of California, Los Angeles Los Angeles, California
2008 – 2009	Eugene V. Cota-Robles Fellowship University of California, Los Angeles Los Angeles, California
2009 – 2010	Graduate Student Researcher University of California, Los Angeles Los Angeles, California
2010	Norm Baily Award for Best Student Paper Southern California Chapter of the AAPM Los Angeles, California
2010	M.S., Biomedical Physics University of California, Los Angeles Los Angeles, California
2011 – 2012	Eugene V. Cota-Robles Fellowship University of California, Los Angeles Los Angeles, California
2012 – 2013	Graduate Student Researcher University of California, Los Angeles Los Angeles, California

PUBLICATIONS

Mathieu KB, Turner AC, **Khatonabadi M**, McNitt-Gray MF, Cagnon CH, Cody DD. Varying kVp as a means of reducing CT breast dose to pediatric patients.
Phys Med Biol. 2013 Jul 7;58(13):4455-69. doi: 10.1088/0031-9155/58/13/4455.

Khatonabadi M, Kim HJ, Lu P, McMillan KL, Cagnon CH, DeMarco JJ, McNitt-Gray MF. The feasibility of a regional CTDIvol to estimate organ dose from tube current modulated CT exams. Med Phys. 2013 May;40(5):051903. doi: 10.1118/1.4798561.

Fahimian BP, Zhao Y, Huang Z, Fung R, Mao Y, Zhu C, **Khatonabadi M**, DeMarco JJ, Osher SJ, McNitt-Gray MF, Miao J. Radiation dose reduction in medical x-ray CT via Fourier-based iterative reconstruction. Med Phys. 2013 Mar;40(3):031914. doi: 10.1118/1.4791644.

Khatonabadi M, Zhang D, Mathieu K, Kim HJ, Lu P, Cody D, Demarco JJ, Cagnon CH, McNitt-Gray MF. A comparison of methods to estimate organ doses in CT when utilizing approximations to the tube current modulation function. Med Phys. 2012 Aug;39(8):5212-28. doi: 10.1118/1.4736807.

Zhang D, Cagnon CH, Villablanca JP, McCollough CH, Cody DD, Stevens DM, Zankl M, Demarco JJ, Turner AC, **Khatonabadi M**, McNitt-Gray MF. Peak skin and eye lens radiation dose from brain perfusion CT based on Monte Carlo simulation. AJR Am J Roentgenol. 2012 Feb;198(2):412-7. doi: 10.2214/AJR.11.7230.

Chong D, Brown MS, Kim HJ, van Rikxoort EM, Guzman L, McNitt-Gray MF, **Khatonabadi M**, Galperin-Aizenberg M, Coy H, Yang K, Jung Y, Goldin JG. Reproducibility of volume and densitometric measures of emphysema on repeat computed tomography with an interval of 1 week. Eur Radiol. 2012 Feb;22(2):287-94. doi: 10.1007/s00330-011-2277-1.

Turner AC, Zhang D, **Khatonabadi M**, Zankl M, DeMarco JJ, Cagnon CH, Cody DD, Stevens DM, McCollough CH, McNitt-Gray MF. The feasibility of patient size-corrected, scanner-independent organ dose estimates for abdominal CT exams. Med Phys. 2011 Feb;38(2):820-9.

CONFERENCE PROCEEDINGS

Khatonabadi M, Zhang D, Yang J, DeMarco JJ, Cagnon CC, McNitt-Gray MF: The relationship between organ dose and patient size in tube current modulated adult thoracic CT scans. In Medical Imaging 2012: Physics of Medical Imaging; San Diego, California, USA.

Zhang D, **Khatonabadi M**, Kim H, Jude M, Zaragoza E, Lee M, Patel M, Poon C, Douek M, Andrews D, Doepke L, Cagnon C, DeMarco J, McNitt-Gray M: Diagnostic accuracy at several reduced radiation dose levels for CT imaging in the diagnosis of appendicitis. Medical Imaging 2012: Physics of Medical Imaging; San Diego, California, USA.

Khatonabadi M, Sandberg J, Eshghi N, DeMarco JJ, Angel E, Turner AC, Zhang D, Cagnon CC, McNitt-Gray MF: The accuracy of estimated organ doses from Monte Carlo CT simulations using cylindrical regions of interest within organs. In Medical Imaging 2011: Physics of Medical Imaging; Lake Buena Vista, Florida, USA. SPIE; 2011: 79612G.

CONFERENCE PRESENTATIONS

Khatonabadi M, O'Connell T , Sadickson A D, Cagnon CH, McNitt-Gray MF: An Automated Method to Estimate Organ Dose from Tube Current Modulated (TCM) CT Scans Using Software to Extract Regional Tube Current Values. Oral Presentation, 99th Scientific Assembly and Annual Meeting of the Radiological Society of North America (RSNA); Chicago, Illinois. 2013.

Khatonabadi M, Zhang D, Kim H, Cody D D, Arbique G,Greenberg S, Cagnon CH, DeMarco JJ, McNitt-Gray MF: Predictive Models for Estimating Organ dose from Fixed and Tube Current Modulated CT Scans using Regional CTDIvol and Water Equivalent Diameter. Oral Presentation, 99th Scientific Assembly and Annual Meeting of the Radiological Society of North America (RSNA); Chicago, Illinois. 2013.

Khatonabadi M, Mueller J; McMillan K; Zankl M, Cody D D, Cagnon CH, Demarco JJ, McNitt-Gray MF: Validation of Monte Carlo Simulation Dosimetry Method Using In-Vivo Measurements in Patients Undergoing CT Examinations. Oral Presentation, 99th Scientific Assembly and Annual Meeting of the Radiological Society of North America (RSNA); Chicago, Illinois. 2013.

Khatonabadi M, D Oria, K Mok, C Cagnon, DeMarco J, McNitt-Gray M: Calculating Size Specific Dose Estimates (SSDE): The Effect of Using Water Equivalent Diameter (WED) Vs. Effective Diameter (ED) On Organ Dose Estimates When Applying the Conversion Coefficients of TG 204. Oral Presentation, American Association of Physicists in Medicine (AAPM) 55th Annual Meeting; Indianapolis, IN. AAPM 2013.

Khatonabadi M, G Chu, D Oria, C Cagnon, DeMarco J, McNitt-Gray M: Estimating Organ Dose From CT Scans Performed with Tube Current Modulation. Oral Presentation, American Association of Physicists in Medicine (AAPM) 55th Annual Meeting; Indianapolis, IN. AAPM 2013.

Khatonabadi M, J Mueller, K McMillan, C Flores, D Cody, C Cagnon, DeMarco J, McNitt-Gray M: The Accuracy of Monte Carlo Based Dose Estimates Compared to In-Vivo Dose Measurements. Oral Presentation, American Association of Physicists in Medicine (AAPM) 55th Annual Meeting; Indianapolis, IN. AAPM 2013.

Khatonabadi M, Zhang D, Hoffman J, Cagnon CH, Demarco JJ, McNitt-Gray MF: The Influence of Patient Centering on Organ Dose in Computed Tomography. Poster, 98th Scientific Assembly and Annual Meeting of the Radiological Society of North America (RSNA); Chicago, Illinois. 2012

Khatonabadi M, Zhang D, Kim G, Lu P, McMillan K, Cagnon CH, DeMarco JJ, McNitt-Gray MF: CT Dose Estimates: How closely do they approximate detailed Monte Carlo based organ dose estimates? Oral Presentation, 98th Scientific Assembly and Annual Meeting of the Radiological Society of North America (RSNA); Chicago, Illinois. 2012

Khatonabadi M, Zhang D, Cagnon CH, Demarco JJ, McNitt-Gray MF: Water Equivalent Diameter (Dw) As a Patient Size Metric for Estimating Organ Dose to Patients Undergoing CT Exams. Oral Presentation, 98th Scientific Assembly and Annual Meeting of the Radiological Society of North America (RSNA); Chicago, Illinois. 2012

Zhang D, Jude C M, Zaragoza E, Kim H, **Khatonabadi M**, McNitt-Gray M F: Moving Beyond Image Noise vs. CTDI: Investigating the Relationship Between Observer Performance and Patient Radiation Dose (Organ Dose) for a Clinical Task of Diagnosis of Appendicitis Using CT. Oral Presentation, 98th Scientific Assembly and Annual Meeting of the Radiological Society of North America (RSNA); Chicago, Illinois. 2012

Jude C M, Zhang D, Kim H, **Khatonabadi M**, Zaragoza E, McNitt-Gray M F: Observer Performance at Reduced Radiation Dose Levels in the CT Diagnosis of Appendicitis. Oral Presentation, 98th Scientific Assembly and Annual Meeting of the Radiological Society of North America (RSNA); Chicago, Illinois. 2012

Elgart S, **Khatonabadi M**, Adibi A, Ruehm SG, McNitt-Gray M f, Iwamoto KS: Assessing the Repair of DNA Damage from Multi-Pass CT Protocols in Human Lymocytes. Oral Presentation, 98th Scientific Assembly and Annual Meeting of the Radiological Society of North America (RSNA); Chicago, Illinois. 2012

Zhang D, **Khatonabadi M**, Jude C, Zaragoza E, Kim H, Lee M, Andrews-Tang D, Poon C, Douek M, Patel M, Doepke L, McNitt-Gray S, Cagnon C, DeMarco J, McNitt-Gray M: The Tradeoff Between Diagnostic Performance and Radiation Dose for CT Imaging in the Diagnosis of Appendicitis Across Observers with Various Levels of Experience. Oral Presentation, American Association of Physicists in Medicine (AAPM) 54th Annual Meeting; Charlotte, NC. AAPM 2012.

Khatonabadi M, McNitt-Gray M: Linear Relationship between Average (global) and Regional Average Tube Current (mA) in Tube Current Modulated CT Scans. Oral Presentation, American Association of Physicists in Medicine (AAPM) 54th Annual Meeting; Charlotte, NC. AAPM 2012.

Khatonabadi M, Zhang D, C Cagnon, DeMarco J, McNitt-Gray M: Tube Current Modulation and Patient Size Adjustment for CT Dosimetry Software ImPACT in Thoracic CT Exams. Oral Presentation, American Association of Physicists in Medicine (AAPM) 54th Annual Meeting; Charlotte, NC. AAPM 2012.

Saxon SR, **Khatonabadi M**, McNitt-Gray M, Ruehm SG, Adibi A, Iwamoto KS: Assessing the Repair of DNA Damage From Multi-Pass CT Protocols. Oral Presentation, American Association of Physicists in Medicine (AAPM) 54th Annual Meeting; Charlotte, NC. AAPM 2012.

Zhang D, **Khatonabadi M**, Cagnon C, DeMarco J, McNitt-Gray M: The Relationship of Image Noise and Organ Dose as a Function of Patient Size for Abdominal CT Exams at 5 Different Dose Levels When Tube Current Modulation Is Used. Oral Presentation, American Association of Physicists in Medicine (AAPM) 54th Annual Meeting; Charlotte, NC. AAPM 2012.

Khatonabadi M, Zhang D, C Cagnon, DeMarco J, McNitt-Gray M: Improving Size Specific Dose Estimates (TG 204): Extension to Tube Current Modulated CT Scans with Regional and Local CTDIvol Values. Oral Presentation, American Association of Physicists in Medicine (AAPM) 54th Annual Meeting; Charlotte, NC. AAPM 2012.

Khatonabadi M, Zhang D, Banola A, Doria D, DeMarco JJ, Cagnon CC, McNitt-Gray MF: Organ dose correlation with an attenuation based patient size Metric. Oral Presentation, European Congress of Radiology (ECR) 2012 Annual Meeting, Vienna, Austria, March 2012.

Zhang D, **Khatonabadi M**, Kim H, Jude M, Zaragoza E, Lee M, Patel M, Poon C, Douek M, Andrews D, Doepke L, Cagnon C, DeMarco J, McNitt-Gray M: Diagnostic accuracy at several reduced radiation dose levels for CT imaging in the diagnosis of appendicitis. Poster, European Congress of Radiology (ECR) 2012 Annual Meeting, Vienna, Austria, March 2012.

Zhang D, **Khatonabadi M**, Kim H, Jude M, Zaragoza E, Lee M, Patel M, Poon C, Douek M, Andrews D, Doepke L, Cagnon C, DeMarco J, McNitt-Gray M: The Effect of CT Dose Reduction on Performance of a Diagnostic Task. Oral Presentation, European Congress of Radiology (ECR) 2012 Annual Meeting, Vienna, Austria, March 2012.

Zhang D, **Khatonabadi M**, Kim H, Jude M, Zaragoza E, Lee M, Patel M, Poon C, Douek M, Andrews D, Doepke L, Cagnon C, DeMarco J, McNitt-Gray M: The Effect of Patient Organ Dose Reduction on Diagnostic Accuracy of a CT Clinical Task. Poster, European Congress of Radiology (ECR) 2012 Annual Meeting, Vienna, Austria, March 2012.

Saxon SR, **Khatonabadi M**, McNitt-Gray M, Ruehm SG, Iwamoto KS: DNA damage repair kinetics from ionising radiation in the range of doses experienced in CT studies. Oral Presentation, European Congress of Radiology (ECR) 2012 Annual Meeting, Vienna, Austria, March 2012.

Khatonabadi M, Zhang D, Yang J, DeMarco JJ, Cagnon CC, McNitt-Gray MF: The relationship between organ dose and patient size in tube current modulated adult thoracic CT scans. Oral Presentation, Medical Imaging 2012: Physics of Medical Imaging; San Diego, California, USA.

Zhang D, **Khatonabadi M**, Kim H, Jude M, Zaragoza E, Lee M, Patel M, Poon C, Douek M, Andrews D, Doepke L, Cagnon C, DeMarco J, McNitt-Gray M: Diagnostic accuracy at several reduced radiation dose levels for CT imaging in the diagnosis of appendicitis. Poster, Medical Imaging 2012: Physics of Medical Imaging; San Diego, California, USA.

McNitt-Gray M, Turner A, Zhang D, **Khatonabadi M**, DeMarco J, Cagnon, c: Reporting dose from CT exams: What to report and how to report it. Poster, 97th Scientific Assembly and Annual Meeting of the Radiological Society of North America (RSNA); Chicago, Illinois. 2011.

Khatonabadi M, Turner A, Zhang D, DeMarco J, Cagnon C , McNitt-Gray M: Linear Relationship between Organ Specific CTDIvol-Normalized Organ Dose and Patient Perimeter for Tube Current-modulated CT Scans. Oral Presentation, 97th Scientific Assembly and Annual Meeting of the Radiological Society of North America (RSNA); Chicago, Illinois. 2011.

Khatonabadi M, Zhang D, Mathieu K, Turner A, Cody D, Stevens D, DeMarco J, Cagnon C , McNitt-Gray M: Organ Dose-based Adjustment of mAs When Using Lower kVp for Adult and Pediatric Chest CT. Poster, 97th Scientific Assembly and Annual Meeting of the Radiological Society of North America (RSNA); Chicago, Illinois. 2011.

Khatonabadi M, Turner A, Zhang D, DeMarco J, Cagnon, C, McNitt-Gray M: The Ability of CTDIvol to Estimate Organ Doses From Typical Tube Current Modulated Abdomen/Pelvis CT Scans. Oral Presentation, American Association of Physicists in Medicine (AAPM) 53th Annual Meeting; Vancouver, BC Canada. AAPM 2011.

Khatonabadi M, Zhang D, Turner A, DeMarco J, Cody D, Stevens D, McNitt-Gray M: Organ Dose Reduction by Lowering Tube Voltage From 120kVp to 80kVp for Fixed Tube Current Chest CT Scans. Poster, American Association of Physicists in Medicine (AAPM) 53th Annual Meeting; Vancouver, BC Canada. AAPM 2011.

Khatonabadi M, Sandberg J, Eshghi N, DeMarco JJ, Angel E, Turner AC, Zhang D, Cagnon CC, McNitt-Gray MF: The accuracy of estimated organ doses from Monte Carlo CT simulations using cylindrical regions of interest within organs. Oral presentation, Medical Imaging 2011: Physics of Medical Imaging; Lake Buena Vista, Florida, USA. SPIE; 2011: 79612G.

Khatonabadi M, Angel E, DeMarco J, Turner A, Zhang D, McNitt-Gray M, Cagnon C: The Accuracy of Organ Doses Estimated from Monte Carlo CT Simulations Utilizing Approximations to the Tube Current Modulation Function. Oral presentation, 96th Scientific Assembly and Annual Meeting of the Radiological Society of North America (RSNA); Chicago, Illinois. 2010.

Khatonabadi M, Angel E, DeMarco J, Turner A, Zhang D, McNitt-Gray M, Cagnon C: The Effect of Incorrect Selection of Reference Patient Size (Adult/Child) When Using Tube Current Modulation (TCM) in CT. Oral presentation, 96th Scientific Assembly and Annual Meeting of the Radiological Society of North America (RSNA); Chicago, Illinois. 2010.

Khatonabadi M, Hall T, Boechat I, Muir S, Cagnon C, McNitt-Gray M, Borgheian S, Woo M: Reducing Radiation Exposure in Pediatric CT: A Shared Responsibility. Quality Story Board, 96th Scientific Assembly and Annual Meeting of the Radiological Society of North America (RSNA); Chicago, Illinois. 2010.

Zhang D, Cagnon C, DeMarco J, McCollough C, Cody DD, McNitt-Gray M, Turner A, **Khatonabadi M**: Estimating Radiation Dose to Eye Lens and Skin from CT Brain Perfusion Examinations: A Monte Carlo Study. Oral presentation, 96th Scientific Assembly and Annual Meeting of the Radiological Society of North America (RSNA); Chicago, Illinois. 2010.

Zhang D, Cagnon C, DeMarco J, McCollough C, Cody DD, McNitt-Gray M, Zankl M, Turner A, **Khatonabadi M**: How Do CTDI and TG111 Small Chamber Dose Perform in Estimating Radiation Dose to Eye Lens and Skin from CT Brain Perfusion Examinations for Patients with Various Sizes: A Monte Carlo Study. Oral presentation, 96th Scientific Assembly and Annual Meeting of the Radiological Society of North America (RSNA); Chicago, Illinois. 2010.

Khatonabadi M, McNitt-Gray M, Turner A, Zhang D, Angel E, Hall T, Boechat I: MO-EE-A4-03: The Effects of Incorrect Choice of Patient Size References (Adult/Child) on Tube Current Modulation. Moderated poster, American Association of Physicists in Medicine (AAPM) 52th Annual Meeting; Philadelphia, PA. AAPM; 2010: 3351.

Zhang D, Cagnon C, DeMarco J, Zankl M, Turner A, **Khatonabadi M**, McNitt-Gray M: SU-GG-I-37: Reducing Eye Lens Dose during Brain Perfusion CT Examinations by Moving the Scan Location or Tilting the Gantry Angle. Oral presentation, American Association of Physicists in Medicine (AAPM) 52th Annual Meeting; Philadelphia, PA. AAPM; 2010: 3109.

Zhang D, Cagnon C, DeMarco J, Zankl M, Turner A, **Khatonabadi M**, McNitt-Gray M: TU-A-201B-04: Estimating Dose to Eye Lens and Skin from Radiation Dose from CT Brain Perfusion Examinations: Comparison to CTDIvol Values. Oral presentation, American Association of Physicists in Medicine (AAPM) 52th Annual Meeting; Philadelphia, PA. AAPM; 2010: 3373.

CHAPTER 1: BACKGROUND AND MOTIVATION

The first medical imaging modality that made it possible to represent patient anatomy as cross-sectional 2D images was Computed Tomography (CT). It was first introduced as a head-only scanner in 1972 and quickly became the standard of practice in Diagnostic Radiology, while continuing to increase in usage and branching into other disciplines of medicine [1]. CT technology has improved beyond what once could be imagined in 1972. Improvements from higher temporal and spatial resolution to increased number of detectors, resulting in Multi-detector CT scanners (MDCT), and of course specific features and technologies to reduced radiation dose such as dose efficient solid state detectors, Tube Current Modulation, and iterative reconstruction techniques [2-4].

The discovery of X-rays in 1895 by Roentgen revolutionized the field of medicine by introducing the X-ray dependent medical specialty, radiology. CT scanners make use of X-ray tubes to produce photons. Photons are generated by first emitting electrons from cathode following thermionic emission and accelerating them towards anode by applying a high voltage power across cathode and anode. Accelerated electrons collide and interact with the anode material, which is usually tungsten in CT scanners, and covert their kinetic energy into heat and electromagnetic radiation via deceleration of charged particles, phenomenon known as bremsstrahlung. The applied voltage across cathode and anode determines the maximum energy in the bremsstrahlung spectrum. The applied peak voltage is defined as kVp and it usually ranges from 75 kVp to 140 kVp in CT scanners. The fluence of the produced photons depends on tube current, the rate of electron flow from the cathode to the anode measured in milliamperes (mA).

In CT, the product of tube current (mA) and exposure time per gantry rotation is denoted as mAs and it can be adjusted by the operator depending on the task in hand.

There are two scanning modes in CT: axial, which was introduced in 1974 and was the only mode up until 1990's when helical or spiral CT was introduced. During axial CT the table moves incrementally after each gantry rotation and acquisition of a section of the anatomy. Although early CT scanners were based on axial CT, today this mode is still used in head and perfusion CT scans. Spiral CT was made possible by slipring technology introduced in 1988, which made continuous rotation of the gantry and detectors possible. In helical mode, the table moves continuously while the detectors are rotating and acquiring images from the exposed sections using interpolation techniques. Following spiral CT was sub-second spiral CT which allowed for larger volumes to be acquired faster, resulting in shorter breath hold and patient comfort. The first multidetector scanner was introduced in 1998 with 4 slices per rotation allowing for faster image acquisition and higher temporal resolution. Following the 4 slice scanner was the 16 slice scanner, introduced in 2001 and then 64 slice scanner in 2003 and 320 slice CT scanner by Toshiba in 2007.

A consequence of these improvements has been CT's increased usage and, therefore, increased radiation dose to the population. A 2003 survey conducted in UK estimated CT's contribution to total effective population's radiation dose to be 47%, while only representing 9% of all x-ray-involved diagnostic exams [5]. A 2006 US radiation dose survey classified CT exams as the largest source of medical exposure in the United States [6]. As a result of the increased utilization of CT and, hence, increased radiation dose to the population, reducing dose from CT has become a major focus of the medical research community, resulting in dose-specific

advances either in the technology itself (e.g. Tube Current Modulation) or optimization of scanning protocols and bringing awareness to the ALARA (As Low As Reasonably Achievable) principle [7-10]. Despite new advances and dose reduction and optimization techniques, radiation dose from CT remains a well-justified concern of the public which has been increasing in the past few years [11-14].

The source of concern is the biological risk associated with exposure of individuals to ionizing radiation, which can be categorized into two kinds: deterministic and stochastic effects. Deterministic effects are the more immediate outcomes of the absorbed dose when exceeding a certain threshold (e.g. >2 Gy), which are typically much larger than doses received from CT exams (10-50 mGy). Nevertheless, deterministic effects, such as hair loss, skin injuries and reddening (erythema), cataracts, and effects such as reduction in cognitive function [15, 16], have been reported especially from CT perfusion studies, in which a specific anatomical region becomes subject to multiple repetitive scanning, and, of course, from accidental overexposures caused by operational errors.

Stochastic effects of radiation describe the potential long term effects of radiation exposure. While typical doses from CT examinations do not cause immediate cell death, the ionization process resulting from interactions, such as photoelectric effect and Compton scattering, can lead to DNA strand breaks. DNA strand breaks are more commonly caused by interaction of DNA with nearby ionized atoms, called hydroxyl radicals, which are produced by ionization of water molecules. These DNA breaks, single or double breaks in the DNA, are usually repaired by cellular repair mechanisms or the cell is forced into Apoptosis. In case of incorrect repair of DNA, cell proliferation continues despite genetic mutation and can eventually lead to

carcinogenesis. Risk from radiation has been described using the linear no-threshold model (LNT), which is based on epidemiological studies including data from 1945 atomic bomb survivors. Radiation dose from CT is considered to be low dose with low linear energy transfer (LET) radiation and radiobiological effectiveness (RBE) of about unity [17]. The accuracy of the LNT model at low doses, such as those typically observed with CT, has been questioned and continues to be a controversial topic. Nevertheless, absorbed dose levels from CT exams are reported to increase risk of carcinogenesis and that this risk decreases with age [14]. Additionally, it has been shown that the most proper metric for assessing risk from ionizing radiation is radiation dose to individual organs exposed to radiation [14, 18-21]. Concerns discussed above suggest that it is necessary to properly assess and monitor radiation dose from CT examinations, in particular radiation dose to individual organs, in order to be able to assess risk.

1.1 Consequences from Rising Concerns on CT Radiation Induced Risk

Concerns about stochastic effects of ionizing radiation have had a tremendous impact on the medical imaging community. One major consequence from these concerns has been the continuous recommendation of reporting and tracking of radiation dose for individual patients undergoing CT exams using patient DICOM dose report, initiated by various agencies and governing bodies such as National Institute of Health (NIH), Food and Drug Administration (FDA), The Joint Commission (TJC), International Atomic Energy Agency (IAEA), American College of Radiology (ACR), and Image Gently. Additionally, the State of California has mandated health facilities to record dose from CT exams under Assembly Bill No. 510 [22-26].

Additional steps towards acknowledging concerns from CT have been initiated by Medical Imaging and Technology Alliance (MITA) and American Association of Physicists in Medicine (AAPM), to generate a set of notification values for CT scans called the "Dose Check" standards, which provides an alert to the CT operator when the scan exceeds pre-determined recommended radiation dose values [27].

Other discussions rising from concerns on CT radiation dose are the assessment of risk versus benefit of CT examinations for an individual. These discussions include but are not limited to justification of ordered CT and the overall net benefit to the patient, potential alternatives to CT, especially for pregnant and younger patients, and communication of risk versus benefits to the patient and the referring physician. A recent publication, investigating patient outcome and predicted cancer risk from CT in young adults, showed that risk of death from the actual illness which resulted in ordering the CT scan is more than an order of magnitude greater than death from radiation induced cancer [28].

Overall, nearly every response to concerns regarding dose from CT has involved reporting, monitoring, and tracking of dose from individual CT exams. Although there are uncertainties regarding the actual magnitude of the probability of radiation-induced cancer, the best approach to respond to these concerns is to know the quantity of dose, to monitor it, to track it, and to report it in order to try to reduce it. In addition to the usefulness of capturing radiation dose information for individual patient as a mean for practicing ALARA, accurate dose estimates can be a very valuable dataset for future epidemiological studies for associating radiation dose with risk, in particular with carcinogenesis. But what is the current measure of CT radiation dose and how accurate are these measurements?

1.2 Conventional CT Dosimetry Assessment and Its Limitations

The current measure of radiation dose from CT, which is reported in patient's DICOM dose report and is used to monitor scanner's output, is based on the Computed Tomography Dose Index (CTDI) [29]. The original CTDI was defined as the radiation dose measured from 14 contiguous sections normalized to the width of the beam [30]:

$$CTDI = (\frac{1}{nT}) \int_{7T}^{7T} D_{Single}(z)dz \qquad \textbf{Eq. 1-1}$$

where n is the number of sections, T is the thickness of the section, and D_{Single} (z) is the dose at point z for a single axial scan. Later on, this index was replaced with $CTDI_{100}$ to use the length of the ion chamber itself, which is 100 mm, as the length of the integration rather than the 14 sections [31].

$$CTDI_{100} = (\frac{1}{NT}) \int_{5\ cm}^{5\ cm} D_{Single}(z)dz \qquad \textbf{Eq. 1-2}$$

where N is the number of channels and T is nominal width of one channel.

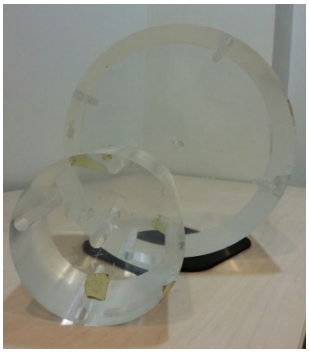

Figure 1-1 32 cm (body) and 16 cm (head) PMMA CTDI phantoms used in CT dosimetry with drilled holes at center and periphery locations for insertion of the 100 mm ionization chamber.

This index utilizes standard cylindrical polymethyl methacrylate (PMMA) phantoms of 32 cm (body phantom) and/or 16 cm (head phantom) diameters (Figure 1-1). It was developed to estimate the collected dose to the center of the scan length from a contiguous axial scan using a 100 mm ionization chamber inserted into the phantom.

Since the dose distribution within the phantom is not homogenous, another modified version of CTDI was developed to average this distribution and was called weighted CTDI ($CTDI_W$), which is defined as the weighted average of the measured central and peripheral doses:

$$CTDI_w = (\frac{1}{3}CTDI_{100})_{Center} + (\frac{2}{3}CTDI_{100})_{Periphery} \qquad \textbf{Eq. 1-3}$$

$CTDI_{vol}$ was the next modification which takes into account helical pitch values different than one in helical CT scans [30, 32-34] and is defined as:

$$CTDI_{vol} = \frac{CTDI_w}{pitch} \qquad \textbf{Eq. 1-4}$$

Today this index is the value reported at the scanner and in the patient's DICOM dose report along with Dose-Length Product (DLP) which is the product of $CTDI_{vol}$ and the scan length in units of mGy*cm.

CTDI is used to monitor a scanner's output for quality assurance and "optimization of patient protection in CT" [35]. It is the standard method for credentialing and assessing scanners. As the name suggests, CTDI is an index for quantifying the radiation output of the scanner by measuring dose to a simple geometry, namely dose to a standard PMMA phantom, and therefore, it is not patient dose [36]. Furthermore, $CTDI_{vol}$ was developed to measure a scanner's output from a fixed tube current scan. In fixed tube current CT scans a single constant tube current

value is utilized along the entire scan length. Figure 1-2 illustrates the tube current versus table position in a fixed tube current CT scan.

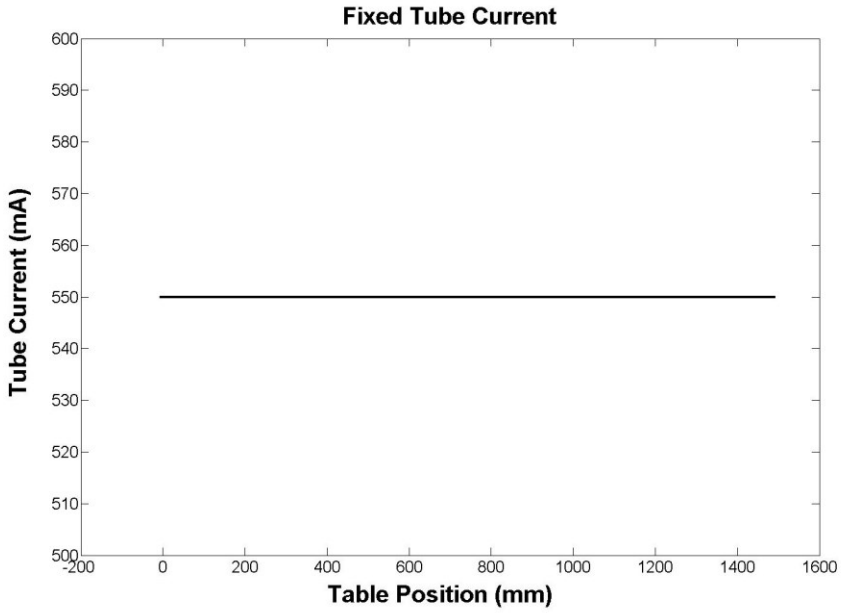

Figure 1-2 An example of fixed tube current CT exam, illustrating a constant tube current (mA) versus table location (mm).

With the advent of Tube Current Modulation (TCM), $CTDI_{vol}$ has again been adjusted. Tube current modulated CT scans no longer make use of a constant tube current to acquire images, but modulate the tube current based on patient size and attenuation. Figure 1-3 demonstrates the tube current versus table position for a tube current modulated CT scan.

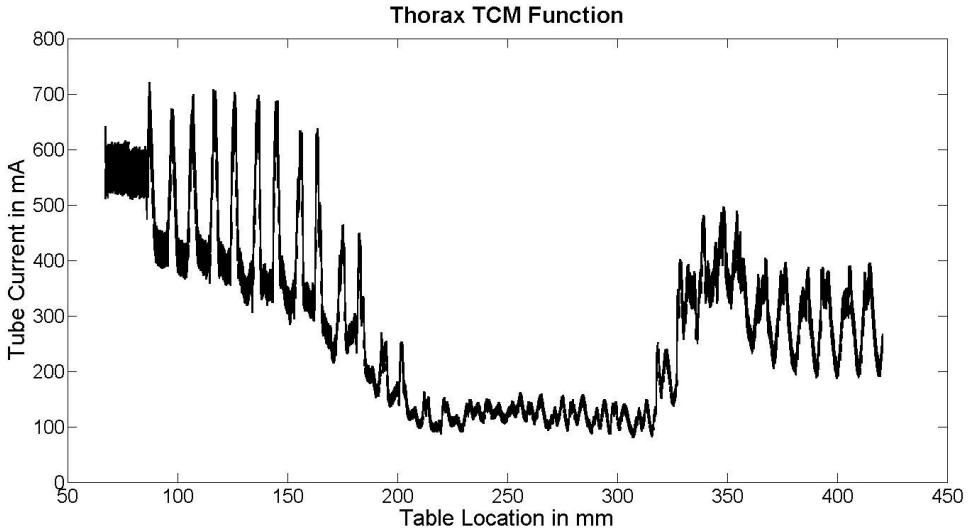

Figure 1- An example of a thorax TCM function, consisting of both x-y and z-axis modulation of the tube current. The tube current (mA) and table location (mm) were extracted from the raw projection data of the TCM exam.

The International Electrotechnical Commission (IEC) has defined $CTDI_{vol}$ for a tube current modulated CT exam (in the standard 60601-2-44 of IEC [37]) as the $CTDI_{vol}$ based on a single averaged tube current value over the entire scan (Figure 1-4). While the original definition of $CTDI_{vol}$ assumed a constant tube current (and therefore technically cannot be defined for a variable tube current scan), this practical definition is now adopted and is the method by which $CTDI_{vol}$ is being reported on scans performed with TCM in current clinical practice (e.g. the dose reports provided by scanners). The average tube current value used to calculate a $CTDI_{vol}$ value for a particular scan can be very different depending on the scanned region. Therefore, the scanner-reported $CTDI_{vol}$ needs to be used cautiously, since it may or may not represent scanner's output at a specific table location.

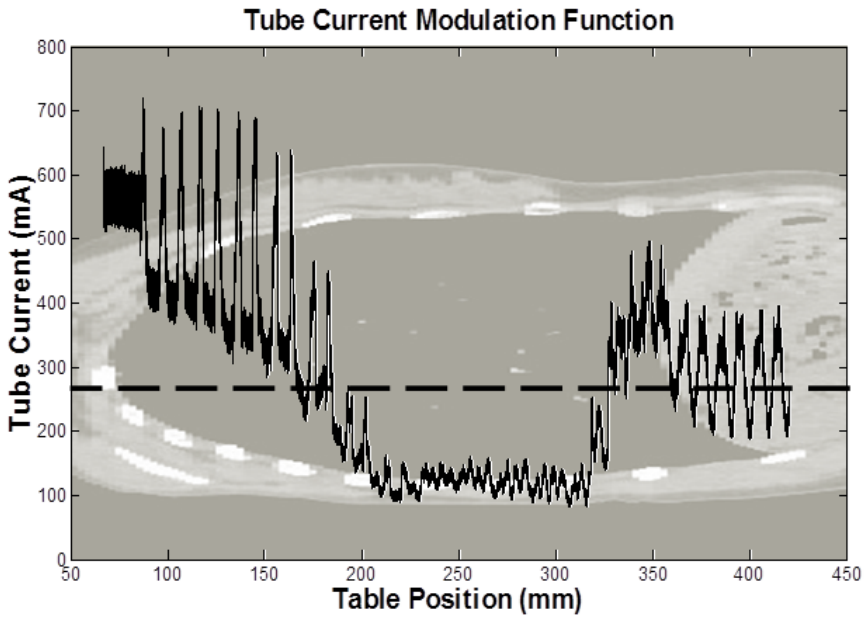

Figure 1-4 TCM function and the average tube current (mA), shown as the dashed line across the scan length, used to calculate a $CTDI_{vol}$ value. This value is reported on patient dose report as the dose from a specific exam.

Therefore there is a need for an adjustment to $CTDI_{vol}$ for tube current modulated CT scans for representing scanner's output more accurately. This adjustment can employ a region-specific or even an organ-specific average tube current value for calculating regional and/or organ-specific $CTDI_{vol}$ (Figure 1-5). Chapter 8 will examine the feasibility of using regional and organ specific $CTDI_{vol}$ to describe TCM exams.

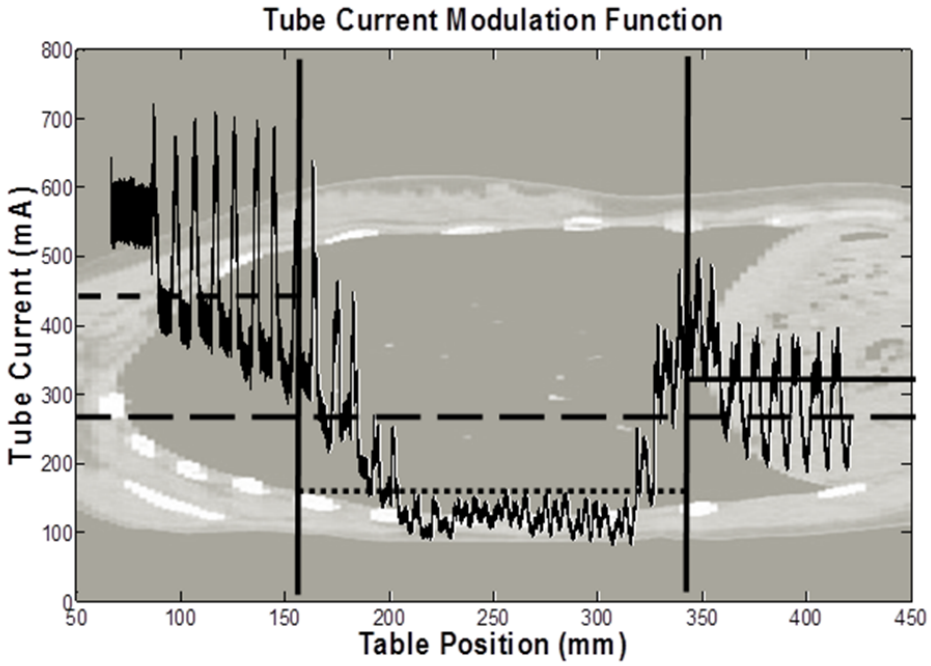

Figure 1-5 Regional adjustments of currently reported $CTDI_{vol}$ for tube current modulated CT exams, by employing multiple $CTDI_{vol}$ values calculated based on regional average of the same attenuating properties.

Regardless of CTDI's limitations, it has been used as a dose metric and continues to be the metric used to report patient dose. For a given set of scan parameters, the scanner's output is the same regardless of whether there is a patient on the table or a cylinder, namely the 32 cm CTDI phantom. However, what is different is the amount of radiation that is absorbed (i.e. the absorbed dose), which depends on shape, size, and composition of the scanned object. If absorbed dose was not dependent on shape, size, and composition, then the ratio of dose to $CTDI_{vol}$ would be a constant value. However, the ratio of dose and $CTDI_{vol}$ is a variable that depends on patient's size, shape, and composition. In other words, $CTDI_{vol}$ depends on the scan parameters used such as the tube voltage, tube current, pitch, exposure time, collimation, and filtration, but it is independent of patient size, meaning two patients of different sizes scanned with the same scan

parameters as mentioned above will have the same $CTDI_{vol}$ value. This is just one reason why $CTDI_{vol}$ is a good measure of scanner output, but not a good measure of patient absorbed dose.

Scanner reported $CTDI_{vol}$ is either reported based on the 16 cm head phantom or the 32 cm body phantom, depending on the exam type; for torso exams the 32 cm phantom and for head exams the 16 cm phantom is used to report $CTDI_{vol}$. Usually on the DICOM dose report it is specified which phantom was used. It is apparent that $CTDI_{vol}$ needs to be adjusted for patient size in order to be a useful quantity. Figure 1-6 recaps currently used $CTDI_{vol}$ to report dose from both fixed and TCM CT exams.

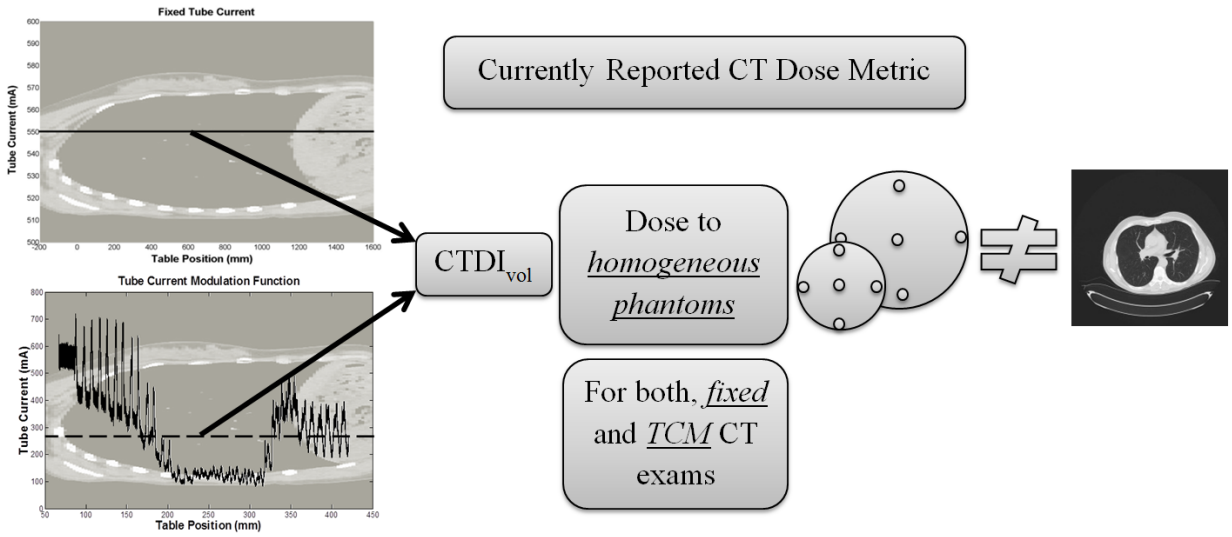

Figure 1-6 A summary of currently used $CTDI_{vol}$ metric as a CT dose metric. This index is dose to homogenous cylinders of either 16 or 32 cm in diameter and can only be reported for a single tube current (mA) value, hence, in TCM, an average mA is first determined for calculating a $CTDI_{vol}$ value for the exam.

1.3 Effective Dose and Its Limitations

Effective Dose was introduced in 1977 by the International Commission of Radiation Protection (ICRP) to provide a summation of doses to radiosensitive organs and tissue subject to ionizing radiation for radiological protection [14, 18-21, 30, 32]. It is defined as:

$$ED = \sum_T W_T H_T \ \ with \ \sum_T W_T = 1 \qquad \textbf{Eq. 1-5}$$

where W_T are dimensionless tissue weighting factors differentiating the relative sensitivity of different organs and tissues with respect to cancer induction and mortality. H_T is the individual organ equivalent dose from tissue/organ T and takes into account the relative biological damage imparted from energy deposition of different types of particles. Effective dose is measured in Sieverts (Sv) and is frequently used to compare radiological examinations with similar diagnostic information and different sources of radiation and naturally available radiation such as background radiation.

Effective dose reflects the risk of non-uniform dose distribution in terms of a uniform, whole body exposure to ionizing radiation. This means dose from a variety of different modalities can be represented and compared to a whole body equivalent dose value, although radiation dose to individual organs might vary across different modalities.

There are two common methods to calculate an effective dose from CT procedures: the original method, which is based on actual organ dose estimates [20, 21, 38, 39], and the more simplified method based on DLP and effective dose conversion coefficients, the *k* factors [5, 40, 41]. Although the latter approach does not require the knowledge of individual organ doses, it is subject to great uncertainties. Calculated effective dose using *k*-factors is not specific to any

single scanner because it is based on data averaged over many scanners and models. Additionally, effective dose based on DLP and *k*-factors is based on tissue weighting factors in ICRP report 60, which were recently revised in ICRP 103. Furthermore DLP is calculated based on scanner-reported $CTDI_{vol}$ value, which in tube current modulated CT examinations is a single averaged value over the entire scan length and might result in under or over-estimation of calculated DLP depending on the type of the exam.

In terms of risk, because effective dose was designed to reflect overall risk averaged over all ages and both sexes for a reference patient, neither method of calculating effective dose (Monte Carlo based organ dose estimates nor the DLP-based *k*-factors) should be used to estimate risk to individual patients. Effective dose provides only an approximate estimate of true risk and therefore should not be used for epidemiologic studies or representation of risk to any one individual.

Another available risk estimation method is provided by conversion factors based on organ doses published by the National Research Council's report on the Biological Effects of Ionizing Radiation (BEIR VII) [18]. This report can be used to calculate the probability of radiation-induced cancer for different radiosensitive organs in males and females with ages from 0 to 80 years old. However, calculation of these probabilities require dose to individual organs. The biggest limitation of BEIR VII [18] is the lack of data. The BEIR VII authors, after analyzing a large number of studies of various populations, conclude that the only studies that meet all their criteria are those of the Japanese atom-bomb survivors. And even those are not perfect: dose was not measured directly, but reconstructed as a function of distance from the blasts. And it is a one-time dose, not continuing. Perhaps the biggest limitation of BEIR VII [18] is that there are not enough numbers of exposed people to investigate reliably the small increases in the incidence of

cancer that small exposures to radiation may cause. So the BEIR VII numbers have large associated uncertainties, and uncertainty in what the uncertainties might be.

As mentioned previously, it has been shown that the most proper metric for assessing risk from ionizing radiation is radiation dose to individual organs exposed to radiation [14, 18-21]. Dose to individual organs exposed to ionizing radiation while accounting for patient's body size and attenuation properties can eventually be useful for individual risk estimates or epidemiologic studies. However, as described in the last two sections, currently available dose estimates and risk methods are very limited. $CTDI_{vol}$, as mentioned before, is not organ dose but simply dose to a homogenous cylindrical phantom used to assess scanner's output. While effective dose is only an approximate estimate of actual risk from low dose ionizing radiation and should not be used to estimate risk to individual patients, it is used frequently as a risk metric in CT dosimetry, calculated mostly using exam's DLP and region-specific k-factors. Although the probability of radiation-induced cancer calculated using data from BEIR VII is more descriptive and easy to understand by general public, it requires quantification of dose to individual organs, which is not easily obtainable. Next section describes different methods and challenges in obtaining dose to individual organs.

1.4 Organ Dose Estimation Methods

As mentioned in the previous section, $CTDI_{vol}$ represents dose to a homogenous PMMA phantom and not dose to individual patients or organs. However, to assess the risk of CT examinations dose to individual organs is preferred but hard to obtain. There are essentially two ways to obtain organ dose estimates, (a) perform physical measurements and (b) use Monte Carlo simulations.

Physical measurements are performed using dosimeters such as ionization chambers, thermoluminescence Detectors (TLD), Optically Simulated Luminescence detectors (OSL), and Metal Oxide-silicon Semiconductor Field Effect Transistor detectors (MOSFET). All the above mentioned detectors, except for ionization chambers, have a high energy-dependent response at low energy beams and require calibration before absolute dosimetry measurements. The calibration process is not only long and error prone; it is also hard to calibrate these inside the geometry using ionization chambers due to small holes specially drilled for detectors such as TLDs. Therefore, usually these are only calibrated against an ionization chamber placed in air. It is important to calibrate these dosimeters not only in air, but also in the object of interest because of beam hardening and hence an increase of the average energy in the object.

Physical measurements are usually performed in anthropomorphic phantoms with tissue equivalent materials to better represent attenuation properties of patients [42-48]. Although these physical phantoms are very advanced and commercially available in various age groups, they fail to adequately represent different patient sizes and compositions. In-vivo measurements are possible, but are invasive and therefore not preferred. UT-MD Anderson recently performed physical in-vivo dose measurements using TLDs which were affixed to the inner lumen of the tip of the catheter used in their Virtual Colonoscopy protocol.

An alternative to physical measurements are Monte Carlo radiation transport codes, which simulate the delivery of radiation from CT scanners to patient models. For accurate dose estimates, these codes require detailed knowledge of the x-ray source in terms of spectrum and filtration information. Additionally, accurate patient models with identified regions of interest, in which energy deposition is simulared, are required. Chapter 4 describes the Monte Carlo radiation transport code, MCNPX, used in this dissertation for organ dose simulations.

Some of the limitations of Monte Carlo methods, besides the highly computational demand, are insufficient patient models capable of representing a variety of different sizes and body habitus and the limited options available for validation of Monte Carlo dose estimates.

Creating voxelized patient models for the purpose of Monte Carlo simulations is a very time consuming process and mostly requires detailed segmentation of individual organs so dose can be tallied in these organs. Chapter 5 summarizes different types of models used in Monte Carlo simulations along with their limitations and describes the process of generating voxelized models from actual patient axial CT images using a combination of segmentation (of only organs of interest) and Hounsfield Unit (HU)-to-tissue lookup tables. The advantage of these types of voxelized models generated from actual patient images over mathematical and computational models is the availability of the TCM function which can be used in Monte Carlo simulations for estimation of dose from TCM CT scans. The look-up table used to generate voxelized models used in this dissertation is validated in chapter 6.

As mentioned above, another major limitation of Monte Carlo based simulation packages is the inadequate validation experiments for ensuring accurate estimates. Most commonly used validation experiments are carried out using simple homogenous phantoms such as CTDI phantoms. Due to their cylindrical and homogenous composition in x,y, and z directions, these phantoms should not be used for validation of Monte Carlo TCM simulations. In Chapter 6 the Monte Carlo simulation package used to estimate dose from tube current modulated CT scans is validated using simple to complex anthropomorphic phantoms along with simulations of in-vivo dose measurements performed at UT-MD Anderson.

Patient TCM information is not readily available for Monte Carlo simulations and requires special programs capable of extracting tube current data from raw projection data. Chapter 7 describes different alternatives and approximation methods that can be used to estimate dose from TCM scans using Monte Carlo simulations. These methods include estimating dose from z-axis-only modulation of the tube current extracted from axial CT images. Figure 1-7 illustrates an example of detailed and z-axis-only TCM function. These alternatives are compared to actual Monte Carlo simulation of TCM scans using detailed information of the tube current extracted from raw projection data.

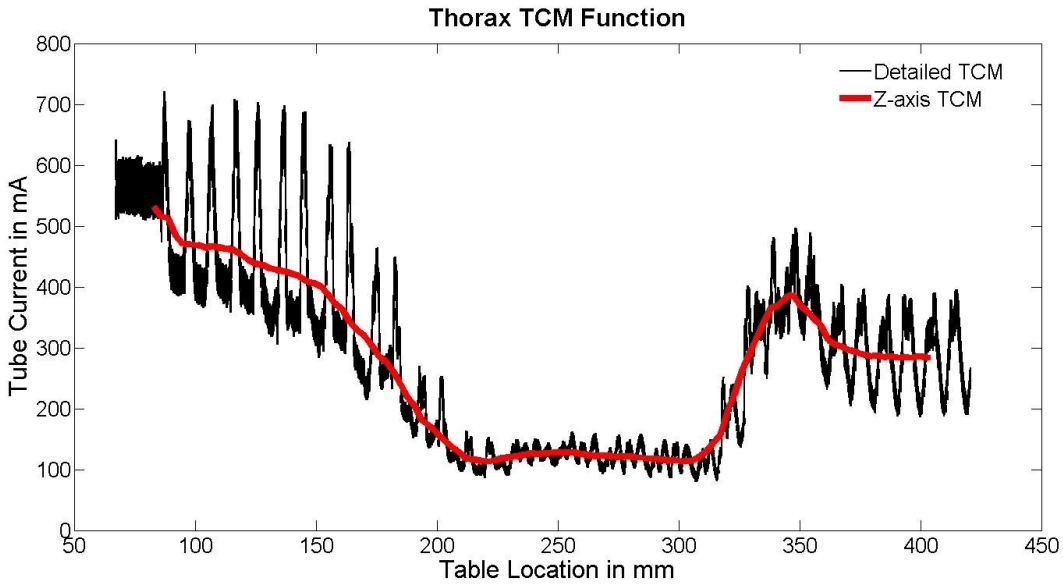

Figure 1-7 An example of a detailed TCM function (in black) versus z-axis-only TCM function (in red). Z-axis-only TCM function does not require raw projection data and is available in the DICOM header of individual images.

1.5 TASK GROUP 204 AND ITS LIMITATIONS

The limitation of $CTDI_{vol}$ to account for patient size was the focus of AAPM Task Group 204, which established conversion factors applied to the scanner-reported $CTDI_{vol}$ to adjust for patient size [49]. The developed conversion factors are based on both fixed tube current measurements and Monte Carlo simulations performed by multiple groups [36, 50, 51], including the work of Turner et al., in which it was shown that $CTDI_{vol}$ can be used to account for radiation output differences among CT scanners and protocols, by normalizing organ doses by $CTDI_{vol}$ and correlating $CTDI_{vol}$-normalized organ doses (denoted as $\overline{nD}_{organ}$) with patient perimeter. For each organ a unique set of empirically determined A and B coefficients were generated to correlate $\overline{nD}_{organ}$ with patients' perimeters using an exponential relationship between organ dose, $CTDI_{vol}$, and patient size ($\overline{nD}_{organ} = A\, exp(B \times perimeter)$). For each patient undergoing a CT exam, the scanner-reported $CTDI_{vol}$ along with patient's perimeter could be used to estimate organ doses from fixed tube current CT exams. However, these coefficients were generated from fixed tube current scans (Figure 1-2), and therefore could only be applied to patients undergoing CT examinations with constant tube current. Figure 1-8 summarizes the concept of SSDE and its calculation.

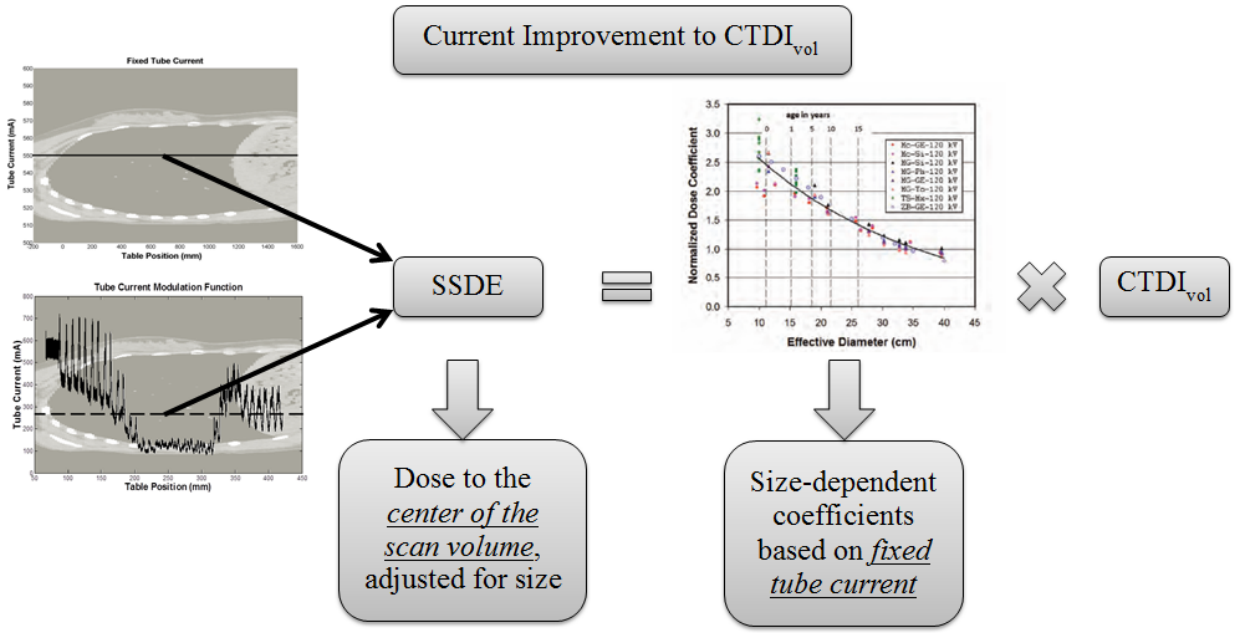

Figure 1-8 A summary diagram of recently published SSDE, which adjusts scanner-reported $CTDI_{vol}$ for size using size-dependent (effective diameter) coefficients developed from fixed tube current dose measurements and simulations. SSDE is also reported for TCM exams despite its inability to take into account varying tube current.

Considering the fact that almost all clinical protocols utilize TCM, there is a need to generate similar coefficients that take into account TCM. Chapter 8 investigates the feasibility of regional and organ-specific tube current information to account for TCM in dose estimations. Additionally, coefficients introduced by Turner et al., were generated using simulated abdominal organ doses within only 8 mathematical models with perimeters ranging from 36 to 125 cm. Therefore, there is also a need to expand on the patient models and different anatomical regions that formed the basis for these coefficients for a more robust dose estimation model.

The same limitation is observed with the AAPM TG 204 report. Although the report describes Size Specific Dose Estimates (SSDE) for body exams, it should not be used to address scans performed with tube current modulation, because the conversion factors are established based on

fixed tube current measurements and simulations. In addition, the size adjusted $CTDI_{vol}$ is by no means the same as organ dose, but rather dose to the center of the scan volume in which the type of CT exam is not specified.

Another limitation of the TG 204 report and the above mentioned studies is the inability of the chosen patient size metrics (perimeter, effective diameter, anterior-posterior (AP) width, lateral (LA) width, and summation of the AP and LA width) to describe patient's composition and attenuation properties. Organ dose and $CTDI_{vol}$ would be directly proportional if dose did not depend on size, shape, and composition; therefore the metric chosen to describe the patient, has to take all of these characteristics into account, especially when TCM is used. A specific TCM profile is not only the result of patient's size but it modulates according to patient attenuation properties as well; hence, an attenuation metric should be a more appropriate size metric for describing organ dose. As an example, the measured effective diameter of a patient taken in the thoracic area and abdominal region can be the same, but due to lower density and attenuation properties of lung compared to abdomen, for the same amount of CT output, the thorax will have a higher absorbed dose than abdomen (Figure 1-9).

Chapter 9 compares currently used effective diameter with attenuation-based metrics using their correlations with normalized organ dose in both thoracic and abdominal regions to establish the most appropriate size metric for organ dose estimation.

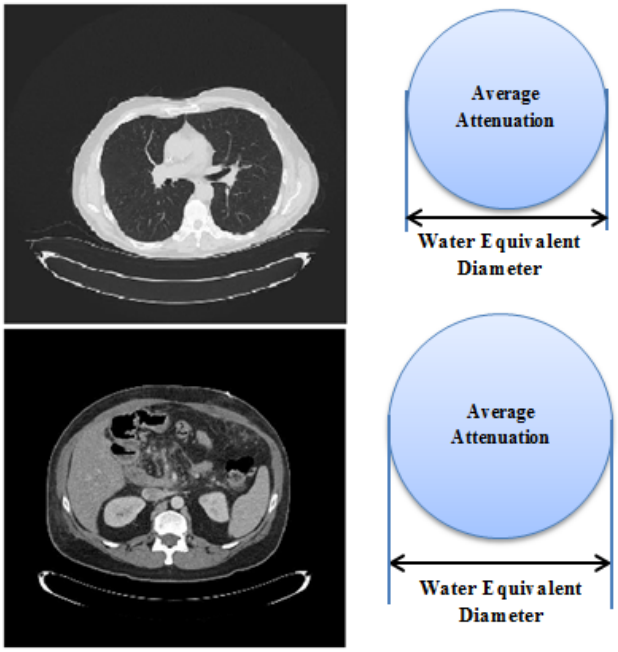

Figure 1-9 Shown are two regions, thorax and abdomen, with the same effective diameter but different average attenuation. Water equivalent diameter is described as the diameter of a circle of water with equal attenuation as the patient.

1.6 Discussion and Overview

Although quantifying and reporting of radiation dose has proven to be an important step towards understanding biological effects of radiation, there is not a feasible way of measuring dose to individual organs. Instead, Monte Carlo simulations have been a reasonable alternative to physical measurements. Two major limitations of MC based simulation methods are the high computational demand and limited patient models available for use in MC simulations. Due to these limitations, a number of groups have been creating look-up tables that utilize $CTDI_{vol}$ and a patient size metric to estimate organ doses using a limited number of models. AAPM Task Group 204 published conversion factors based on measurements and Monte Carlo simulations to adjust scanner-reported $CTDI_{vol}$ for patient size and calculate Size Specific Dose Estimates (SSDE). However, this report did not take into account Tube Current Modulation (TCM), which

is utilized in almost every clinical protocol. In addition, currently used size metrics take into account only physical morphological measures such as perimeter, but do not account for patient's composition or density (such as low attenuating lungs in the thoracic region).

Considering the limitations outlined above, it is apparent that there is a need for introducing both a new patient size metric capable of describing individual patient's attenuation properties for better dose estimates and an adjusted $CTDI_{vol}$ which accounts for regional variations within a single CT exam due to modulation of the tube current; providing both of these improvements will result in improved ability to estimate organ dose for scans using TCM.

Figure 1-10 summarizes currently used CT dose metrics with new contributions as a result of this dissertation.

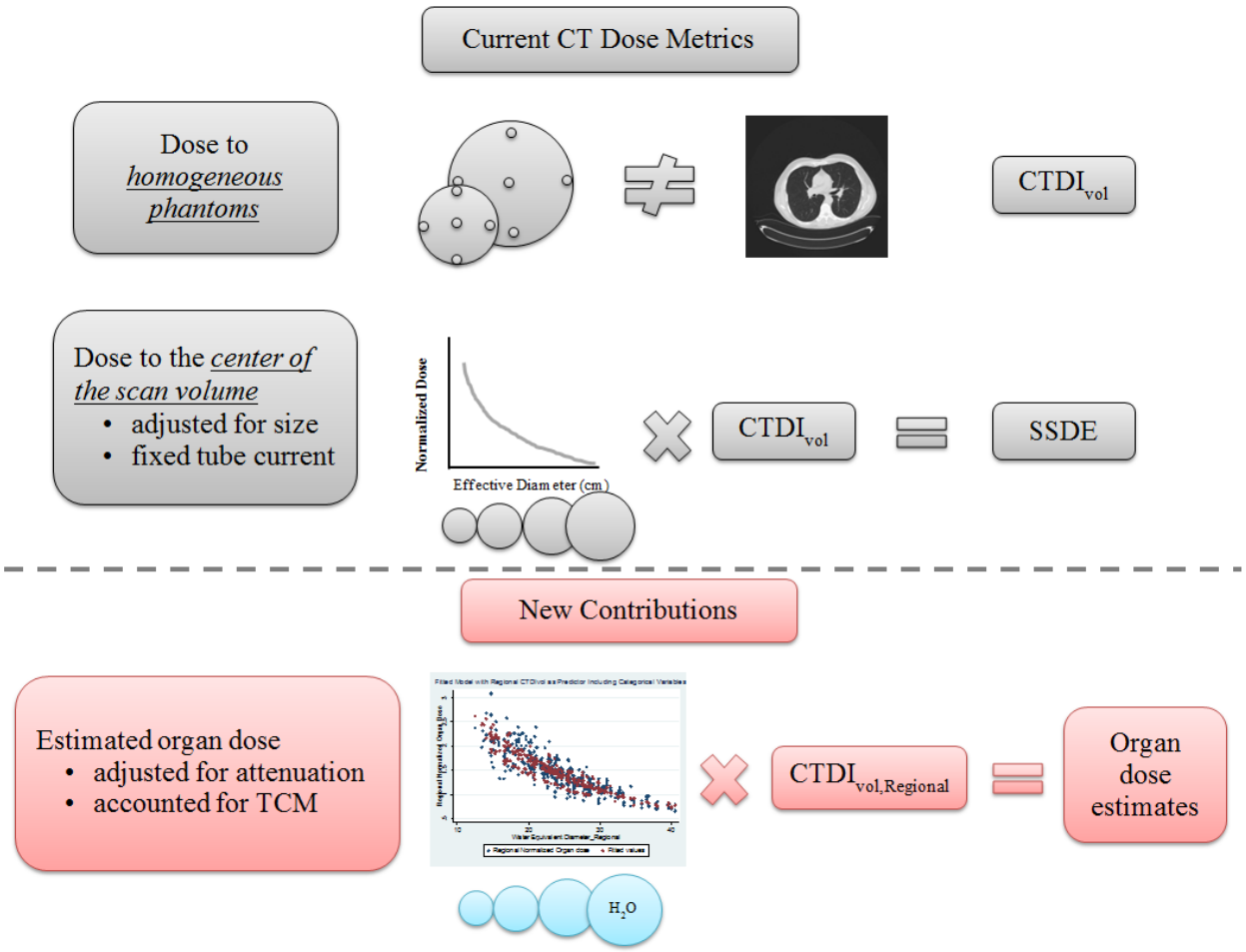

Figure 1-10. Currently used CT dose metrics are shown with definitions and limitations along with new contributions to the field of medical physics achieved as a result of this dissertation.

CHAPTER 2: SPECIFIC AIMS

The goal of this dissertation is to develop a robust predictive model that can estimate organ doses from tube current modulated CT exams. This work starts off with a detailed validation of a previously developed Monte Carlo simulation package which can utilize patient-specific TCM information for estimating organ dose from tube current modulated CT exams. In order to estimate organ dose from TCM exams, detailed tube current information for each individual exam is required for the simulations. This information can be extracted from the raw projection data of individual scans, hence, it is not readily available from CT manufacturers and therefore effective approximation methods had to be employed. Furthermore, to be able to account for the variation of the tube current across a single CT scan, adjustment methods to the currently used CT metric, $CTDI_{vol}$, which can be utilized as a normalization quantity, had to be explored and established. Additionally, a more appropriate size metric capable of describing patient's composition and attenuation properties was investigated and used as a predictor of organ dose from tube current modulated CT exams.

The overall hypothesis of this research is that accuracy of estimation of organ dose from Computed Tomography exams can be improved by taking into account the commonly used feature in CT protocols, Tube Current Modulation, employing a more appropriate CT dose metric for TCM exams, and a patient size metric capable of describing attenuation properties of the patient. To carry out the proposed research, the specific aims of this study are as follows:

SA-1 To validate a Monte Carlo based model of a tube current modulated CT scan by comparing point measurements performed in different geometries, from simple to complex, with Monte Carlo simulations.

SA-2 To investigate the feasibility of a TCM-adjusted CT Dose Index (CTDI) that can take into account regional variations of tube current observed within a single CT exam for improving accuracy of organ dose estimation in CT examinations utilizing TCM.

SA-3 To investigate attenuation-based patient size metrics that take into account both patient morphology and composition for accurate estimation of organ dose from tube current modulated CT scans.

SA-4 To assess the generalizability of the CT dose and size metrics derived from specific aims 1 and 2, in predicting organ dose across CT scanners from different manufacturers.

CHAPTER 3: TUBE CURRENT MODULATION IN MDCT SCANNERS

3.1 INTRODUCTION

CT manufacturers began implementing Automated Exposure Control (AEC) systems into CT scanners over a decade ago, and today most clinical protocols use AEC to reduce radiation dose from CT exams while maintaining appropriate image quality. All clinical protocols at UCLA medical center make use of this feature except for neuro-perfusion CT studies, which are performed using a fixed tube current.

One form of AEC is Tube Current Modulation (TCM) in CT; this results in modulation of the tube current across a single exam. The concept of TCM was first introduced by Kalender and Gies in 1998 as a mean of dose reduction for CT exams, without increasing pixel noise. The principle idea was to distribute the dose for a full rotation using patient's attenuation as the driving force of tube current [52-54]; increasing tube current in projections that are more attenuating and reducing tube current for less attenuating projections. In the thorax, this typically means increasing the tube current in the LAT (lateral) projections while reducing tube current in the AP (anterior-posterior) or PA (posterior-anterior) projections.

Pixel noise is the sum of the square of individual projection noise and it is mainly affected by highly attenuating path lengths, i.e. quantum noise. Quantum noise, or statistical noise, is the result of too few photons reaching the detector after traversing a longer, higher attenuating path length within the object. Therefore pixel noise can be kept constant by increasing the tube current (mA) for longer, higher attenuating projections, while decreasing the mA for shorter, lower attenuating path lengths. Figure 3-1 illustrates the concept behind constant pixel noise.

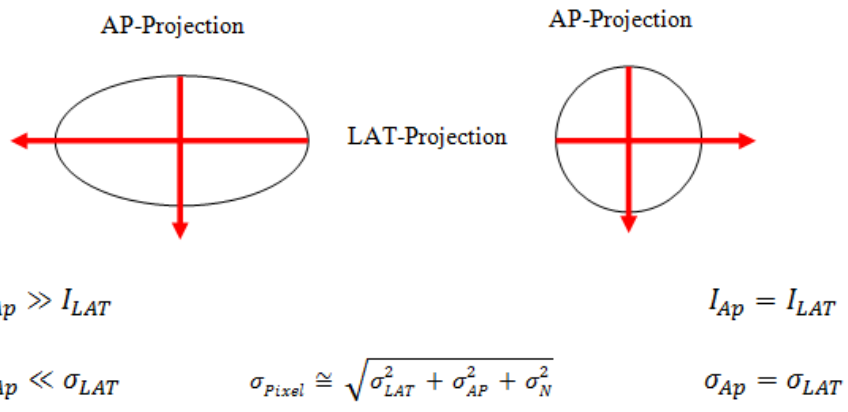

Figure 3-1 An illustration of the output intensity in two different objects and their corresponding noise values. The shape and therefore the attenuation of the elliptical object can be made use of to modulate the initial intensity to achieve similar noise values from both, AP and LAT projections, hence, reducing dose without increasing pixel noise [53].

TCM consists of two types of modulations: the angular or x-y modulation, which is the modulation in the x-y or axial plane, and the z-axis, longitudinal modulations, which describes the modulation of the tube current along the z-axis [55].

The angular or x-y modulation changes the tube current based on the projection's path length through the patient. This is in contrast to a fixed tube current scan where a constant tube current value (mA) is used for all the projections. In angular modulation, for less attenuating path lengths, the tube current decreases, while for more attenuating path lengths it increases to compensate for the greater attenuation in order to keep the overall pixel noise unchanged [52, 54]. Angular modulation is recognized by the peaks and valleys in the TCM function. The mA variance between the peaks and valleys depends on the degree of the asymmetry of the scanned object. For example, a more pronounced difference between the mA value of the LAT and AP projection is observed in the regions of shoulders and pelvis, while there is minor angular

modulation in the head, which is more symmetric and circular. Figure 3-2 illustrates the basic principles of the angular modulation.

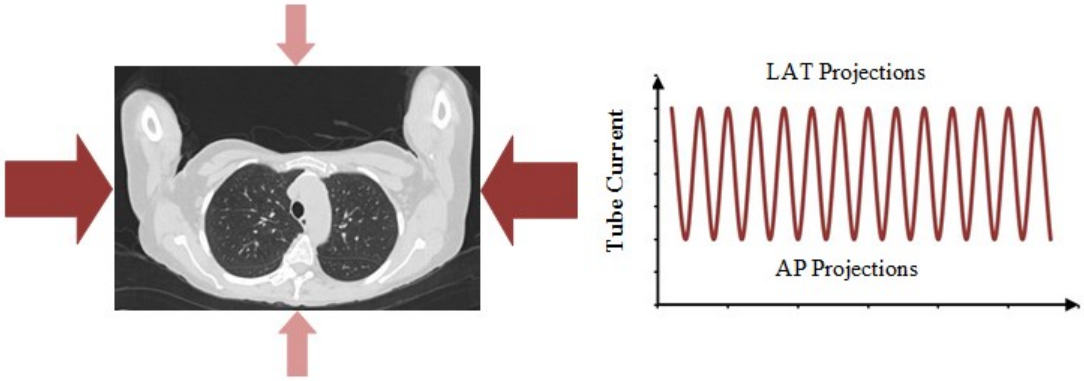

Figure 3-2 Angular modulation of the tube current based on the projection's path lengths which results in peaks and valleys within the TCM function.

Although the basic principle of angular modulation is the same across CT scanners from different manufacturers, the implementation is different. Some scanners make use of LAT and AP localizer scans as an attenuation map to estimate the size of the patient in either direction to establish the asymmetric properties for adjusting tube current. Some use the information from a single localizer along with a predefined sinusoidal function to adjust the tube current. Another approach is the online feedback of the measured attenuation properties during each rotation to adjust the tube current of the next rotation [56].

The longitudinal z-axis modulation changes the tube current along the scanning direction and reduces the tube current for sections of the body with lower density, such as lungs, while increasing the tube current for areas with higher density, such as shoulders and pelvis [57]. The purpose of z-axis modulation is to maintain a similar noise level across the entire image series regardless of different attenuating regions within a single exam. This also results in a similar noise level from patient to patient regardless of size and shape differences. Most scanners make

use of a single localizer to predict the modulation of the tube current along the scanned region based on a user-specified desired noise level. Noise selection and optimization approach is different among scanners and will be discussed in the next sections for individual scanners used in this dissertation. Figure 3-3 demonstrates the z-axis modulation.

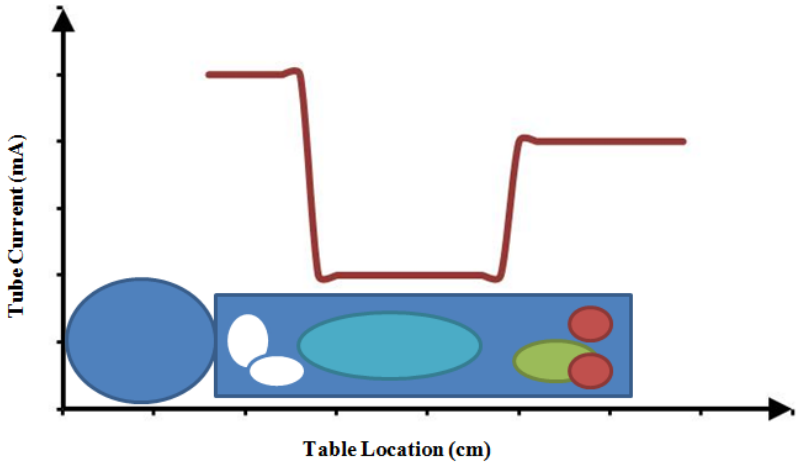

Figure 3-3 Z-axis modulation results from different attenuating region across patient's body. To compensate for the higher attenuation section of the shoulder, the mA increases while it decreases in the thoracic region due to low attenuating lungs, and again increases to compensate for increased attenuation in abdomen.

Most scanners use a combination of both of these types of modulations, called the x-y-z modulation. The combination of angular and longitudinal modulation modulates the tube current during each gantry rotation in the x-y plane and at every single table location (z), resulting in a 3 dimensional (3D) x-y-z modulation of the tube current. Figure 3-4 demonstrates different levels of tube current modulation in CT, starting from no modulation, representing fixed tube current settings, to a combination of angular and longitudinal, resulting in a 3D modulation of the tube current.

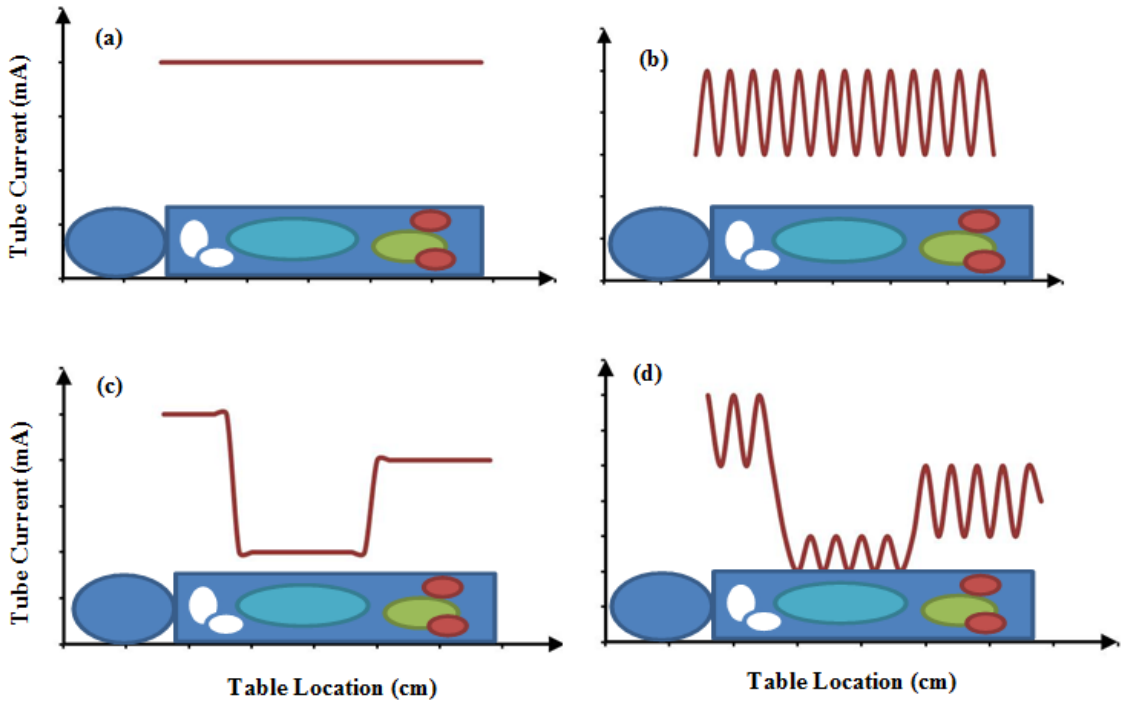

Figure 3-4 A visualization of different levels of tube current modulation with (a) representing no modulation, (b) angular modulation, resulting from an asymmetric object, (c) longitudinal modulation to compensate for different attenuating regions within the scan length, and (d) a combination of angular and longitudinal modulation, 3D modulation [58].

3.2 SIEMENS CARE DOSE 4D

Siemens TCM algorithm is called Care Dose 4D and is a combination of angular (x-y) and longitudinal (z) modulation of the tube current, as a result of adjustment for patient size and attenuation. The angular modulation is a real-time, online modulation of the tube current based on patient attenuation utilizing projection data that lags 180° from the initial projection. The z-axis modulation is performed using attenuation information extracted from a single localizer, called Topogram [59]. Based on a single topogram, either a lateral or an AP, the attenuation profile obtained from patient's long axis in the direction of the scan is measured and used to estimate the perpendicular direction using a proprietary algorithm (Figure 3-4).

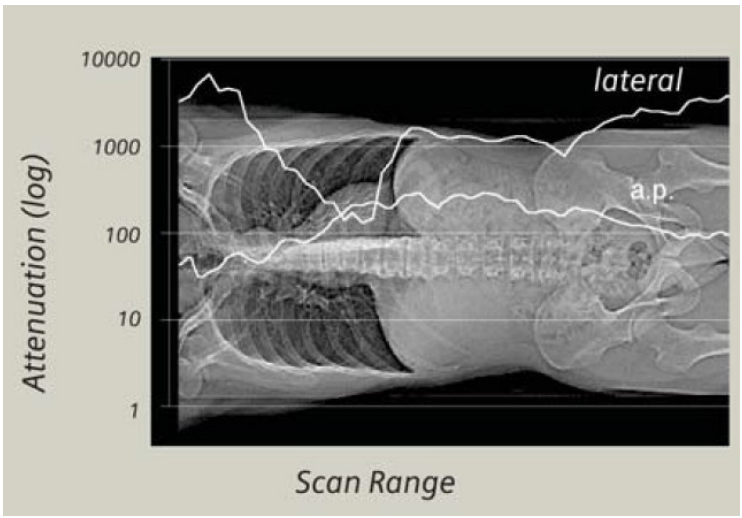

Figure 3-5 Illustration courtesy of Siemens Medical Systems. An example of LAT and AP attenuation profiles, measured from an AP acquired topogram. Here the lateral attenuation profile was estimated from the AP information.

Calculated and estimated attenuation profiles are used to estimate the corresponding tube current using an analytic function which describes the correlation between tube current and attenuation. The degree of change in tube current is defined by the modulation "strength". There are three different strengths: weak, average, and strong. For small, "slim" patients, the different settings of weak, average, and strong result in a weak, average, or strong *decrease* in tube current, while for larger, "obese" patients, the strengths result in a weak, average, or strong *increase* in the tube current [60, 61]. Figure 3-6, a courtesy of Siemens Medical Systems, illustrates different modulation strength for slim and obese patients.

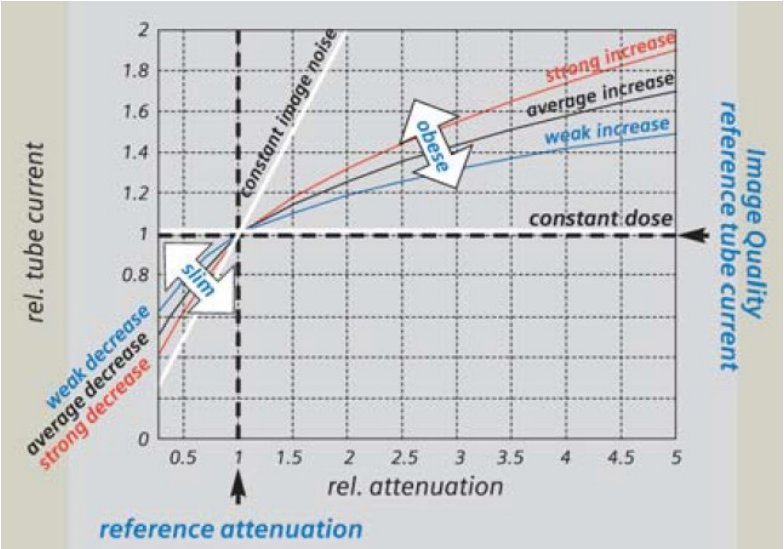

Figure 3-6 Illustration courtesy of Siemens Medical Systems. Adaptation of tube current based on the relationship between tube current and attenuation described by different modulation strengths: weak, average, and strong.

As previously mentioned, modulation of tube current is based on the desired level of image quality which can be set by the user. In Care Dose 4D this operator selected parameter is called the *image quality reference mAs*. This parameter is the mean *effective mAs* used by the scanner for a reference patient. This reference patient is described as a 70 to 80 kg (or 155 to 180 lbs.) if the adult reference/protocol is selected, and as a typical 5 year old of 20 to 45 kg if the child reference option is selected. Based on the *image quality reference mAs*, Care Dose 4D adapts the *effective mAs* to patient's size and attenuation properties along the scanned region. *Effective mAs* takes into account the influence of pitch on dose and image quality and is defined as:

$$Effective\ mAs = mA \times rotation\ time/Pitch \qquad \text{Eq. 3-1}$$

3.2.1 Maximum Tube Current and Its Effect on TCM Functions

Tube Current Modulation depends on the ability to increase and decrease the tube current over a wide range of mA values. However, there are always limitations of instantaneous mA; the maximum tube current achieved by the scanner is limited by the x-ray tube and generator

capacity. Reaching this maximum mA may occur when the scanned patient has a very large cross sectional area, in which the required tube current to achieve the appropriate image quality would exceed the instantaneous allowed tube output. In some instances the scanner will not allow exposure until parameters are adjusted to decrease the allowed instantaneous tube current. In Siemens scanners, the user interface is based on effective mAs, so the user does not directly specify mA; however, changing the pitch and rotation time can alter the effective mAs (as described in Eq. 3-1). Therefore, increasing rotation time or decreasing pitch will decrease the instantaneous mA and allow an exposure to be taken without exceeding the instantaneous mA limit. However, sometimes the desired tube current may exceed the generator limit locally rather than throughout the entire scan length, resulting in local clipping of the tube current due to reaching the maximum tube output. In these instances exposures will be allowed with the knowledge of locally decreased image quality within the images [56] (Figure 3-7).

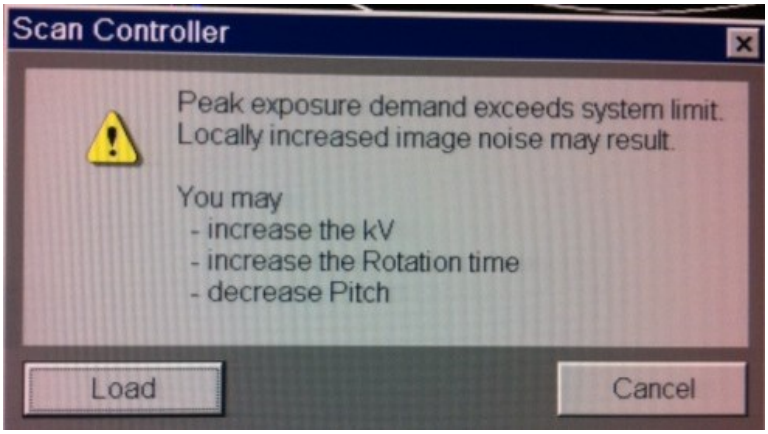

Figure 3-7 Popup message warning against locally decreased image quality and displaying possible actions to be taken to avoid exceeding the system limit.

When the operator chooses to proceed with the exposure without any changes made to the suggested parameters, the TCM algorithm becomes subject to limitations of allowed instantaneous mA due to generator power, resulting in a rather more *compromised* modulation of the tube current. Examining the actual TCM function of one of these exams, one can observe a loss of longitudinal modulation in the tube current, while still maintaining the x-y modulation. The resulting dose from a maxed out TCM function is very similar to dose from fixed tube current CT exam, mostly due to the loss of the z-axis-only modulation. As it will be shown in Chapter 7, the effect of TCM is primarily due to z-axis modulation [62], hence, its loss in the TCM function results in doses comparable to those resulting from fixed tube current scans.

Figure 3-8 illustrates examples of a properly functioning TCM function (a), locally maxed out tube current function with mostly maintained z-axis modulation throughout the entire scan (b), and an entirely maxed out TCM function with no z-axis modulation (c).

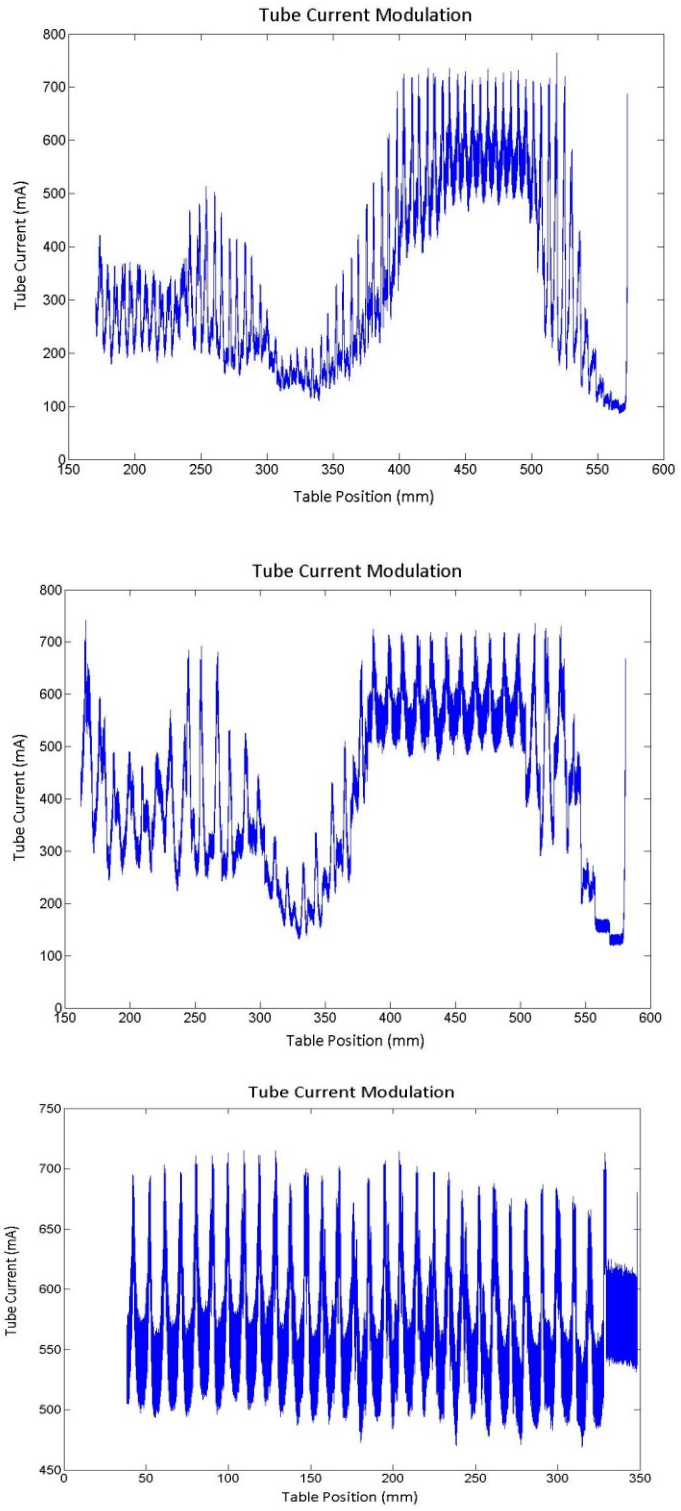

Figure 3-8 Examples of appropriately modulated TCM function (a), locally maxed out TCM function (b), and maxed out TCM throughout the entire exam, resulting in insignificant longitudinal z-axis modulation (c).

3.3 GE AUTOMA/SMARTMA

CT scanners from GE Healthcare (GE) also use a combined 3D tube current modulation approach called AutomA 3D. AutomA 3D consists of two separate components: AutomA and Smart mA. AutomA is responsible for the longitudinal z-axis modulation of the tube current, while SmartmA delivers the angular, x-y modulation. AutomA can be used with or without the angular modulation component, SmartmA.

SmartmA makes use of a sinusoidal function to modulate the tube current during each rotation using attenuation information extracted from a single radiographic localizer called "scout". AutomA works in conjunction with an image quality index value set by the user called "Noise Index" (NI). This noise index allows the user to set a desired image quality and corresponds to the standard deviation of pixel values in the central region of the image of a uniform water phantom. Using the localizer, patient's attenuation is obtained and mapped into mA values using a lookup table for modulating the tube current. In addition to the noise index, minimum and maximum mA values can be set to define the range of the modulated tube current across a scan. Figure 3-9 illustrates an example of TCM resulted from GE AutomA [56, 61, 63].

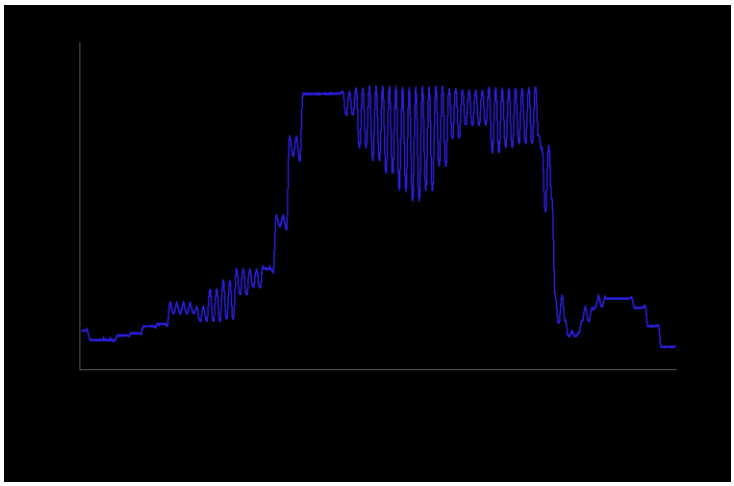

Figure 3-9 A whole body TCM function from GE AutomA 3D.

3.4 TOSHIBA SUREEXPOSURE 3D

Toshiba also uses a 3D modulation system called SureExposure 3D. This feature has two methods for optimizing the tube output. One uses the standard deviation of CT numbers in Hounsfield units, and the other method uses an image quality level. For example, there are three global image quality levels for adult abdomen protocol: High, standard, and Low Dose quality (Figure 3-10a).

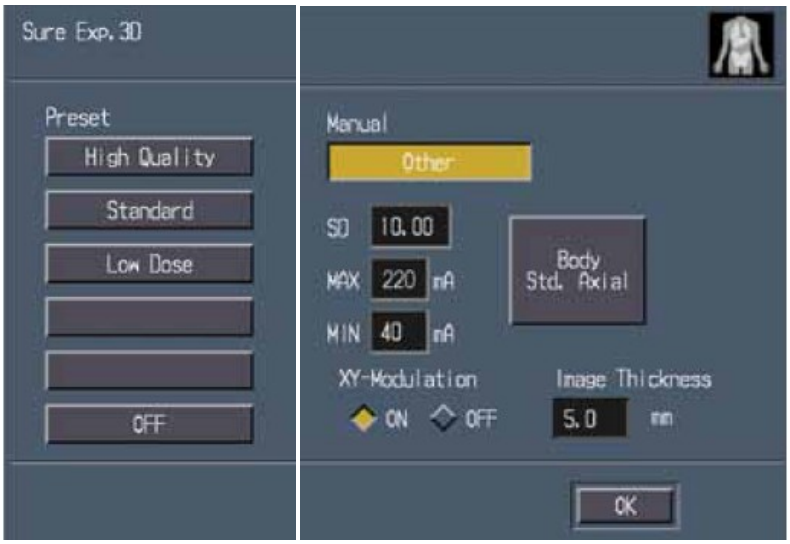

(a) (b)

Figure 3-10 (a) Three different global settings for choosing an appropriate image quality level. (b) A more user-specific and scan-specific selection of the image quality using user-specified noise level using SD and minimum and maximum mA values.

For other protocols that require specific image quality levels, a noise level using standard deviation can be used along with a minimum and maximum mA value (Figure 3-10b). However, both of these settings are based on standard deviation of pixel values measured in homogenous water phantom [55]. Similar to GE, the user will also have to specify a minimum and maximum tube current values. Lateral and frontal localizers called "scanograms" are used to map the

selected image quality or standard deviation to tube current values. Diameter measurements performed on the lateral and frontal localizer will be used along with intensity information to oscillate the tube current during each gantry rotation.

Table 3-1 shows an overview of image quality parameters for each manufacturer's AEC system used in this dissertation.

Manufacturer	AEC System	TCM Technique	Optimization Method	mA Settings	Required Image Localizer
Siemens	Care Dose 4D	x-y-z modulation	Quality Reference mA for standardized sized patient	Quality Reference mAs (specified by manufacturer)	Either AP or LAT
GE	AutomA 3D	x-y-z modulation	Noise Index, sets required image noise	A min and a max value can be set by the user	Either App or LAT
Toshiba	SureExposure 3D	x-y-z modulation	Standard deviation set for a required image noise	A min and a max value can be set by the user	Both AP and LAT

Table 3-1 An overview of manufacturer's AEC systems and their methods for setting exposure levels.

CHAPTER 4: UCLA MDCT MONTE CARLO DOSIMETRY PACKAGE

This chapter will discuss the Monte Carlo methods, in particular, a previously developed modified version of the Monte Carlo source code which was used in this dissertation. Different components of the Monte Carlo method used for this research will be discussed, especially the component of modeling Tube Current Modulation.

4.1 MONTE CARLO METHODS AND THEIR USE IN CT DOSIMETRY

Monte Carlo method is a numerical stochastic process. It describes a system of continuous random events until the convergence of numerical results. It is applied in a variety of different scientific fields and as described by Rogers [64], it has been used for over 50 years in the field of Medical Physics, in the context of radiation transport for the purpose of radiation dosimetry. Using random number sampling from the probability distributions which control a physical process, Monte Carlo methods simulate random tracks of individual particles. Information on energy deposition of particles traversing an object can be obtained by simulating a large number of histories [65].

As described by Rogers and Bielajew [65], all Monte Carlo simulation codes have four major components: the probability distributions and cross-section data used for simulating different interactions within a geometry, the actual algorithms written for the transport of the particles, the process and method by which the geometry of the question in hand is described, and the examination and interpretation of the information obtained during the simulation.

There are four widely used general purpose Monte Carlo radiation transport packages: EGSnrc, GEANT4, PENELOPE, and MCNP. One of the first Monte Carlo codes, developed in a high-

energy physics lab, was the EGS (Electron Gamma Shower) code which remains the most widely used Monte Carlo transport code in medical physics. PENELOPE (Penetration and ENErgy LOss of Positiron and Electron), was developed at the university of Barcelona to specifically simulate electron-photon showers [66]. GEANT was developed at CERN for particle physics applications and is capable of simulating the transport of many particles such as protons, neutron, pions, etc. [64, 67]. MCNP is another general purpose Monte Carlo N-Particle transport code that can be used to simulate the transport of photons, neutrons, electrons, and coupled neutron-photon and neutron-electron. It was originally developed at Los Alamos National Laboratory for simulating neutron interactions, such as fission. All four of these general purpose Monte Carlo codes mentioned above are used in the field of Medical Physics in both radiation therapy and diagnostic imaging. A recent AAPM Task Group, TG 195, has been established to compare these four codes and benchmark them against each other using a series of diagnostic radiology relevant simulation tasks from simple to more complicated geometries and source movements which were performed with each code and compared to each other.

Monte Carlo simulation has been more widely used in the clinic and is probably more essential in radiation therapy for treatment planning purposes and dose distribution verifications. That said, it has also been used in diagnostic radiology, specifically CT, as a research tool. One of the earliest papers on Monte Carlo model for simulating absorbed dose in Computed Tomography was by Beck et al. [68] in 1983, looking at the dose variation within the x-y plane of an elliptical geometry. In 1991, Jones and Shrimpton [38] published the first set of normalized organ doses simulated using Monte Carlo methods and normalized using $CTDI_{vol,air}$. This study later became the basis for the CT Dosimetry package ImPACT [69]. In 1995, Atherton and Huda investigated the effects of photon energy spectrum, bowtie filter, and size and composition of the scanned

object on the dose distribution within the object using Monte Carlo simulations [70]. In the same year, Huda et al. published another paper in which Monte Carlo methods were used to investigate the relationship between dose as a function of the radius of the cylindrical dosimetry phantoms [71]. A similar topic was covered by Boone et al. in 2000, investigating peripheral doses using the 32 and 16 cm CTDI cylindrical phantoms in axial and helical mode (pitch =1) [72]. In a series of papers, Caon at al. used Monte Carlo methods to simulate CT axial mode and validated their model using voxelized CTDI phantom to within 7%. Later, the developed Monte Carlo method was used to estimate dose to a computational phantom, named Adelaide [73-75]. More papers focusing on modeling CT geometry and source were published starting 2003 with the first being from UCLA by Jarry et al. [76]. In this paper, MCNP4B was used to model spiral CT, which was validated using measurements in phantoms with varying complexity. The following two publications by DeMarco et al. [77, 78] focused on dose estimation from Multi-detector CT scanners (MDCT) with more validation in cylindrical and anthropomorphic phantoms, and investigating the effect of patient size on effective dose using the GSF family of voxel phantoms [79]. These publications were the foundation of the subsequent papers from UCLA. Angel et al. published a paper in which a method was introduced to estimate organ dose to the fetus for pregnant patients who undergo abdomen/pelvis CT exams using a linear relationship that was observed between Fetal dose and the perimeter of the mother [80].

The next series of papers published from UCLA were focused on Tube Current Modulation (TCM) and its effects on organ dose [81, 82]. These were the first papers using Monte Carlo methods to model TCM and estimate organ dose from tube current modulated CT exams. Meanwhile, there were other groups using Monte Carlo methods to estimate dose to organs. A series of papers were published from Duke University specifically targeting estimation of dose to

pediatric patients and correlating Monte Carlo based organ dose to risk using Monte Carlo simulations [83-85]. Some other groups working on Monte Carlo simulations in the context of estimating organ dose from CT examinations are the group from Rensselaer Polytechnic Institute (RPI) [86, 87], University of Florida lead by Dr. W. Bolch [88-90], and University of Erlangen, Germany under Dr. W Kalender [91-94]. The groups from RPI and Florida have been two of the pioneers in creation of human models used in radiation dosimetry, which will be addressed in more details in next chapter. RPI has developed the CT Dose Reporting software based on Monte Carlo simulations which models CT source as a point source with a total of 16 virtual x-ray sources along a single axial rotation. For helical and contiguous axial simulations, virtual x-ray sources are placed along the corresponding trajectories, while each rotation is made use of 16 virtual x-ray sources [86]. The research group from Florida has been mainly working on developing computational hybrid phantoms for Monte Carlo based dose estimation methods, which will be discussed in next chapter. They have created an age-based lookup table generated from a Monte Carlo simulation package based on a Siemens SOMATOM 16, for estimation of organ dose from fixed tube current CT exams. Work from University of Erlangen has been mostly focused on creating dose maps rather than organ doses using Monte Carlo methods. Their recent study explored GPU applications in Monte Carlo simulations to reduce computation time and achieve fast on-site dose calculations [94].

There have been significant developments in Monte Carlo simulation techniques which have led to improvements in the ability to simulate radiation dose to patients from CT scans. The following sections will focus on the Monte Carlo simulation package build at the university of California, Los Angeles using the general-purpose Monte Carlo code MCNPX.

4.2 MONTE CARLO N-PARTICLE EXTENDED (MCNPX)

MCNPX (Monte Carlo N-Particle eXtended) is an extension of MCNP code, also developed at Loa Alamos National Laboratory. This code is capable of simulating the passage of 34 different particles, including heavy ions, through objects and over a wide range of energies. MCNP uses a Markov Chain Monte Carlo algorithm that can simulate the trajectory of one particle at a time through a specified geometry set by the user until the particle reaches a cutoff energy, also set by the user, or leaves the geometry due to some interactions (such as scatter). This process is repeated for each simulated particle whose passage is independent of previously simulated particle. The number of histories (particles) to be simulated is set by the user in the input file used by MCNP as a set of instructions regarding geometry of the problem, radiation source, materials, and types of outputs.

MCNP input file can be categorized into three sections: cell cards, surface cards, and data cards. Cell cards are used to specify the shape and material compositions of the problem. Surface cards are used to set boundaries and limits to the cell cards. The data card specifies the problem type, source and tally specifications, and material and cross-section requirements.

The particle is specified using the "MODE" card. This card specifies the particles to be tracked in the problem. More than one particle can be tracked at a time. In the context of CT dosimetry, the MODE is set to "p" to indicate tracking of photons. Source specification is either described using the source card, "SDEF", or, if a more complicated source description is needed, as the case in this dissertation, the FORTRAN source code of MCNP needs to be modified to represent the simulated source and to replace the SDEF card in the input file. In case source is not specified by the user using the SDEF card in an input file, MCNPX will use a file named

"source.f" for the simulations. This file is usually used when a more user-specified source is required for the simulations.

The next section of the input file is the specification of the tally card. This card is used to specify the type of information the user requires as the output of the Monte Carlo simulations. These can range from fluence information to energy deposition.

The material specification of the geometry is described using the material card. It specifies the material using atomic number of the elemental composition of the material along with atomic density or weight fraction of each component. In this way, materials that consist of single elements (e.g. Al slabs), molecules (e.g. Water) and complex materials (e.g. Plexiglas) can be described.

4.3 MODELING MDCT IN MCNPX

This section describes the modifications to source.f that allow the simulation of a MDCT scanner geometry and spectrum within MCNPX. These modifications facilitate the initialization of position, direction, and the energy of the simulated particles.

Dummy variables called IDUM and RDUM cards are utilized in the input file when a user-modified version of MCNPX (modified source.f) is used to specify scanner and scan specific variables. IDUM cards are integer arrays and RDUM cards are floating point arrays. In the modified source.f for this dissertation, IDUM cards are used to specify a CT scanner's x-ray source model which includes: type of scanner, spectra and filter specifications, as well as scan mode (helical, axial, variable tube current etc.). The code uses IDUM variables as the conditional

portion of if/then statements to select different options. RDUM cards are used to specify the actual CT examination parameters such as: collimation, scan length, pitch, and tube start angle.

After specifying IDUM and RDUM variables to select scanner and scan-specific parameters, the code uses a text file, chosen using the IDUM variables which identify the desired scanner type, energy (80, 100, 120, 135, 140 kVp), and bowtie filter options, to randomly select the energy of the simulated photon.

The x-ray output from a CT scanner can be characterized by its photon energy spectrum (Figure 4-1(a)), which represents the number of emitted photons as a function of energy. An energy spectrum expressed as number of photons per energy interval can be transformed to an energy probability distribution function (PDF) by normalizing each absolute value by the total number of photons of the spectrum (Figure 4-1(b)). Finally, the PDF can be used to determine a cumulative distribution function (CDF), which expresses the probability that a random energy value is less than or equal to a specified value (Figure 4-1(c)). Mathematically, the CDF, described as a function of energy, P(E), is defined in terms of the energy PDF, p(e):

$$P(E) = prob(\xi \leq E) = \int_{E_{min}}^{E} p(e)de \qquad \textbf{Eq. 4-1}$$

The random variable algorithm used in this work to obtain an energy value for each photon, does so by sampling the scanner-specific x-ray energy spectrum. This requires the distribution to be expressed as a cumulative distribution function (CDF).

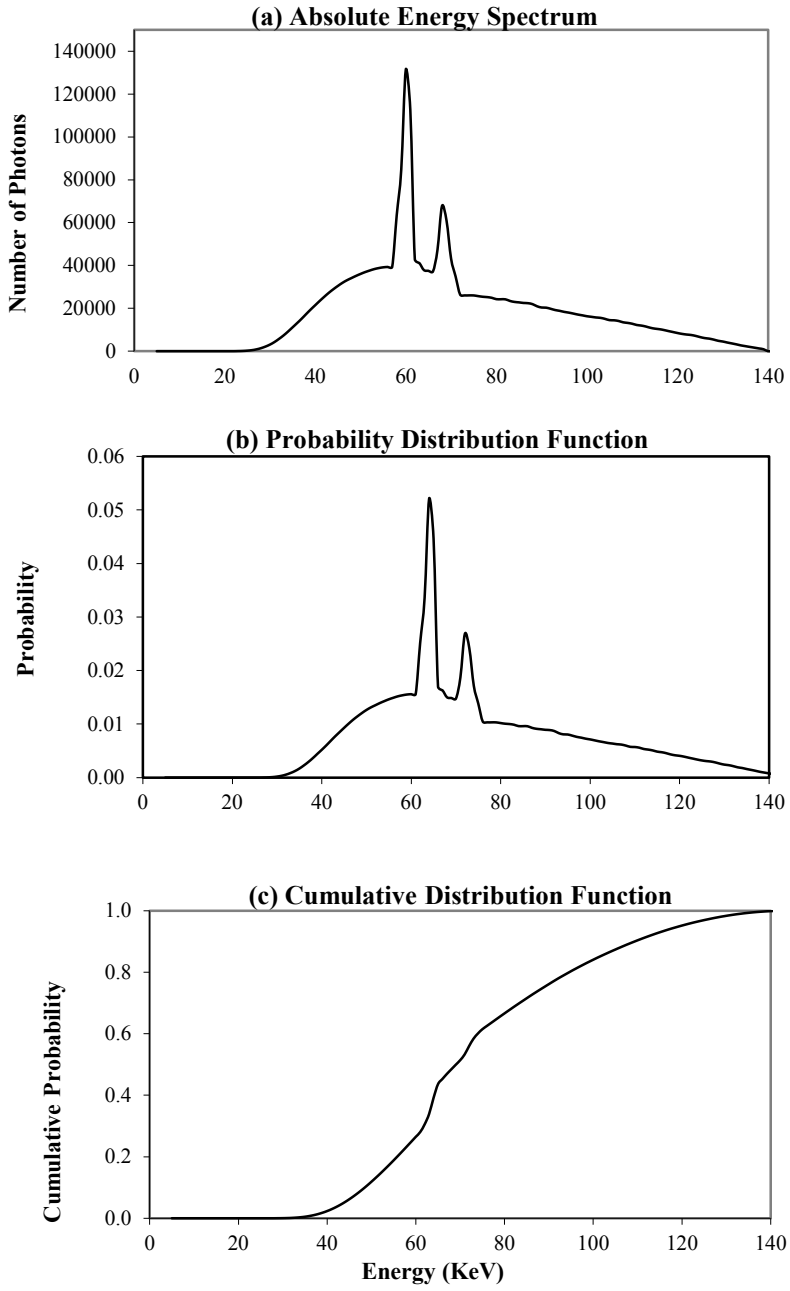

Figure 4-1 Examples of a photon spectrum (a), the probability function of the spectrum (b), and the cumulative distribution function (c).

After assigning an energy value to the photon, initial position and direction of the photon has to be determined. The position of the source will be determined by the chosen source motion (single axial, contiguous axial and helical motion). Each of these selections will allow the source

to exist in a set of specific positions, from which the code randomly samples with a uniform probability.

The position of the virtual source in x-z plane, shown in Figure 4-2, is calculated from angle β and the source-to-isocenter distance, which is a constant value hard-coded into the code. This distance varies among different CT scanner models and manufacturers. The angle β, however, is assigned a value by either randomly sampling from a 360° rotation, or, if fixed source positions are required, it can also be assigned a value specified by the user. For helical scans, β is obtained by randomly sampling from a 360° rotation plus adding an angular offset to simulate helical motion. For TCM simulations, β is sampled from a text file called "vmas" which contains a table with a column of angles and corresponding tube current values and table locations.

The y-coordinate also depends on the selected source motion. For helical scans, the y-coordinate is determined by randomly sampling from the scan length which is the product of pitch, collimator width and number of rotations. For a continuous axial scan, the y-component of the source position is assigned a value by randomly selecting a slice and multiplying it by the collimator opening. In this mode, the number of slices in y-direction is obtained by dividing the scan length by collimator opening and slice intervals. In TCM mode, the y positions are another column within the "vmas" file from which individual photon's y-coordinates are sampled from.

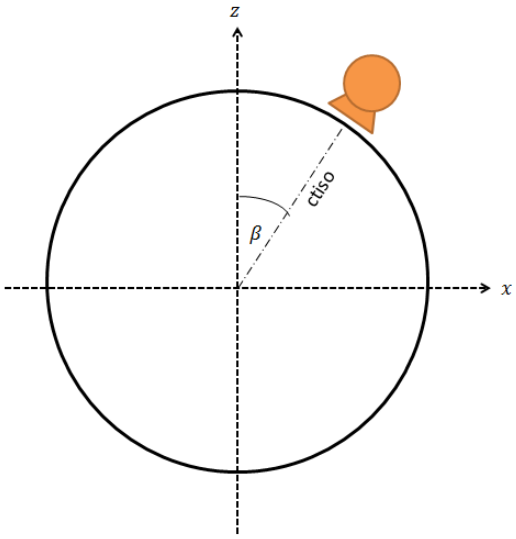

Figure 4-2 A diagram of sampling a 360° rotation to calculate the x and z coordinates of the source position. Ctiso represents the source-to-isocenter distance and β represents the angle between ctiso and z-axis.

After the position of the simulated photon has been selected, its trajectory, described as a three dimensional unit vector (u,v,w), will be determined. These vectors are obtained by randomly sampling from a "virtual" plane that is centered at isocenter and is perpendicular to the line between the source position and isocenter, as shown in Figure 4-3. The width of the plane (x,y) is determined from the fan angle and the length of the plane (z) is defined by the width of the selected collimation. This plane is randomly sampled to determine the direction of the photon. Because this plane is a perpendicular plane that is randomly sampled from, it is not directly sampling a *diverging* beam from a point. Instead, a $1/r^2$ correction is used, which utilizes the source-to-isocenter distance and the distance the photon travels until it interacts with the "virtual" plane.

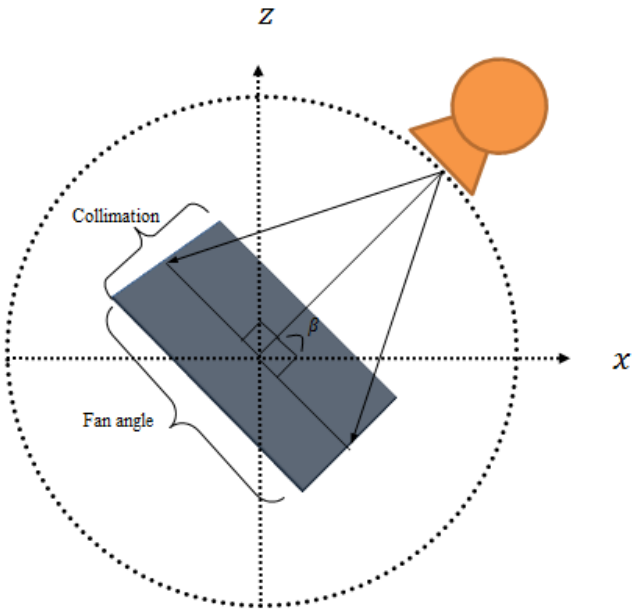

Figure 4-3 A diagram of the "virtual" plane used to sample the direction of the photons from.

MCNPX uses a statistical source weighting factor in its calculations. Each photon is given an initial weight value (typically 1). As a single photon passes through an object, there is a chance it is absorbed, which physically means all of its energy goes into the material. Of course, there is some probability that this interaction will not occur and the photon will enter a new region of material and possibly deposit all of its energy. MCNPX handles this phenomenon by altering the statistical weight of the photon as it passes through material based on its probability of interaction. It is possible to alter the initial statistical weight value of the particle in order to model attenuation without actually transporting the particle using the MCNPX engine. This is how attenuation due to the scanner filtration (inherent and bowtie) is modeled in the modified version of source.f, since modeling the actual filtration, in particular, inherent information, requires the knowledge of detailed description of the x-ray tube and overall is more complicated and also computationally more expensive. For a given angle, there is a corresponding amount of

filtration that the photon would traverse through. The appropriate weight factor is calculated using the exponential attenuation assumption:

$$\frac{I}{I_O} = \exp(-filter\ pathlength \times \mu_{filter\ material}) \qquad \textbf{Eq. 4-2}$$

Finally, the filtration description, which is described using path length as a function of angle is used to calculate the initial source weight for each photon to account for attenuation through the bowtie filter. Additionally, this weight will be multiplied by another factor which takes into account the inverse square intensity drop off of a point source.

Information on scanner spectrum, geometry and material composition of the bowtie filter is essential for modeling MDCT scanners. This information is proprietary and usually not available to research groups. Spectra and bowtie information used in this dissertation were obtained using the "equivalent source method" described by Turner et al. This method makes use of information such as HVL (half value layer), QVL (quarter value layer), and attenuation profile of the bowtie filter which can be measured while the CT x-ray tube is stationary [95].

4.4 Modeling of Tube Current Modulation in MCNPX

Tube Current Modulation (TCM) is a widely available dose reduction technique and a feature very frequently used in many clinical protocols to reduce dose while maintaining desired image quality [52, 53, 55]. Tube current modulation algorithms are either based on angular modulation, z-axis modulation, or a combination of these two, which forms a "three-dimensional" modulation most commonly used in conventional TCM algorithms [55, 59]. TCM algorithms perform differently across different CT scanner manufacturers and, generally, they tend to differ in implementation and optimization variables used for adjusting the tube current. Theoretical

predictions of TCM values for an individual patient based on Kalender [52] and Gies [54] are feasible; however, these theoretical TCM functions are too simplified and differ from currently used commercialized TCM algorithms. Across different CT manufacturers, TCM implementations and optimization variables are different, as it will be described in Chapter 3, and vary by approach, calculations based on one or two localizers, etc. Therefore, this dissertation focused on using actual TCM functions taken from real scans of patients. These TCM functions are extracted from raw projection data of clinical cases of actual patients (and phantoms where they were employed). In addition, Chapter 7 describes a study where an approximation method is described to obtain z-axis-only modulation from DICOM header of patient images

Three sets of information can be extracted from the raw projection data: tube current I, table location z, and x-ray tube angle Θ. The tube current value I is a function of table position z and tube angle Θ, $I(z, \Theta)$ [81]. This information is organized in a text file referred to as *vmas* file, which contains three columns of data: table location starting at zero, tube angle adjusted to reflect angular coordinate system in MCNPX, and the tube current values. The header of the *vmas* file contains the number of lines within the text file. Once the scan mode is selected to be variable tube current using an IDUM card, the text file gets read in order to determine the maximum tube current value within the text file and to generate normalized tube current values by dividing each value by the maximum tube current value. The "vmas" file is then used by MCNPX to randomly select an index ranging from 1 to the length of the file using *int (rang()*index)*. The corresponding tube angle, table location, and normalized tube current selected using random sampling on the index number, is used to set the position, direction, and the weight of the simulated photon, respectively. The process of selecting photon energy and the

virtual attenuation to account for bowtie filter was described in the previous section. Figure 4-4 illustrates an example of TCM function and its simulated Monte Carlo version.

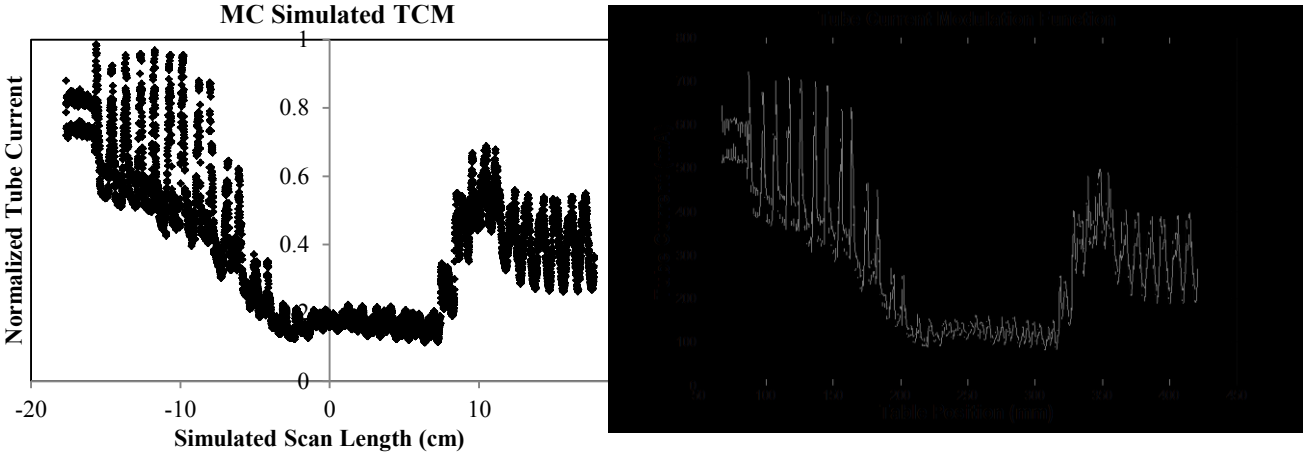

Figure 4-4 (Left) Monte Carlo simulated Thorax TCM function for 10^8 photons. (Right) Actual Thorax TCM function extracted from the raw projection data.

4.5 Dose Calculation and Post Processing of Simulation Output

All MDCT simulations are performed in photon mode, at which all secondary electrons are assumed to deposit energy at the photon interaction site. Dose is calculated using collision kerma (kinetic energy released in matter), which is equal to absorbed dose under the condition of charge particle equilibrium (CPE), which in turn is satisfied by the assumption of energy deposition of electrons at the interaction site. For each simulated photon, MCNPX tally type *F4 was used to track energy fluence in specified regions (i.e. regions of interest or specific organs) and multiplied by mass-energy absorption coefficients (μ_{en}/ρ) to convert to collision kerma. Under CPE, dose to a region of interest (ROI) is given by:

$$Dose \xrightarrow{CPE} kerma_{col} = \sum_{E=0}^{kVp}(\psi_E \times E \times \left(\frac{\mu_{en}}{\rho}\right)_{E,Z}) \qquad \textbf{Eq. 4-3}$$

where ψ_E is the total particle fluence for a given energy in the ROI multiplied by energy of the particle to reflect the energy fluence and $(\mu_{en}/\rho)_{E,Z}$ is the mass-energy absorption coefficient which depends on the energy and material.

MCNPX reports the above calculated dose as normalized dose per simulated photon. Additionally, these simulations do not take into account photon fleuene for a given energy and collimation opening. Therefore MCNPX output has to be converted from dose /particle to an absolute dose while taking into account the fluence change with width of beam collimation and energy.

The resulting dose per simulated photon for each volume of interest has to be multiplied by a normalization factor to convert to dose per mAs (product of the tube current and rotation time). This normalization factor is scanner, collimation, and kVp dependent, and is used to take into account the fluence changes from varying the beam collimation. As described by Jarry, et al. [76], normalization factors that are specific to selected kVp and collimation width are calculated using the ratio of measured and simulated CTDIair which uses the measured dose in air using the 100 mm ionization chamber at the isocenter of the gantry.

$$NF_{kVp,NT} = \frac{(CTDI_{air,measured})_{kVp,NT}}{(CTDI_{air,simulated})_{kVp,NT}} \qquad \textbf{Eq. 4-5}$$

To obtain absolute dose in mGy, the calculated dose per mAs has to be multiplied by the total mAs, which is the mAs per rotation multiplied by the number of rotations. For fixed tube current simulations, the mAs per rotation is a constant value. Hence total mAs is simply the product of mAs and the number of rotations for a scan. In tube current modulation, the mAs varies with table location and tube angle. As described in the previous section, the maximum tube current

(mA) within a *vmas* file was used to normalize the tube current data and used as source weights for the simulated photons. Therefore, the resulting dose per mAs has to be multiplied by the maximum mAs used to normalize the tube current data.

$$Dose_{TCM,kVp,NT} = MC\ Output \times CF_{MeV \rightarrow mGy} \times NF_{kVp,NT} \times Max.mAs \times \frac{Scan\ Length}{Pitch \times NT} \quad \textbf{Eq. 4-6}$$

where CF is the conversion factor from MeV to mGy.

This process of organ dose simulations and calculations was performed for all patient models used in this dissertation.

CHAPTER 5: CREATION OF VOXELIZED PATIENT MODELS FOR USE IN MONTE CARLO SIMULATIONS

The following chapter describes the collection of patient images, raw projection data, and the subsequent creation of voxelized patient models used in the Monte Carlo simulations. All activities were approved by the Institutional Review Boards at each of the four institutions where the data collection took place.

5.1 INTRODUCTION

The patient model is an essential component of Monte Carlo dosimetry simulations and has been evolving from stylized geometric mathematical phantoms to detailed voxelized and computational models of patient anatomy. Mathematical phantoms are those which make use of mathematical shapes, such as cylinders, ellipses, cones, spheres, and simple planes. These have been used since 1966 for organ dose estimations [96-98]. One of the original mathematical phantoms is the Medical Internal Radiation Dose (MIRD) phantom, which was developed by the Society of Nuclear Medicine (Figure 5-1). As defined by ICRP (International Commission on Radiological Protection), these MIRD-like mathematical phantoms represent an "average or standard individual" with masses in agreement with the ICRP data on reference man, but are still different from representing an actual patient model with realistic organ shapes and locations, which vary from individual to individual [99].

Improvement to these mathematical phantoms came in 1984 when Gibbs [100] introduced the first voxelized models followed by Williams et al. [101] in 1986 and in 2002 by Petoussi-Henss et al. [79] at GSF—National Research Center for environment and Health, Germany. These voxelized models made use of CT or MRI images of individuals to create a three dimensional

representation of the human body by assigning different compositions and labels to voxels based on the organ they were part of. The GSF-family of voxel phantoms are the result of almost thirty years of effort and includes 12 phantoms with different gender, age, type (whole body, torso, thorax etc.), weight, and height specificities [79, 102]. Three of these voxelized phantoms with identified and segmented organs are illustrated in Figure 5-2.

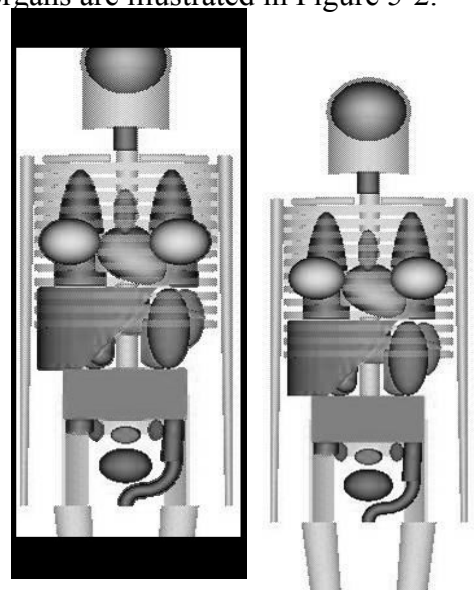

Figure 5-1 Organs are represented with mathematical shapes such as spheres, cones, cylinders, and ellipses (left). Patient model looks unrealistic in terms of organ shapes and locations (right).

Figure 5-2 From left, three adult phantoms from the GSF-Family of voxelized models, Helga, Donna, and Irene are illustrated.

Another type of human phantoms is the BREP (Boundary Representation) phantoms. These are computational human phantoms which have exterior and interior anatomical features of the human body using NURBS (Non-Uniform Rational B-Spline) or polygonal mesh methods, which are collectively called BREP methods. The main advantage of these phantoms over the voxelized models based on CT or MRI images, is their ability to deform and adjust organ sizes [103]. The recent additions to the human BREP phantoms have been introduced by the Radiation Measurement and Dosimetry Group from Rensselaer Polytechnic Institute and Nuclear and Radiological Engineering department at the University of Florida. RPI's phantoms are the pregnant female models at 3-, 6-, and 9-month gestational period. These models are made using advanced 3D surface geometries, which allow the organ masses of both the mother and fetus to be adjusted to match those recommended in ICRP Publication 89 for reference individuals [104, 105]. Another phantom developed at RPI is the 4D VIP-Man Model, with segmented red bone marrow and adjustable organ sizes [106, 107].

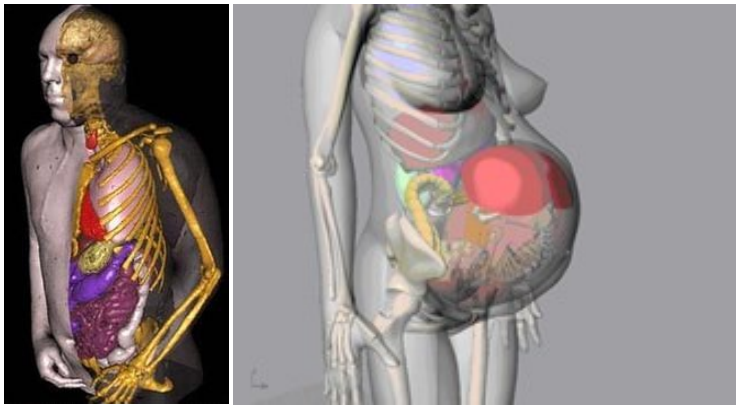

Figure 5-3 (Left) deformable computational phantom, called VIP-man. (Right) RPI's 9-month pregnant model.

The UF family of reference hybrid phantoms are also deformable phantoms based on NURBS and consists of 8 models: adult male and female, 15- year male and female, 10year, 5-year, 1-year, and a new born model [108-110].

The progress of building human-like models for use in radiation dosimetry since MIRD phantom, introduced 1960's, has been remarkable and very suitable for the vast majority of radiation dosimetry problems in therapeutic and diagnostic medical imaging. However, these models can only be used for conventional fixed tube current (mA) CT dosimetry such as the work published by AAPM Task Group 204 [49]. These models do not have any tube current modulation information ($I(z, \Theta)$). While some have tried to predict what the TCM information would be, this is very scanner and setting specific. Therefore, to be able to estimate dose from tube current modulated CT examinations, having an appropriate model of the patient is necessary, but the patient's TCM data resulting from the CT scan is required for accurate dose estimation as well. What has been attempted in the past by RPI is to select TCM profiles from actual pregnant patients to match the three gestational stages of their pregnant models [104]. Even though the models are good representations of pregnant patients in terms of anatomy, the TCM functions used to assess dose were not obtained for these models and this may limit the accuracy of the TCM functions and, thus, the organ dose estimates. In addition to not using model-specific TCM profiles for the patient models, dose from TCM was only assessed based on the longitudinal modulation of the tube current. Although it has been shown that the z-axis modulation has the most effect on organ dose compared to x-y modulation [62, 111], this might not be the case for pregnant patients because of the extreme difference between lateral and anterior-posterior lengths in the abdominal region of pregnant patient, causing a large difference between peaks and valleys of the x-y modulation.

Because prospectively modeling TCM from a CT exam is extremely difficult, in this work we have chosen to collect actual patient data and retrospectively analyze the actual TCM functions that were experienced during actual patient scans. This would eliminate the need for reverse

engineering or estimating the TCM function for various scanners and allow the work to focus on what actually happens in patient scans and estimate the organ doses that result from those scans. This chapter covers the collection and the process of creating voxelized models used in this dissertation for estimating dose from tube current modulated CT exams.

5.2 Collection of Patient Models and Patient Inventory

Institutional Review Boards at four medical institutions approved the collection of patient CT images from three major CT manufacturers (Siemens, GE, and Toshiba) for use in creating voxelized models. Images were collected from: (a) Siemens CT scanners at the University of California, Los Angeles, (b) GE Scanners at the UT-MD Anderson Cancer Center in Houston, Texas, and (c) Toshiba Scanners from the UT Southwestern Medical Center, Dallas, Texas, and Arkansas Children's Hospital in Little Rock, Arkansas. Images from 64 slice CT scanners (Siemens Sensation 64, GE LightSpeed VCT, and Toshiba Aquilion 64) for two major examinations, the thorax and the abdomen/pelvis, including both adult and pediatric patients, were collected for use in Monte Carlo simulations. Besides collecting image data from the Siemens scanner, raw projection data was gathered for extraction of the tube current modulation data for use in simulations and for reconstructing images at 500 mm Field of View (FOV) to ensure the full coverage of anatomy within the images. Raw projection data from the GE and Toshiba scanners were not available and, therefore, approximations had to be made to account for TCM during Monte Carlo simulations. These approximation methods are covered in detail in chapter 6. To make certain that the patient cohort included a variety of different sizes; the reconstructed FOV was used to categorize patients. Figure 5-4 illustrates one of the smallest and the largest patients used in this study.

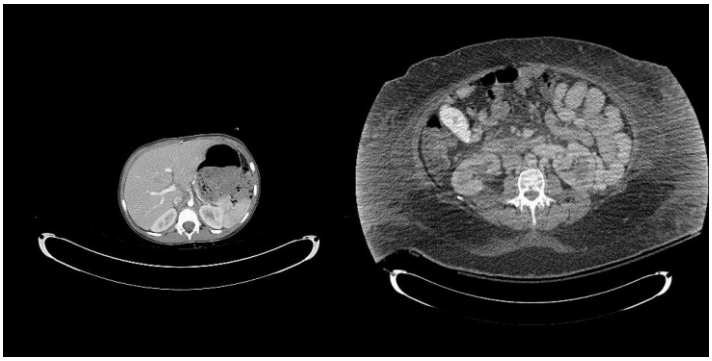

Figure 5-4 An example of one of the smallest and largest patient models used in this dissertation.

In addition to patient images, CT dose reports were collected for each patient for recording of each scan's $CTDI_{vol}$ value. Reported $CTDI_{vol}$ values were used in Chapter 8 to investigate methods that account for regional variations in tube current data when predicting organ dose.

A total of 314 patients from all three scanners were collected for creating voxelized models for use in Monte Carlo simulations. Table 5-1 summarizes the collected patient cohort.

Patient Cohort	Siemens		GE		Toshiba	
	Abdomen/Pelvis	Thorax	Abdomen/Pelvis	Thorax	Abdomen/Pelvis	Thorax
Male	30	29	10	10	15	17
Female	32	42	9	9	11	24
Pediatric	20	29	5	9	13	18
Total	181		52		98	

Table 5-1 Number of patient models for each age/gender category and for each exam type. For the chest exams lungs and glandular breast tissue, and in the abdomen/pelvis exams liver, kidneys, and spleen were contoured.

5.3 THE PROCESS OF CREATING VOXELIZED MODELS

Voxelized patient models were generated from clinically indicated chest and abdomen/pelvic scans acquired on the Siemens Sensation 64, GE LightSpeed VCT, and Toshiba Aquilion 64 scanners. The collected images were anonymized and imported into workstations for contouring of organs in interest. The software used for contouring organs, called the "Marking Tool", is part of the Quantitative Imaging Work Station (QIWS) platform designed by the Institute for Computer Vision and Imaging Biomarker (CVIB) at UCLA [112].

Depending on the type of the CT exam, organs that were fully encompassed within the scan region were chosen and explicitly contoured on each slice using manual and semi-automated techniques (Figure 5-5). Specifically, lungs and glandular breast tissue were segmented in the chest models, while liver, spleen, and kidneys were segmented on abdomen/pelvis models. These organs are some of the most radiosensitive organs and also relatively easy to contour. The voxels within the contoured organs were assigned an elemental composition and density based on ICRU Report 44's composition of body tissue tables [113]. Using previously developed methods, each voxel outside of the segmented regions was assigned to one of the six tissue types (air, water, lung, fat, muscle, and bone) and subdivided into one of seventeen tissue density levels based on CT numbers using a validated Hounsfield Unit-to-tissue lookup table [113, 114]. Table 5-2 illustrates a version of this lookup table with different density levels for lung, fat, muscle, and bone. Any pixel with CT numbers greater than -930 HU was set to air with a density of 0.001293 g/cm^3, while pixels with CT numbers between -5HU and +5HU were set to water with density of 1.0 g/cm^3. A simple validation of this lookup table is described in more details in chapter 6.

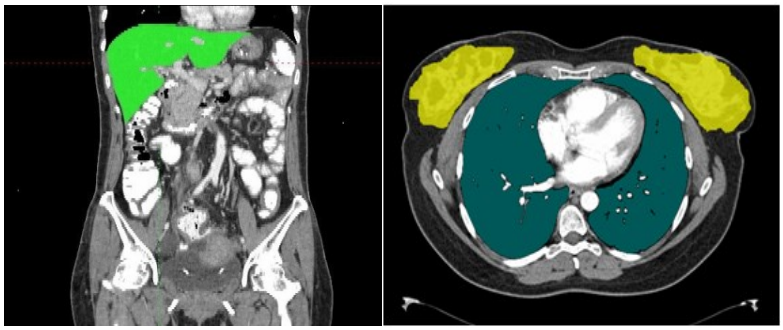

Figure 5-5 An example of segmented liver, lungs, and glandular breasts tissue.

Level	Lung		Fat		Muscle		Bone	
	CT # (HU)	ρ (g/cm^3)	CT # (HU)	ρ (g/cm^3)	CT # (HU)	ρ (g/cm^3)	CT # (HU)	ρ (g/cm^3)
1	(-930) → (-800)	0.048	(-200) → (-135)	0.85	(+5) → (+53)	1.06	(+280) → (+460)	1.48
2	(-800) → (-650)	0.1254	(-135) → (-70)	0.925	(+53) → (+100)	1.14	(+460) → (+640)	1.68
3	(-650) →(-500)	0.2987	(-70) →(-5)	0.98	(+100) →(+280)	1.26	(+640) →(+820)	1.89
4	(-500) →(-350)	0.4721					(+820)	2.1
5	(-350)→ (-200)	0.6455						

Table 5-2 HU-to-tissue lookup table used to create voxelized models from axial CT images.

5.4 IMPLEMENTATION OF VOXELIZED MODELS INTO MCNPX

The repeated structure geometry in MCNPX was used to describe the geometry of the voxelized patient models. This feature in MCNPX makes it possible to describe cells and surfaces only one time despite appearing more than once in the geometry.

Each segmented organ is assigned a marking ID in the segmentation software. Each pixel on the two dimensional axial CT image is assigned a universe number in MCNPX. The surfaces of a box that holds the three dimensional array of voxels is defined, and the FILL card is used to fill the box with a lattice structure. The lattice is defined using LAT, U, and FILL cards. LAT = 1 is used to specify a lattice composed of six surfaces, hexagonal. U card is used on the cell description to specify that the lattice is the only structure in its universe. The lattice is then filled using FILL card and the dimensions of the image set with a previously defined voxel sizes. The

filling of the lattice starts from the leftmost index; first along the x-axis, then the y-axis, and finally the z-axis.

The lattice geometry can be visualized using the Geometry Plotter, which can be used to plot a two-dimensional view of the geometry described in the input file. IP commend in MCNPX is used to initiate and plot the geometry embedded in the input file. Figure 5-6 illustrates the actual CT images with the two dimensional segmentations and the corresponding two dimensional geometry plotted using the geometry plotter in MCNPX.

As demonstrated on the top images of Figure 5-6, the segmentation of the glandular breast tissue on the images involves, first, the segmentation of the region that contains any glandular tissue including some adipose tissue and, then, further automatic separation into adipose and glandular tissue using CT number. The outcome is visible on the top right image of Figure 5-6.

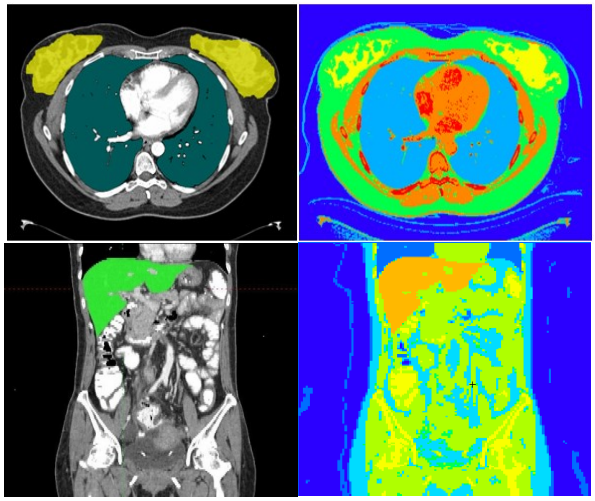

Figure 5-6 (Left) demonstrates the axial CT images with segmented organs and (right) illustrates the voxel representation of the patient and the contoured organs (liver, lungs, glandular breasts tissue)

This process of segmenting organs and generating a voxelized model was performed for each of the collected patient images used in this dissertation.

CHAPTER 6: VALIDATION OF THE MDCT MONTE CARLO CODE

In this chapter, a series of validation experiments were carried out to increase the confidence in the accuracy of the results obtained using the Monte Carlo code described in Chapter 4. These experiments were of increasing complexity, moving from fixed to variable tube current and from simple geometric objects to more complex, human-like phantoms.

6.1 INTRODUCTION

To measure organ dose to patients undergoing CT examinations, the only feasible approach is to use simulations using Monte Carlo radiation transport codes [50, 51, 62, 73, 76-78, 80, 81, 94, 115, 116]. However, as described in chapter 4, Monte Carlo based simulations require an extensive knowledge of the simulated CT scanner and the patient, such as the CT x-ray source spectrum (energy and flux), filtration, bowtie, collimation, and imaging parameters for a specific examination such as tube current, kVp, scan length, pitch, tube start angle, and rotation time. In addition to the required information for simulating a specific scanner, these codes have to be validated and benchmarked against actual experimental measurements to ensure the accuracy of simulated organ doses.

Most of these validation steps, performed by different groups focusing on Monte Carlo simulations, have made use of the Computed Tomography Dose Index (CTDI) phantoms and compared actual CTDI measurements with simulated values, while some recent publications have incorporated anthropomorphic phantoms to provide a more challenging test condition than the homogeneous and geometric CTDI phantom [83, 90, 92, 117-119]. However, none of these validations incorporated any complex variation of the tube current such as the ones seen in TCM mode, and only focused on simulations and validations of fixed tube current settings. Deak et al. validated a Monte Carlo model of an MDCT in a variety of different objects, including CTDI

phantoms, and, specifically, a homogenous liver phantom used to validate TCM modeling within the Monte Carlo tool. The liver phantom is a simple elliptical phantom with homogenous inserts along the z-axis. In addition to simple geometry, the simulated protocol was a single axial scan with limited modulation in the tube current, failing to validate the accuracy of the techniques used to model the longitudinal x-ray source motion resulting from helical scans with various values of pitch [93].

In this chapter, the Monte Carlo code used for all patient organ dose simulations performed in this dissertation are validated in multiple steps, using different phantoms, from simple to complex geometries, and in different scan mode settings, fixed and modulated tube current.

In the first section of the validation process, a set of phantoms including 32 and 16 cm CTDI phantoms are used to make different in-phantom dose measurements at different positions and different scanning modes (fixed tube current and TCM) using a small 0.6 cc ionization chamber. Simulations using the model of the MDCT scanner used for the measurements are performed using a) geometric descriptions of the phantoms in MCNPX using cell and surface cards and b) voxelized models of the phantoms utilizing axial CT images and the validated HU-to-tissue lookup table discussed in Chapter 5. Part b will include an anthropomorphic thorax phantom which is too complex to be modeled in MCNPX using cell and surface cards.

Although these validations can ensure the accuracy of dose estimates in the validated environment (CTDI or anthropomorphic phantoms), it does not ensure the accuracy of simulated organ doses, unless a direct comparison, i.e. comparing in-patient physical measurements and simulations, is conducted. The next section takes the validation process a step further by using actual patients and validating a MDCT scanner model using in-vivo dose measurements. This

step requires axial CT images for creating voxelized models of the patients and will make use of the tissue lookup table for creating them.

6.2 MONTE CARLO VALIDATION USING PHANTOMS

6.2.1 Physical Phantoms Used for Measurements

Five different geometries, ranging from simple to complex, were used for validating the modifications to the sourse.f of MCNPX to simulate MDCT scanners. These geometries included the 32 and 16 cm cylindrical phantoms, used in almost all Monte Carlo based validation studies, an elliptical phantom, water equivalent rectangular phantoms, and an anthropomorphic chest phantom.

The first two phantoms provide the simplest geometry as they are homogeneous in composition and homogeneous in shape. They are cylindrical phantoms of two different sizes (32 and 16 cm in diameter), known as CTDI phantoms, and are used regularly in CT dosimetry. These are homogenous cylindrical phantoms made off of polymethyl methacrylate (PMMA) with insert holes at five different positions: center, 12:00, 3:00, 6:00, and 9:00 o'clock positions (Figure 6-1).

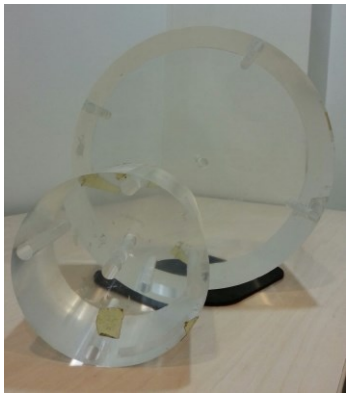

Figure 6-1 32 and 16 cm CTDI phantoms used for point measurements at center and 12:00 o'clock positions.

The next phantom provides a slightly more complex environment as the shape is not homogeneous and the composition changes only across sections. This elliptical phantom consists of three different homogenous sections: muscle, lungs, and fat. While each section is of homogenous composition in the x-y plane, when taken together, they provide a phantom that is heterogeneous along the z-axis. All three sections have insert holes at five different positions: center, 12:00, 3:00, 6:00, and 9:00 o'clock positions (Figure 6-2).

Figure 6-2 Three-sectional elliptical phantom, consisting of fat, lung, and, muscle equivalent martials from left to right.

The next phantom is homogeneous in composition, but provides some shape complexity in the x-y plane. The rectangular water equivalent phantoms are regularly used in radiation oncology for IMRT QA procedures. These were used because of their unique shape to provide variation for the x-y component of the TCM function. These phantoms are either solid blocks of equivalent water or have an insert hole in the middle for dose measurement purposes (Figure 6-3). Three of these phantoms, with one having an ion chamber insertion hole, were used in this section.

Figure 6-3 Rectangular solid water phantom.

The anthropomorphic chest/lung phantom (Radiology Support Devices, INC, Long Beach, CA) was used as the most complex scanned phantom in the in-phantom validation section. This phantom is a thorax phantom, extending from the neck to below the diaphragm, and is constructed using the skeleton of a male subject who is 175 cm tall and 73.5 kg weight. The materials used in this phantom are equivalent to soft tissue and bone, while animal lungs matching the size of the adult male were molded to fit the pleural cavities of the phantom in their inflated state (Figure 6-4).

Figure 6-4 Anthropomorphic Chest/Lung phantom with removal lungs.

6.2.2 Dosimetry Device

Standard dosimeters used to measure dose inside phantoms, in particular anthropomorphic phantoms, are detectors such as: thermoluminescent dosimeters (TLD), metal-oxide-semiconductor field-effect transistors (MOSFET), and optically simulated luminescence (OSL) dosimeters. However, these dosimeters need to be calibrated using ionization chambers beforehand to describe their energy dependency and dose linearity for absolute dosimetry. The calibration process is not only long and error prone, it is also hard to calibrate these inside the geometry using ion chambers due to small holes specially drilled for solid state detectors such as TLDs. Therefore, these are usually only calibrated against an ionization chamber placed in air. It is important to calibrate these dosimeters not only in air, but also in the object of interest because of beam hardening, and hence, an increase of the average energy in the object.

To avoid the calibration process and to be able to accurately measure absolute dose for the purpose of validating the Monte Carlo code, an ionization chamber was used for the absolute dosimetry measurements of this section. The RadCal ionization chamber with the active volume of 0.6-cc was utilized along with RadCal MDH 1015 meter for all the dose measurements. The 0.6-cc chamber's small volume can serve as a point dosimeter and was small enough to fit in all the geometries described above (Figure 6-5).

Figure 6-5 MDH 1015 and 0.6cc ionization chamber used for the measurements (courtesy of RadCal).

6.2.3 Dose Measurements

For geometries described above, a set of either four or six measurements were performed depending on the shape and availability of holes for inserting the ion chamber. All measurements were performed on a Siemens Sensation 64 CT scanner. All the scans were performed using helical mode, while the scan length covered the entire phantom.

Raw projection data for a total of twenty two acquisitions, fixed and TCM, was collected and used to extract information such as detailed tube current data, tube start angle and scan length, for the simulations. Additionally, images for each acquisition was reconstructed at 500 mm FOV and 1.2 mm slice thickness and collected for creating voxelized models of each acquisition.

All acquisitions were performed with 120 kVp, 0.5 rotation time, pitch of 1, 24x1.2 collimation, and 200 Quality Reference mAs, when using Care Dose 4D, and 200 effective mAs during fixed tube current acquisitions.

For each of these phantoms, a topogram was performed to help centering the phantom. When the ion chamber position was changed for performing measurements at a different position, the position of the phantom itself remained unchanged and kept in the center of the gantry at all times.

For the 32 and 16 cm CTDI phantoms, measurement at center and 12:00 o'clock were performed for each scanning mode, fixed and modulated tube current.

For the elliptical phantoms dose measurements were performed at three positions: center, 12:00, and 3:00 o'clock, using both fixed and tube current modulated modes.

For the rectangular water phantoms, two measurements, once inside the rectangular water phantom and once on the surface of the phantom, were performed using fixed tube current and TCM. The section containing the insertion hole for the ion chamber was placed between two other sold rectangular water phantoms.

Similarly, for the anthropomorphic phantom, measurements in depth and on the surface of the phantom in both modes, fixed and TCM, were performed. The lungs of the anthropomorphic phantoms can be removed and separated from the rest of the phantom; this capability was used to perform dose measurements inside the anthropomorphic phantom by taping the chamber inside the phantom parallel to the scan direction. Figure 6-5 illustrates the procedure of making in-depth measurements inside the anthropomorphic phantom.

Figure 6-6 Set-up of in-depth dose measurements using the anthropomorphic phantom.

6.2.4 Building Geometries in MCNPX

All the geometries were built in MCNPX using predefined cell and surface cards, except for the anthropomorphic phantom, for which only a voxelized model was feasible. In addition to building geometric models, voxelized models of all the other geometries were created from the resulting image data and used to evaluate the HU-to-tissue look-up table.

The geometries of CTDI phantoms, elliptical phantoms, and rectangular water equivalent phantoms were built in MCNPX using surface cards such as planes described by PX, PY, PZ, and surfaces defined by macrobodies such as RCC (Right Circular Cylinder) and RPP (Rectangular Paralleliped). Additionally, the chamber and its active region were modeled as explicitly as possible. The CT scanner table was approximated as a 1 cm thick rectangular carbon slab and modeled with each phantom. The following figures illustrate these geometries in two views, axial and sagittal, plotted using MCNPX geometry plotter.

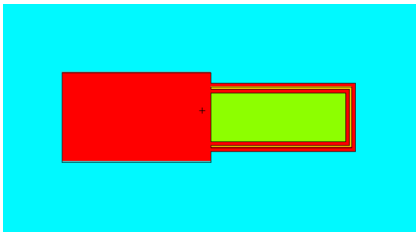

Figure 6-7 Sagittal view of the 0.6cc ionization chamber with the green tip representing the active region.

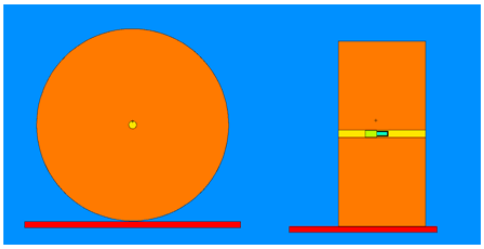

Figure 6-8 From left: axial view of the 32 cm CTDI phantom geometry built in MCNPX and sagittal view with visible ion chamber in the center.

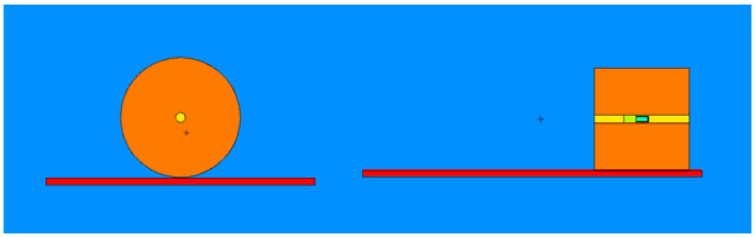

Figure 6-9 From left: axial view of the 16 cm CTDI phantom geometry built in MCNPX and sagittal view with visible ion chamber in the center. Red bar represents the table built as a 1 cm thick carbon board.

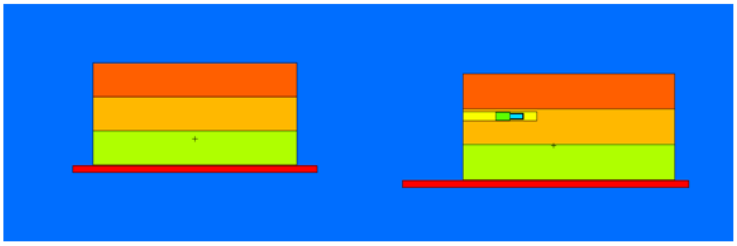

Figure 6-10 From left: axial view of the three rectangular water slabs and sagittal view of the slabs with the middle one containing the chamber for in-depth dose measurement.

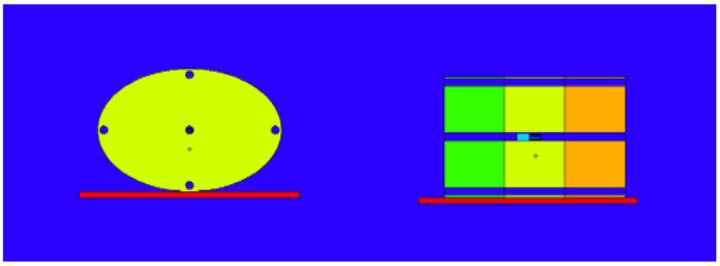

Figure 6-11 From left: axial view of the three-sectional elliptical phantom and sagittal view with ionization chamber in the center hole.

For the more complex geometry of the anthropomorphic phantom, only the voxelized model generated from the axial CT images was utilized in the simulations. The active region of the ionization chamber was identified and segmented on all the corresponding images. The segmented region was set to air, while the HU-to-tissue lookup table discussed in chapter 5 was used to assign different materials within the image to the pixels making up the image. The CT table was segmented out independently and set to carbon. Figure 6-12 shows three views of the voxelized model visualized using the MCNPX geometry plotter.

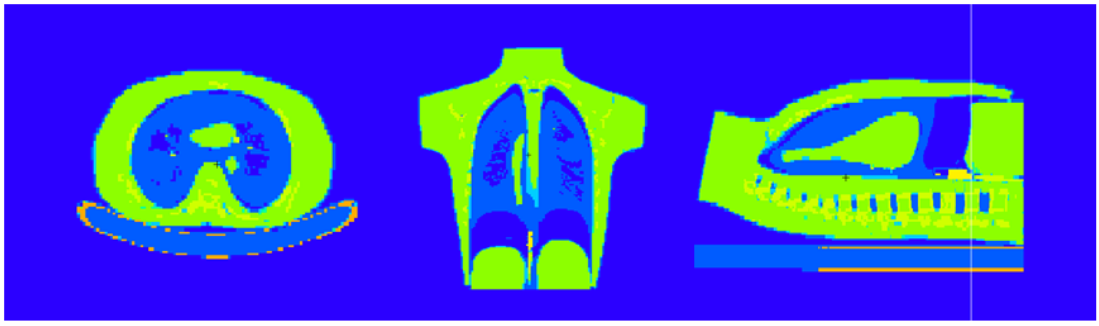

Figure 6-12 From left: axial, coronal, and sagittal view of the voxelized model of the anthropomorphic phantom.

In addition to the voxelized model of the anthropomorphic phantom, voxelized models of the rectangular solid water phantoms and the elliptical phantoms were also generated using the same HU-to-tissue lookup table.

For the CTDI phantom, a separate lookup table had to be created in which CT numbers can be assigned to PMMA rather than tissues. Table 6-1 illustrates this table which was generated based on three materials: air, PMMA, and chamber wall.

Air		Chamber Wall		PMMA	
CT # (HU)	**ρ (g/cm^3)**	**CT # (HU)**	**ρ (g/cm^3)**	**CT # (HU)**	**ρ (g/cm^3)**
-650	0.001293	(-650) → (+70)	1.76	(+70) → (+170)	1.19

Table 6-1 HU-to-material lookup table used to generate voxelized models of CTDI phantoms.

6.2.5 Monte Carlo Simulations

For every model, voxelized and MCNPX-built geometries, generated in section 6.2.4, two sets of simulations corresponding to fixed tube current and modulated tube current were performed using the Siemens Sensation 64 MDCT model. Collected raw projection data was used to extract information such as tube start angle and scan length for the fixed tube current simulations. For all

the TCM acquisitions, tube current data was also extracted from collected raw projection data using a MatLab script provided by Siemens. Using data regarding scanning parameters and extracted information from projection data, MCNPX input files were generated for all models.

Simulations were performed using MCNPX modified source.f described in chapter 4, and absolute doses were calculated using the normalization factor for 120 kVp and 24x1.2 collimation.

In addition to simulations utilizing raw projection data for extraction of TCM data, TCM simulations were performed using z-axis-only tube current information from the DICOM header of the image data. This approximated TCM function is readily accessible; however, it eliminates the x-y modulation of the TCM function, which does not significantly contribute to dose reduction in TCM mode. This approximation method to the detailed TCM function is explained and explored in more details for patients undergoing tube current modulated CT in Chapter 7.

All simulated doses were compared to dose measurements by calculating percent differences between simulated and measured doses. Table 6-2 summarizes used phantoms, different geometries, and simulations performed.

Phantom	Geometry	Fixed Simulations	TCM Simulations	
			Detailed TCM	z-axis-only TCM
CTDI - 16	Build	✓	✓	✓
	Voxelized	✓	✓	✓
CTDI - 32	Build	✓	✓	✓
	Voxelized	✓	✓	✓
Elliptical	Build	✓	✓	✓
	Voxelized	✓	✓	✓
Rectangular water blocks	Build	✓	✓	✓
	Voxelized	✓	✓	✓
Anthropomorphic	Voxelized	✓	✓	✓

Table 6-2 Summary of all the simulations performed across different phantoms.

6.2.6 Validation of the HU-to-Tissue Lookup Table

The Visible Human is one of the GSF models, which was created from axial CT images of a donated body of an executed man from Texas. The GSF model of the visible human contains a large number of segmented organs and tissues, including all ICRP critical organs. In addition to the GSF version of the visible human with all organs and tissues segmented and assigned elemental composition and density based on ICRU report 44, the CT images of the visible human were obtained from the National Library of Medicine [120]. The axial CT images of the visible human were imported into a workstation and used to segment out lungs, spleen, and kidneys. The voxelized model of the Visible Human was generated using the HU-to-tissue lookup table as described in chapter 5.

The MCNPX geometry plotter was used to visualize the GSF visible human model and HU-to-tissue lookup table generated voxelized model, referred to as the voxelized visible human. Figures 6-13 through 6-15 illustrate three views of both models side by side.

For the GSF visible human and voxelized visible human, fixed tube current simulations were performed using Siemens Sensation 64 MDCT model with 120 kVp, 24x1.2 collimation, pitch of 1, and rotation time of 0.5. A total effective mAs of 200 was used to calculate an absolute organ dose for the segmented organs. Organ doses resulting from both models (GSF visible human and voxelized visible human) were compared to each other by calculating percent differences for each organ.

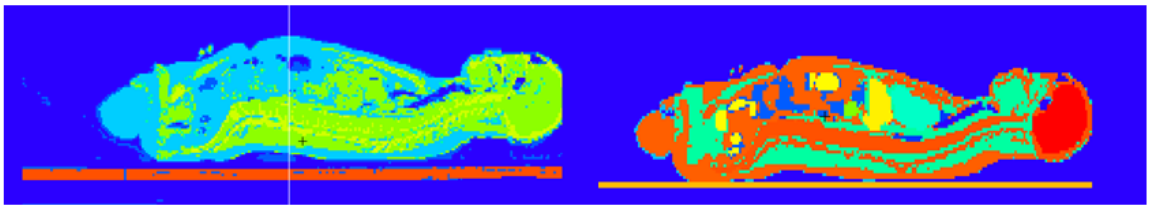

Figure 6-13 Left: Sagittal representation of the voxelized visible human using the lookup table. Right: Sagittal view of the GSF visible human with detailed segmentations. The differences in colors indicate the more detailed segmentation of the GSF model (right) than the voxelized model using the limited HU-to-tissue look-up table.

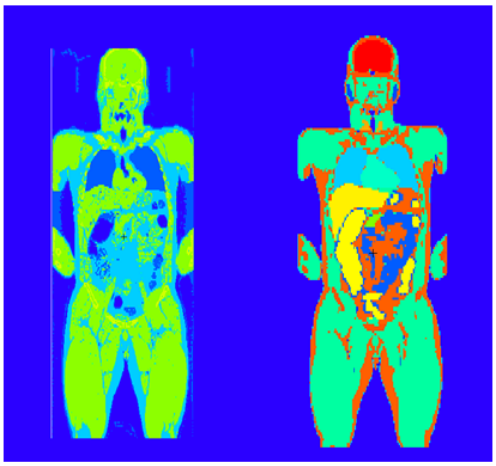

Figure 6-14 Left: Coronal representation of the voxelized visible human using the lookup table. Right: Coronal view of the GSF visible human with detailed segmentations.

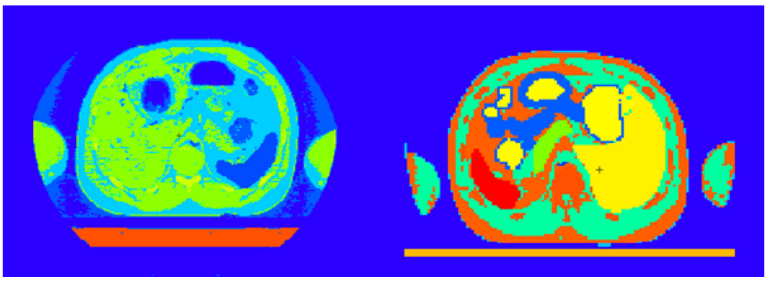

Figure 6-15 Left: Axial representation of the voxelized visible human using the lookup table. Right: Axial view of the GSF visible human with detailed segmentations.

6.3 In-Vivo Monte Carlo Validation

6.3.1 Virtual Colonoscopy Procedure at MD Anderson

The UT-MD Anderson Cancer Center Institutional Review Board (IRB) approval was obtained to perform in-vivo rectal radiation dose measurements for ten patients undergoing Virtual colonoscopy (VC) (also known as CT colonography (CTC)). CTC was first described in 1994 by Dr. David Vining as a minimally invasive means for identifying colorectal polyps and colorectal lesions [121]. The procedure consists of 1) bowel cleansing with cathartic agents, 2) gas insufflations with carbon dioxide, 3) computed tomography (CT) scanning of the abdomen-pelvis in supine and prone positions, and 4) image analysis for identification of lesions. IRB approval was granted for this study to affix two TLDs in the inner lumen of the standard rectal catheter tips used in 10 patient VC studies at MD Anderson Cancer Center (Figure 6-16).

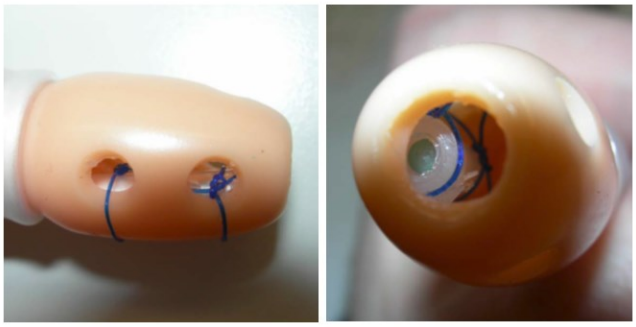

Figure 6-16. Two views of the rectal catheter tip containing TLD capsules.

Four dose contributors of the accumulated dose administered to patient's rectum were from two scout images and both prone and supine CT scans. Table 6-3 lists the parameters used for all four scans.

Series	Description	Scan Type	Area	Rotation Time	Image Thickness	Pitch	kVp	mA
1	Scout Supine	AP and Lateral	Mid-Sternum to Trochanter				120	10
2	Supine	Helical	Diaphram to Symphesis	0.5	1.25	0.984	120	100
3	Scout Prone	AP and Lateral	Mid-Sternum to Trochanter				120	10
4	Prone	Helical	Diaphram to Symphesis	0.5	1.25	0.984	120	100

Table 6-3 MD Anderson CT imaging protocol for Virtual Colonoscopy.

In order to reduce the chances of TLD-100 material coming in direct contact with patients, or TLDs becoming dislodged from the rectal catheter, or patients and researchers receiving an infection as a result of participation in this study, a process was put in place to ensure both patient and investigator safety in handling the TLDs

6.3.2 TLD Readouts and Determination of TLD Dose Response

Once a minimum of 14 days had passed from the actual VC procedure, the TLD readout was performed by the Radiologic Physics Center (RPC) at MD Anderson. RPC provided the following information for the purpose of calculating patient rectal dose: TLD aliquot charge reading Q (in μC), aliquot TLD mass m (in mg), sensitivity correction factor K_s (in cGy/μC/mg) and fading correction factor K_f (unit-less). These values were used in Equation 6-1 to calculate dose to TLDs which were reported as dose to muscle.

$$D_{TLD,Uncorrected} = \frac{Q}{m} \times K_s \times K_f \qquad \textbf{Eq. 6-1}$$

To further correct the calculated value for linearity, a calibration curve at 120 kVp was generated using identical measurements performed with a 0.6cc Farmer ionization chamber and TLDs. The Farmer chamber was placed in the 32 cm CTDI phantom and irradiated using the VC protocol shown in Table 6-3. The resulting exposure was corrected for muscle using the f-factor of air to muscle. Next, the Farmer chamber was replaced with TLD-loaded insert rod and irradiated with the same VC protocol. This procedure was repeated from 20 mAs to 170 mAs tube current with 10 mAs increments for both, the Farmer chamber and TLDs. The resulting calibration curve from these measurements is shown in Figure 6-17. A linear regression model was used to fit the data and the resulting linear regression equation was used to correct the resulting TLD dose values from Equation 1 for linearity (Equation 6-2).

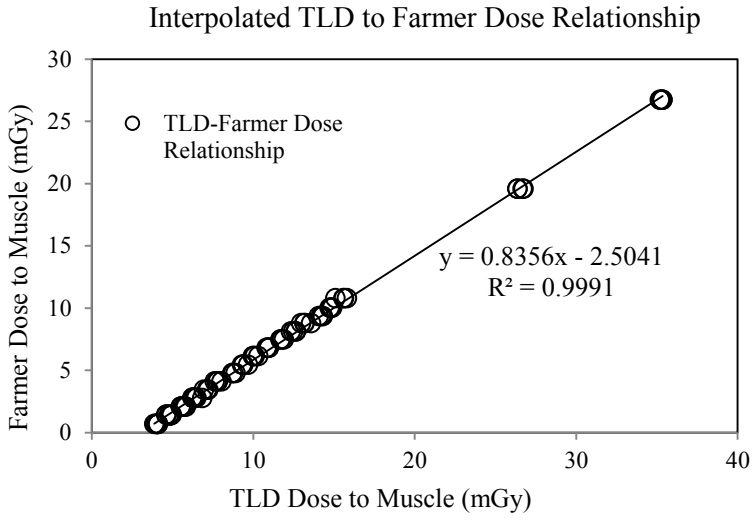

Figure 6-17 Linear regression model predicting Farmer ionization chamber response from TLD dose measurements uncorrected for linearity and energy.

$$D_{TLD} = D_{Farmer\ Chamber} = 0.8356 \times D_{TLD,Uncorrected} - 2.5041 \qquad \textbf{Eq. 6-2}$$

6.3.3 Voxelized Virtual Colonoscopy Models

Axial CT images (prone and supine) of all ten Virtual Colonoscopy patients were collected for creating voxelized models for use in simulations. Three out of ten collected patients were reconstructed at 500 mm FOV (Field Of View) with the entire anatomy present on the images. The rest were reconstructed at 360 mm, 380 mm, and 420 mm reconstructed FOV with zero to minor loss of anatomy on the images. Anonymized images were imported into a workstation for the segmentation process. The TLDs were identified and contoured as a whole entity on each image set. The rectal catheter was also identified and segmented along with the CT table and contrast media in the patient if seen on the images. Contoured TLDs, rectal catheter, table, and contrast if present, were set to muscle, plastic, graphite, and water, respectively (Figure 6-18). A Hounsfield Unit-to-tissue lookup table was used to assign each voxel outside the segmented region as one of the six tissue types (air, water, lung, fat, muscle, and bone) with 17 different tissue density levels as a function of voxel CT number [82, 122].

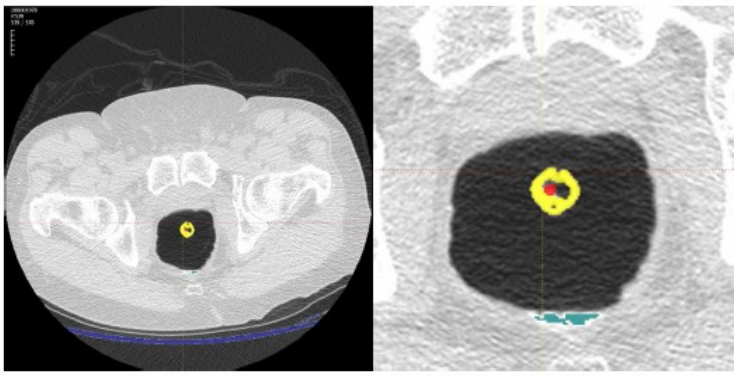

Figure 6-18 Left: axial CT images of the segmented TLD in the rectal. Right: zoomed image of the TLD (red dot) and the tip of the rectal catheter (yellow).

For all but one patient, two sets of voxelized models were generated: one from the prone scan and the other from the supine scan. For this patient, an additional decubitus scan was performed. For this specific patient, three sets of voxelized models were created and used to simulate dose to segmented TLDs.

6.3.4 GE LightSpeed VCT Source Model

A Multidetector row CT (MDCT) scanner (GE LightSpeed VCT, GE Healthcare) was modeled on the platform of MCNPX. The default MCNPX particle source code was modified to model the scanner (geometry and spectrum) as described in chapter 4. The CT x-ray source trajectory was reproduced by simulating a helical source path while using a point source to emit photons. The initial position and direction of each simulated photon was randomly selected based on scanner geometry specifications such as source-to-isocenter distance and fan angle. Each simulated photon was provided with a statistical weight for modeling the bowtie filter of the scanner [76-78]. The "equivalent source" method described by Turner et al. [95] was used to generate scanner-specific spectrum and filtration description to model the scanner's x-ray source. Simple validation methods using measurements and simulations of $CTDI_{100}$ at the center and periphery of both 32 and 16 cm CTDI phantoms were used to validate the scanner model [95]. Simulation results across all tested conditions agreed with measurements to within 1.3%.

6.3.5 Simulated VC Examination

For each voxelized model, a fixed tube current scan was simulated using Virtual Colonoscopy scan parameters shown in Table 1. Since voxelized models are based on the image data, the z-axis over-ranging distance used for helical reconstruction is missing not only on the image data, but also on the voxelized models. Hence, the scatter contribution from the over-ranging distance

was not taken into account when simulating dose to the TLDs [62]. This contribution is assumed to be negligible because the region in which energy is tallied is not close to edge of either side of the image data, in addition to the region (TLDs) being small in size.

Another scan parameter not modeled in these simulations is the tube start angle, which was arbitrarily set to zero for all patients due to unavailable information of the actual angle (no raw projection data was available, only image data which does not include information about the start angle). As described by Zhang et al. [123], tube start angle can have a considerable effect on surface dose. However, the TLDs where more internally placed in the patients, and therefore, we expect to see very little variation in terms of dose. Simulations at 90, 180, and 270 degrees were performed to show the variation of dose with respect to tube start angle.

Additionally, projectional simulations at the 12 o'clock position using each patient's scan length were implemented to estimate dose from the radiographic localizers. Dose from scouts were estimated to be very small and otherwise could have been ignored.

Simulated doses from all scans (prone and supine), including the projectional radiograph, were summed up for each patient and compared to the reported TLD measurements from MD Anderson.

6.4 RESULTS

6.4.1 In-Phantom Validations

Table 6-4 summarizes all the measurements and simulated doses for the simple geometries built using predefined cell and surface cards available in MCNPX, along with percent differences calculated between measured and simulated values. The Root Mean Square of the absolute percent error is 5.26% and 4.92% for fixed and TCM simulations, respectively. The z-axis-only

simulations resulted in the highest RMS of 14.4%, mostly caused by rectangular solid water slabs which resulted in highest percent difference of 37.18% and 15.95%, for in-depth and surface positions, respectively. Except for the rectangular water phantom, the overall agreement between measurements and simulated values are within less than 10%.

	Fixed Tube Current			Tube Current Modulation				
Phantoms/Positions	**Measured (mGy)**	**Simulation (mGy)**	**% Diff**	**Measured (mGy)**	**Detailed TCM Simulation (mGy)**	**% Diff**	**z-axis-only Simulation (mGy)**	**% Diff**
16cm CTDI Center	27.59	29.64	7.43	7.21	7.40	2.68	7.05	-2.27
16cm CTDI 12:00	27.68	28.78	3.97	7.20	7.75	7.68	7.19	-0.17
32cm CTDI Center	10.07	10.29	2.13	12.16	12.11	-0.42	11.48	-5.55
32cm CTDI 12:00	15.46	16.31	5.49	18.13	17.67	-2.58	17.41	-3.97
Elliptical Center	36.27	35.25	-2.79	11.90	12.92	8.63	13.06	9.77
Elliptical 12:00	27.94	28.26	1.12	7.88	8.02	1.84	8.36	6.20
Elliptical 3:00	20.94	19.52	-6.78	6.56	6.18	-5.83	6.13	-6.57
Water Equivalent Depth	19.18	20.88	8.83	10.25	10.80	5.38	14.06	37.18
Water Equivalent Surface	23.65	22.91	-3.15	13.36	13.08	-2.06	15.49	15.95
% Min		-6.78			-5.83		-6.57	
% Max		8.83			8.63		37.18	
% Average		1.81			1.70		5.62	
% RMS		5.26			4.92		14.40	

Table 6-4 Comparison of measured and simulated doses performed using differently shaped phantoms at a variety of positions. Simulations were performed using MCNPX-built geometries of all four phantoms.

Table 6-5 summarizes the results obtained from the organ dose simulations of the GSF model and the voxelized version using the HU-to-tissue lookup table. To validate the HU-to-tissue lookup table, doses simulated to lungs, kidneys, and spleen were estimated for each model and compared to each other. The Root mean Square of the absolute percent error across all three organs was 7.5%.

Organ	GSF Visible Human (mGy)	Voxelized Visible Human (mGy)	% Diff
Lung	16.07	16.87	4.98
Kidneys	13.91	15.1	8.55
Spleen	13.75	14.9	8.36
% Min		4.98	
% Max		8.55	
% Average		7.30	
% RMS		7.48	

Table 6-5 Simulated lung, spleen, and kidney doses using GS Visible Human versus voxelized version created using tissue lookup table.

Table 6-6 summarizes all the measurements and simulated doses for voxelized models of all five phantoms, built using HU-to-tissue lookup tables, along with percent differences calculated between measured and simulated doses. Similar to the results from MCNPX-built geometries, rectangular water phantom results in the highest percent difference in z-axis only simulations. Overall percent differences are within +/-10%, including the results from the anthropomorphic voxelized model, which, due to its complexity, could not be built in MCNPX using cell and surface cards and was created using tissue lookup table.

Phantoms/Positions	Fixed Tube Current			Tube Current Modulation				
	Measured (mGy)	Simulation (mGy)	% Diff	Measured (mGy)	Detailed TCM Simulation (mGy)	% Diff	z-axis-only Simulation (mGy)	% Diff
16cm CTDI Center	27.59	27.49	-0.36	7.21	7.21	0	7.17	-0.55
16cm CTDI 12:00	27.68	27.94	0.94	7.20	7.53	4.58	7.41	2.92
32cm CTDI Center	10.07	9.45	-6.16	12.16	11.07	-8.96	11.04	-9.21
32cm CTDI 12:00	15.46	14.88	-3.75	18.13	17.98	-0.83	18.74	3.36
Elliptical Center	36.27	41.24	13.70	11.90	11.13	-6.47	11.98	0.67
Elliptical 12:00	27.94	30.22	8.16	7.88	7.37	-6.47	8.42	6.85
Elliptical 3:00	20.94	22.62	8.02	6.56	6.11	-6.86	6.67	1.68
Water Equivalent Depth	19.18	21.12	10.11	10.25	10.77	5.07	14.18	38.34
Water Equivalent Surface	23.65	25.08	6.05	13.36	14.62	9.43	14.28	6.89
Anthropomorphic Depth	29.43	29.66	0.78	13.53	13.62	0.67	13.58	0.37
Anthropomorphic Surface	18.13	19.14	5.57	9.44	9.60	1.69	10.16	7.63
% Min		-6.16			-8.96		-9.21	
% Max		13.7			9.43		38.34	
% Average		3.91			-0.74		5.36	
% RMS		7.02			5.65		12.54	

Table 6-6 Comparison of measured and simulated doses performed using differently shaped phantoms including an anthropomorphic phantom at a variety of positions. Simulations were performed using voxelized models created from the images using tissue and CTDI/PMMA lookup tables.

6.4.2 In-Vivo Dose Validation

Table 6-7 summarizes the results obtained from both measurements and simulations for all ten VC patients. Percent differences range from a minimum of -27.5% to a maximum of 20.3% with an average of -8.8% and a Root Mean Square of absolute percentage of 32%. For eight out of ten patients, the percent differences were less than 10%. The two extreme percent differences reported as the minimum and maximum belong to the two remaining VC models.

Patient Model	Measured TLD Dose (mGy)	Simulated TLD Dose (mGy)	Percent Difference
Patient 1	10.30	10.16	-1.5
Patient 2	12.79	13.61	6.5
Patient 3	9.87	10.19	3.3
Patient 4	9.12	9.42	2.7
Patient 5	13.14	12.94	-1.5
Patient 6	11.48	13.81	20.3
Patient 7	10.04	10.75	7.0
Patient 8	17.92	17.69	-1.3
Patient 9	10.29	10.55	2.6
Patient 10	24.56	17.80	-27.6
Min	9.12	9.42	-27.6
Max	24.56	17.80	20.3
Average	12.96	12.69	1.1
STD	4.81	3.07	11.9

Table 6-7 Tabulated measurements and simulated doses to TLDs with their percent differences, assuming tube start angle at 0 degrees.

As mentioned in the methods, due to unavailable information of the tube start angle, all simulations for prone and supine scans used 0 degree (12'O Clock position) as their tube start angle. Since TLDs were placed more internally within the patients, we anticipated a very small effect on dose to TLDs due to tube start angle. Table 6-8 summarizes results from three other angles; 90, 180, and 270 degrees.

Patient Model	Measurements	90 deg Simulations	Percent Difference	180 deg Simulations	Percent Difference	270 deg Simulations	Percent Difference
Patient 1	10.30	10.32	0.2	10.72	4.1	10.61	3.0
Patient 2	12.79	13.41	4.8	13.24	3.5	13.13	2.6
Patient 3	9.87	10.21	3.5	10.36	5.0	10.18	3.2
Patient 4	9.12	9.58	4.5	9.37	2.2	9.30	1.5
Patient 5	13.14	12.82	-2.4	12.95	-1.4	12.72	-3.2
Patient 6	11.48	13.71	19.4	13.56	18.2	13.68	19.2
Patient 7	10.04	10.69	6.5	10.67	6.3	10.79	7.4
Patient 8	17.92	17.92	0.0	17.98	0.4	17.83	-0.5
Patient 9	10.29	10.03	-2.4	9.53	-7.3	10.04	-2.4
Patient 10	24.56	18.05	-26.5	20.02	-18.5	19.33	-21.3
Min	9.12	9.58	-26.5	9.37	-18.5	9.30	-21.3
Max	24.56	18.05	19.4	20.02	18.2	19.33	19.2
Average	12.96	12.67	0.75	12.84	1.23	12.76	0.94
STD	4.81	3.16	11.47	3.61	9.49	3.41	10.05

Table 6-8 Tabulated measurements and simulated doses at 90, 180, and 270 degrees along with percent differences from the measurements.

6.5 DISCUSSION

There is no doubt as to the usefulness of Monte Carlo methods in medical imaging. However, the accuracy of this method is a major subject and needs to be addressed before any reporting of simulated organ dose results. In this chapter, a multistep validation process was conducted to confirm the accuracy of Monte Carlo simulation results in this dissertation. These simulations included validation of the process of creating voxelized model using tissue and CTDI/PMMA lookup tables, validation of fixed and modulated tube current in simple and complex geometries, and validation of the z-axis-only simulations in case of unavailable detailed TCM data. In addition to in-phantom validations, direct in-patient measurements were also compared to simulations to further validate and confirm the absolute dosimetry simulations performed in this dissertation.

Overall, the calculated percent difference across all models and scanning modes were within 10%, except for z-axis-only simulation results from rectangular water phantoms, which resulted

in 37% difference compared to physical measurement. This phantom is homogenous in z direction but varies considerably in x-y direction, i.e. the difference between the peak and valleys in the tube current, generated due to the asymmetric shape of the phantom, is noticeably large. Figure 6-19 illustrates the detailed TCM data versus z-axis-only modulation of the TCM, extracted from the DICOM header of the image data for this phantom. The minimum and maximum tube current values due to the x-y modulation of the tube current are significantly different from each, hence the averaged values of these minimum and maximum tube current values (represented by z-axis-only modulation) have a large standard deviation. Therefore, the approximation of the x-y-z modulation by z-axis-only modulation is a very rough approximation for this specific phantom. Figure 6-20 demonstrates the detailed TCM versus z-axis-only TCM for all of the other phantoms, none of which behave as the rectangular phantom does due to their more circular shapes.

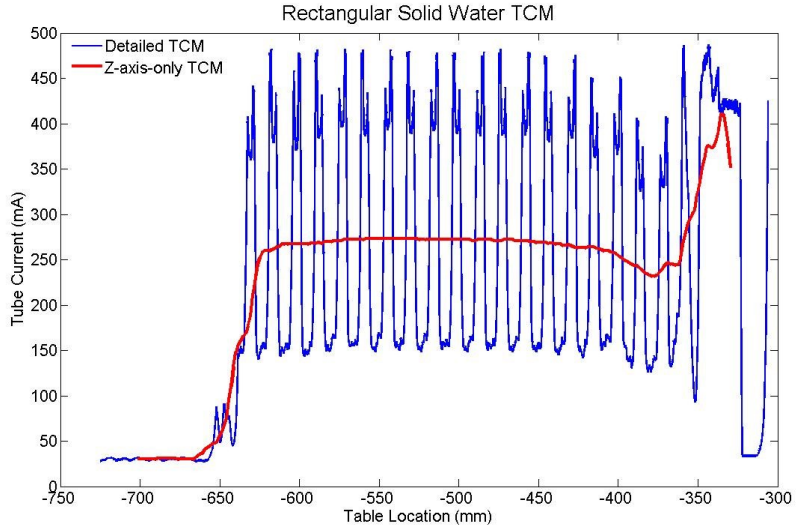

Figure 6-19 Detailed TCM function, shown in blue, illustrates an extreme modulation in the x-y direction caused by the asymmetric shape of the water phantom. The thickness of the homogenous water phantom in AP direction was much smaller than the lateral dimension, resulting in extreme minimum and maximum tube current values in the x-y planes. Z-axis-only modulation, shown in red, is a rough average of the minimum (150 mA) and maximum (480 mA) tube current values, hence not a good estimate of the detailed TCM function.

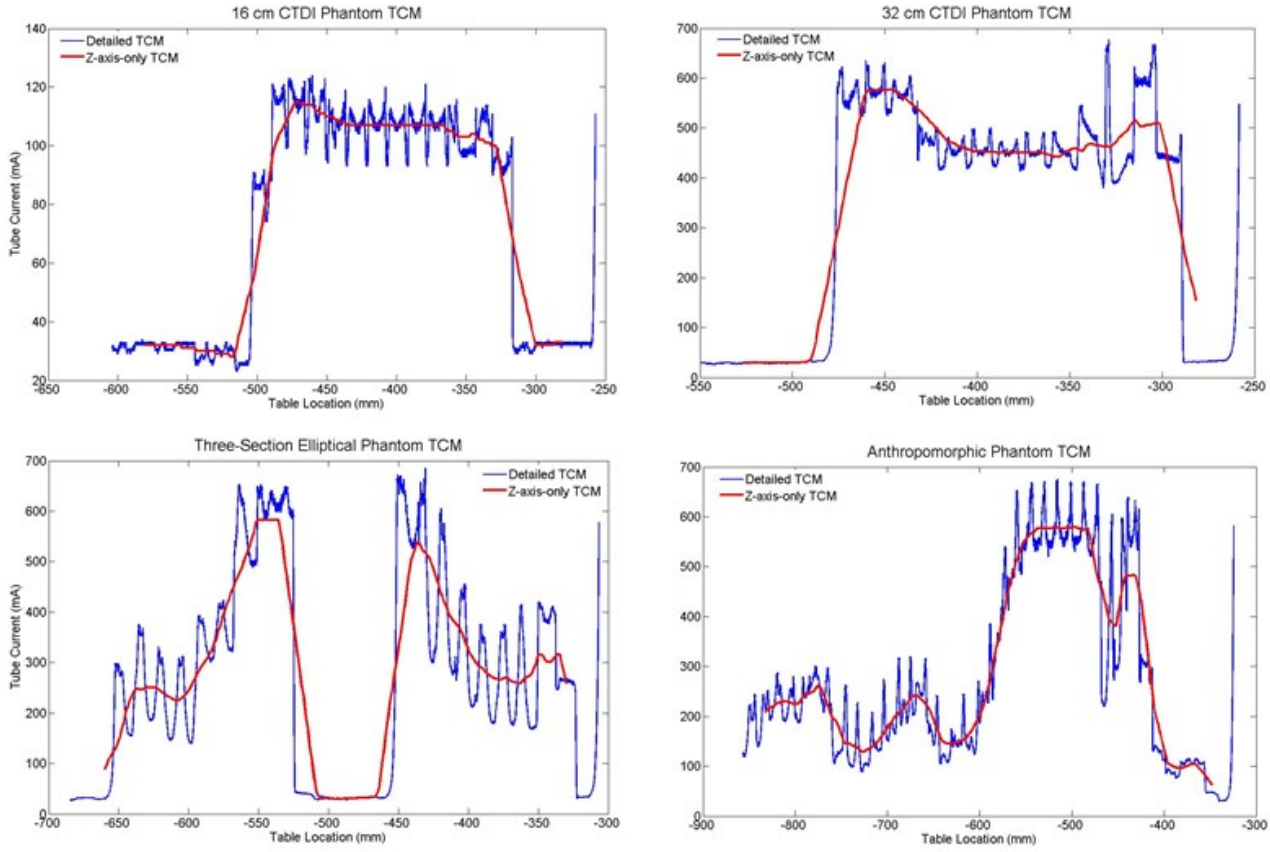

Figure 6-20 Detailed TCM (blue) versus z-axis TCM (red) for the cylindrical CTDI, elliptical, and anthropomorphic phantoms. Neither one of the TCM functions demonstrates extreme x-y modulation as seen with the rectangular phantom.

The in-vivo Monte Carlo Validation process compared direct measurements of dose with Monte Carlo based simulated dose estimates and is the first study to validate a Monte Carlo model of a MDCT scanner using in-vivo measurements as part of the validation process. Comparisons resulted in reasonable agreements between measurements and simulations; for eight out of ten patients, simulated results were within less than 8% of measurements. For two out of ten patients, patient model 6 and patient model 10, percent differences were approximately 20% and

-30%, respectively. Monte Carlo simulations overestimated TLD dose measurements for patient model 6 and underestimated the measurements for patient model 10.

Investigating the disagreement between measurements and simulations for these two models uncovered some possible causes for these differences. Image data for patient model 6 was reconstructed at 360 mm DFOV (Display Field of View), while the patient was scanned with arms beside the body. As illustrated in Figure 6-21, arms are not entirely visible within the DFOV and hence not modeled in the voxelized model of the patient. This resulted in higher dose values from simulations since less tissue was modeled in the voxelized model than the actual scan had encountered. Additionally, missing anatomy was observed at the level of the position of the TLDs, which also contributed to higher simulated dose estimates.

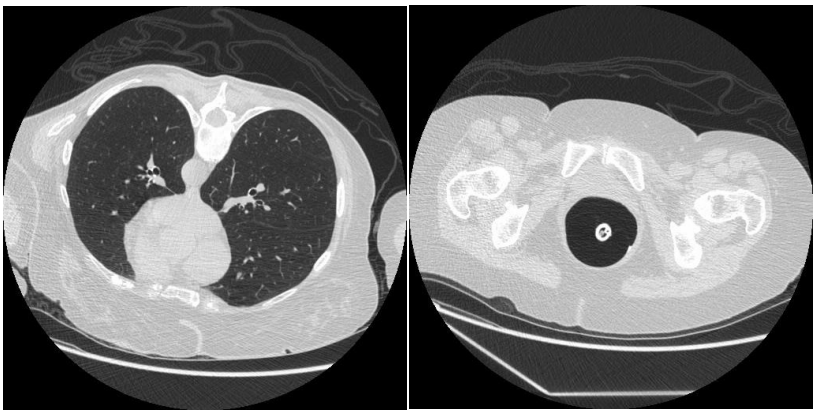

Figure 6-21 An example of missing anatomy within the reconstructed FOV resulting in incomplete voxelized models.

While an overestimation was observed for patient model 6, an underestimation was noticed for patient model 10. As illustrated in Figure 6-22, for this particular patient the prone image series consisting of 464 images did not cover the entire TLD, i.e. the last image within the series (image 464) had visible TLDs. This indicates that part of the TLD, not visible in the images, fell within the z-axis over-ranging distance. Hence, the generated voxelized model based on these

images is missing part of the dosimeter. Since the dosimeter is right at the end of the image series, z-axis over-ranging, which is not modeled for these patients, has a bigger effect on dose. Scatter from the over-ranging distance contributes significantly to the total dose measured by this specific TLD.

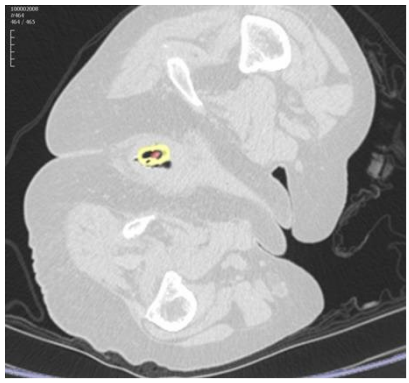

Figure 6-22 Last image of the series used to create voxelized patient mode 10. TLD was visible on the last image, indicating that scan did not completely cover the entire TLD.

Other possible reasons for discrepancies between measurements and simulated values resulting from voxelized models, is the shift in x-y plane in the reconstructed images to center the anatomy in the display field of view. Since the image data is used to create the model, the center of the reconstructed image in the x-y plane will be assumed to be the same as the center of the virtual gantry in the Monte Carlo model of the CT scanner. However, if the images were reconstructed at different x and y positions other than x=0 and y=0, the region of interest is no longer simulated at its true position during the actual scan. Figure 6-23 illustrates this shift in x and y plane. If this information is known, it can be corrected for by shifting the entire geometry to the actual position at which the scan was performed.

Figure 6-23 Demonstration of shifted images in the x-y plane. Due to mis-centering of the patient during the actual scan, reconstructed images are shifted in the x-y plane to center the anatomy within the DFOV. The center of the reconstructed images will be used as the center of the gantry in simulated scans; i.e. simulating a shifted position rather than the actual position of the patient within the gantry.

6.6 CONCLUSION

The focus of this chapter was to validate the Monte Carlo models of the MDCT scanners used in this dissertation, specifically the validation of the retrospective modeling of the tube current modulation. Overall, simulated and measured doses proved to be within reasonable agreement. This was established not only in simple, but also in more complex geometry and actual in-vivo measurements. While discrepancies can be due to the Monte Carlo model itself, such as modeling of the spectra, filtration, and source movement, most of discrepancies investigated in this work were caused by patient modeling and inadequate information on patient images and scan parameters.

The HU-to-tissue lookup tables were validated to within 7% using the GSF model of visible human and proved to be a reasonable approximation for generating voxelized models without detail segmentations of the entire body other than the region of interest. While the lookup table

proved to be an adequate approach for creating voxelized models from axial CT images, there are essential requirements that images have to meet to be useable for creation of voxelized models. These requirements include images reconstructed at largest FOV to ensure complete visibility of the anatomy, and reconstructed images at x=0 and y=0 to ensure the transfer of actual patient position within the gantry to the virtual scanner. In addition to these requirements, there are scanning parameters that are equally important to be known for the simulations; these include: tube start angle, scan length, and possibly the x-y plane shift in cases where images were not reconstructed at x=0 and y=0.

Another parameter of importance is the z-axis over-ranging distance, which is not modeled in the voxelized models, but as shown for patient number 10, it can have an effect on dose depending on where the region of interest lies within the scan length. A possible approximation of the dose contribution due to z-axis over-ranging, could be an interpolation of dose to the region of interest using its distance to the end of image data. This could be performed for multiple regions of interest and create a dose lookup table based on the distance of the ROI to the end of image data.

CHAPTER 7: A COMPARISON OF METHODS TO ESTIMATE ORGAN DOSES IN CT WHEN UTILIZING APPROXIMATIONS TO THE TUBE CURRENT MODULATION FUNCTION

This chapter describes methods by which Tube Current Modulation can be approximated for use in Monte Carlo simulations in case raw projection data is not available.

This chapter is based on Khatonabadi M, Zhang D, Mathieu K, Kim HJ, Lu P, Cody D, Demarco JJ, Cagnon CH, McNitt-Gray MF. The Accuracy of Organ Doses Estimated from Monte Carlo CT Simulations Utilizing Approximations to the Tube Current Modulation. Med. Phys. 39, 5212 (2012)

7.1 INTRODUCTION

TCM is a widely available dose reduction technique and a feature very frequently used in many clinical protocols to reduce dose while maintaining desired image quality [52, 53, 55]. Tube current modulation algorithms are either based on angular modulation, z-axis modulation, or a combination of these two, which forms a three-dimensional modulation most commonly used in conventional TCM algorithms [55, 59]. The angular or x-y modulation changes the tube current based on the projection's path length through the patient. For less attenuating path lengths, the tube current decreases while for the more attenuating paths, it increases to compensate for the greater attenuation [52, 54]. The z-axis modulation further reduces the tube current for sections of the body with lower density, such as lungs, and increases the tube current for areas with higher density, such as shoulders [57]. Therefore the nature of generating a TCM function makes the outcome of this feature very patient- and scan-specific. Angel et al. used TCM values extracted from the raw projection data to account for TCM in the Monte Carlo simulations by changing the weight of each simulated photon based on the TCM data [81]. However, these raw

projection data are not easily accessible and special programs may be needed to extract the tube current values.

Other studies have used Monte Carlo based software programs such as ImPACT and PCXMC to estimate organ dose from tube current modulated scans. Israel et al. [124] used ImPACT and estimated dose to 91 patients who underwent tube current modulated CT by computing dose for each image, using extracted tube current values from the image data, and summing it for whole-organ and whole-body dose estimates. The patient size limitation of ImPACT was overcome by establishing weight correction factors for different anatomical regions by modeling the adult chest and abdomen as cylinders of water and estimating the dose for a given x-ray tube potential. In addition to the limitation of estimating patient-specific organ doses, the difference between actual dose and the estimated dose is unknown and could not be assessed in this study.

He et al. [111] used PCXMC 2.0.1 to investigate how x-ray tube current modulation affects patient dose in chest CT examinations by using weighting factors for each projection. The investigated tube current modulation function was an idealized scheme based on the basic principles of tube current modulation technique, but not specific to any one manufacturer's algorithm nor what is being used clinically. The idealized TCM schemes were modeled as a function of x-ray tube angle, using intervals of 15º, and longitudinal axis of the patient. In addition to finer intervals (about 0.03º), some manufacturers' TCM algorithms also incorporate empirical data driven from observer studies to generate a TCM function.

The purpose of this study was to compare organ dose estimates obtained using a detailed TCM function with organ dose estimates obtained using approximations to the detailed TCM function. In this work, the detailed TCM function has been extracted from the raw projection data with

assistance from manufacturers. Two approximations to the detailed TCM function were evaluated. The first was a post-reconstruction technique using tube current information in the DICOM header of each CT image [125, 126]. The second was a single tube current value equal to the average tube current value over the entire TCM function reported by the scanner (can also be calculated using tube current values extracted from the DICOM header). The study comparison is based upon simulating tube current modulated CT exams of 40 patients and estimating radiation dose to the lung tissue and glandular breast tissue using three different methods. Organ dose estimates from different methods will be compared to the organ doses obtained using the detailed TCM method which will serve as the reference method.

7.2 Materials and Methods

7.2.1 Monte Carlo Simulation Code

To estimate organ doses from tube current modulated chest CT scans, a previously developed and validated Monte Carlo based CT dosimetry package, modeling scanner's geometry, spectrum, and filtration, was used [76-78, 81, 95]. The Monte Carlo code used is MCNPX (Monte Carlo N-Particle eXtended v2.6.0) radiation transport code developed at Los Alamos National laboratory [127, 128]. All simulations were performed in photon transport mode with a low-energy cutoff of 1 keV. This mode only tracks photon interactions and assumes secondary electrons deposit their energy at the photon interaction site. This assumption satisfies the condition of charged particle equilibrium (CPE), under which one can further assume that collision kerma is equal to absorbed dose.

7.2.2 MDCT Source Models

Two MDCT scanners were modeled in this study; a Sensation 64 (Siemens Healthcare, Forchheim, Germany) and a LightSpeed 16 (GE Healthcare, Waukesha, WI). The Monte Carlo

CT source simulates a helical source path using a point source to emit photons whose initial position and direction are randomly selected from the helical path based on the scanner source-to-isocenter distance and fan angle. The equivalent source model of Turner et al. [95] was used to generate scanner-specific spectrum and filtration for each MDCT scanner. Each scanner model was validated by simulating $CTDI_{100}$ at the center and periphery of both 32 and 16 cm CTDI phantoms and comparing these values to physical measurements. Number of simulated photons was chosen so that statistical errors were less than 1%. The simulation results agreed with the measurements to within 1.3% and 1.8% across all values for Siemens and GE, respectively.

7.2.3 Voxelized Patient Models

Twenty adult female chest models were developed using the methods previously introduced by Angel et al. [81] and were obtained with IRB approval. These models were derived from MDCT scans acquired on a Siemens Sensation 64 performed with CARE Dose 4D (TCM algorithm used in Siemens MDCT scanners, modulating tube current in three dimensions (x,y,z)) and scanner settings of 120 kVp, 24x1.2 mm collimation, Quality Reference mAs of 275, pitch values between 0.8 and 1.2, rotation time of 0.5 seconds, and reconstructed image thickness of 3 mm. The raw projection data and reconstructed DICOM image data were anonymized for each model. Image data were used to generate voxelized patient models; lungs and glandular breast tissue were identified using methods described by Angel et al. [81]; voxels within the contoured lungs and glandular breast tissue were assigned to the corresponding organ as defined by ICRU Report 44 [129]. Each voxel outside the segmented region was identified as one of the six tissue types (air, water, lung, fat, muscle, and bone) and subdivided into 17 different tissue density levels as a

function of CT numbers [129]. Figure 7-1 illustrates the axial view of one of the segmented CT images with its voxelized representation.

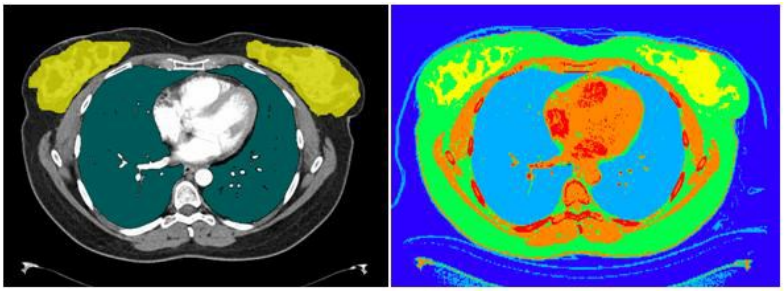

Figure 7-1 Segmented lungs and glandular breasts on an axial CT image (left), voxelized model of the same image graphically represented using MCNPX geometry visualization software (right).

To further compare each approximation method to the reference method, a second test condition was created using a second scanner (GE LightSpeed 16) with a different TCM algorithm. A set of twenty pediatric female whole body scans were obtained from this scanner with IRB approval and used to create voxelized models using the methods described above. These patients ranged from 8 to 17 years old and these scans were part of PET/CT exam covering the chest, abdomen and pelvic regions.

These models were derived from scans that were performed with a three dimensional (x,y,z) tube current modulation (SmartmA), pitch of 1.375, rotation time of 0.5 seconds, and 3.75 mm reconstructed image thickness. The maximum tube current value on the SmartmA was set to 120 mA for a 100 kVp scan and 110 mA for a 120 kVp scan (differs depending on patient's age). All of these pediatric patient whole body scans were performed using a bismuth breast shield. The shield was placed on patient's chest after the scout was acquired to eliminate its effects on the TCM algorithm. For each patient model, the TCM function and reconstructed DICOM image data were obtained and anonymized.

As with the adult patient models, the CT image data were used to generate voxelized models. Lungs and glandular breast tissue were identified and contoured using methods described by Angel et al. [81]; voxels within the contoured lung and glandular breast tissue were assigned to the corresponding organ as defined by ICRU Report 44 [129]. Each voxel outside the segmented region was identified as one of the six tissue types (air, water, lung, fat, muscle, and bone) and subdivided into 17 different tissue density levels as a function of CT numbers [129].

To investigate the effects of scanned anatomical region on the performance of the approximation methods, data from the thoracic region of the twenty pediatric female whole body models described above were used to create simulated thoracic scans. To do this only the TCM data from approximately 2 cm above the thoracic inlet to 2 cm below the costophrenic angles were used for the chest exam simulations. This was done to explore the effects of the region over which the average tube current is taken for the fixed tube current method (e.g. the average tube current value can be quite different when it is taken over the chest region compared to the average over the whole body region) which may affect simulated organ dose estimates.

7.2.4 Tube Current Modulation Model

For each patient model, detailed TCM function was extracted from the raw projection data. The TCM function of most of these patients follows the basic concepts of the TCM algorithms as shown in the blue curve in Figure 7-2. The angular modulation is recognized by the peaks and valleys in the function, representing the increase of tube current in the lateral direction and decrease of tube current in the anterior-posterior direction. In addition, the modulation along the z-axis based on different anatomical regions is also evident. Some cases demonstrate the tube current at its maximum value due to multiple reasons including selection of a high Quality Reference mAs, fast rotation time which results in a high instantaneous tube current value, and

some models included the arms within the scan range (which increases the local attenuation of that region of anatomy). In these situations where the tube current has reached the upper limit, the modulation along the z-axis becomes very small and the tube current is approximately constant over a range of anatomy.

In each case, the tube current value I is a function of table position z and tube angle Θ. For a given patient, all tube current values, I(Θ, z), were normalized to the maximum tube current value used in that acquisition. Then for each simulated photon the normalized value was used to modify its contribution to each dose tally by varying its MCNPX source weight value at each (Θ, z) position along the path of the source. This modeling of the tube current modulation represents the three-dimensional modulation (angular modulation (x-y) and z-axis modulation) of tube current for each patient, hence the name "detailed" TCM function method.

For all 20 pediatric models, detailed TCM functions were obtained from the scanner with assistance from the manufacturer. The TCM functions for these pediatric patients are noticeably different from the adult patients; most of these differences appear to be related to differences in the scanner and settings such as the maximum and minimum limits set by SmartmA.

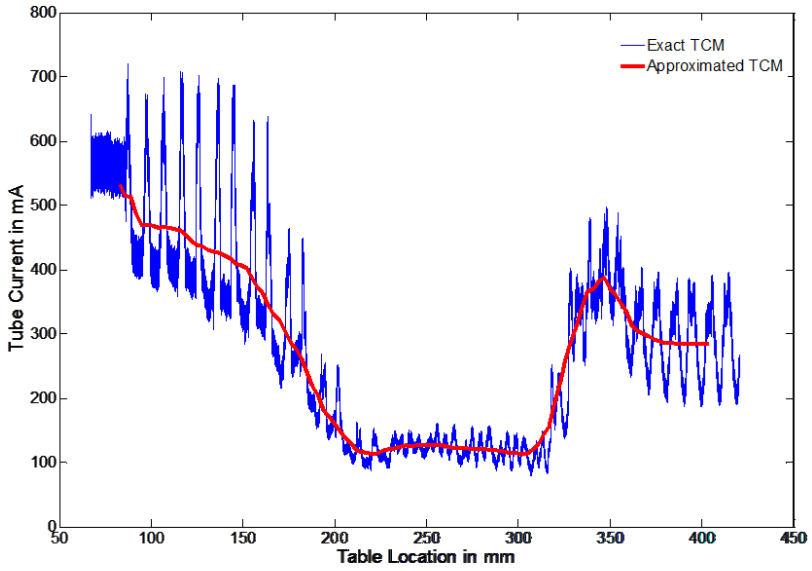

Figure 7-2 A chest TCM function with angular and longitudinal modulation in blue and z-axis-only modulation in red.

In helical mode, over-ranging refers to the region where anatomy is irradiated by the x-ray beam that is beyond the extent of image data; this is because of the need for extra data at both ends of the planned scan length for reconstruction purposes. The over-ranging region can be determined from start and end locations of the image data and locations of x-ray beam on and x-ray beam off, which are described in the tube current data that are extracted from the raw projection data. This is illustrated for each patient model group in Figures 7-3, 7-4, and 7-5. Because the detailed TCM method extracts tube current data from raw projection data, there is tube current data available from the over-ranging region. However, for the adult chest and pediatric whole body models, there is no image data – and hence no anatomy in the over-ranging region. Therefore for these models, over-ranging is approximated by modeling the tube current data, but with anatomy missing in the over-ranging region (Figure 7-3, 7-4). On the other hand, z-axis over-ranging is fully taken into account for the pediatric chest models because for these models both the tube current data and image data in the over-ranging region are available (Figure 7-5).

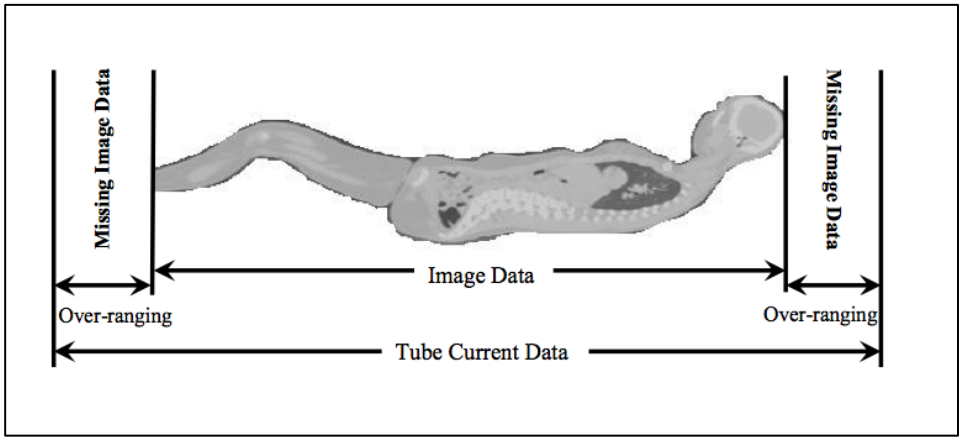

Figure 7-3 Over-ranging region illustrated for an adult female chest model. The figure does not represent the actual distance and is purely for illustration purposes. The models are generated from the image data and therefore do not include the anatomy of the over-ranging region, denoted as missing image data.

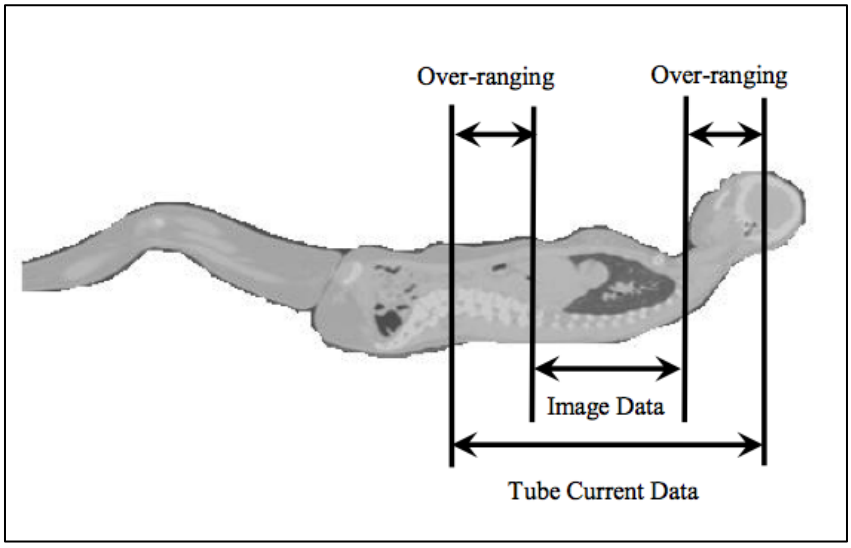

Figure 7-4 Over-ranging distance shown for the whole body pediatric models. For these models the missing image data does not include a huge amount of anatomy as compared to the adult female chest models shown in Figure 5-3.

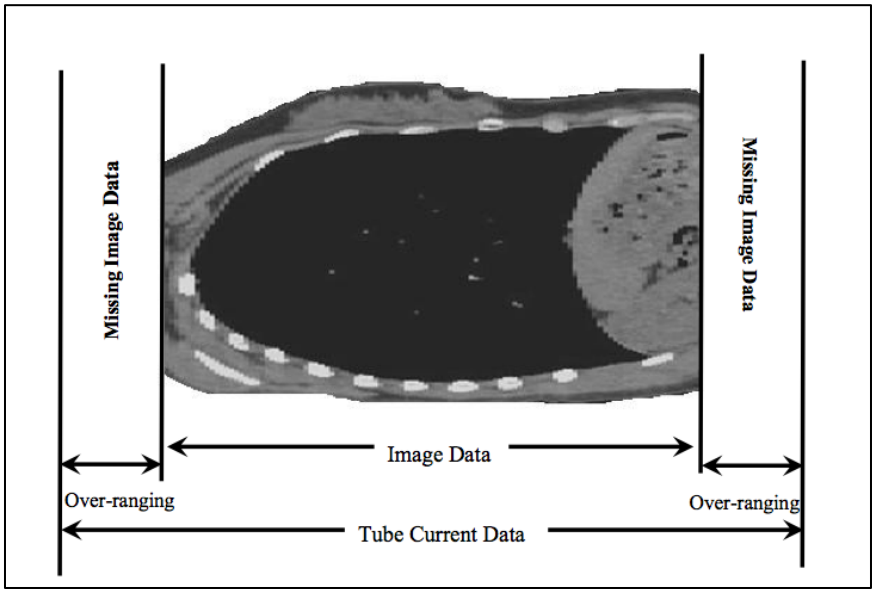

Figure 7-5 Pediatric female whole body models were used to simulate chest exams. For these chest models the over-ranging includes the anatomy due to models originating from whole body exams. The over-ranging distance was calculated from image data table location, extracted from the DICOM header of the image data, and tube current data table locations extracted from the raw projection data.

7.2.5 Longitudinal Approximated TCM Method

The longitudinal approximated TCM function was obtained from each patient's actual CT images via the DICOM header. Each image's DICOM header contains a unique tube current value along with a corresponding table location. The tube current reported in the DICOM header is the average value of the tube current over the rotation(s) used to reconstruct that image. Tube current and table location values for each image were read from the DICOM header of the image data using a MATLAB routine. Since tube angle is not available in the DICOM header of the image data, all simulations utilizing the longitudinal approximated TCM function were assumed to start at zero degree (12:00 position). Using each scan's length (which is based on image data and is calculated from the first and last slice table location values), scan's collimation settings,

and pitch, the number of rotations for each scan was calculated for use in assigning each table location a unique tube angle value.

The longitudinal approximated TCM function essentially only represents the z-axis modulation of the tube current but does not include the effects of over-ranging. Regardless of the availability of the image data from the over-ranging region, this method does not take into account over-ranging because the tube current data for the over-ranging distance is not available in the DICOM header. Figure 7-2 illustrates an example of a detailed TCM function and the longitudinal approximated TCM function, demonstrating the latter's inability to account for over-ranging.

7.2.6 Fixed (Average) Tube Current Method

The average tube current method is a fixed tube current simulation using a constant tube current value which is the average tube current over the entire scan length. This average is reported by the scanner, from which an average $CTDI_{vol}$ is calculated, but can also be calculated from the tube current data extracted from the DIOCM header. This average is shown in green for three models (Figures 7-6 through 7-8). Since this method, similar to the previous one, is entirely based on image data, it does not take into account over-ranging.

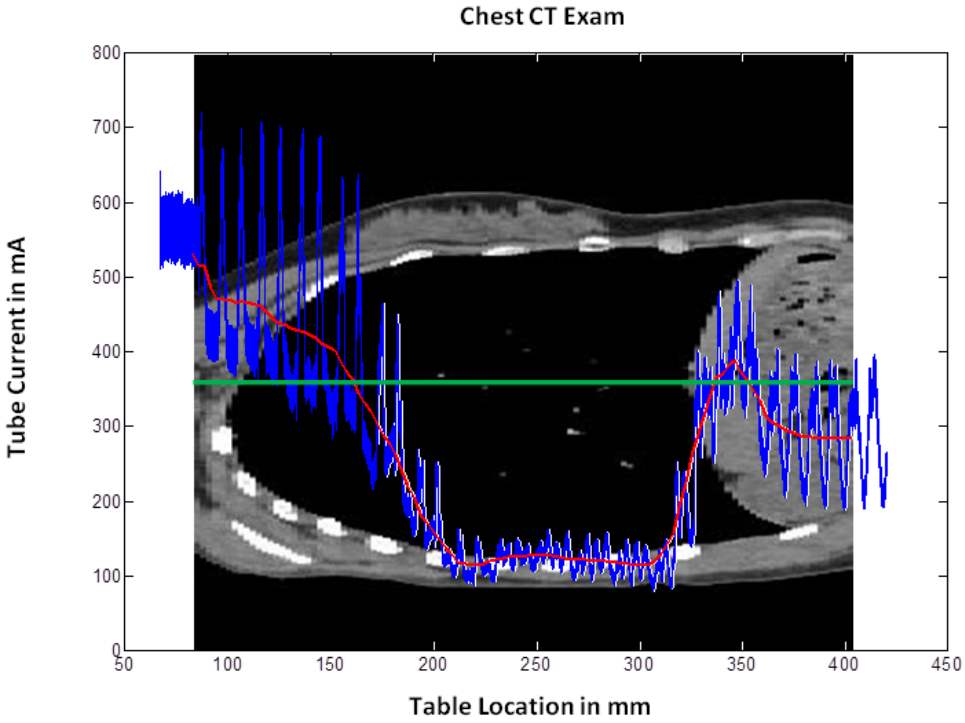

Figure 7-6 Siemens chest TCM function example with detailed modulation extracted from the raw projection data in blue, the z-axis only modulation extracted from the image data in red, and finally the average tube current approach in green.

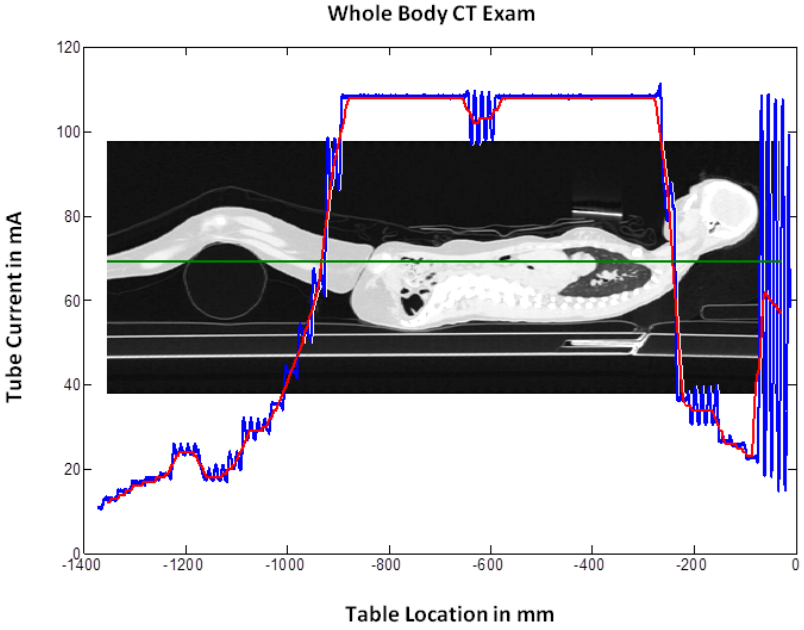

Figure 7-7 GE whole body exam TCM function example with detailed modulation extracted from the raw projection data in blue, the z-axis only modulation extracted from the image data in red, and finally the average tube current approach in green.

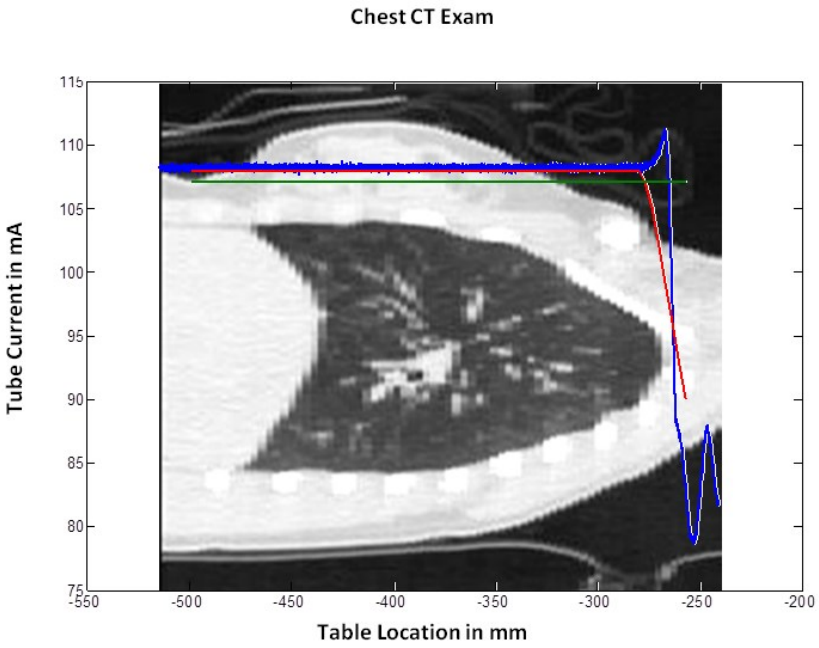

Figure 7-8 GE chest exam TCM function example with detailed modulation extracted from the raw projection data in blue, the z-axis only modulation extracted from the image data in red, and finally the average tube current approach in green.

7.2.7 Simulated CT Exams

For all three sets of patient models (adult female chest, pediatric female whole body, and pediatric female chest) three sets of simulations were performed each using a different TCM method: detailed TCM function method (reference), longitudinal approximated TCM function method, and fixed tube current method using a single tube current value averaged over the entire scan length. Different scan simulations and patient combinations are shown in Table 6-1.

Patient Models	Exam	Z-axis Over-ranging	Detailed TCM	Longitudinal Approximated TCM	Fixed Tube Current
20 Adult	Chest	NA (Figure 7-6)	✓	✓	single ave. mA over the scan length
20 Pediatric	Whole Body	NA (Figure 7-7)	✓	✓	single ave. mA over the whole body scan length
20 Pediatric	Chest	✓ (Figure 7-8)	✓	✓	single ave. mA over the chest region

Table 7-1 Different patient data sets and TCM methods to estimate organ dose illustrated in tabular form. Detailed TCM method uses a three dimensional modulation of the tube current, extracted from the raw projection data. For this simulation set the z-axis over-ranging was taken into account only for pediatric chest models. Longitudinal approximated TCM method uses only a z-axis modulation of the tube current which is extracted from the DICOM header of the image data. The fixed tube current method is a fixed tube current simulation utilizing a single tube current value equal to the average tube current calculated from the TCM function of the scan.

TCM methods were compared based on estimates of organ doses obtained with each method. The first set of tests was performed using 20 adult female chest models described above. For each patient model, each of the three methods (detailed TCM, longitudinal approximated TCM and fixed tube current scan using an average tube current) were utilized to obtain doses to lung and glandular breast tissue. Figure 7-6 illustrates the detailed, longitudinal approximated and fixed tube current functions for an adult patient model. These models are entirely based on image data and therefore the detailed TCM method simulations do not take into account over-ranging for these models (Figure 7-3).

The second set of tests was performed using 20 pediatric female whole body models described above. For each patient model, each of the three methods (detailed TCM, longitudinal approximated TCM and fixed tube current using average tube current over the entire whole body scan) were utilized. From each simulation both the dose to lung and glandular breast tissue were obtained and compared to the results from the reference method.

As mentioned before the TCM functions of these pediatric patients are different compared to the adult patient models acquired on Sensation 64 scanner and it is assumed to be due to an upper and lower limit set by SmartmA, GE's TCM algorithm. Nevertheless these data sets were used not to test the TCM algorithm, but to test the ability of approximation methods to match the results from the detailed TCM method, regardless of how it performed. Additionally, because these patients were all scanned on a different scanner than the adult patients, it allowed comparisons that included TCM algorithms from different manufacturers. Figure 7-7 illustrates the differences in the detailed TCM, longitudinal approximated TCM, and fixed tube current method for a pediatric patient model. Similar to the adult female chest models, detailed TCM method simulations do not take into account over-ranging for these models (Figure 7-4).

The third set of tests was performed to assess the effects of different scanned anatomical region on the performance of approximation methods. In these tests, the female pediatric models were used to simulate chest exams by only utilizing the thoracic region of the TCM functions. For each pediatric female model, each of the three methods (detailed TCM, longitudinal approximated TCM, and fixed tube current using average tube current over the chest region) were utilized. From each simulation, both the dose to lung and glandular breast tissue were obtained. Figure 7-8 shows only the thoracic region of the patient model illustrated in Figure 7-7, demonstrating information used to simulate dose from each method. Notice that the average tube current (average =108 mA) over the thoracic region is much higher than the average (average = 69 mA) over the entire body as shown in Figure 7-7.

Since our pediatric voxelized chest models are generated from whole body CT exams and tube current data are available for the entire scan length, we were able to account for z-axis over-ranging for the chest detailed TCM function simulations (Figure 7-5).

7.2.7 Dose Calculations

Absorbed dose in mGy was calculated for each model's lungs and glandular breast tissue. Dose was calculated using collision kerma, which is equal to absorbed dose under the assumption of charge particle equilibrium. For each simulated photon MCNPX tally type *F4 was used to track energy fluence in contoured regions and multiplied by mass energy-absorption coefficients (μ_{en}/ρ) to convert to collision kerma. The resulting dose per simulated photon for each organ was then multiplied by a normalization factor to convert to dose per mAs. This normalization factor is scanner, collimation, and kVp dependent and is used to take into account the fluence changes from varying the beam collimation.

To obtain absolute dose in mGy the calculated dose per mAs has to be multiplied by the total mAs, which is the mAs per rotation times the number of rotations. The mAs per rotation is different for each set of the simulations. For the detailed TCM method simulation the mAs per rotation is the maximum tube current value obtained from the raw projection data times the rotation time, for the longitudinal approximated TCM simulations this value is equal to the maximum tube current value obtained from the image data times the rotation time, and for the fixed tube current simulation it is equal the average mAs reported on the patient's dose report.

7.2.8 Dose Comparison and Statistical Analysis

To investigate the accuracy of organ dose estimates (mGy) obtained using different methods percent differences from organ doses obtained using detailed TCM function simulations were calculated. For each organ the root mean square error (RMSE) of the percent error values were also calculated for all simulation results. Furthermore to examine the difference between each method and the detailed TCM function (reference), scatter plots with identity lines and Bland-Altman plots were generated for each method using the simulated organ doses. Scatter plots with

identity lines are useful to illustrate how two comparable data sets agree with each other. In this case simulated organ doses were used to generate scatter plot for each alternative method, to see their agreement with doses obtained using the detailed TCM method. From each scatter plot Pearson's correlations were calculated after the normality check. For comparing each alternative method with the reference, instead of using a difference test with the null hypothesis being, the two data sets do not differ from each other, we used an equivalence test. The problem with the difference test is that if the analysis does not show a statistically significant difference between two data sets, the null hypothesis cannot be rejected. But not being able to find any difference between two data sets does not prove that they are similar. Not being able to find a difference may just be due to the sample size; too small to detect any difference between two data sets. In equivalence test the null hypothesis tests for similarities and if the data sets differ by more than delta. The alternative hypothesis tests if the data sets differ by less than delta, i.e. they are similar. The null hypothesis, the absolute value of percent difference between alternative and detailed TCM method ≥ delta

(i.e.$\left|\frac{organ\ dose\ from\ alternative\ method - organ\ dose\ from\ detailed\ TCM\ method}{organ\ dose\ from\ detailed\ TCM\ function} \times 100\right| \geq \Delta$), was tested for the alternative methods, longitudinal approximated TCM function and fixed tube current. The minimum deltas (i.e. minimum equivalence limit) were reported[130, 131].

7.3 RESULTS

Table 7-2 shows the results of each method for the adult patient models. Specifically, it shows the percent differences in estimated organ doses (for both lung and glandular breast tissue) between the detailed TCM estimates and each of the other methods. These results show that the smaller differences are between the detailed and longitudinal approximated TCM method, with

mean differences of -5% and -1% for breasts and lungs, respectively; these compare to mean differences of 11% and 8% for the fixed tube current method (using average tube current) for breasts and lungs, respectively. The RMSE are also smallest for the longitudinal approximated TCM compared to the fixed tube current method.

Table 7-3 shows the results of the equivalence tests, which demonstrate similar trends. Longitudinal approximated TCM function method and the detailed TCM method (reference) are equivalent within 3% and 1% for breasts and lungs, respectively. Calculated delta values are smaller for the longitudinal approximated TCM function than for the fixed tube current method; and in general the deltas are smaller for lungs than they are for breasts.

Figures 7-9 and 7-10 show both scatter plots with identity lines and Bland-Altman plots for the two alternative methods of estimating breasts and lung dose. Scatter plots with identity lines were used to illustrate the agreement between each alternative method and detailed TCM method. In this case an identity line was drawn as a reference. The more the two data sets agree, the more the scatters tend to concentrate in the surrounding area of the identity line. It is apparent that the organ dose estimates from the longitudinal approximated TCM function are closer to the results from the detailed TCM function than the estimates from fixed tube current method. On the scatter plots for the longitudinal approximated TCM function the fitted data falls either nicely right on the identity line (Figure 7-10, lungs) or closely along it (Figure 7-9, breasts). The Pearson's correlations are higher for this method than for the fixed tube current method, which is also graphically illustrated in the scatter plots by the fitted line (Figures 7-9 and 7-10). As the RMSE values for lungs and breasts suggest, differences between the detailed TCM method and each of the other methods are smaller for lungs than they are for breasts.

In the Bland-Altman plots, both the mean and the line representing the mean of the two data sets if they were equivalent are shown. Standard deviations are larger for fixed tube current compared to the longitudinal approximated TCM method in both organs.

Breasts		
Statistics	**% difference detailed-longitudinal approx.**	**% difference detailed-fixed TC**
Mean (SD)	-5 (7)	11 (21)
Minimum	-25	-13
Maximum	5	60
RMSE	9	23
Lungs		
Statistics	**% difference detailed-longitudinal approx.**	**% difference detailed-fixed TC**
Mean (SD)	-1 (2)	8 (10)
Minimum	-6	-8
Maximum	3	25
RMSE	3	12

Table 7-2 Summary of organ dose percent differences calculated for each method with respect to organ dose estimates from detailed TCM function for adult female chest models. Organ estimates from detailed TCM simulations are the reference in these comparisons.

minimum equivalence limit to detailed TCM method				
Population	**Longitudinal Approx. TCM**	**p-value**	**Fixed Tube Current**	**p-value**
Adult Female Chest-Breasts	3%	<0.0001	4%	0.0034
Adult Female Chest-Lungs	1%	0.0006	4%	<0.0001

Table 7-3 Summary of the equivalence test performed to determine the level of minimum equivalency between each method and the detailed TCM method, which is considered the reference. For example, in the case of adult female chest breasts, the mean of longitudinal approximated TCM method and detailed TCM method are equivalent within 3% with a significant p-value (0.0001) <0.05, indicating that the alternative hypothesis is accepted, i.e. the data sets are similar

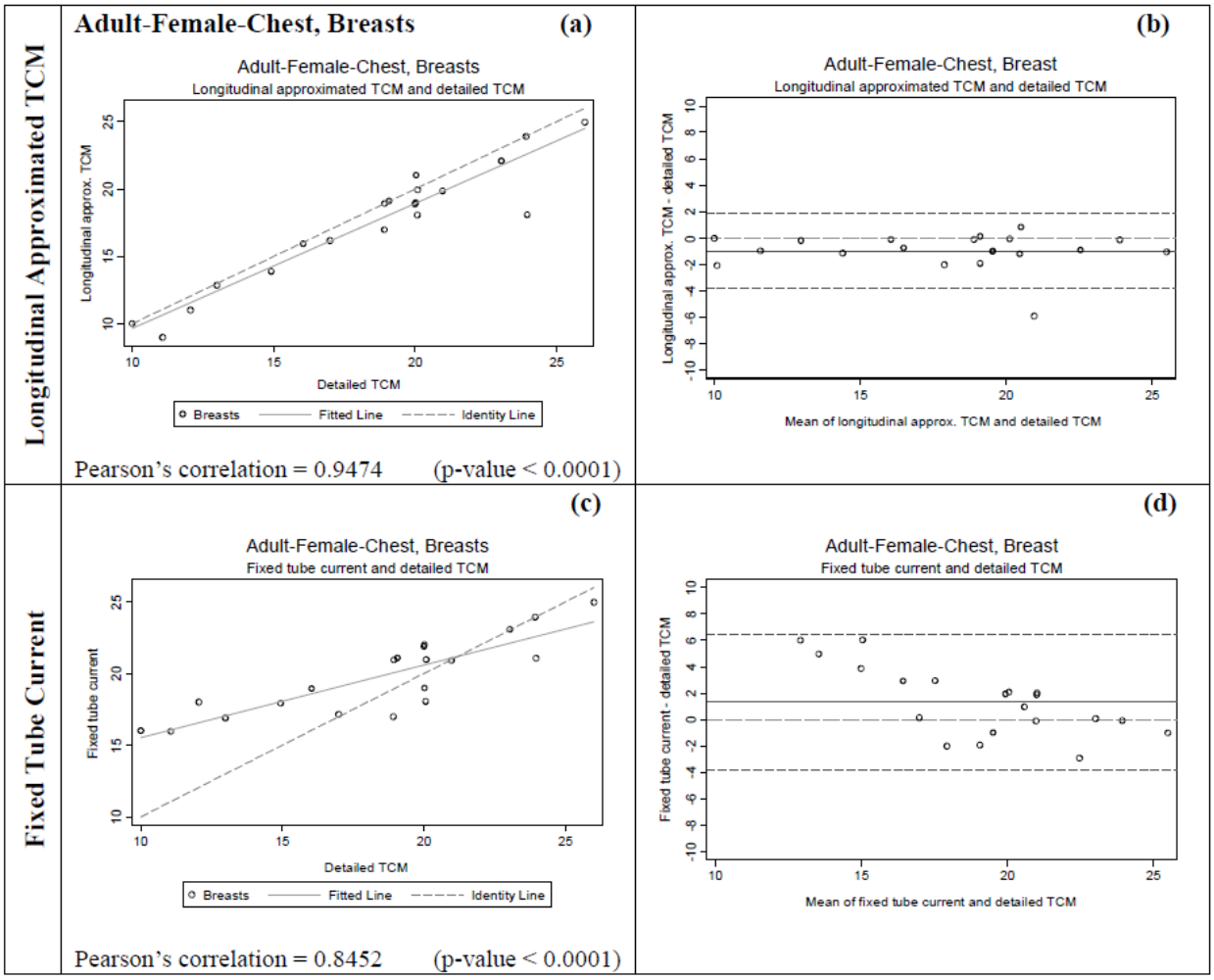

Figure 7-9 Summary of the statistical analysis performed on the breast dose data for adult patient models in mGy. Graphs (a) and (c) are the scatter plots for each method, while (b) and (d) are Bland-Altman graphs showing mean and standard deviation of the breast dose (mGy). The x axis of the scatter plot shows doses in mGy from detailed TCM function (X1) and the y axis represents doses in mGy from either the longitudinal approximated TCM or fixed tube current (X2). The x axis of the Bland-Altman graphs is (X1+X2)/2 and the y axis represents (X2-X1). For both methods the means are very close to the y=0 lines, however, the standard deviation is larger for the fixed tube current method compared to the longitudinal approximated TCM method.

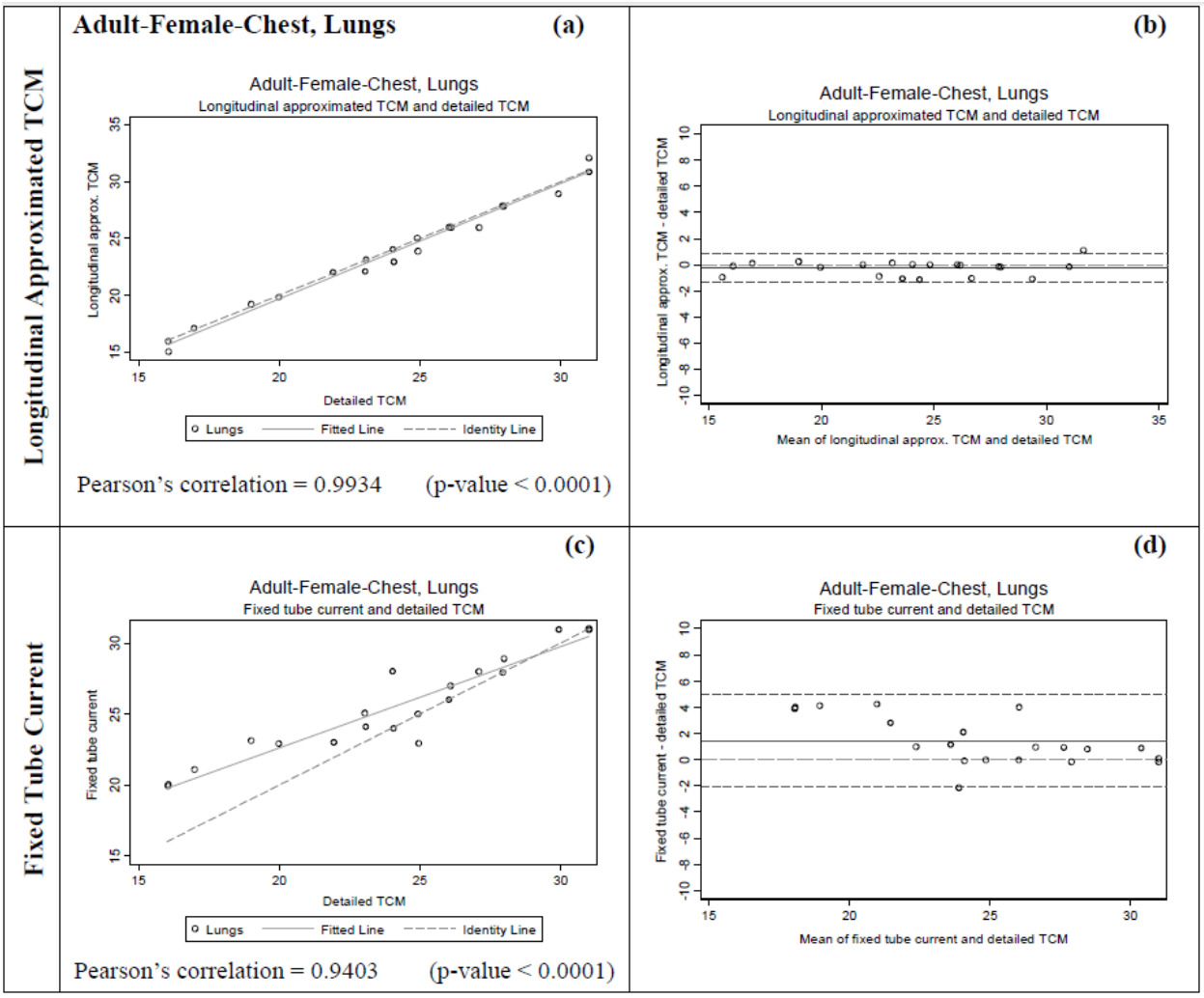

Figure 7-10 Summary of the statistical analysis performed on the lung dose data for adult patient models in mGy. The graphs on the left are the scatter plots for each method ((a) and (c)); while the ones on the right are Bland-Altman graphs ((b) and (d)) to show mean and standard deviation of the data. The x axis of the scatter plot shows lung dose in mGy from detailed TCM function (X1) and the y axis represents lung dose in mGy from either the longitudinal approximated TCM or fixed tube current (X2). The x axis of the Bland-Altman graphs is (X1+X2)/2 and the y axis represents (X2-X1). The mean for longitudinal approximated TCM method is closer to the y=0 line, indicating a higher similarity between detailed TCM method and the longitudinal approximated TCM method. The standard deviation is also much smaller for the longitudinal approximated TCM method compared to the fixed tube current method.

Table 7-4 shows the results for the pediatric whole body patient models. This table shows the percent difference in estimated organ doses (for both lung and glandular breast tissue) between the detailed TCM estimate and each of the other methods. These results also show small

differences between the detailed and longitudinal approximated TCM method with mean differences of 2% and 0% for breasts and lungs, respectively; these compare to mean differences of -32% and -31% for the fixed tube current method using average tube current for breasts and lungs, respectively. The RMSE are also smaller for the longitudinal approximated TCM method compared to the fixed tube current method.

Table 7-5 shows the results of the equivalence tests; calculated delta values are much smaller for the longitudinal approximated TCM method than for the fixed tube current method. Figures 7-11 and 7-12 show both scatter plots and Bland-Altman plots for the two methods of estimating breasts and lung dose, respectively for the pediatric whole body patient models. It is apparent that the organ dose estimates from the longitudinal approximated TCM method are closer to the results from the detailed TCM method. On the scatter plots for the longitudinal approximated TCM function the fitted data falls nicely right on the identity line for both lungs (Figure 7-11) and breast (Figure 7-12). The Pearson's correlations are higher for the longitudinal approximated TCM method compared to the fixed tube current method.

Note that the organ dose estimates obtained from the fixed tube current method, based on an average tube current, are rather poor here. This is primarily because this average is a poor estimate of the actual tube current used in the chest region, as demonstrated in Figure 7-7. This is another motivation for simulating thoracic exams using the pediatric whole body patient models so that a more representative tube current value can be used over the chest region; demonstrating the dependency of this method's performance on the scanned anatomical region.

Breasts		
Statistics	**% difference detailed-longitudinal approx.**	**% difference detailed-fixed TC**
Mean (SD)	2 (7)	-32 (11)
Minimum	-5	-45
Maximum	25	-7
RMSE	7	34
Lung		
Statistics	**% difference detailed-longitudinal approx.**	**% difference detailed-fixed TC**
Mean (SD)	0 (1)	-31 (10)
Minimum	-2	-42
Maximum	3	-5
RMSE	1	32

Table 7-4 Statistical summary for pediatric whole body data set, showing a lower mean difference as well as lower RMS value for organ doses estimated using the longitudinal approximated TCM function.

minimum equivalence limit to detailed TCM method				
Population	**Longitudinal approx. TCM**	**p-value**	**Fixed Tube Current**	**p-value**
Pediatric Female Whole Body-Breasts	2%	0.0214	29%	<0.0001
Pediatric Female Whole Body-Lungs	1%	0.0007	27%	<0.0001

Table 7-5 Summary of the test performed for pediatric female whole body patient models to determine the level of minimum equivalency between each method and the detailed TCM method, which is considered the reference. For example, in the case of pediatric whole body lung, the mean of fixed tube current method and detailed TCM method are equivalent within 29% with a significant p-value (0.0001) <0.05, indicating that the alternative hypothesis is accepted. However, this minimum equivalence limit (29%) is much larger compared to the longitudinal approximated TCM method (2%).

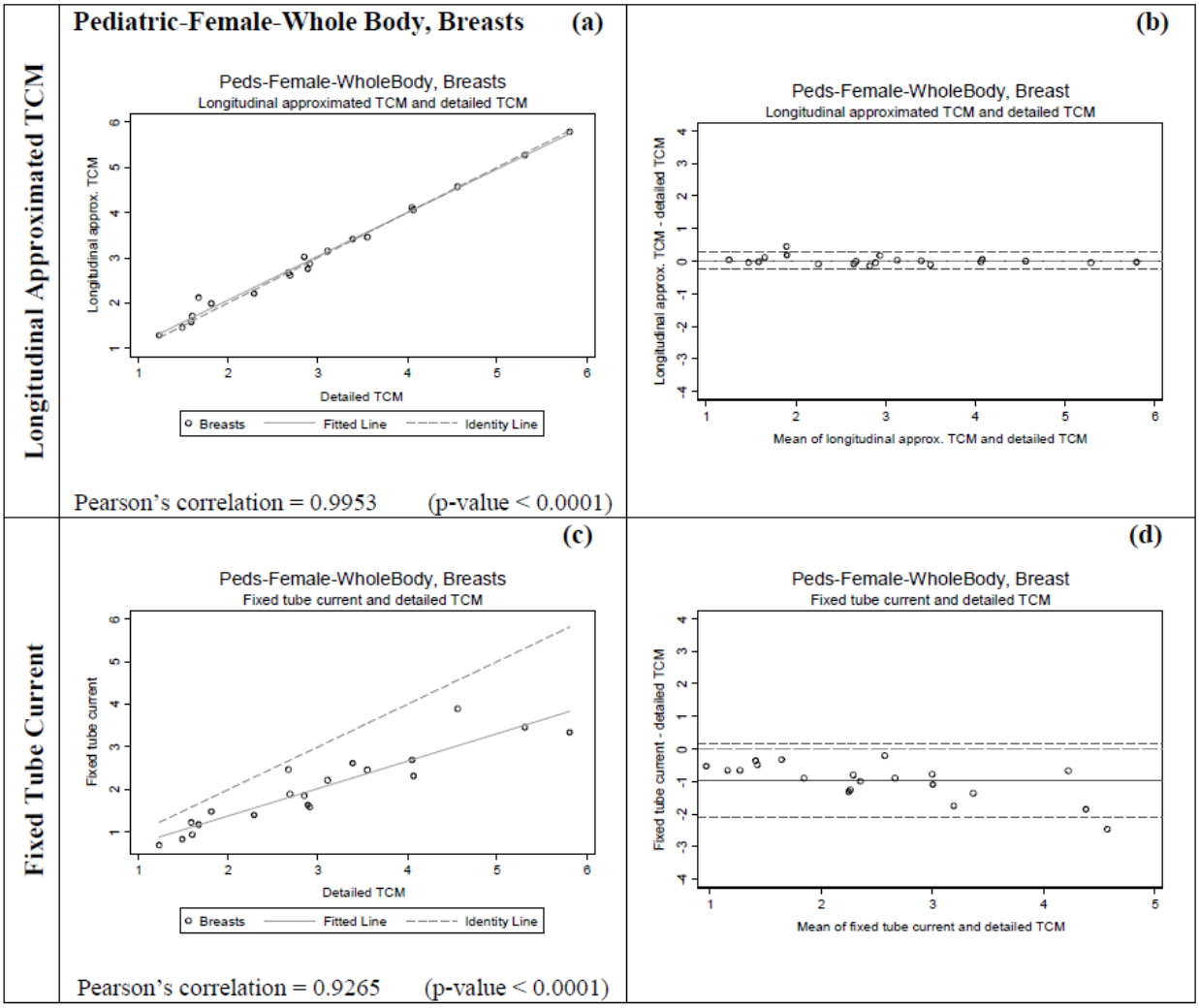

Figure 7-11 Summary of the statistical analysis performed on the breast dose data for pediatric patient whole body models in mGy. The graphs on the left are the scatter plots for each method, while the ones on the right are Bland-Altman graphs to show mean and standard deviation of the data. The x axis of the scatter plot shows breast dose in mGy from detailed TCM function (X1) and the y axis represents breast dose in mGy from either the longitudinal approximated TCM or fixed tube current (X2). The x axis of the Bland-Altman graphs is (X1+X2)/2 and the y axis represents (X2-X1). The mean for longitudinal approximated TCM method is closer to the y=0 line, indicating a higher similarity between reference and the longitudinal approximated TCM method. The standard deviation is also much smaller for the longitudinal approximated TCM method compared to the fixed tube current method.

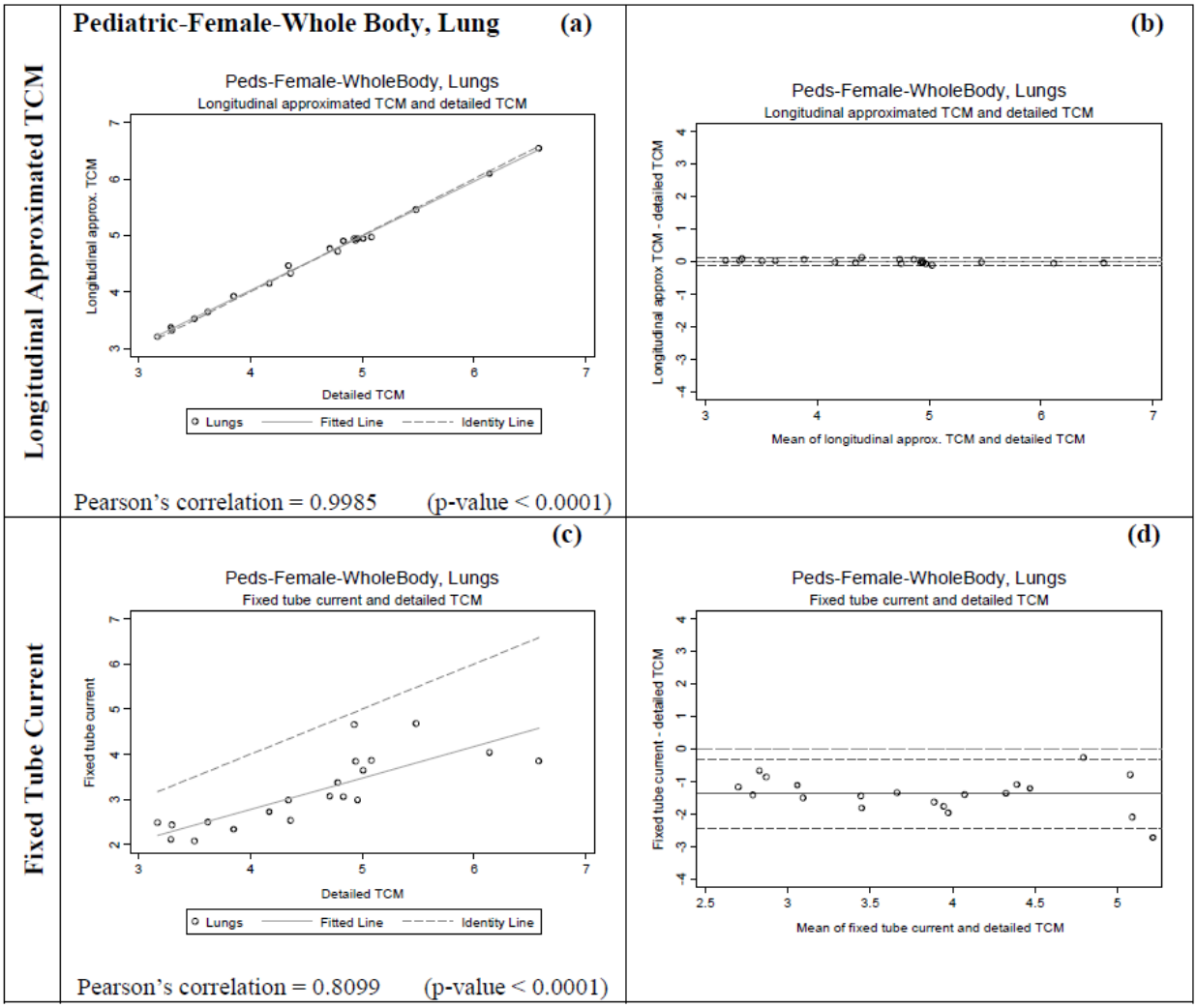

Figure 7-12 Summary of the statistical analysis performed on the lung dose data for pediatric patient whole body models in mGy. The graphs on the left are the scatter plots for each method, while the ones on the right are Bland-Altman graphs to show mean and standard deviation of the data. The x axis of the scatter plot shows doses in mGy from detailed TCM function (X1) and the y axis represents doses in mGy from either the longitudinal approximated TCM or fixed tube current (X2). The x axis of the Bland-Altman graphs is (X1+X2)/2 and the y axis represents (X2-X1). The mean for longitudinal approximated TCM method is closer to the y=0 line, indicating a higher similarity between reference and the longitudinal approximated method. The standard deviation is also much smaller for the longitudinal approximated TCM method compared to the fixed tube current method.

Table 7-6 shows the results for the pediatric chest exam simulations. This table shows the percent difference in estimated organ doses (for both lung and glandular breast tissue) between the detailed TCM estimate and each of the methods, with the fixed tube current now being only

based on the chest region. While these results show small differences between the detailed and longitudinal approximated TCM method, with mean differences of 2% and -2% for breasts and lungs, respectively, this table also shows mean differences of only -6% and -3% for the fixed tube current method, using the regional average tube current, for breasts and lungs, respectively. The RMSE are also smaller for the longitudinal approximated TCM compared to the fixed tube current method, but the difference is small. In fact, most of the large percent differences in breast tissue estimates are due to differences between very small numbers (i.e. cases where there is not much glandular breast tissue and so doses are very small).

Table 7-7 shows the results of the equivalence tests, which demonstrate that the calculated delta values are very similar between methods. Figures 7-13 and 7-14 show both scatter plots and Bland-Altman plots for the two methods of estimating breasts and lung dose, respectively for the pediatric chest patient models. As opposed to previous sets of results, these figures show that there is not much difference between the two methods, for either breasts or lung dose estimates. The scatter plots for both methods show the fitted data fall nicely right on the identity line for both breasts (Figure 7-13) and lungs (Figure 7-14). The Pearson's correlations are also similar in both methods.

Breasts		
Statistics	**% difference detailed-longitudinal approx.**	**% difference detailed-fixed TC**
Mean (SD)	2 (9)	-6 (10)
Minimum	-7	-32
Maximum	32	-6
RMSE	9	11
Lungs		
Statistics	**% difference detailed-longitudinal approx.**	**% difference detailed-fixed TC**
Mean (SD)	-2 (2)	-3 (3)
Minimum	-5	-10
Maximum	1	2
RMSE	3	4

Table 7-6 Statistical summary for pediatric chest data set, showing similar mean differences and RMS value for organ doses estimated using both methods.

minimum equivalence limit to detailed TCM method				
Population	Longitudinal approx.TCM	p-value	Fixed Tube Current	p-value
Pediatric Female Chest-Breasts	3%	0.0391	2%	0.0023
Pediatric Female Chest-Lungs	2%	<0.0001	2%	<0.0001

Table 7-7 Summary of the test performed for pediatric female chest patient models to determine the level of minimum equivalency between each method and the detailed TCM method, which is considered the reference standard. For example, in the case of pediatric female chest breasts, the mean of longitudinal approximated TCM method and detailed TCM method are equivalent within 3% with a significant p-value (0.0391) <0.05, indicating that the alternative hypothesis is accepted.

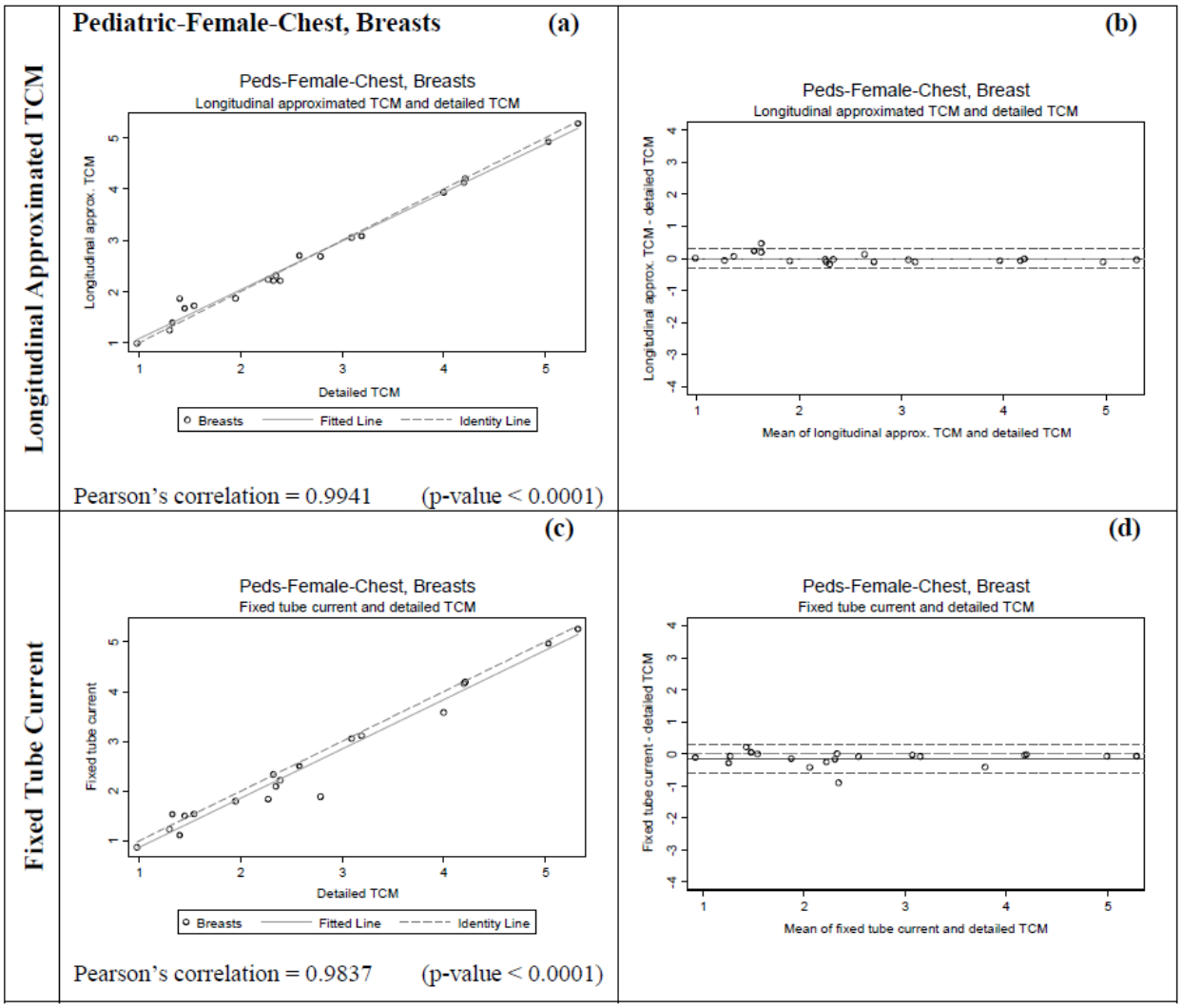

Figure 7-13 Summary of the statistical analysis performed on the breast dose data for pediatric chest patient models in mGy. The graphs on the left are the scatter plots for each method, while the ones on the right are Bland-Altman graphs to show mean and standard deviation of the data. The x axis of the scatter plot shows breast dose in mGy from detailed TCM function (X1) and the y axis represents breast dose in mGy from either the longitudinal approximated TCM or fixed tube current (X2). The x axis of the Bland-Altman graphs is (X1+X2)/2 and the y axis represents (X2-X1). For both methods the means are very close to the y=0 lines, however, the standard deviation is larger for the fixed tube current method.

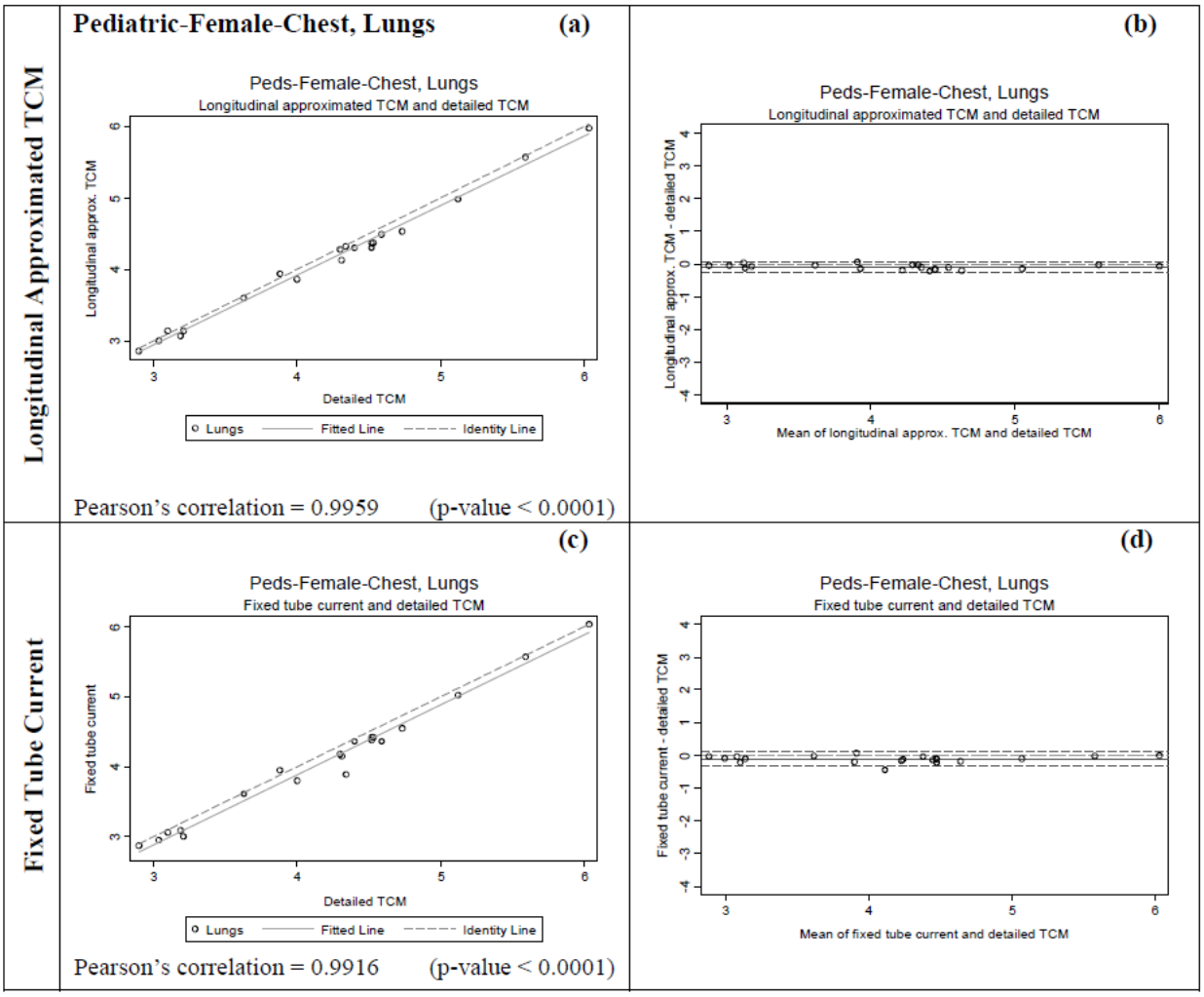

Figure 7-14 Summary of the statistical analysis performed on the lung dose data for pediatric chest patient models in mGy. The graphs on the left are the scatter plots for each method, while the ones on the right are Bland-Altman graphs to show mean and standard deviation of the data. The x axis of the scatter plot shows lung dose in mGy from detailed TCM function (X1) and the y axis represents lung dose in mGy from either the longitudinal approximated TCM or fixed tube current (X2). The x axis of the Bland-Altman graphs is (X1+X2)/2 and the y axis represents (X2-X1). For both methods the means are very close to the y=0 lines and the standard deviations are small.

7.4 Discussion and Conclusion

This work demonstrates that the longitudinal approximated TCM function obtained from the image data is a reasonable surrogate to the detailed TCM function for use in Monte Carlo dose simulations. This was shown to be true for two different patient populations, anatomical regions, and also using two different scanner manufacturers (GE and Siemens) and therefore two different tube current modulation algorithms (CareDose4D and Smart mA). Even though the longitudinal approximated TCM function only represents the z-axis modulation of the TCM algorithm and it does not capture the over-ranging information that the detailed TCM function does, we demonstrated that it provides organ dose estimates that are close to the results obtained using the detailed TCM function which represents a three dimensional modulation of tube current (z-axis and angular x-y modulation). These results confirm that the effect of TCM is primarily due to the z-axis modulation of the tube current [111]. More importantly the longitudinal approximated TCM method was shown to perform consistently across scanners, exams, and patient models.

The above results also demonstrate that the organ dose percent differences and the RMSE values for breasts are higher compared to lungs across all patients. This finding is also apparent in the scatter plots, Bland-Altman plots, and the equivalence test. These results suggest that angular modulation has a stronger effect on smaller peripheral organs (breasts) than larger and more central organs (lungs). Due to smaller size and the position of the breasts, the modulation of the tube current in the x-y plane contributes more to breast dose than to lung dose.

In addition to being more sensitive to the angular modulation, smaller, more peripheral organs are also more sensitive to the tube start angle as shown by Zhang et al. [132]. The tube start

angle for the detailed TCM function simulations was extracted from the projection data, which is randomly assigned, however, the tube start angle for the longitudinal approximated TCM function simulations was set to zero because this information is not available in the DIOCM header of the image data. Knowing the tube start angle would improve the statistics for the smaller, more peripheral organs and therefore make the longitudinal approximated TCM function more robust.

Furthermore the scan lengths used for the longitudinal approximated TCM method and the fixed tube current method were entirely extracted from the image data, which does not include the z-axis over-ranging. Knowing the actual scan length from beam on to beam off will further improve the performance of the longitudinal approximated TCM method. Additionally, only the pediatric chest models were able to account for z-axis aver-ranging in the detailed TCM simulations, because only these models contained information for both the tube current data and image data in the over-ranging region. The other two sets of models, the adult female chest and the pediatric whole body models, contained only the tube current data but not the image data, because these models are entirely based on image data which does not contain the missing image data due to the over-ranging region. This can be improved by modeling voxelized blocks of water at each end of the image data, mimicking to the over-ranging region.

In the adult female chest models longitudinal approximated TCM method performed consistently across all patients, i.e. the method underestimated lung and breast dose compared to the reference method, the detailed TCM method. This underestimation is illustrated in the scatter plots showing the fitted line under the unity line. However, for the fixed tube current method the scatter plots do not show a consistent trend in this method's performance; sometimes it underestimates while other times it overestimates organ dose. This effect is due to the fact that

the performance of the fixed tube current method depends on how closely the average tube current over the scan length represents the actual TCM function over a certain region. Depending on the shape of the TCM function this average may or may not be a good representation of the TCM function at a specific location.

For the adult female chest models the largest absolute percent difference between detailed TCM and longitudinal approximated TCM was 25% for breasts (longitudinal approximated TCM method underestimated breast dose by 25%). The glandular breast tissues for this specific patient fell more laterally than other patients. This resulted in a higher sensitivity of breasts to angular modulation for this patient. For another patient a maximum difference of 11% was observed. This patient had her arms in the scan region adjacent to her breasts, which resulted in an increase in the lateral tube current. This again resulted in a higher sensitivity of breasts to the angular modulation.

Overall it was shown that estimating organ dose using a fixed single tube current value adjusted for patient size (i.e. the average effective mAs) introduces errors in organ dose values up to 60% and 45% for adult female chest and pediatric female whole body models, respectively (Tables 7-2 and 7-4)**.** However, for a few female adult chest patients these percentages were less than 10% for both organs. For these patients, it was found that the overall average tube current value used to estimate organ dose happened to be very similar to the average tube current of the slices (images) containing breasts and lungs. Table 6-8 illustrates these findings for some adult female chest models. To confirm these findings the same analysis was done for a model whose fixed tube current simulation results were -45% different from those obtained with the detailed TCM function simulations; these results are shown at the bottom row of Table 7-8 (Patient Model 10). The percent difference between the overall average tube current used for this patient and the

average tube current value of the locations that contained breasts was about -40%, which seems to explain most of these differences.

Adult Female Chest	Fixed Tube Current mA reported on dose report (used for fixed tube current method)	Detailed TCM mA averaged over slices containing breasts	% mA Difference	% Organ Dose Difference
4	578	578	0.0	-2.6
5	520	540	3.7	3.7
9	514	481	-6.9	-8.1
11	570	574	0.7	0.8
12	352	291	-21.0	-4.1
15	568	567	-0.2	1.3
18	560	564	0.7	2.5
19	558	552	-1.1	0.5
10	470	335	-40.3	-45.7

Table 7-8 Comparisons between average tube current values (mA) from patient dose report used in the fixed tube current simulations and slices containing breasts.

In addition it was found that some of these patients' TCM function had little or no z-axis modulation due to the tube current reaching its maximum limit, which in turn resulted in their average tube current being very similar to their z-axis modulation function. Patient number 15 is an example of patients with almost no z-axis modulation. This patient's detailed TCM and longitudinal approximated TCM are shown in Figure 7-15. The rapid up and down of the tube current is due to the x-y modulation resulting from the elliptical shape of the patient. As illustrated by the longitudinal approximated TCM function there is only very little z-axis modulation in this patient.

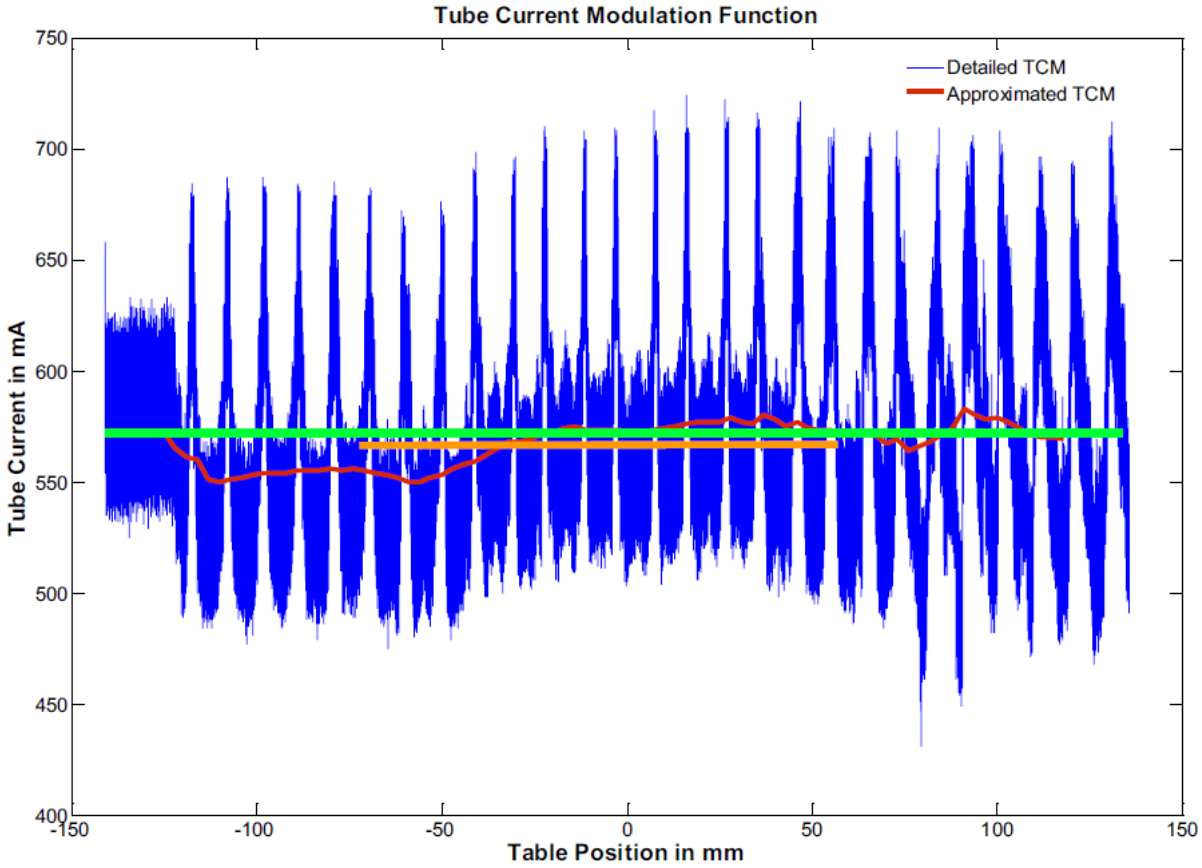

Figure 7-15 Illustrated is a TCM example of a maxed out tube current during an exam. Green represents the average tube current value obtained from the dose report (an average mA over the entire exam) and orange represents the average mA over images containing breasts.

Similar findings were seen for the pediatric patient models. The longitudinal approximated TCM function performed consistently across all patients while the fixed tube current method had different outcomes depending on the average tube current used. This effect was pronounced when the pediatric models were used to also simulate thoracic exams. Fixed tube current simulations performed best in the pediatric chest models compared to the pediatric whole body simulations. As illustrated in Figures 7-7 and 7-8, the improved performance of the fixed tube current method in chest exams is due to the use of two different average tube current values

(shown in green in Figures 7-7 and 7-8). For the whole body scans the average tube current value used is much lower than the actual tube current over the thoracic region, shown in blue. However, for the chest simulations the tube current was averaged only over the chest region and therefore is more representative of the actual tube current or tube output over lungs and breasts. These results are also illustrated in the scatter plots and the delta values, showing an improvement in the minimum equivalency level from 30% to 2%.

These results suggest that fixed tube current method is not very reliable; its performance is very much dependent on the TCM function for an individual patient. Using the knowledge of the TCM function one can improve results from fixed tube current simulations; this may be achieved by using region- and organ-specific average tube current instead of an average tube current from the entire scan length.

For almost all of the pediatric female models, moderate angular modulation was observed in their TCM function as compared to adult female models. Additionally, z-axis tube current modulation algorithms appear to be very different in these two scanners. Nevertheless the longitudinal approximated TCM method performs as a reasonable approximation to the detailed TCM function independent of the type of the tube current modulation algorithm. For the pediatric female models the maximum difference between detailed TCM and longitudinal approximated TCM was 25% and 32% for breasts for whole body and chest exam simulations, respectively. After investigating the data it was found that the same patient caused these percentages. This specific patient had very small amount of glandular breast tissue and the resulting organ doses are very small. The difference between these two small numbers result in a relatively high percent difference, even though numerical difference was small – only 0.5 mGy.

Comparing with adults who have higher doses, the dose percent differences for pediatric patients are more sensitive due to smaller dose values.

In summary, this work has shown that the detailed tube current modulation function can be approximated by using the tube current values extracted from the DICOM header information and will yield reasonably similar results when estimating organ doses. Figure 7-16 illustrates a summary of all data and the performance of each method across models and scanners. This was shown across two patient populations, two scanner types and two different TCM algorithms. The longitudinal approximated TCM method is based on readily available image data and achieves excellent agreement with methods that use more detailed information. In addition, it was shown that the fixed tube current method can often yield misleading results, especially when scans contain anatomic regions with different attenuation properties such as a whole body or a chest/abdomen/pelvic scan. Future work will include other radiosensitive organs to confirm the performance of the longitudinal approximated TCM method across different exam types and organs.

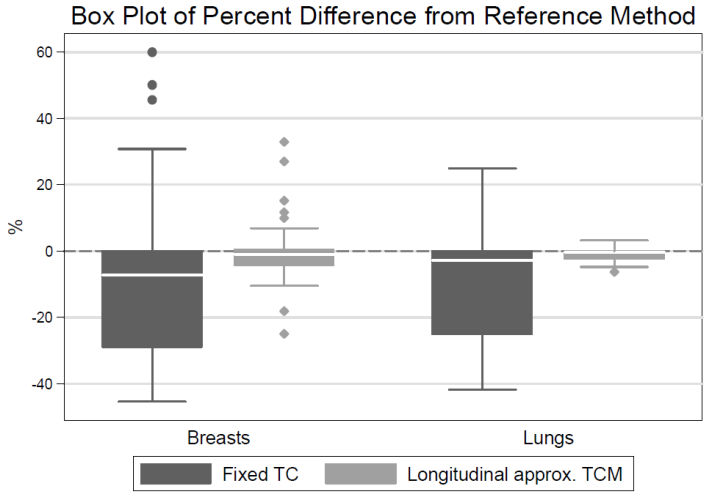

Figure 7-16 Summary of results represented as a box plot of organ dose percent difference from the reference method across all methods and models.

CHAPTER 8: REGIONAL AND ORGAN-SPECIFIC $CTDI_{VOL}$ FOR ESTIMATING DOSE FROM TCM EXAMS

This chapter is based on Khatonabadi M, Kim HJ, Lu P, McMillan KL, Cagnon CH, Demarco JJ, McNitt-Gray MF. The feasibility of regional CTDIvol to estimate organ dose from tube current modulated CT exams. Med. Phys. 40, 051903 (2013)

8.1 INTRODUCTION

The population radiation exposure due to CT examinations has increased over several decades and as a result agencies such as Food and Drug Administration, International Atomic Energy Agency, American College of Radiology, National Institutes of Health, and Image Gently recommend reporting radiation dose from CT exams [6, 25, 26, 133, 134]. In addition, the State of California mandates health facilities to record dose from CT exams under Assembly Bill No. 510[22]. Currently the only values that can easily be calculated and reported, are $CTDI_{vol}$ and DLP, even though neither represents patient dose nor takes into account patient specific factors such as size [36].

Recently, AAPM Task Group 204[49] described the Size Specific Dose Estimate (SSDE), which accounts for patient size by providing conversion factors. These conversion factors vary by patient effective diameter and convert $CTDI_{vol}$ to the SSDE, which is the dose in the middle of the scan volume. These conversion factors were generated from fixed tube current measurements and Monte Carlo simulations and therefore did not specifically address scans performed with Tube Current Modulation (TCM), which is the dominant mode of scanning in clinical practice today.

The Computed Tomography Dose Index (CTDI) was introduced over three decades ago as an index of scanner radiation dose [29, 30] and has been adapted to measurements in a 100 mm ionization chamber ($CTDI_{100}$) and to helical scanning ($CTDI_{vol}$) in cylindrical plastic phantoms. Despite its limitations in keeping up with new technologies, it is widely used for quality assurance, accreditation, and dose monitoring [34, 35].

TCM techniques were introduced over a decade ago and since then most clinical protocols have implemented this feature to reduce patient dose while maintaining acceptable image quality[52, 53, 55, 56]. TCM algorithms perform differently across different CT scanner manufacturers but the basic principle is the modulation of the tube current in x-y-z directions. In most scanners the x-y or angular modulation adjusts the tube current based on the projection‘s path length through the object, while the z-axis modulation adjusts the tube current for different attenuations along the scan length [57, 81].

With the advent of TCM, $CTDI_{vol}$ has again been adjusted. The International Electrotechnical Commission (IEC) has defined $CTDI_{vol}$ for a tube current modulated exam (in the standard 60601-2-44 of IEC [37]) as the $CTDI_{vol}$ based on a single average tube current value of the entire scan. While the original definition of $CTDI_{vol}$ assumed a constant tube current (and therefore technically cannot be defined for a variable tube current scan), this practical definition is now adopted and is the method by which $CTDI_{vol}$ is being reported on scans performed with TCM in current clinical practice (e.g. the dose reports provided by scanners).

This leads to the situation depicted in Figure 8-1, where a TCM scan is performed and the actual tube current varies significantly throughout the scan, yet only a single value of $CTDI_{vol}$ is reported based on the average value of the tube current across the entire scan. Figure 7-1a

depicts the actual tube current value as a function of table position for a chest exam and Figure 7-1b depicts the same information for an abdomen/pelvis scan. These figures show the significant variation in tube current that occurs as the scan proceeds across areas of varying attenuation characteristics, which result in the (appropriate) variations in tube output milliamperage along the longitudinal direction. In each figure, the dashed line shows the average tube current throughout the entire scan which is the value upon which the scanner reported $CTDI_{vol}$ is based.

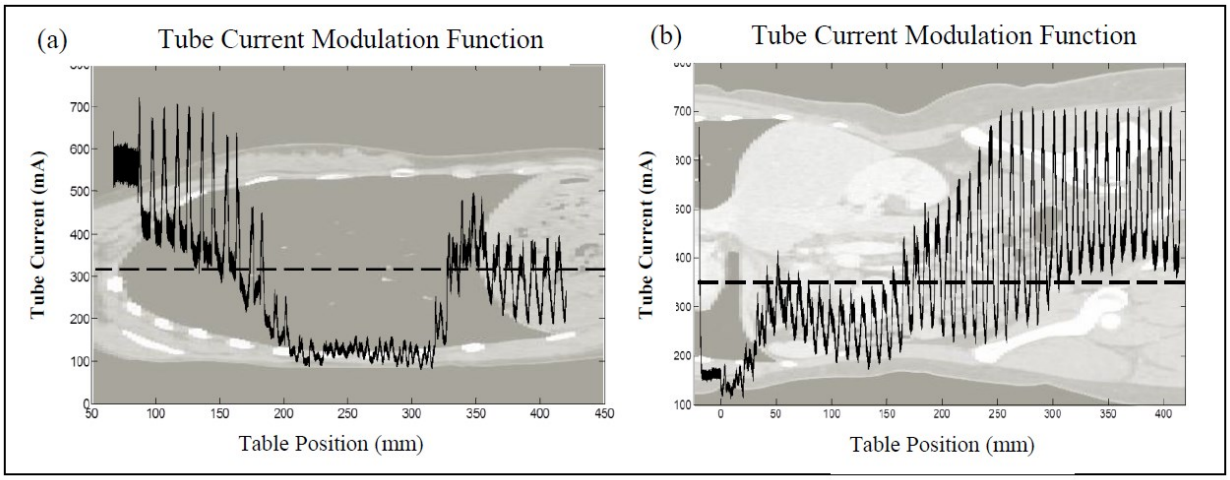

Figure 8-1 (a) An example of a chest exam's TCM profile, illustrating the variation of tube current along patient's z-axis and within the axial plane (the high frequency component). (b) An example of an Abdomen/Pelvis exam's TCM profile, illustrating three different attenuating regions: lungs, abdomen and pelvis. $CTDI_{vol}$ reported by the scanner is based on the global average tube current (dashed line).

There have been several previous efforts to estimate dose to patients under TCM conditions [81, 111]. One of these efforts, Schlattl et al. [135, 136], published dose conversion coefficients for seven voxelized models (baby, child, Jo, RCP-AM, RCP-AF, Irene, and Donna) using idealized TCM profiles based on Gies [54] and Kalender et al. [52]. Even though the fundamental concepts of TCM are uniform across all CT manufacturers, they tend to differ in implementation and optimization variable and are not the same as the idealized TCM described by Gies and Kalender. Besides not representing any manufacturer-specific TCM algorithm, Schlattl's work did not use any quantitative size metric to categorize its patient models.

In this manuscript, we investigate an adaptation of the TG 204 approach that takes into account the effects of the actual varying tube current in TCM scans. To do this, we will evaluate the scanner-reported global $CTDI_{vol}$ as a predictor of organ dose in a TCM setting and compare against more local versions of scanner output (regional and organ-specific $CTDI_{vol}$) as a predictor for organ dose. The utility of regional and organ-specific $CTDI_{vol}$ as normalization factors in tube current modulated scans will be explored using Monte Carlo simulations of tube current modulated chest and abdomen/pelvis exams

8.2 METHODS

8.2.1 Monte Carlo Simulation Code

A previously developed and validated Monte Carlo based CT dosimetry package was employed to estimate organ doses from tube current modulated chest and abdomen/pelvis CT exams [76-78, 137]. A modified source code of MCNPX (Monte Carlo N-Particle eXtended v2.6.0), a radiation transport code developed at Los Alamos National laboratory, was used for the simulations [127, 128]. All simulations were performed in photon transport mode with a low-energy cutoff of 1 keV. The photon transport mode only tracks photon interactions and assumes secondary electrons deposit their energy at the photon interaction site. This assumption meets with the condition of charged particle equilibrium (CPE), under which kerma can be assumed to be equal to absorbed dose.

8.2.2 MDCT Source Models

A Multidetector row CT (MDCT) scanner, (Sensation 64, Siemens Healthcare, Forchheim, Germany) was modeled in the Monte Carlo simulations. The default MCNPX particle source

code was modified to model the scanner. The CT x-ray source was modeled by simulating a helical source path while using a point source to emit photons whose initial position and direction were randomly selected based on scanner geometry variables such as source-to-isocenter distance and fan angle. The bowtie filter was modeled by varying the statistical weight of each simulated photon [76-78]. The approach described by Turner et al. [137] was used to generate scanner-specific spectrum and filtration description to model the scanner. The scanner model was validated by simulating $CTDI_{100}$ at the center and periphery of both 32 and 16 cm CTDI phantoms and comparing simulated values to physical measurements. Simulation results across all tested conditions agreed with measurements to within 3.7% [137].

8.2.3 Voxelized Patient Models used in Monte Carlo

Voxelized patient models originating from actual CT scans were used in the Monte Carlo simulations. 39 abdomen/pelvis CT scans acquired on a Siemens Sensation 64 with CareDose 4D, 120 kVp, 275 Quality Reference mAs, 32x0.6 collimation, pitch of 1, and reconstructed image thickness of 3mm, were used to generate voxelized abdomen/pelvis models. Similarly, 32 chest CT scans (20 females and 12 males) with 230 to 250 Quality Reference mAs were utilized to create voxelized models of chest. To ensure all anatomy was included, all images were reconstructed with a full 500 mm display field of view.

In the abdomen/pelvis models liver, spleen and kidneys were contoured and segmented while in the chest models lungs and glandular breast tissue were contoured (the latter was only segmented in female models). Segmented organs were assigned to the corresponding organ using material composition and densities defined by ICRU Report 44 [113]. Each voxel outside the segmented

region was identified as one of the six tissue types (air, water, lung, fat, muscle, and bone) and subdivided into 17 different tissue density levels as a function of voxel CT number [80, 81, 114].

8.2.4 Monte Carlo TCM Model

For each patient model TCM data was extracted from the raw projection data and was modeled in Monte Carlo using the method described by Angel et al. [81]. TCM data consists of three variables: tube current I, table location z, and tube angle Θ. The tube current value I is a function of table position z and tube angle Θ, I(z, Θ). For a given patient, all tube current values, I(z, Θ), were normalized to the maximum tube current value. The normalized tube current data is used in the Monte Carlo simulations as source weights for simulated photons sampled from the table location and tube angle data.

8.2.5 Simulated CT Exams

For each voxelized model, Monte Carlo simulations were initiated utilizing each patient's actual TCM information extracted from the raw projection data. The simulated exam lengths were also extracted from the raw projection data, including the z-axis over-ranging. However, due to the voxelized models entirely originating from image data none of the voxelized models include the image data corresponding to the over-ranging region [62]. As a result the simulated organ doses may slightly underestimate actual dose since there is no dose contribution due to scatter from the over-ranging region; this is assumed to be an insignificant contribution for the organs of interest in this study as they are bigger organs and are not adjacent to the boundaries of the scan region.

8.2.6 Dose Calculations

For each patient model, absorbed dose was calculated for all identified organs. Organ doses were calculated using collision kerma, which is equal to absorbed dose under the assumption of charge particle equilibrium. For each simulated photon MCNPX tally type *F4 was used to track energy fluence in organs of interest and multiplied by mass energy-absorption coefficients (μ_{en}/ρ) to convert to collision kerma. The resulting dose per simulated photon for each organ was converted to dose per tube current (mA) by multiplying the Monte Carlo output by a normalization factor, which is scanner, collimation, and kVp dependent and is used to take into account the fluence changes from varying the beam collimation. Absolute organ doses were obtained by multiplying dose per mAs (tube current times rotation time) by the product of maximum tube current value obtained from each patient's TCM data, the exam's number of rotations, and rotation time [81].

8.2.7 Regional and organ-specific $CTDI_{vol}$

In addition to recording the scanner-reported $CTDI_{vol,global}$, regional and organ-specific $CTDI_{vol}$ values were calculated from patient's image data using a MATLAB (Mathworks, Natick, MA) routine. Regional and organ-specific $CTDI_{vol}$ values and the global $CTDI_{vol}$ were used as normalization factors and compared to each other. An exponential relationship between normalized organ dose and effective diameter, similar to the form used in TG 204, was used to assess each $CTDI_{vol}$ as a normalization quantity, as shown in Equation 7-1.

$$Normalized\ Organ\ Dose = \frac{Organ\ Dose}{CTDI_{vol}} = A \times e^{-B \times Effective\ Diameter} \quad \textbf{Eq. 8-1}$$

For the abdomen/pelvis exams a regional $CTDI_{vol}$ was calculated based on the average tube current value for the abdomen section, defined as the top of liver to the iliac crest, of the original exam along with three organ-specific $CTDI_{vol}$ (Figure 8-2). Using a MATLAB function, tube current values and corresponding slice locations were extracted for each patient model. Images containing the abdomen region were manually identified using the starting and ending image numbers as inputs to the function to calculate an average tube current value between those images. Similarly image numbers of images containing liver, kidneys, and spleen were identified to calculate an average tube current (I) value for each organ. Based on these average tube current values, as shown in Eq. 8-2, new $CTDI_{vol}$ values were calculated and named: $CTDI_{vol,Abd}$, $CTDI_{vol,Liver}$, $CTDI_{vol,Spleen}$, and $CTDI_{vol,Kidneys}$.

$$CTDI_{vol,Regional} = CTDI_{vol,Global} \times \frac{I_{Regional}}{I_{Global}} \quad \textbf{Eq. 8-2}$$

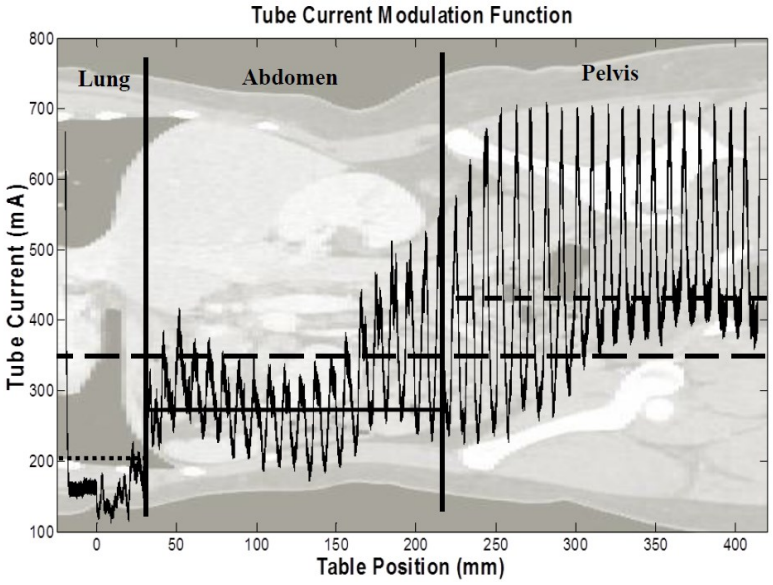

Figure 8-2 An example of an Abdomen/Pelvis exam's TCM profile, illustrating three different attenuating regions: lungs, abdomen, and pelvis. The horizontal continuous line through all three regions represents the average tube current over the entire scan length (i.e. global average tube current). The horizontal line at each section represents the average tube current over that specific section.

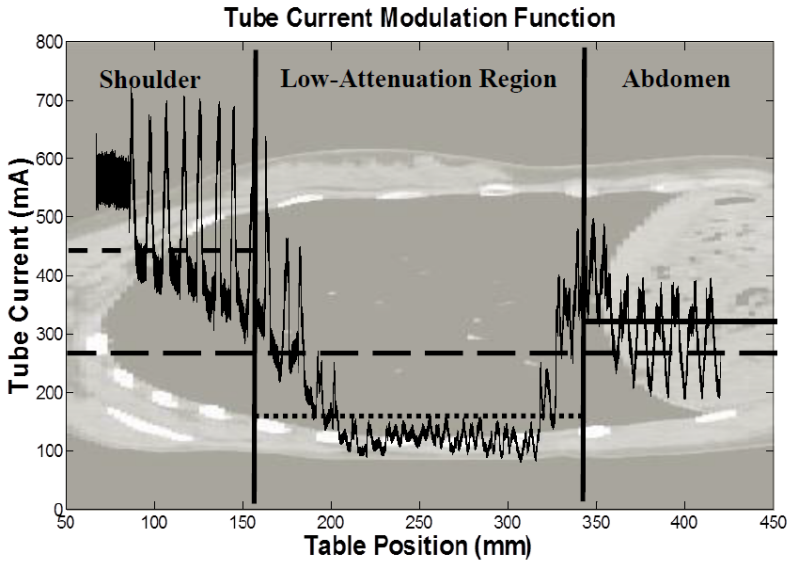

Figure 8-3 An example of a Chest exam's TCM profile, illustrating three different attenuating regions: shoulder, low-attenuation region (encompasses most of the lungs, excluding shoulders, scapula, and abdomen). The horizontal continuous line through all three regions represents the average tube current over the entire scan length. The horizontal line at each section represents the average tube current over that specific section.

Similarly for the chest exams a regional $CTDI_{vol}$, $CTDI_{vol,LowAtt}$, defined as the region between the inferior edge of the scapula and superior boundary of the liver, which included most of the lungs but excluded shoulder and any abdominal organ, along with two organ-specific $CTDI_{vol}$ values ($CTDI_{vol,Lungs}$ and $CTDI_{vol,Breasts}$) were calculated and used as normalization factors (Figure 8-3). Table 8-1 summarizes different $CTDI_{vol}$ values and their abbreviations.

Exam	Regional		Organ-Specific	
	Definition	**Abbreviation**	**Definition**	**Abbreviation**
Abdomen	top of liver to the iliac crest	$CTDI_{vol,Abd}$	images containing liver	$CTDI_{vol,Liver}$
			images containing spleen	$CTDI_{vol,Spleen}$
			images containing kidneys	$CTDI_{vol,Kidneys}$
Chest	inferior edge of the scapula and superior boundary of the liver	$CTDI_{vol,LowAtt}$	images containing lungs	$CTDI_{vol,Lungs}$
			images containing breasts	$CTDI_{vol,Breasts}$

Table 8-1 Tabular description and abbreviation of different $CTDI_{vol}$ values.

8.2.8 Size Metric

The equivalent diameter as described in AAPM Task Group 204 report was used as the reference size metric, shown in Equation 8-1, to assess the performance of different $CTDI_{vol}$ values as normalization quantities.

Using the definition from TG 204 report, equivalent diameters were calculated for each patient using a set of lateral and anterior-posterior (AP) measurements performed on each axial CT image. Using these measurements, for each image an effective diameter was calculated. For each patient a single averaged effective diameter was reported and used to investigate correlation with normalized organ doses.

8.2.9 Statistical Analysis

Linear regressions were used to assess the effect of patient size on absolute organ doses and $CTDI_{vol}$. A scatter diagram with a linear fitted line is shown to demonstrate the relationship between the dose (absolute organ dose and scanner-reported $CTDI_{vol}$) and patient effective diameters. The coefficient of determination (R^2) was reported to quantify the proportion of variation explained by the effective diameter.

For normalized organ doses, the log-transformation of normalized organ dose is used to fit a linear regression with the covariate of effective diameter using each $CTDI_{vol}$ value (global, regional, and organ-specific) in turn. The coefficient of determination from the linear regression was reported to evaluate the benefit of using each normalized $CTDI_{vol}$ value. A scatter diagram with a fitted exponential curve, as described by Equation 8-1, is shown (using original, non log-transformed data) to demonstrate the relationship between the normalized organ dose and patient

effective diameter for each organ. Pearson's correlations and 95% confidence interval were reported from the log-transformed linear regression. The 95% confidence intervals of regional and organ-specific normalized dose were compared with global normalized dose. A p-value smaller than 0.05 was considered to be significant. All data were analyzed using Stata 12.0 (StataCorp; College Station, TX).

8.3 RESULTS

8.3.1 Abdomen/Pelvis Models

Figure 8-4a shows the absolute value of kidney doses estimated from Monte Carlo simulations plotted as a function of the average effective diameter over the entire scan length. Figure 8-4b, 8-4c, and 8-4d show the scanner reported $CTDI_{vol,global,}$ $CTDI_{vol,Abd}$, and $CTDI_{vol,Kidneys}$, respectively, also plotted as a function of average effective diameter. Each figure also reports the correlation between absolute dose and average effective diameter. These figures show that, as expected in tube current modulated exams, smaller patients receive lower dose, whereas larger patients receive somewhat higher dose. Similar behaviors were observed for liver, spleen, and their $CTDI_{vol}$ values. Figure 8-5 shows kidney doses normalized by global, regional, and organ-specific $CTDI_{vol}$ metrics. Figure 8-5a shows kidney doses normalized by global $CTDI_{vol,global}$ as well as the associated correlation between the normalized organ dose and patient size. Figure 8-5b shows kidney doses normalized by regional and organ-specific $CTDI_{vol}$ ($CTDI_{vol,Abd}$, and $CTDI_{vol,Kidneys}$) as well as the associated correlations between the normalized organ dose and patient size. The increasing R^2 shows the benefit of using regional and organ-specific $CTDI_{vol}$ normalized dose over global $CTDI_{vol}$ value. For example, using the same effective diameter only 7% of the variation of normalized kidney dose can be explained by $CTDI_{vol,global}$, whereas 56%

and 79% of the variation can be explained when using the regional and organ-specific $CTDI_{vol}$ as normalization quantities. Similar behaviors were observed for liver and spleen. Table 8-2 summarizes the results for all three abdominal organs.

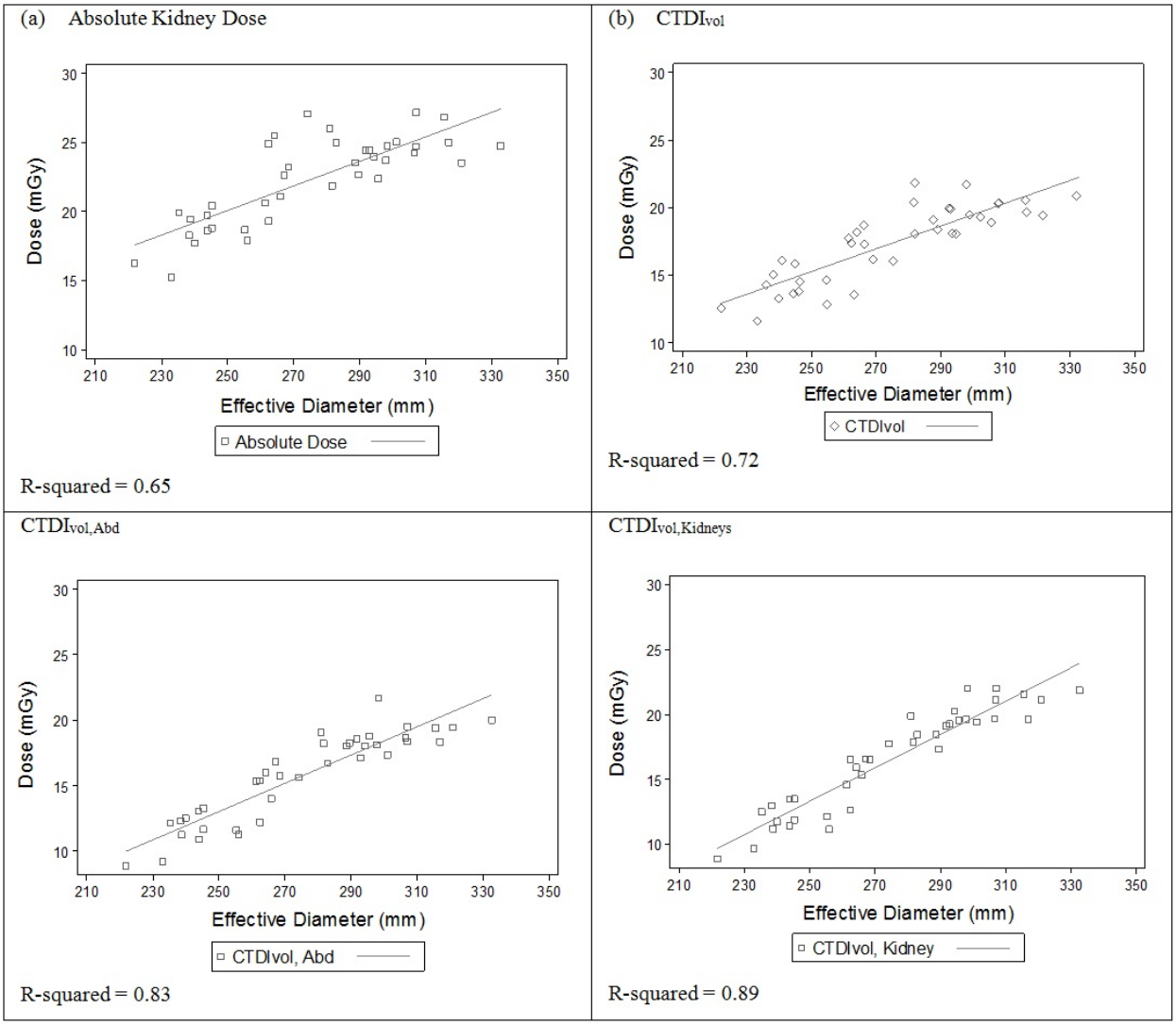

Figure 8-4 Absolute Monte Carlo simulated kidney doses (mGy) versus effective diameter (a) and $CTDI_{vol}$ values versus effective diameter (b-d). In this small dataset with a small range of different sizes, TCM mode appears to result in lower doses for smaller patients and higher doses for larger patients.

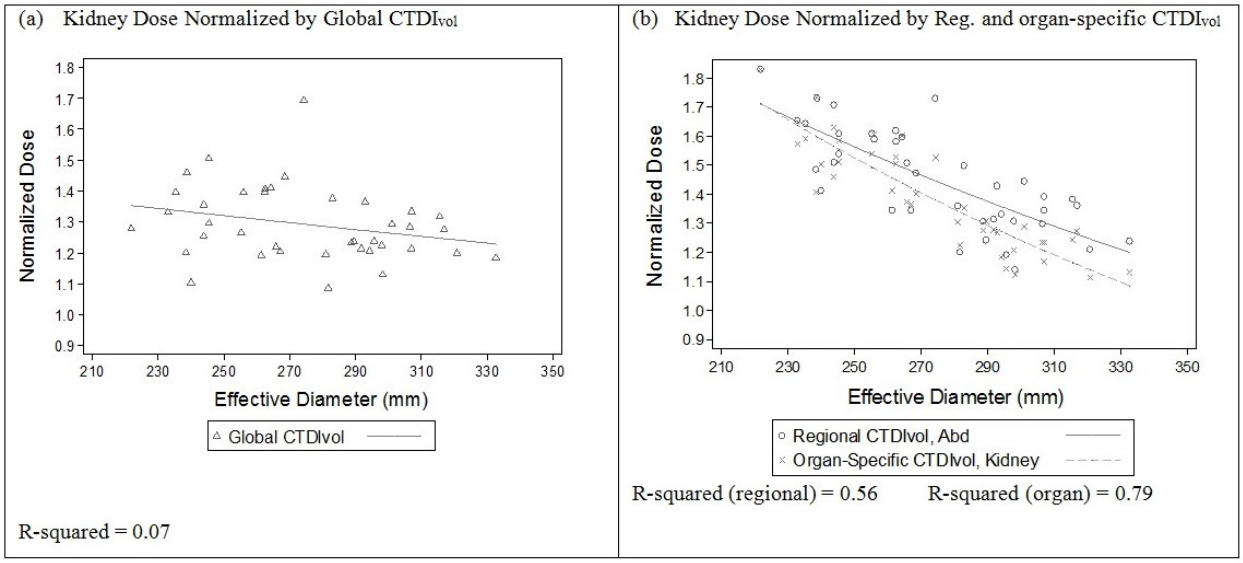

Figure 8-5 For kidneys, normalized dose by regional and organ-specific $CTDI_{vol}$ show a higher correlation with size compared to global $CTDI_{vol}$. Similar improvements were seen for liver.

Overall the results demonstrate that the regional and organ-specific $CTDI_{vol}$ values yield greater correlations with effective diameter compared to those of $CTDI_{vol,global}$. Additionally for all three abdominal organs correlations of regional and organ-specific $CTDI_{vol}$ with the effective diameter were significantly greater than the correlation of $CTDI_{vol,global}$ with the effective diameter, whereas the correlations between regional and organ-specific $CTDI_{vol}$ were not statistically different (Table 8-2). Among abdominal organs, spleen showed the poorest correlations with size, while the best correlations were observed for liver. When comparing correlations, $CTDI_{vol,liver}$ and $CTDI_{vol,kidney}$ (organ-specific $CTDI_{vol}$) performed as better normalization quantities than $CTDI_{vol,Abd}$ (regional $CTDI_{vol}$). For spleen both regional and organ-specific $CTDI_{vol}$ performed equally.

Table 8-2 R^2, Pearson correlation, and 95% confidence interval of normalized dose and effective diameter‡

Model	Organ	n	Global $CTDI_{vol}$		Regional $CTDI_{vol}$		Organ-Specific $CTDI_{vol}$	
			r (95% CI)	R^2	r (95% CI)	R^2	r (95% CI)	R^2
Abd/Pel	Liver	39	-0.5108 (-0.712, -0.233)	0.26	-0.8769† (-0.934, -0.776)	0.77	-0.9269† (-0.961, -0.864)	0.86
	Spleen	39	-0.0225 (-0.336, 0.295)	0.0005	-0.6935† (-0.828, -0.484)	0.48	-0.6761† (-0.817, -0.458)	0.46
	Kidney	39	-0.2730 (-0.542, 0.047)	0.07	-0.7510† (-0.862, -0.571)	0.56	-0.8897† (-0.941, -0.798)	0.79

‡ log transformation is applied for Pearson correlation and 95% confidence interval

† statistically significant improvement (p-value < 0.05) compared to global $CTDI_{vol}$ by using log transformation

8.3.2 Chest Models

Figures 8-6 and 8-7 summarize the breast dose results obtained for the female chest models. In 6a-d absolute organ doses, $CTDI_{vol}$, regional $CTDI_{vol}$ ($CTDI_{vol,LowAtt}$), and organ-specific $CTDI_{vol}$ ($CTDI_{vol,Breasts}$) illustrate a similar relationship with effective diameter as observed for abdominal organs (as shown in Figure 8-4 for kidneys). Similar behaviors were observed for absolute lung dose and $CTDI_{vol}$ values.

Similar to the abdomen/pelvis cases, regional and organ-specific $CTDI_{vol}$ explained more of the variation with effective diameter than $CTDI_{vol,global}$ (Figure 8-7). Especially for breasts, which only occupies a portion of the chest region, organ-specific $CTDI_{vol}$ appears to be a more appropriate normalization quantity (58% and 83% by regional and organ-specific, whereas only 8% by $CTDI_{vol,global}$); whereas for lungs both regional and organ-specific $CTDI_{vol}$ perform equally. For lungs there was no statistically significant difference between any of the normalization quantities (Table 8-3); this may be expected because lungs occupy most of the thoracic scan length.

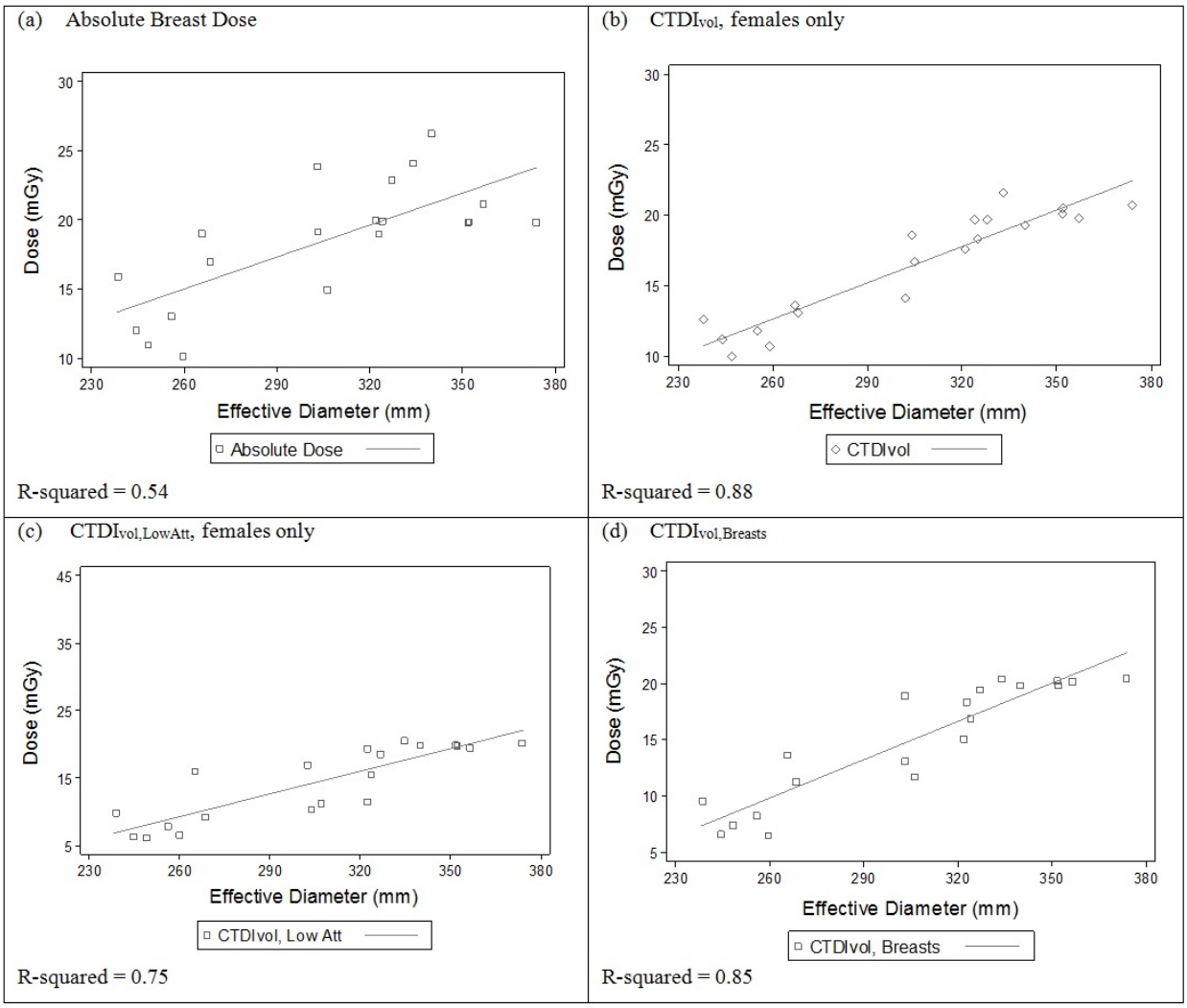

Figure 8-6 Absolute Monte Carlo simulated breast dose (mGy) versus effective diameter (a) and $CTDI_{vol}$ values versus effective diameter (b-d). Similar to the abdominal organs and abdomen/pelvis $CTDI_{vol}$ values, for this small number of patients TCM appears to result in lower doses for smaller and higher doses for larger patients.

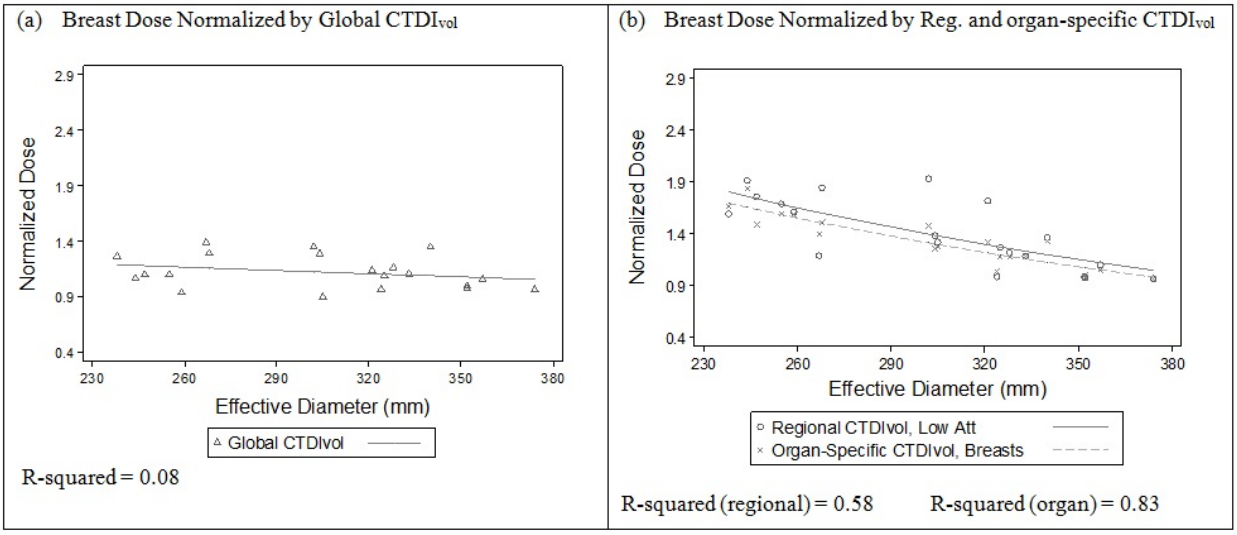

Figure 8-7 For breasts, normalized organ dose by regional and organ-specific $CTDI_{vol}$ show a higher correlation with patient size than global $CTDI_{vol}$.

Table 8-3 R^2, Pearson correlation, and 95% confidence interval of normalized dose and effective diameter‡

Model	Organ	n	Global $CTDI_{vol}$		Regional $CTDI_{vol}$		Organ-Specific $CTDI_{vol}$	
			r (95% CI)	R^2	r (95% CI)	R^2	r (95% CI)	R^2
Chest	Breasts	20	-0.2835 (-0.645, 0.182)	0.08	-0.7620 (-0.901, -0.482)	0.58	-0.9130† (-0.965, -0.789)	0.83
	Lungs	32	-0.6824 (-0.833, -0.438)	0.47	-0.7474 (-0.869, -0.539)	0.56	-0.7384 (-0.865, -0.525)	0.55

‡ log transformation is applied for Pearson correlation and 95% confidence interval
† statistically significant improvement (p-value < 0.05) compared to global $CTDI_{vol}$ by using log transformation

8.4 DISCUSSION

When TCM scanning methods are used, the global $CTDI_{vol}$ reported by the scanner may not adequately represent the wide range of tube current variations observed in different attenuating regions. Therefore more regional descriptions of scanner output may be required to represent the different output conditions encountered within the scan. Similarly a single $CTDI_{vol}$ may not be adequate as a quantity for normalizing out differences in scan parameters and patient size in tube current modulated scans due to different regions within the same scan being subject to different

attenuation properties and hence different tube output. A more locally based average tube current/$CTDI_{vol}$, which only encompasses sections of similar attenuating regions, can more accurately assess TCM scans.

This study showed the feasibility of using regional $CTDI_{vol}$ values to normalize out differences in scan parameters in TCM mode. For all three abdominal organs the correlations with patient size improved when organ doses were normalized by regional and organ-specific $CTDI_{vol}$ values. This improvement was specifically more satisfactory for liver and kidneys compared to spleen. Normalized spleen dose by regional and organ-specific $CTDI_{vol}$ improved the R^2 value from 0% correlation to about 50% correlation with size, whereas for liver and kidneys the improved R^2 was as high as almost 80%. One possible explanation is the small number of patient models used in this study.

Similar to the abdomen/pelvis models, normalized breast dose by regional and organ-specific $CTDI_{vol}$ in the female thoracic models resulted in higher correlations with patient size compared to the global $CTDI_{vol}$. In lungs, however, the improvement of R^2 was not statistically significant once lung dose was normalized by regional and organ-specific $CTDI_{vol}$. Most of the thorax consists of lungs and therefore regional and lung-specific average tube current values are very close to the global average tube current value; hence an insignificant improvement was to be expected. Additionally the lung dataset consisted of both females and males and this was suspected to further have impacted the correlations because there are differences in anatomy between females and males in the thoracic region. To further investigate this hypothesis a gender-specific analysis was performed.

A separate analysis focusing on each gender individually showed improved R^2 for normalization by regional and organ-specific $CTDI_{vol}$ for both genders. Table 7-4 and Figures 7-8 and 7-9

illustrate the results of the gender-specific analysis. Looking at absolute lung doses for females and males (Figure 8-8a), it was determined that females receive higher lung dose compared to males, which could be due to their different shape in the thoracic region caused by lateral location of glandular breast tissue. However, this difference between females and males was not apparent in the scanner-reported $CTDI_{vol}$ values for these patients (Figure 7-8b), indicating once again limitations of using CTDI.

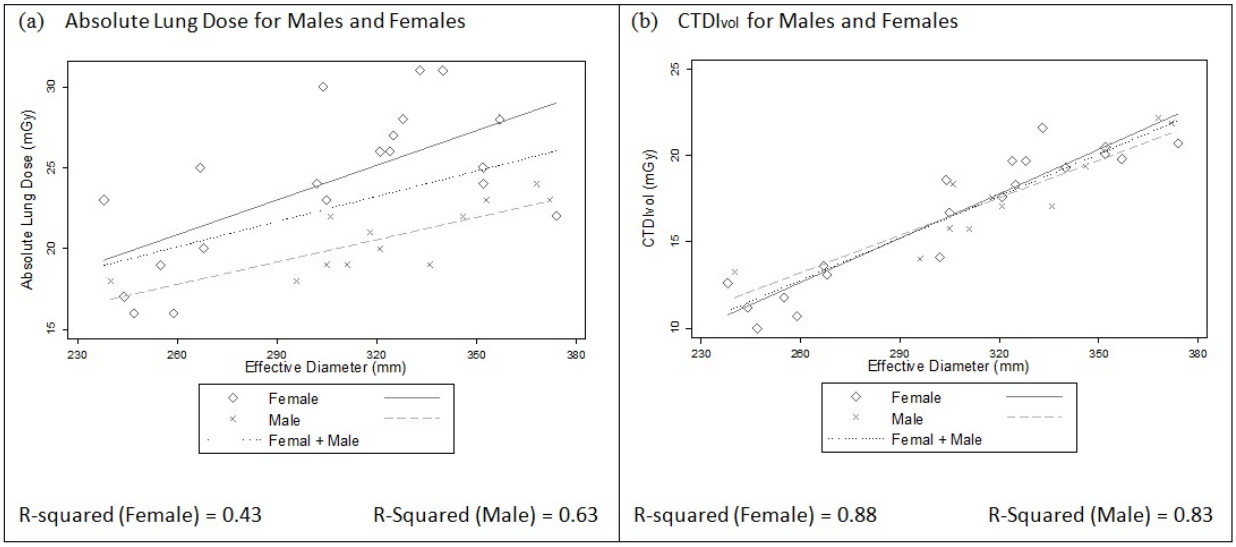

Figure 8-8 Gender-specific analysis performed on the lung data. Absolute lung doses (a) and $CTDI_{vol}$ (b) values are separated into females and males and illustrated versus effective diameter. A visible separation between females and males is demonstrated by the absolute lung doses; however, $CTDI_{vol}$ values do not depict a similar conclusion.

Table 8-4 summarizes the R^2, Pearson correlation, and 95% confidence interval between normalized dose and effective diameter, by using log linear regression. Even though the R^2 values increased (Figure 8-9a-c) when the analysis is separated into females and males, the improvements are not statistically significant. Similar gender-specific analysis was performed on abdomen/pelvis models to investigate whether similar gender-specific behavior is evident, but no difference was observed between females and males in the abdomen (Figure 8-9d).

Table 8-4 R^2, Pearson correlation, and 95% confidence interval of normalized dose and effective diameter‡

Model	Organ	n	Global $CTDI_{vol}$ r (95% CI)	Global $CTDI_{vol}$ R^2	Regional $CTDI_{vol}$ r (95% CI)	Regional $CTDI_{vol}$ R^2	Organ-Specific $CTDI_{vol}$ r (95% CI)	Organ-Specific $CTDI_{vol}$ R^2
Chest	Lungs - Female	20	-0.7228 (-0.883, -0.412)	0.54	-0.8399 (-0.935, -0.632)	0.71	-0.7447 (-0.893, -0.451)	0.55
	Lungs - Male	12	-0.9716 (-0.992, -0.899)	0.92	-0.9650 (-0.990, -0.877)	0.93	-0.9254 (-0.979, -0.750)	0.86

‡ log transformation is applied for Pearson correlation and 95% confidence interval
† statistically significant improvement (p-value < 0.05) compared to global $CTDI_{vol}$ by using log transformation

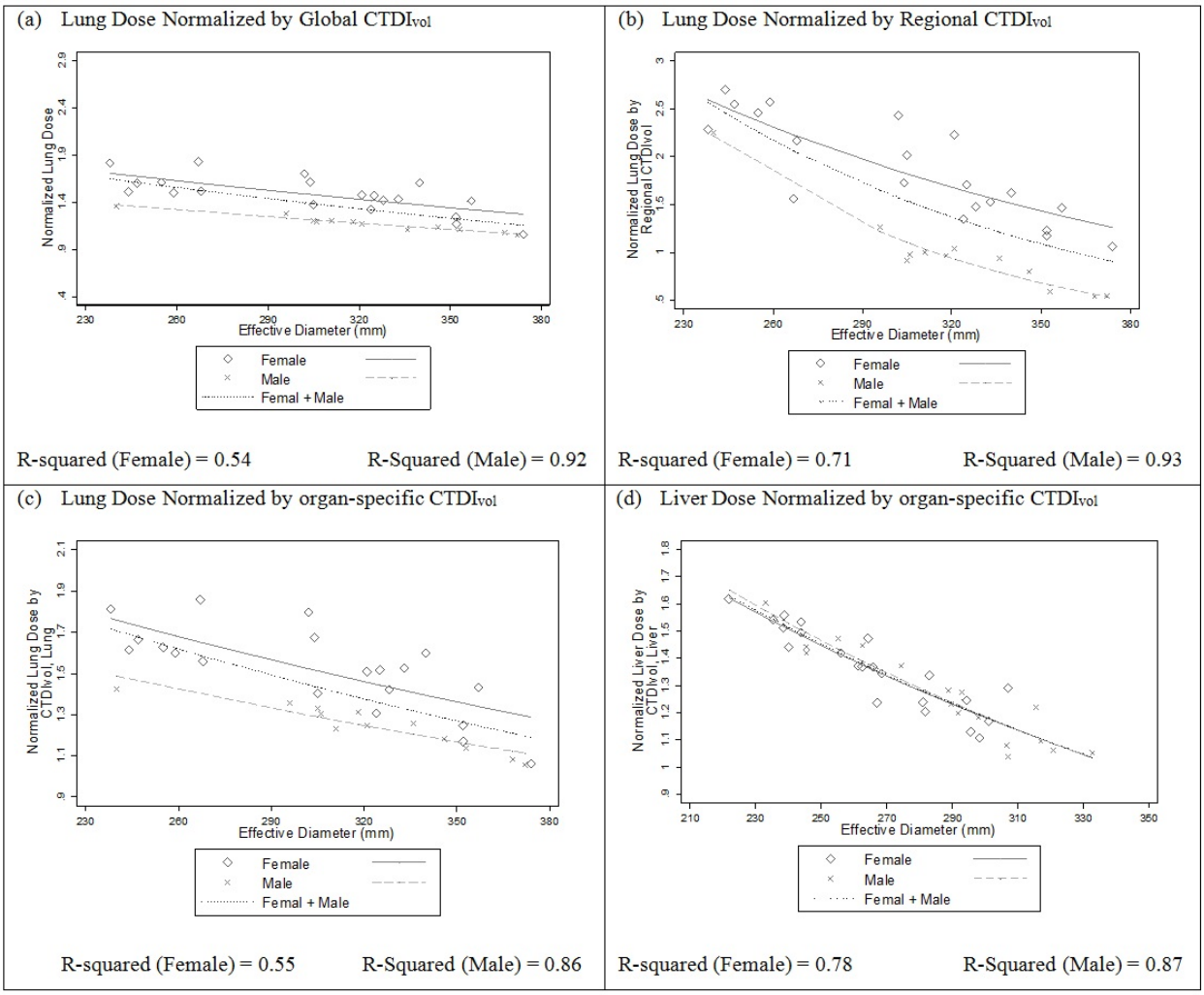

Figure 8-9 Gender-specific analysis performed on the lung data. Lung doses are separated into females and males and normalized by global (a), regional (b) and lung-specific $CTDI_{vol}$ (c). All three plots demonstrate an obvious segregation between females and males in the chest models. This gender separation is not seen in the abdominal organ liver (d).

The size metric used in this study was the effective diameter as defined by AAPM Task Group 204. The correlation between effective diameter and normalized organ doses was as high as 83 % for breasts and 86% for liver. However, this size metric is entirely based on the patient morphology (lateral and AP dimensions) and does not take into account any attenuation properties. This is especially crucial in the thorax due to low attenuating lungs, which make up most of the thorax. Future studies will explore correlations between normalized dose and attenuation-based size metric such as water equivalent diameter [138-141]. Additionally, a more locally based size metric, such as an average water equivalent diameter corresponding to the same portion as the regional or organ-specific $CTDI_{vol}$ used for normalization may be a better size indicator. In future studies a sensitivity analysis will be conducted to determine the most appropriate way to report one size metric per patient.

Another limitation of this study is the limited range of patient sizes and number of patients investigated. Future studies will include a variety of sizes including pediatric and obese patients, to allow for extending the exponential curves to both extremes.

In this study regional and organ-specific tube current data was calculated based on the anatomic ranges (both regional and organ-specific) extracted for each patient manually, which is not practical to do on a large scale. However, different regions might be identified from the topogram/scout of the patient or from the image data itself. As we have shown in this study regional $CTDI_{vol}$ may yield acceptable results and provide a good alternative to organ-specific $CTDI_{vol}$ and therefore, even a regional identification may be sufficient to provide information for organ dose estimates. If that is the case, then methods may be available to perform this regional identification in an automated fashion; in a recent study by Sodickson et al. [142] an informatics toolkit was developed to extract anatomy-specific $CTDI_{vol}$ values. This toolkit could be deployed

to extract the desired regional $CTDI_{vol}$ values described in this work to possibly provide a fully automated and robust estimate of patient dose that accounts for both the local effects of TCM and patient size.

This study is attempting to improve CT dose metrics such as $CTDI_{vol}$ and SSDE, by providing better ways to estimate patient dose under TCM mode. However, it is still an estimate and therefore capable of under- or overestimating actual dose in certain situations. As the CT community is trying to come up with improved models to estimate organ dose and obtain the best size metric to correlate dose with, different groups have been exploring Graphics Processing Unit (GPU) applications in Monte Carlo simulations to reduce the computational time of such high computationally demanding simulations[94, 143, 144]. The results look very promising and might enable real-time Monte Carlo simulation on individual patients undergoing CT in the future; however there are still significant remaining technical, logistical and resource issues such as automated on-line segmentation of organs among others. In the interim, the methods described here hope to move our clinical practices away from $CTDI_{vol}$ and DLP to improved dose metrics such as SSDE and beyond.

CHAPTER 9: ATTENUATION-BASED METRIC FOR ESTIMATING DOSE TO PATIENTS UNDERGOING TCM CT EXAMS

This chapter investigates different size metrics in combination with regional and organ-specific $CTDI_{vol}$ to establish the most appropriate size metric to be used as a predictor for organ dose in tube current modulated CT exam.

9.1 INTRODUCTION

Turner et al. [51] showed the value of using $CTDI_{vol}$ as a normalization factor, resulting in scanner-independent organ dose coefficients that are size dependent. Using size information and scanner-reported $CTDI_{vol}$, organ dose coefficients can be used to estimate organ dose from fixed tube current CT exams. Therefore, a true estimation of patient size is essential in obtaining accurate estimates of organ dose from either fixed or tube current modulated CT exams.

AAPM Task Group 204 utilized effective diameter as a size descriptor to adjust scanner-reported $CTDI_{vol}$ for size. Effective diameter is the diameter of a circle that has the same cross sectional area as the patient at a given z-axis or longitudinal location. This was used to obtain the Size-Specific Dose Estimates (SSDE). Effective diameter can be estimated using measured lateral and anterior-posterior distance of the patient using either the projection x-ray used as a localizer or axial CT images (Figure 9-1). These measurements can be either performed on work stations using electronic measuring tools or physical devices such as calipers. Equations 9-1 through 9-5 show the calculation of effective diameter using lateral and anterior-posterior measures of the patient, adapted from TG 204 [49].

$$r_1 = \frac{LAT}{2} \qquad \textbf{Eq. 9-1}$$

$$r_2 = \frac{AP}{2} \qquad \textbf{Eq. 9-2}$$

$$A = \pi r_1 r_2 \qquad \textbf{Eq. 9-3}$$

$$effective\ Diameter = 2\sqrt{\frac{A}{\pi}} \qquad \textbf{Eq. 9-4}$$

$$effective\ Diameter = \sqrt{LAT \times AP} \qquad \textbf{Eq. 9-5}$$

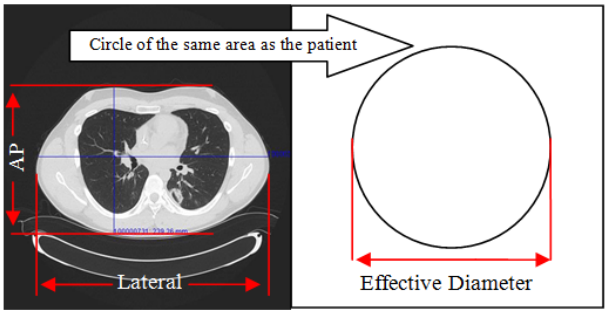

Figure 9-1 The anterior-posterior (AP) and lateral measures of a patient shown with the corresponding effective diameter, which is the diameter of a circle with the same area as the patient.

Effective diameter is a simple physical measure of the patient, but it fails to describe a patient's composition and attenuation properties. Knowing that it is not solely the physical dimensions of the patient that affects the amount of absorption of energy but the patient attenuation properties, it is reasonable to hypothesize an improved dose estimate once an attenuation-based metric is used to describe the differences among patients instead of measures of physical dimensions such as effective diameter. As an example, the measured effective diameter of a patient taken in the thoracic area and abdominal region can be the same, but due to lower density and attenuation properties of lung compared to abdomen, for the same amount of CT output, thorax will have a higher absorbed dose than abdomen. Hence, results from TG 204 may underestimate actual dose to the thoracic region because TG 204 lookup value using the measured effective diameter will

result in a lower dose. This issue was one of the main criticisms of the TG 204 report, which is hoped to be solved once an attenuation-based metric is adapted.

Water is a major component of human body and therefore for dose calculation purposes, a scanned subject may be modeled as a cylindrical water phantom [145, 146]. The diameter of this cylindrical phantom, called water equivalent diameter (D_W), is chosen so that the phantom has the same average attenuation as the scanned subject [141, 147]. The water equivalent diameter is defined as:

$$D_W = \rho \times 2\sqrt{A_{Patient}/\pi} \qquad \textbf{Eq. 9-6}$$

where ρ is the average attenuation of the patient defined as:

$$\rho = \sum(\frac{I(x,y)}{1000} + 1)/N \qquad \textbf{Eq. 9-7}$$

where $(\frac{I(x,y)}{1000} + 1)$ is equal to the linear attenuation coefficient value of a single pixel at a certain x and y coordinate derived from the definition of the Hounsfield Unit scale defined as $HU = \frac{(\mu_{material} - \mu_{water})}{\mu_{water}} \times 1000$. N is the number of voxels within the patient, and $A_{Patient}$ is the area of the patient defined as:

$$A_{Patient} = N \times A_{Pixel} \qquad \textbf{Eq. 9-8}$$

with A_{Pixel} being the area of each pixel. Calculation of D_W requires segmentation methods to separate out body from the surrounding air and CT bed.

The approximated water equivalent diameter metric, D_{Wa}, is defined similarly with the exception of the average attenuation being inside the radical, as shown in Eq. 9-9. This simplifies the

calculation of the water equivalent diameter, in which no contouring is required and the entire image can be used to calculate $A_{Patient}$, A_{Pixel}, and ρ. However, this method is expected to be less accurate since it is using a square root of average attenuation instead of average attenuation to keep the overall water-equivalent area (A_w) unchanged.

$$D_{Wa} = 2\sqrt{A_w/\pi} \qquad \textbf{Eq. 9-9}$$

$$A_W = \rho \times A_{image} \qquad \textbf{Eq. 9-10}$$

Although this method includes the surrounding air in the calculation, which can be more or less for one patient versus the other, it does not dramatically affect the value of A_w. For instance, if less surrounding air is included in the calculation of D_{Wa}, the mean CT number (ρ) increases but the area of the image, A_{image}, decreases proportionally so that the product A_w remains unchanged. Hence, for calculating D_{Wa}, the average density or mean CT number ρ is taken inside the radical to keep A_w unchanged.

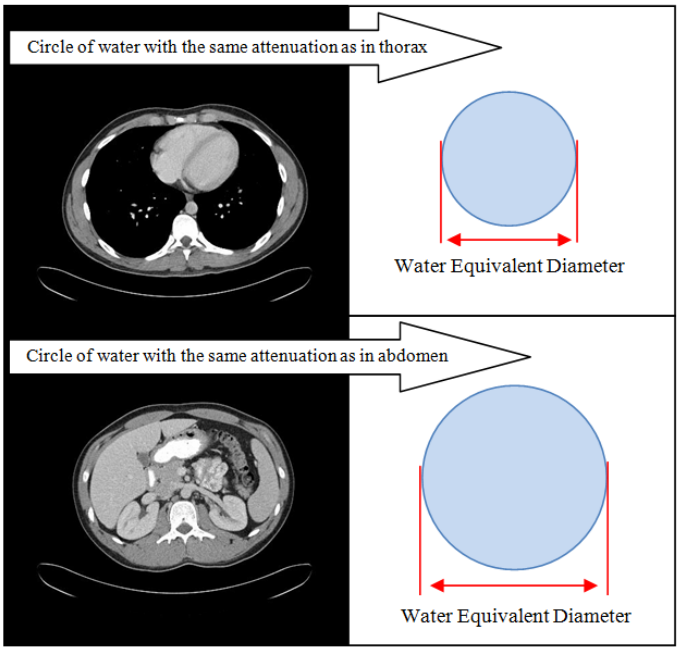

Figure 9-2 Top image illustrates the water equivalent diameter of a single axial thoracic CT image with its water equivalent circle, which has the same attenuation/density of the thoracic image. Bottom section demonstrates the water equivalent diameter of a single axial abdomen CT image whose attenuation is the same as the circle of water shown to the right.

In the abdominal region, the various tissues can be approximated to water with a density close to $1 g/cm^3$. Therefore, the hypothesis is that for the abdominal region, the mean CT number ρ is close to unity and so D_W is almost equal to *effective diameter*. However, in the thoracic area, due to low attenuating lungs with lower density compared to the density of water the mean CT number is smaller than unity and therefore D_W is smaller than *effective diameter*. Figure 9-3 illustrates the difference between D_W and *effective diameter* in thoracic and abdomen/pelvis regions. The difference between *effective diameter* and D_W is not as profound in abdomen/pelvis as it is in thorax; in particular the difference becomes significant in the low attenuating region of the thorax which contains most of the lung and is defined as the region between the inferior edge of the scapula and superior boundary of the liver. As shown in Figure 9-3, all abdomen/pelvic

CT scans start or extend in the thoracic region, including some section of the lungs. Hence, the difference between *effective diameter* and D_w increases in this specific region, represented here with a red ellipse in Figure 9-3.

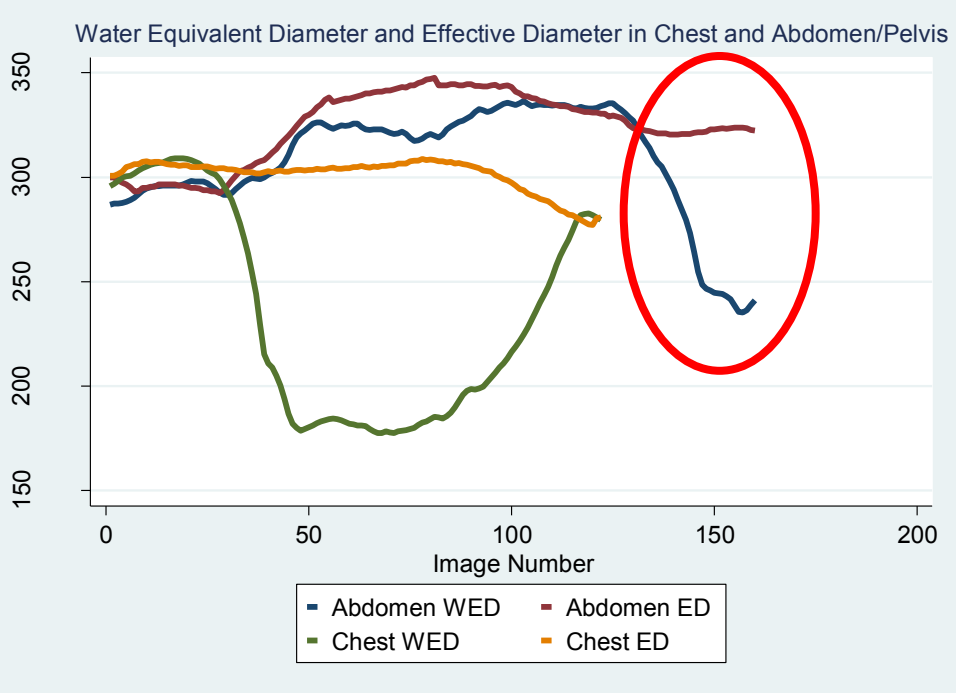

Figure 9-3 The difference between effective diameter and D_W in abdomen/pelvis and thorax, showing almost no difference between these two size metrics in abdominal regions while there is a visible differences between these metrics in the thoracic areas.

This chapter will investigate three different size metrics, *effective diameter*, water equivalent diameter (D_W) and approximated water equivalent diameter (D_{Wa}), as dose predictors and conducts a sensitivity analysis to establish the most appropriate region of measuring these metrics.

9.2 METHODS

To investigate the performance of different size metrics as organ dose predictors, the exponential relationship between normalized organ dose and size was explored for each size metric (Eq. 9-11). For normalizing organ dose, both regional and organ-specific $CTDI_{vol}$ values, $CTDI_{vol,regional}$, and $CTDI_{vol,organ}$ (introduced in Chapter 8) were used.

$$Normalized\ Organ\ Dose = \frac{Organ\ Dose}{CTDI_{vol}} = A \times e^{-B \times Size} \qquad \textbf{Eq. 9-11}$$

9.2.1 Voxelized Models and Monte Carlo Simulations

101 Thoracic (51 females and 50 males) and 82 abdomen/pelvis scans acquired on Siemens Sensation 64 MDCT were used to generate voxelized models for use in Monte Carlo simulations. All voxelized models were generated from images reconstructed at 500 mm DFOV to ensure coverage of the entire body. The data set consisted of a large range of sizes from pediatric to very large adult patients. Thoracic models included 30 pediatric patients and abdomen/pelvis models contained 20 pediatric patients. Liver, spleen, and kidneys were identified and segmented on the abdomen/pelvis CT images, while thoracic images were used to identify and segment lungs and glandular breast tissue, which was only segmented on female models. Chapter 5 describes a more detailed procedure on creating voxelized models.

Using Monte Carlo methods discussed in chapter 4, organ doses from thoracic and abdomen/pelvic CT scans using actual patient models, with their corresponding TCM data, were simulated. Organ doses resulting from thoracic (lungs and glandular breast tissue) and abdomen/pelvis (liver, spleen, and kidneys) CT simulations were calculated from the Monte Carlo outputs using Eq. 4-6.

9.2.3 Regional and Organ-Specific $CTDI_{vol}$

For each patient, calculated regional and organ specific $CTDI_{vol}$, using scanner-reported $CTDI_{vol}$ and regional and organ-specific averaged tube current values, were used as normalization factors for Monte Carlo simulated organ doses. As shown in chapter 8, regional and organ-specific $CTDI_{vol}$ values are better normalization quantities in tube current modulated CT scans compared to global, scanner-reported $CTDI_{vol}$. Both $CTDI_{vol,regional}$ and $CTDI_{vol,organ}$ will be used to investigate the most appropriate size metric as an organ dose predictor. Table 9-1 summarizes the definition of regional and organ-specific $CTDI_{vol}$ values in abdomen/pelvis and chest CT exams.

Exam	$CTDI_{vol,regional}$		$CTDI_{vol,organ}$	
	Definition	**Abbreviation**	**Definition**	**Abbreviation**
Abdomen	top of liver to the iliac crest	$CTDI_{vol,Abd}$	images containing liver	$CTDI_{vol,Liver}$
			images containing spleen	$CTDI_{vol,Spleen}$
			images containing kidneys	$CTDI_{vol,Kidneys}$
Chest	inferior edge of the scapula and superior boundary of the liver	$CTDI_{vol,LowAtt}$	images containing lungs	$CTDI_{vol,Lungs}$
			images containing breasts	$CTDI_{vol,Breasts}$

Table 9-1 Tabular description and abbreviation of different $CTDI_{vol}$ values.

As an example, Figure 9-4 demonstrates an abdomen/pelvis TCM function and regions used to calculate different $CTDI_{vol}$ values.

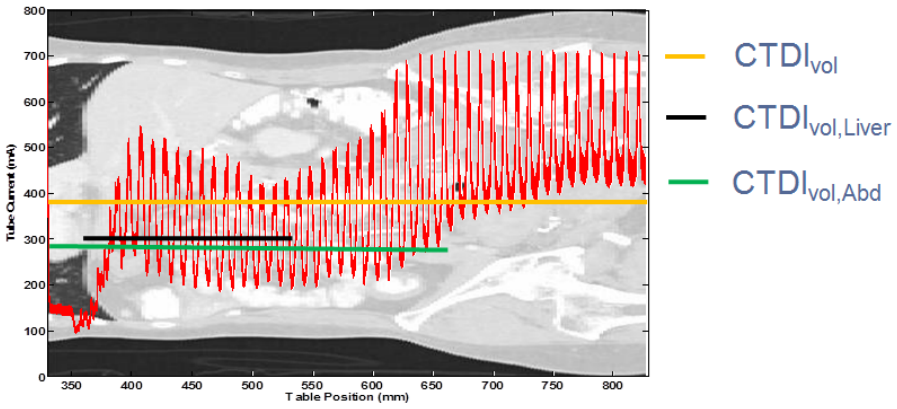

Figure 9-4 Representation of an abdomen/pelvis TCM function along with regions used to calculate $CTDI_{vol}$, $CTDI_{vol,regional}$ (in this case abdomen), and $CTDI_{vol,organ}$ (in this case liver).

9.2.2 Size Metrics

A semi-automated segmentation code was written to segment out the whole body from the surrounding air and the table for calculating *effective diameter* and D_W, water equivalent diameter, on each axial image. The whole body segmentation code is based on a combination of Otsu thresholding and 3 dimensional Region Growing (Figure 9-5).

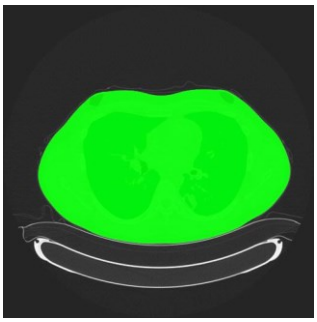

Figure 9-5 Segmentation to separate patient's body from the surrounding air and the bed. The "body ROI", shown in green, will be used to calculate an effective diameter and water equivalent diameter, while the entire image is used to calculate approximated water equivalent diameter per slice.

The code was applied on each set of patient images to segment out the body from the surrounding air and the table; the segmented region was used to calculate an effective diameter and D_W per slice. Additionally, pixel values of entire axial image (including the surrounding air) within a series were used to calculate an approximated water equivalent diameter, D_{Wa}, per image. Per patient, each size metric was reported in three different ways:

1. As a *global* average size metric, $\textit{effective diameter}_{global}$, $D_{W,\text{global}}$, $D_{Wa,global}$
2. As a *regional* average size metric calculated using images within abdomen region for abdomen/pelvis models and low attenuating region for thoracic models (i.e. $\textit{effective diameter}_{LowAtt}$, $D_{W,LowAtt}$, $D_{Wa,\text{LowAtt}}$, $\textit{effective diameter}_{Abd}$, $D_{W,Abd}$, $D_{Wa,Abd}$).
3. As an *organ-specific* average size metric calculated for images that contained the organ of interest, e.g. $\textit{effective diameter}_{Lung}$, $D_{W,\text{Lung}}$, $D_{Wa,Lung}$.

The definition of regional and organ-specific in both, abdomen/pelvis and thorax, are given in table 9-1 and match the regions for which regional and organ-specific CTDI_{vol} values were calculated. Figure 9-6 illustrates two size metrics, *effective diameter* and D_W, calculated for each image within a male and female chest series and, as shown, averaged over three different regions: global, regional, and organ-specific, in this case averaged over images containing lungs. Effective diameter is almost constant across the scan length for the male model. However, it is increasing with image number for the female model up until beginning of the abdomen. This difference between male and female could be due to anatomical differences between genders in the chest area.

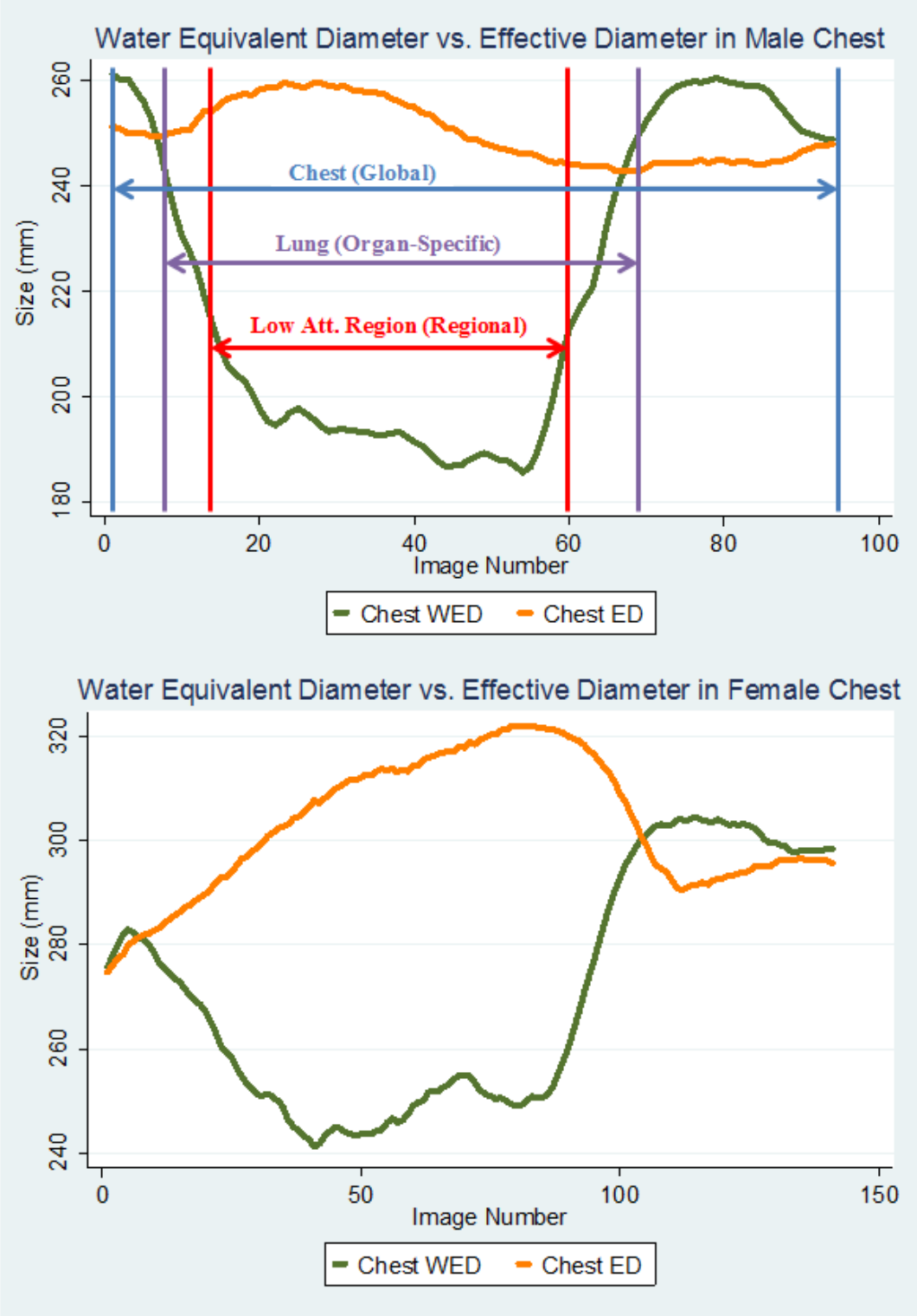

Figure 9-6 Difference between water equivalent diameter and effective diameter illustrated for both male and female model. There are not only differences between size metrics but there are also differences between male and female in the thoracic region.

Overall, for thoracic models, nine size metrics were calculated per male patient and twelve per female patients. In abdomen/pelvis models, fifteen size metrics were calculated for each patient; nine organ-specific, three regional, and three global.

9.2.3 Statistical Analysis

Linear regressions were used to assess the effect of different size metrics on absolute organ doses and $CTDI_{vol}$. A scatter diagram with a linear fitted line is shown to demonstrate the relationship between dose (absolute organ dose) and each size metric.

For normalized organ doses, the log-transformation of normalized organ dose was used to fit a linear regression with the covariate of different metrics using each $CTDI_{vol}$ value (regional and organ-specific) in turn. The coefficient of determination (R^2) was reported to quantify the proportion of variation explained by different size metrics and to evaluate the benefit of using each size metric. A scatter diagram with a fitted exponential curve, as described by Equation 9-11, is shown (using original, non log-transformed data) to demonstrate the relationship between normalized organ dose and individual size metrics for each organ. Pearson's correlations and 95% confidence interval were reported from the log-transformed linear regression. The 95% confidence intervals of different size metrics were compared to each other across each $CTDI_{vol}$ value. A p-value smaller than 0.05 was considered to be significant. All data was analyzed using Stata 12.0 (StataCorp; College Station, TX).

9.3 RESULTS

9.3.1 Absolute Organ Dose versus Size Metric

While in fixed tube current scans, organ dose *decreases* with *increasing* patient size. As also shown in chapter 8, in TCM scans, organ dose *increases* with *increasing* patient size. This trend is seen for all three size metrics and their subsequent measures. Figure 9-7 demonstrates the relationship between absolute organ dose and size metric for kidneys and lungs.

Size Metric	Kidneys	Lung
Global Eff. Dia.	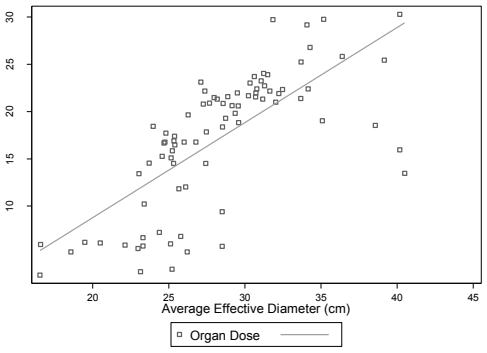	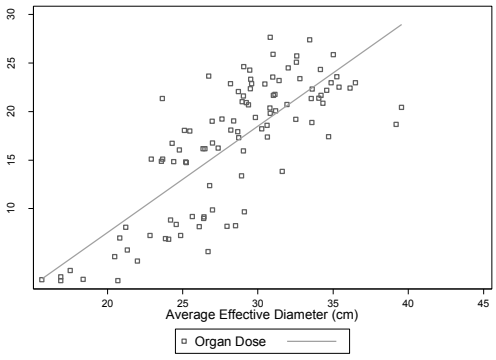
Global Approx. Water Equiv. Dia.	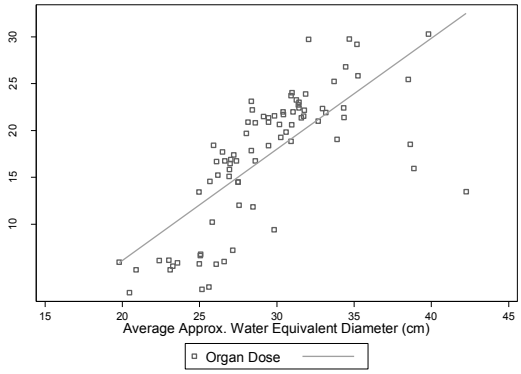	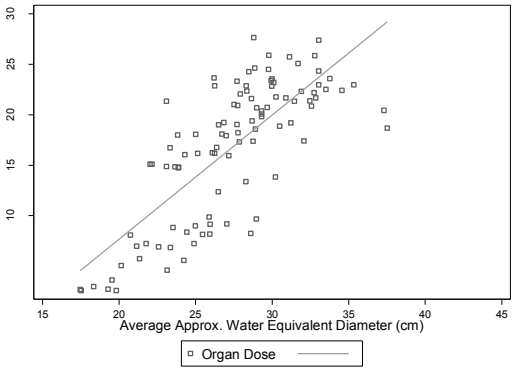

Global Water Equiv. Dia.	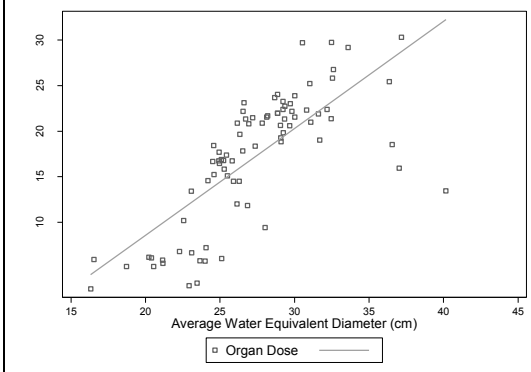	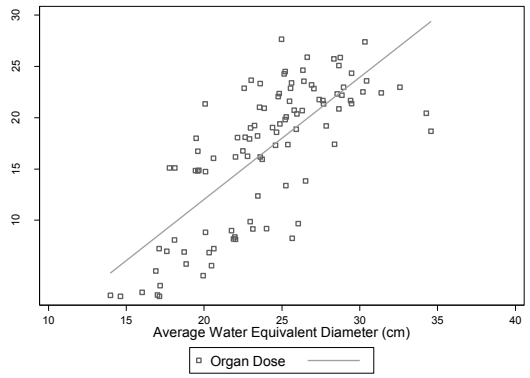

Figure 9-7 Illustration of kidney and lung dose versus three size metrics, both are showing an increase in magnitude with increased size.

In addition to the previously observed trend between absolute organ dose and size, for some of the larger patients, a decrease in kidney and lung dose is observed. This was also seen for liver, spleen, and breasts as demonstrated in Figures 9-8 and 9-9.

Size Metric	Liver	Spleen
Global Water Equiv. Dia.	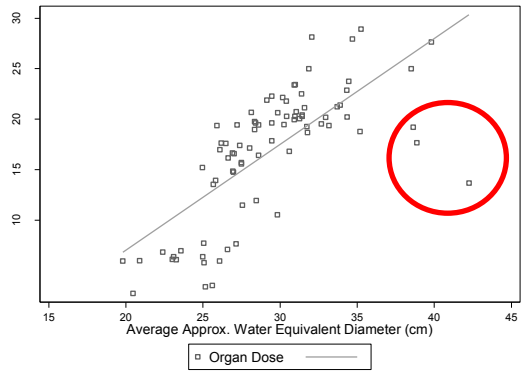	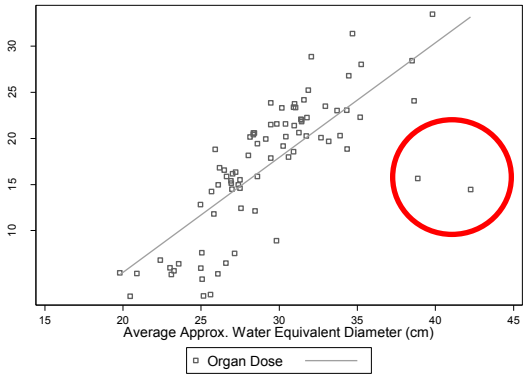

Figure 9-8 Illustration of liver and spleen dose versus Ave. Water Equiv. Diameter and the decrease in dose with increased size for some of the larger patients shown in the red circle.

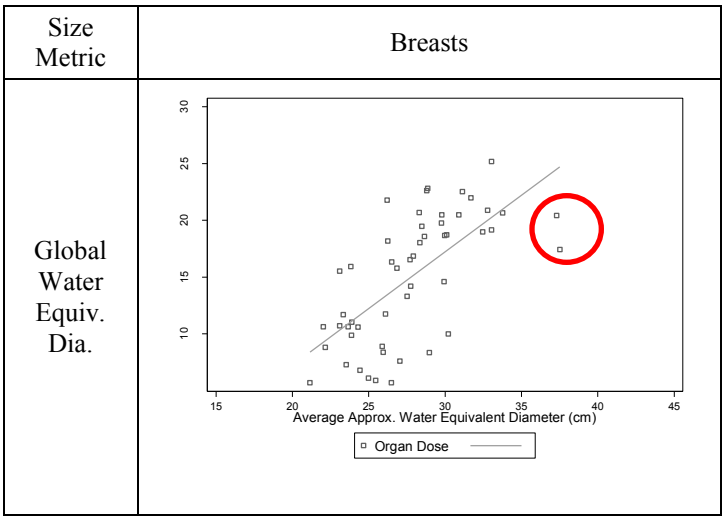

Figure 9-9 Illustration of breast dose versus Ave. Water Equiv. Diameter with two patients identified to have lower doses despite their large water equivalent diameter.

9.3.2 Comparison of Size Metrics for Normalized Dose by $CTDI_{vol,regional}$

The relationship between organ dose normalized by $CTDI_{vol,regional}$ and size metrics, as shown by Eq. 9-10, was investigated and compared across all metrics. Tables 9-2 through 9-6 summarize these results for all five organs, while Figure 9-8 shows the exponentially fitted data for normalized kidney and lung dose.

Tables 9-2 through 9-4 summarize the R^2, Pearson correlation, and the 95% confidence interval of normalized abdominal organ doses and different size metrics. Although the R^2 value slightly increases for D_W and D_{Wa} compared to *effective diameter*, this increase is not statistically significant. Furthermore, different variation of measuring size (i.e. global average, regional average, and organ-specific averaged size metric) within each size metric does not seem to make a statistically significant difference.

Table 9-2 R^2, Pearson correlation, and 95% confidence interval of normalized liver dose by $CTDI_{vol,regional}$ and size metrics‡

Organ	Metric	n	$CTDI_{vol,Abd}$					
			$Size\ Metric_{global}$		$Size\ Metric_{Abd}$		$Size\ Metric_{Liver}$	
			r (95% CI)	R^2	r (95% CI)	R^2	r (95% CI)	R^2
Liver	Eff. Dia.	82	-0.9181 (-0.947, -0.876)	0.84	-0.9261 (-0.952, -0.887)	0.86	-0.9207 (-0.948, -0.879)	0.85
	D_w	82	-0.9365 (-0.959, -0.903)	0.88	-0.9452 (-0.964, -0.916)	0.89	-0.9431 (-0.963, -0.913)	0.89
	D_{wa}	82	-0.9434 (-0.963, -0.913)	0.89	-0.9507 (-0.968, -0.924)	0.90	-0.9492 (-0.967, -0.922)	0.90

‡ log transformation is applied for Pearson correlation and 95% confidence interval

Table 9-3 R^2, Pearson correlation, and 95% confidence interval of normalized spleen dose by $CTDI_{vol,regional}$ and size metrics‡

Organ	Metric	n	$CTDI_{vol,Abd}$					
			$Size\ Metric_{global}$		$Size\ Metric_{Abd}$		$Size\ Metric_{Spleen}$	
			r (95% CI)	R^2	r (95% CI)	R^2	r (95% CI)	R^2
Spleen	Eff. Dia.	82	-0.8686 (-0.913, -0.803)	0.75	-0.8732 (-0.917, -0.810)	0.76	-0.8682 (-0.913, -0.802)	0.75
	D_w	82	-0.8658 (-0.912, -0.799)	0.75	-0.8688 (-0.914, -0.803)	0.75	-0.8547 (-0.904, -0.783)	0.73
	D_{wa}	82	-0.8713 (-0.915, -0.807)	0.76	-0.8694 (-0.914, -0.804)	0.76	-0.8612 (-0.908, -0.792)	0.74

‡ log transformation is applied for Pearson correlation and 95% confidence interval

Table 9-4 R^2, Pearson correlation, and 95% confidence interval of normalized kidney dose by $CTDI_{vol,regional}$ and size metrics‡

Organ	Metric	n	$CTDI_{vol,Abd}$					
			$Size\ Metric_{global}$		$Size\ Metric_{Abd}$		$Size\ Metric_{Kidney}$	
			r (95% CI)	R^2	r (95% CI)	R^2	r (95% CI)	R^2
Kidney	Eff. Dia.	82	-0.8560 (-0.905, -0.785)	0.73	-0.8626 (-0.909, -0.794)	0.73	-0.8627 (-0.909, -0.794)	0.74
	D_w	82	-0.8557 (-0.905, -0.784)	0.73	-0.8702 (-0.915, -0.805)	0.76	-0.8718 (-0.916, -0.808)	0.76
	D_{wa}	82	-0.8678 (-0.913, -0.802)	0.75	-0.8760 (-0.918, -0.814)	0.77	-0.8783 (-0.920, -0.817)	0.77

‡ log transformation is applied for Pearson correlation and 95% confidence interval

Table 9-5 summarizes the statistical analysis for different size metrics investigated using normalized lung dose. Using the same normalization factor ($CTDI_{vol,regional}$), 70% of the variation of size is explained by D_W, while only 43% is explained by *effective diameter*. Similarly the R^2

increases for D_{Wa}; however, the improvement is not statistically significant. The only statistically significant improvement of using D_W over *effective diameter* is observed in regional (low attenuating region of thorax) average of D_W.

Similar to the abdominal organs, no significant improvement in correlation between normalized breast dose and size was observed once attenuation-based metrics (D_W and D_{Wa}) were used (Table 9-6).

Table 9-5 R^2, Pearson correlation, and 95% confidence interval of normalized lung dose by $CTDI_{vol,regional}$ and size metrics‡

Organ	Metric	n	$CTDI_{vol,Low\ Att}$					
			$Size\ Metric_{global}$		$Size\ Metric_{Chest}$		$Size\ Metric_{Lung}$	
			r (95% CI)	R^2	r (95% CI)	R^2	r (95% CI)	R^2
Lung	Eff. Dia.	101	-0.6498 (-0.750, -0.520)	0.42	-0.6579 (-0.756, -0.531)	0.43	-0.6449 (-0.746, -0.514)	0.42
	D_w	101	-0.7148 (-0.799, -0.604)	0.51	-0.8311* (-0.883, -0.759)	0.70	-0.7592 (-0.831, -0.662)	0.58
	D_{wa}	101	-0.6858 (-0.777, -0.566)	0.47	-0.7751 (-0.843, -0.683)	0.60	-0.7154 (-0.799, -0.604)	0.51

‡ log transformation is applied for Pearson correlation and 95% confidence interval

* statistically significant improvement (p-value < 0.05) compared to effective diameter by using log transformation

Table 9-6 R^2, Pearson correlation, and 95% confidence interval of normalized breast dose by $CTDI_{vol,regional}$ and size metrics‡

Organ	Metric	n	$CTDI_{vol,Low\ Att}$					
			$Size\ Metric_{global}$		$Size\ Metric_{Chest}$		$Size\ Metric_{Breasts}$	
			r (95% CI)	R^2	r (95% CI)	R^2	r (95% CI)	R^2
Breasts	Eff. Dia.	51	-0.8100 (-0.887, -0.688)	0.66	-0.8385 (-0.905, -0.732)	0.70	-0.8265 (-0.898, -0.713)	0.68
	D_w	51	-0.7860 (-0.873, -0.652)	0.62	-0.8302 (-0.900, -0.719)	0.69	-0.8023 (-0.883, -0.676)	0.64
	D_{wa}	51	-0.7917 (-0.876, -0.660)	0.63	-0.8341 (-0.902, -0.725)	0.70	-0.8165 (-0.891, -0.698)	0.67

‡ log transformation is applied for Pearson correlation and 95% confidence interval

Figure 9-9 illustrates the exponential fit of normalized kidney and lung dose by $CTDI_{vol,regional}$ versus three different global average size metrics.

Size Metric	Kidneys	Lung
Eff. Dia.	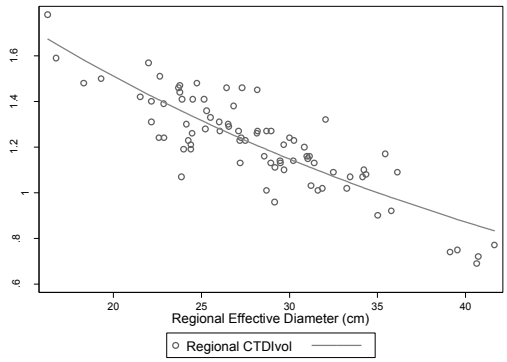	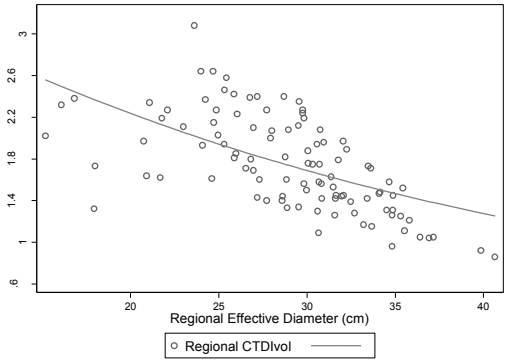
Water Equiv. Dia.	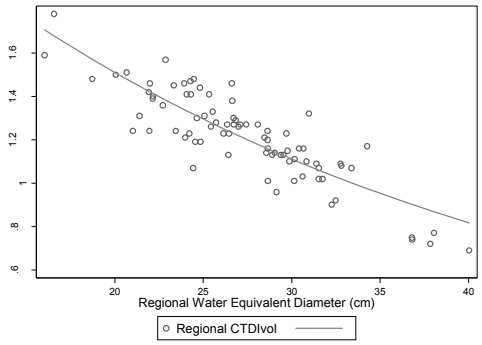	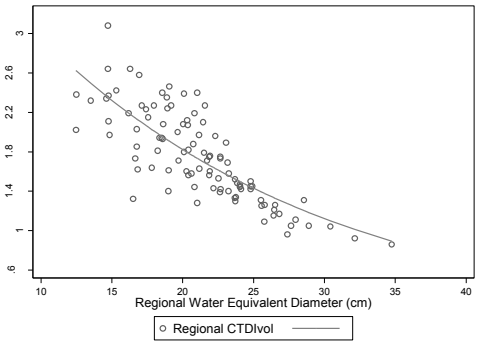
Approx. Water Equiv. Dia.	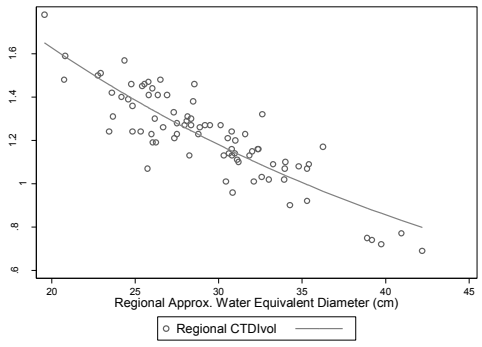	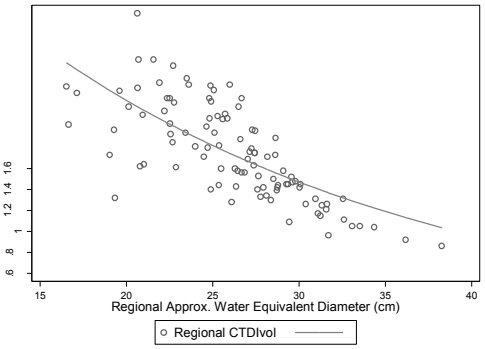

Figure 9-9 Illustration of normalized kidney and lung dose versus regional average effective diameter, approximated water equivalent diameter and water equivalent diameter. The improvement of the fitted data with water equivalent diameter is evident compared to effective diameter.

‘

9.3.3 Comparison of Size Metrics for Normalized Dose by $CTDI_{vol,organ}$

Similar analysis shown in section 9.3.2 was performed in this section while using the organ-specific $CTDI_{vol}$, $CTDI_{vol,organ}$, as the normalization factor.

Tables 9-7 through 9-11 demonstrate the analysis for this section. Although the R^2 increases across all five organs for attenuation based size metrics, D_W and D_{Wa}, the increase is not statistically significant. Additionally there is no statistically significant difference between global, regional, and organ-specific size metrics.

Comparing the results to the previous section, there is no statistically significant difference between $CTDI_{vol,regional}$ and $CTDI_{vol,organ}$ as normalization quantities except for lung dose, whose R^2 increases significantly for regional water equivalent diameter and $CTDI_{vol,LowAtt}$ as normalization factor.

Figure 9-10 shows the exponential fit between normalized organ dose by organ-specific $CTDI_{vol}$ and organ-specific average of the three investigated size metrics, *effective diameter*, D_w, and D_{wa}.

Table 9-7 R^2, Pearson correlation, and 95% confidence interval of normalized liver dose by $CTDI_{vol,organ}$ and size metrics‡

Organ	Metric	n	$CTDI_{vol,Liver}$					
			$Size\ Metric_{global}$		$Size\ Metric_{Abd}$		$Size\ Metric_{Liver}$	
			r (95% CI)	R^2	r (95% CI)	R^2	r (95% CI)	R^2
Liver	Eff. Dia.	82	-0.9194 (-0.947, 0.877)	0.85	-0.9347 (-0.957, -0.900)	0.87	-0.9372 (-0.959, -0.904)	0.88
	D_w	82	-0.9265 (-0.952, -0.888)	0.86	-0.9397 (-0.961, -0.908)	0.88	-0.9463 (-0.965, -0.918)	0.90
	D_{wa}	82	-0.9358 (-0.958, -0.902)	0.88	-0.9475 (-0.966, -0.920)	0.90	-0.9548 (-0.971, -0.931)	0.91

‡ log transformation is applied for Pearson correlation and 95% confidence interval

Table 9-8 R^2, Pearson correlation, and 95% confidence interval of normalized spleen dose by $CTDI_{vol,Organ}$ and size metrics‡

Organ	Metric	n	$CTDI_{vol,Spleen}$					
			Size $Metric_{global}$		Size $Metric_{Abd}$		Size $Metric_{Spleen}$	
			r (95% CI)	R^2	r (95% CI)	R^2	r (95% CI)	R^2
Spleen	Eff. Dia.	82	-0.8581 (-0.906, -0.788)	0.74	-0.8687 (-0.913, -0.803)	0.75	-0.8828 (-0.923, -0.824)	0.78
	D_w	82	-0.8482 (-0.900, -0.774)	0.72	-0.8462 (-0.898, -0.771)	0.72	-0.8559 (-0.905, -0.785)	0.73
	D_{wa}	82	-0.8781 (-0.812, -0.600)	0.72	-0.8477 (-0.899, -0.773)	0.72	-0.8615 (-0.909, -0.793)	0.74

‡ log transformation is applied for Pearson correlation and 95% confidence interval

Table 9-9 R^2, Pearson correlation, and 95% confidence interval of normalized kidney dose by $CTDI_{vol,organ}$ and size metrics‡

Organ	Metric	n	$CTDI_{vol,Kidney}$					
			Size $Metric_{global}$		Size $Metric_{Abd}$		Size $Metric_{Kidney}$	
			r (95% CI)	R^2	r (95% CI)	R^2	r (95% CI)	R^2
Kidney	Eff. Dia.	82	-0.8981 (-0.933, -0.846)	0.81	-0.9116 (-0.942, -0.866)	0.83	-0.9165 (-0.945, -0.873)	0.84
	D_w	82	-0.8871 (-0.926, -0.830)	0.79	-0.8462 (-0.898, -0.771)	0.81	-0.9115 (-0.942, -0.866)	0.83
	D_{wa}	82	-0.9013 (-0.935, -0.851)	0.81	-0.9133 (-0.943, -0.868)	0.83	-0.9222 (-0.949, -0.882)	0.85

‡ log transformation is applied for Pearson correlation and 95% confidence interval

* statistically significant improvement (p-value < 0.05) compared to $CTDI_{vol,regional}$ by using log transformation

Table 9-10 R^2, Pearson correlation, and 95% confidence interval of normalized lung dose by $CTDI_{vol,organ}$ and size metrics‡

Organ	Metric	n	$CTDI_{vol,Lung}$					
			Size $Metric_{global}$		Size $Metric_{Chest}$		Size $Metric_{Lung}$	
			r (95% CI)	R^2	r (95% CI)	R^2	r (95% CI)	R^2
Lung	Eff. Dia.	101	-0.7971 (-0.859, 0.713)	0.64	-0.7906 (-0.854, -0.704)	0.63	-0.8011 (-0.862, -0.718)	0.64
	D_w	101	-0.8170 (-0.873, -0.740)	0.67	-0.7977 (-0.859, -0.713)	0.64	-0.8174 (-0.873, -0.740)	0.67
	D_{wa}	101	-0.8223 (-0.877, -0.747)	0.68	-0.8242 (-0.878, -0.749)	0.68	-0.8278 (-0.881, -0.754)	0.69

‡ log transformation is applied for Pearson correlation and 95% confidence interval

Table 9-11 R^2, Pearson correlation, and 95% confidence interval of normalized breast dose by $CTDI_{vol,organ}$ and size metrics‡

Organ	Metric	n	$CTDI_{vol,Breasts}$					
			$Size\ Metric_{global}$		$Size\ Metric_{Chest}$		$Size\ Metric_{Breasts}$	
			r (95% CI)	R^2	r (95% CI)	R^2	r (95% CI)	R^2
Breasts	Eff. Dia.	51	-0.8157 (-0.891, -0.697)	0.67	-0.8288 (-0.899, -0.717)	0.69	-0.8350 (-0.903, -0.727)	0.70
	D_w	51	-0.7833 (-0.871, -0.647)	0.61	-0.8000 (-0.881, -0.673)	0.64	-0.8020 (-0.883, -0.676)	0.64
	D_{wa}	51	-0.8054 (-0.885, -0.681)	0.65	-0.8259 (-0.897, -0.712)	0.68	-0.8279 (-0.898, -0.716)	0.69

‡ log transformation is applied for Pearson correlation and 95% confidence interval

Size Metric	Kidneys	Lung
Ave. Eff. Dia.	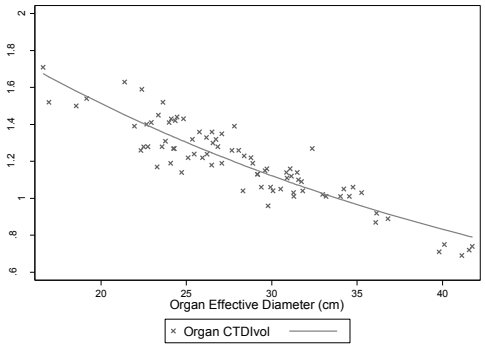	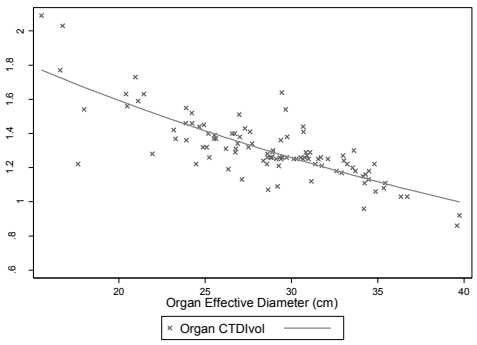
Water Equiv. Dia.	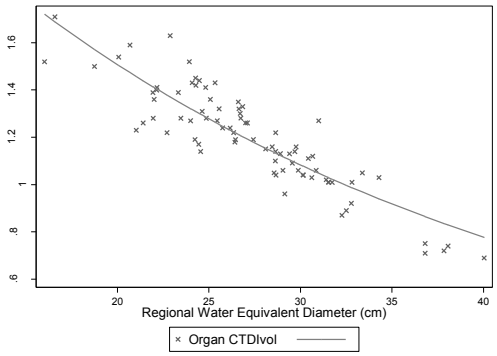	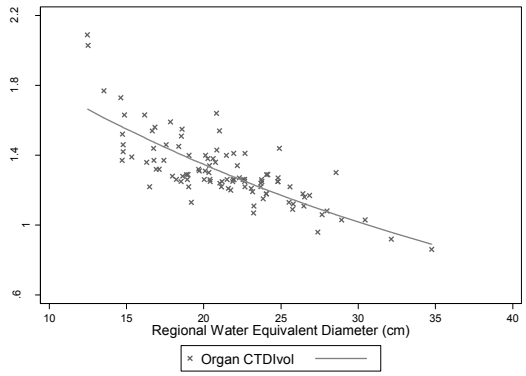

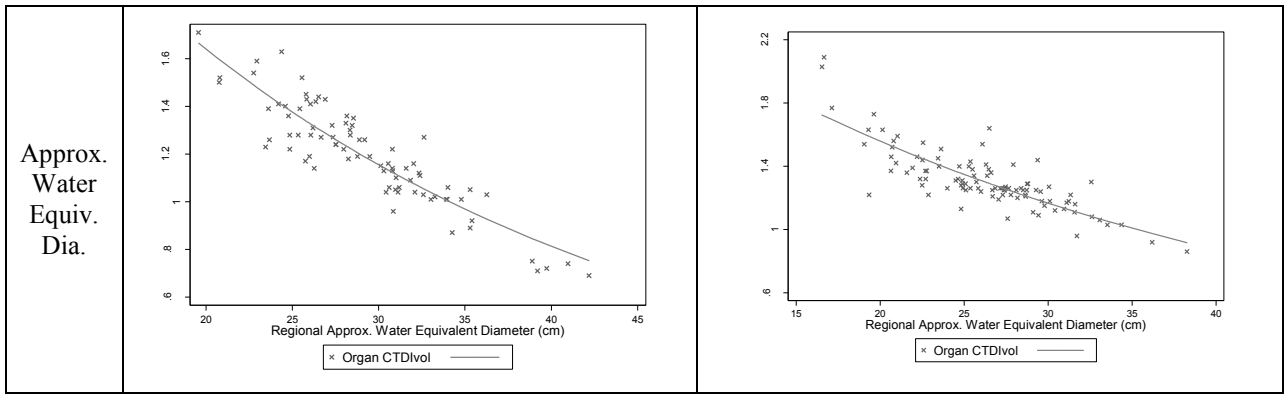

Figure 9-10 Illustration of $CTDI_{vol,organ}$ normalized kidney and lung dose versus organ-specific averaged effective diameter, approximated water equivalent diameter and water equivalent diameter.

9.4 DISCUSSION

The exponential relationship between normalized dose and patient size was investigated for different size metrics to obtain the most appropriate metric as a predictor of dose. Additionally, absolute organ doses were plotted versus size metrics to explore the behavior of absolute dose form tube current modulated CT exams with respect to patient size.

As previously observed [81, 148], in tube current modulated CT scans, patient dose increases as the size increases, while in fixed tube current scans, dose decreases with increasing patient size. However, as shown for all five organs in Figures 9-4 through 9-6, for bigger patient sizes, a drop in dose rather than the expected increase was observed. To investigate this sudden decrease in dose for larger patients, patients were identified and their TCM functions were studied.

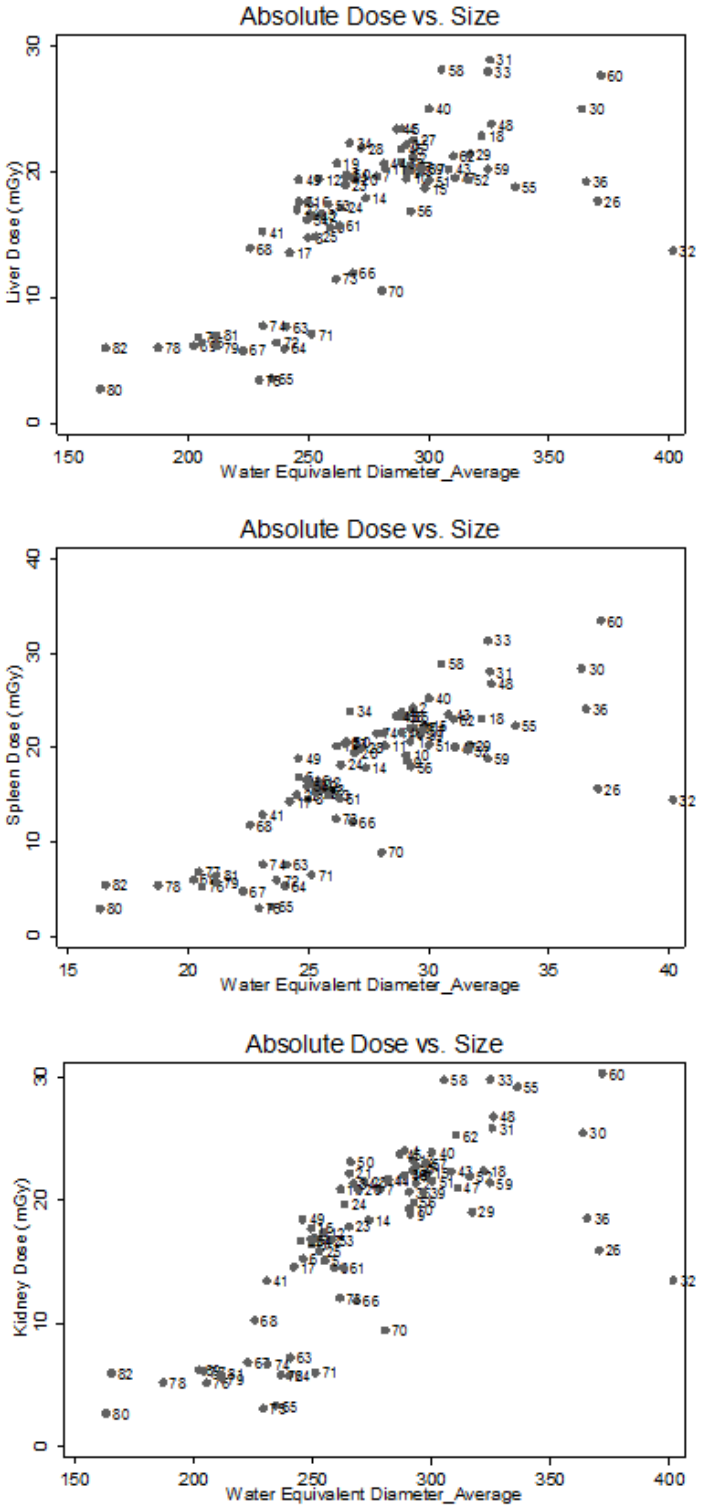

Figure 9-11 Organ dose versus size scatter plots identifying large patients with lower organ doses. For all three abdominal organs, same large patients have identified with lower organ doses.

Across all three abdominal organs, Patient numbers 26, 32 and 36 received lower doses and do not follow the expected behavior of an increase in dose with respect to an increase in size that is usually observed in TCM exams.

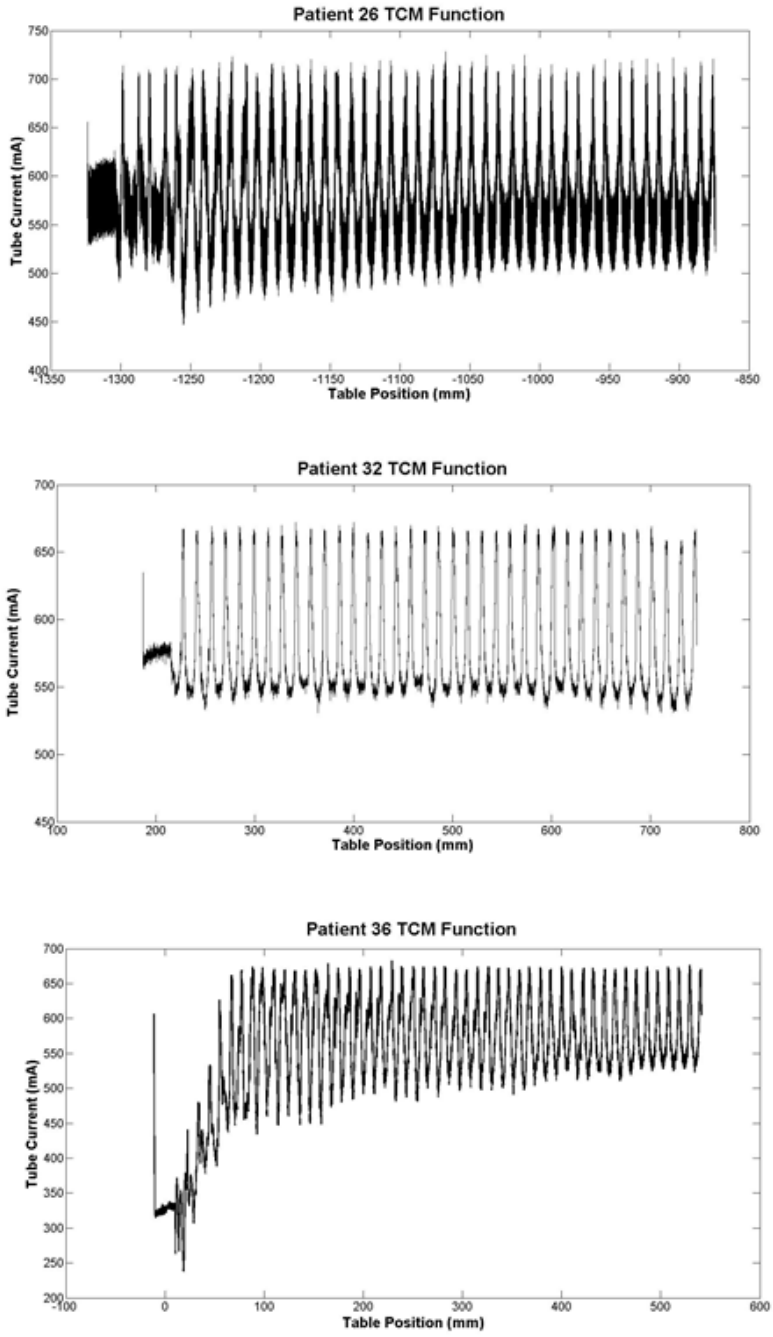

Figure 9-12 Illustration of TCM functions of patient numbers 26, 32, and 36; all three functions are examples of maxed out TCM function with little or no z-axis tube current modulation.

Figure 9-12 demonstrates the TCM functions for patient number 26, 32, and 36. All three TCM functions are maxed out due to reaching generators power limit caused by large patient size, as described in Chapter 3. Comparing these three functions with a typical abdomen/pelvis TCM function (Figure 9-13), it is apparent that the z-axis modulation portion of the TCM is lost due to tube current reaching its maximum value. Once the tube current reaches a maximum, the expected relationship between dose and size in TCM mode no longer holds and patient dose starts decreasing with increasing size (behaving as in fixed tube current mode).

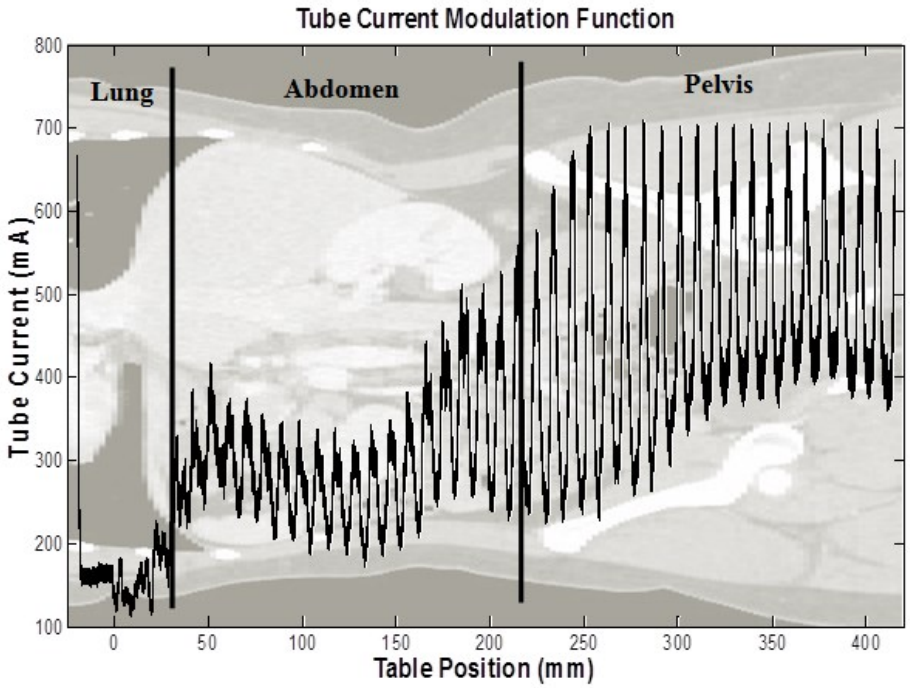

Figure 9-13 An example of a typical abdomen/pelvis TCM function.

To illustrate the transition from TCM to fixed tube current mode for large patients, for each patient, fixed tube current simulations were performed and results were plotted versus average water equivalent diameter along with doses from TCM simulations (Figure 9-14).

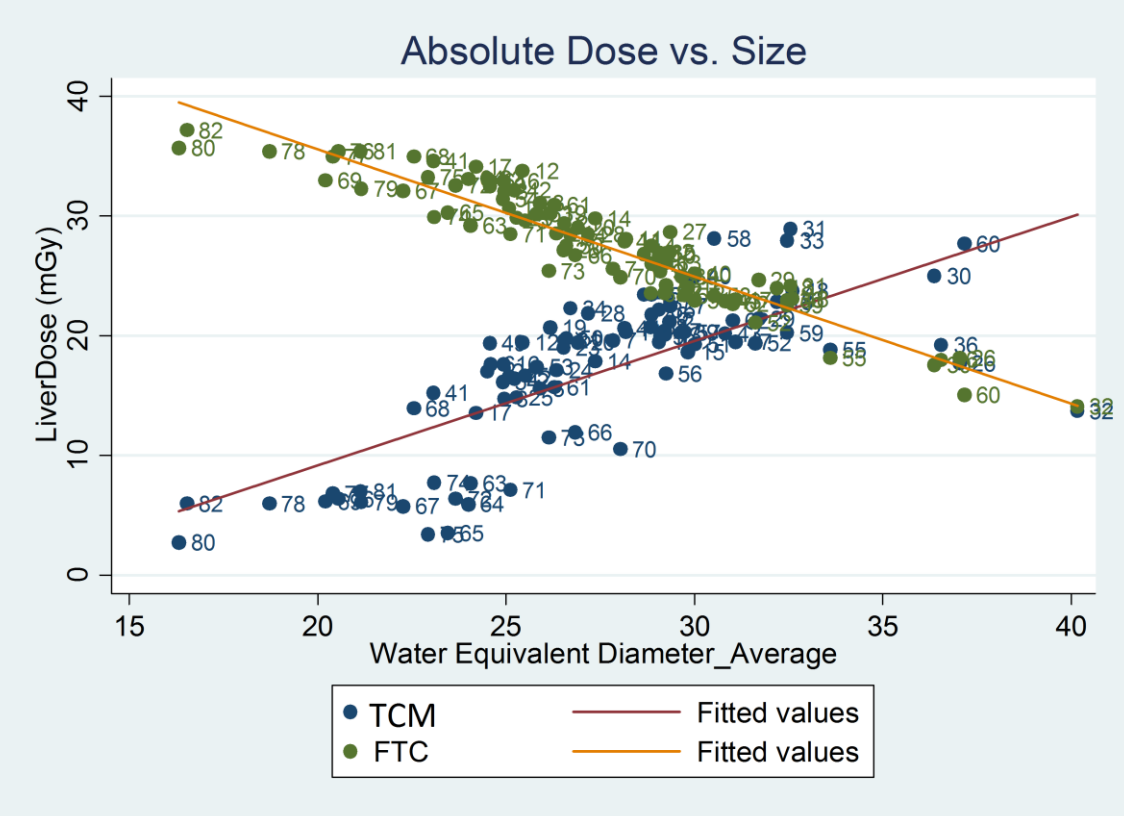

Figure 9-14 Liver doses resulting from fixed (FTC) and modulated tube current (TCM) simulations versus average water equivalent diameter.

As shown in Figure 9-12, for patients 26, 32, and 36, doses from TCM and FTC are relatively very close to each other. However, there are patients in the same size range (patient number 60 and 30), who do not behave like patients 26, 32, and 36. Examining the TCM functions for patient number 30 and 60, a "less" maxed out tube current with preserved z-axis modulation across the scan length is observed (Figure 9-15). Examining the scanning protocols for these patients, two parameters are discovered to be different across these patients. All five patients are scanned using Quality Reference mAs of 275, collimation of 32x0.6, and 120 kVp. However, rotation time and pitch are different across these patients. Table 9-12 lists rotation time and pitch values for these patients.

Patient	26	32	36	30	60
Rotation Time	0.5	0.5	0.5	1	1
Pitch	1	1	0.8	0.75	0.8

Table 9-12 Rotation time (sec) and pitch values used to scan large patients.

As described in Chapter 3, when the peak exposure demand exceeds system limit, the operator is given the option to still load and proceed with the exposure or change parameters such as kVp, rotation time, and pitch to avoid maxing out the tube current. For patients 30 and 60, the operator increased the rotation time to 1 second per rotation and decreased the pitch to 0.75 and 0.8, respectively. However; for patient 26, 32, and 36 the operator either never received the caution message (Figure 9-16) or chose to proceed with the exposure without adjusting the suggested parameters for patient 26, and 32, while decreased pitch to 0.8 for patient 36, which still resulted in locally maxed out tube current.

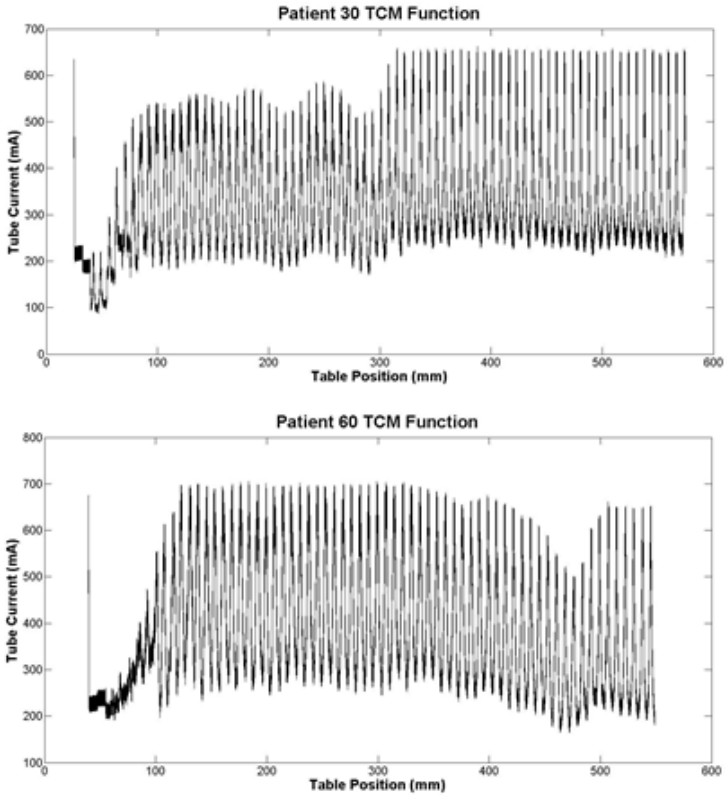

Figure 9-15 TCM function of patient 30 and 60 with preserved z-axis modulation of the tube current with little or no locally maxed out tube current.

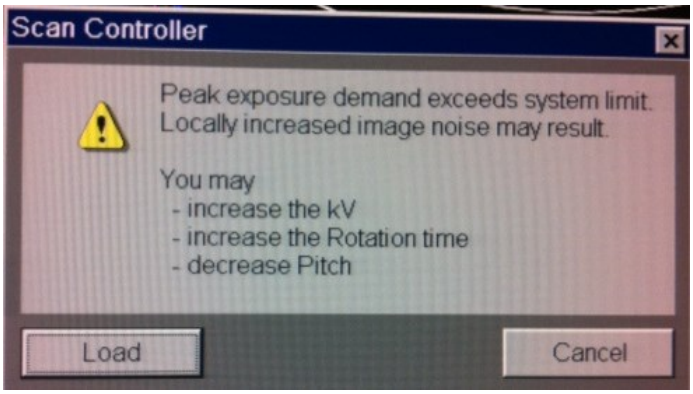

Figure 9-16 Popup message warning against locally decreased image quality and possible actions to be taken to avoid exceeding the system limit.

As seen with the abdominal organs, liver, spleen, and kidneys, a similar transition from TCM to fixed tube current (FTC) is also evident for lungs and breasts. For lungs, TCM and FTC simulation results for patients 196, 150, and 188 are almost overlapping, indicating a loss of z-axis modulation in the TCM function and behaving as a fixed tube current exam. Similarly, for breast dose, TCM and FTC simulation results overlap for both patients, patient number 150 and 188 (Figures 9-17 and 9-18).

TCM function for these patients were examined to make certain the overlapping of TCM and FTC results is due to loss of z-axis modulation caused by maxed out tube current. Figure 9-19 shows the TCM functions of these patients with maxed out tube current and no z-axis modulation. As a comparison, Figure 9-20 illustrates a typical thoracic TCM function.

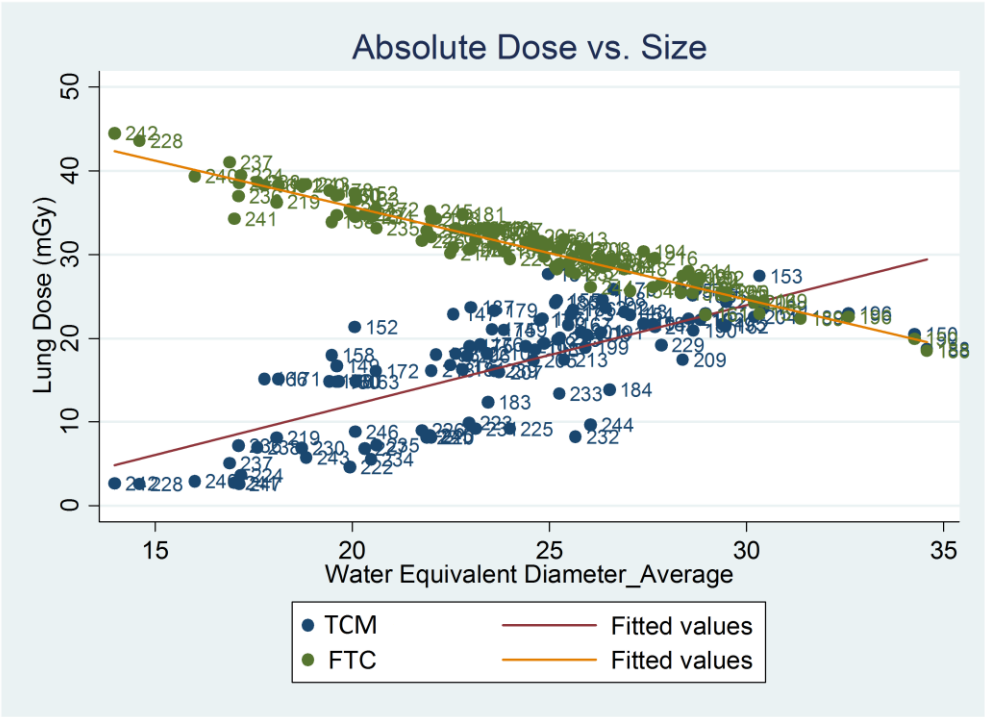

Figure 9-17 Lung doses resulting from fixed and modulated tube current simulations versus average water equivalent diameter.

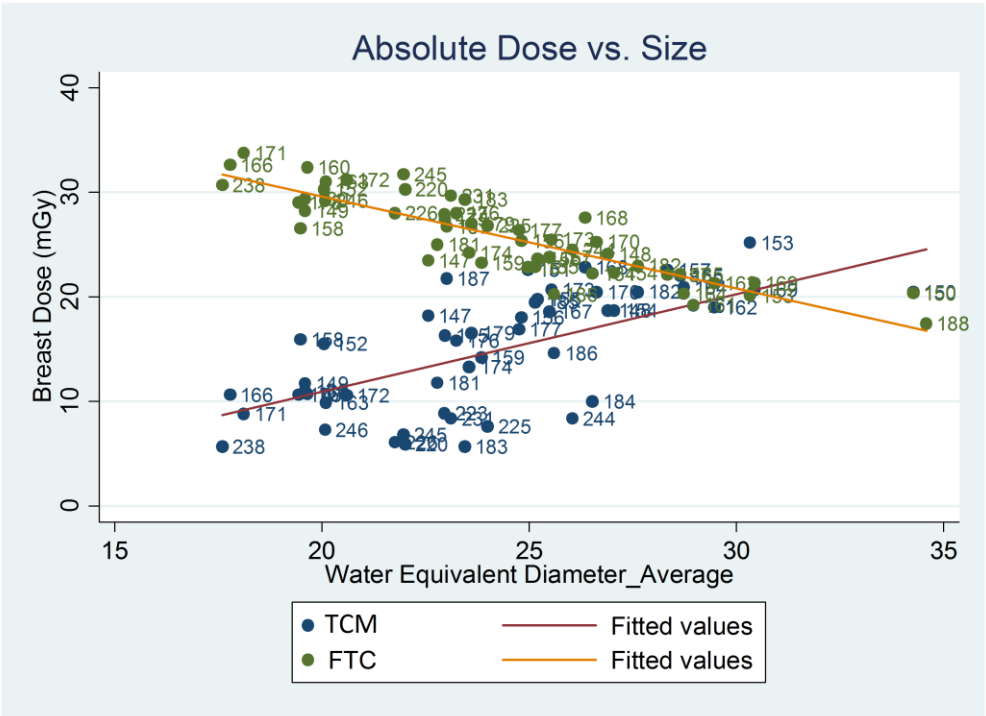

Figure 9-18 Breast doses resulting from fixed and modulated tube current simulations versus average water equivalent diameter. TCM and FTC are completely overlapping for patient numbers 150 and 188.

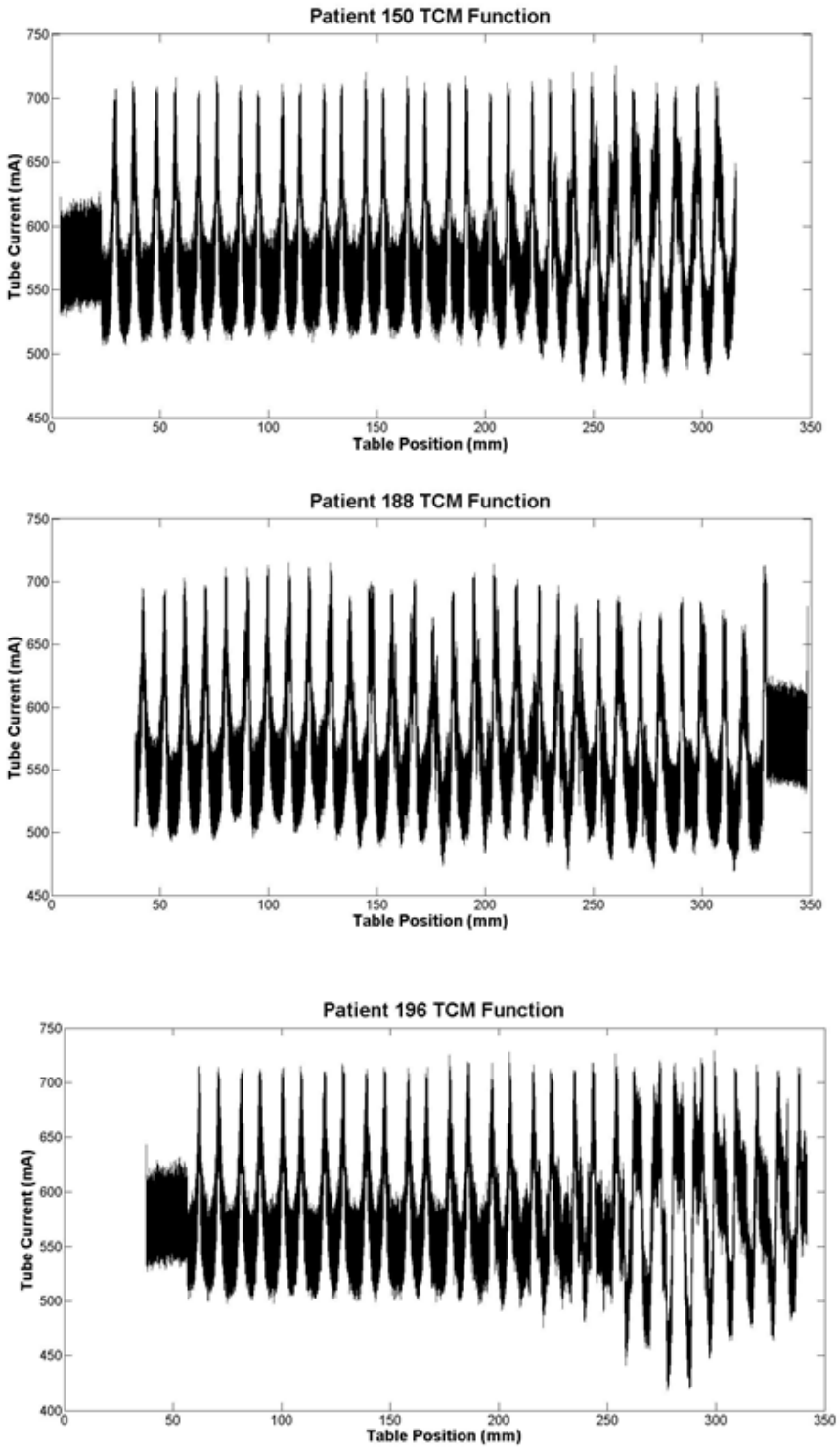

Figure 9-19 Illustration of TCM functions of patient numbers 150, 188, and 196; all three functions are examples of maxed out TCM function with little or no z-axis tube current modulation.

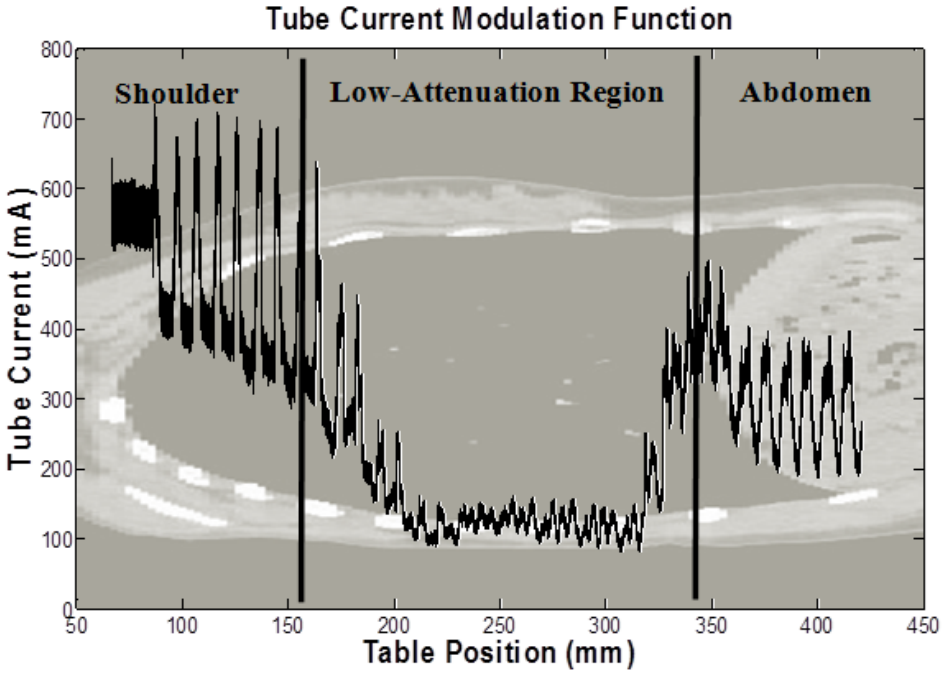

Figure 9-20 An example of a typical thoracic TCM function.

Next, the relationship between normalized organ doses by regional $CTDI_{vol}$, $CTDI_{vol,regional}$, and different size metrics was examined to investigate the appropriateness of attenuation-based metrics, D_W and D_{Wa}, over *effective diameter*. As expected for the abdominal organs, no significant improvement was observed once D_W and D_{Wa} were used as patient size metrics. Furthermore, no statistically significant difference was observed between global, regional and organ-specific measures of a size metric. Similarly, for normalized organ dose by $CTDI_{vol,organ}$, no statistically significant improvement was observed with attenuation-based size metrics for the abdominal organs. Additionally, no statistically significant improvement was observed when comparing results from $CTDI_{vol,regional}$ and $CTDI_{vol,organ}$, as also shown in previous chapter.

For lungs and for breasts, even though the hypothesis was an improvement in the exponential relationship between normalized dose and size metric, the improvements were only statistically significant in lungs for regional $D_{W,LowATT}$ and regional $CTDI_{vol,LowAtt}$.

For four out of five organs, the R^2 value increased; however, the increase in R^2 was only statistically significant for lung dose once regional $D_{W,LowATT}$ and regional $CTDI_{vol,LowAtt}$ were used. These results suggest that there is no difference between investigated size metrics except for regional $D_{W,LowATT}$ and *effective diameter*.

To understand these results, Spearman's correlation was used to investigate the relationship among the investigated three size metrics, *effective diameter*, D_w, and D_{wa}. Spearman's correlation is used to identify and test the strength of a linear relationship between two sets of data. For each organ, Spearman's rank correlation test was performed to calculate the correlation coefficient and its significance among different size metrics. Figures 9-21 through 9-23 show the results of the Spearman's rank correlation test for kidneys, lungs, and breasts.

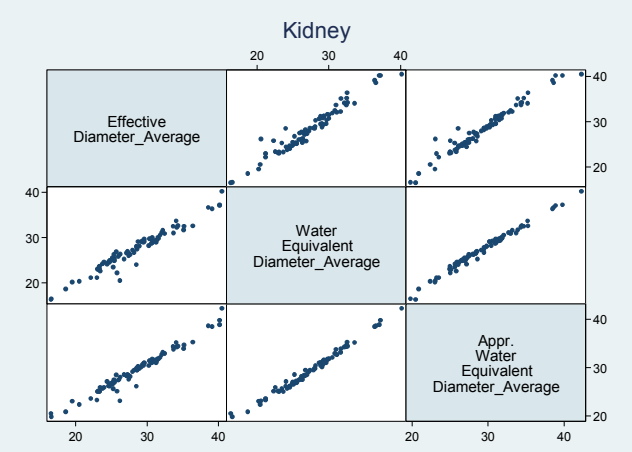

Size Metric	Effective Dia.		D_W	
	Rho	Sig.	Rho	Sig.
D_W	0.96	0.000	1	0.000
D_{Wa}	0.97	0.000	0.99	0.000

Figure 9-21 Spearman's correlations and significance levels between different global average size metrics for kidneys. Similar results were seen for regional and organ-specific size metrics.

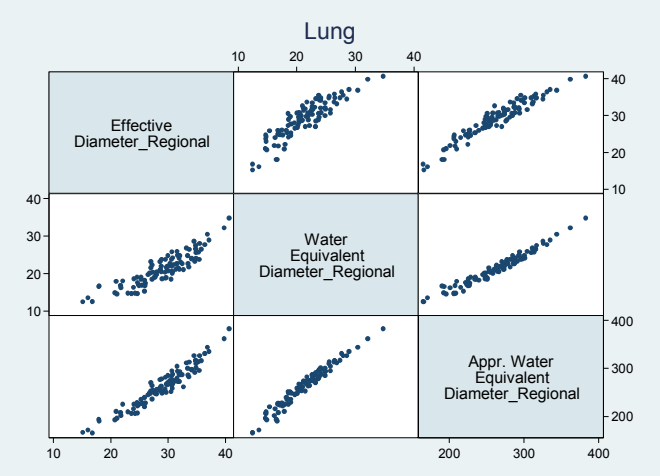

Size Metric	Effective Dia.		D_W	
	Rho	Sig.	Rho	Sig.
D_W	0.89	0.000	1	0.000
D_{Wa}	0.95	0.000	0.98	0.000

Figure 9-22 Spearman's correlations and significance levels between different global average size metrics for lungs. Similar results were seen for regional and organ-specific size metrics.

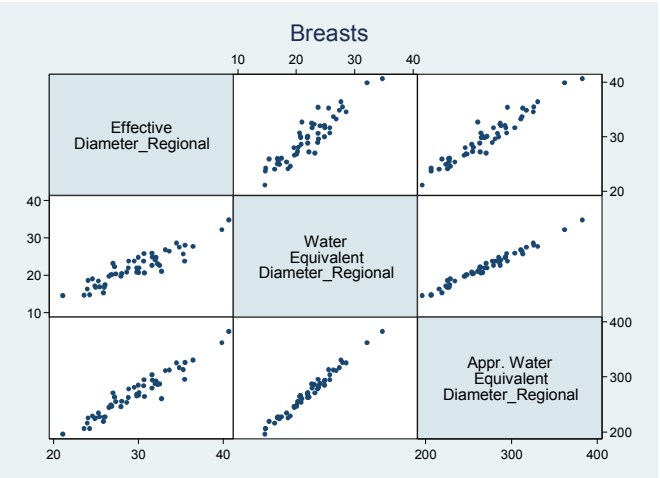

Size Metric	Effective Dia.		D_W	
	Rho	Sig.	Rho	Sig.
D_W	0.90	0.000	1	0.000
D_{Wa}	0.95	0.000	0.98	0.000

Figure 9-23 Spearman's correlations and significance levels between different global average size metrics for breasts. Similar results were seen for regional and organ-specific size metrics.

For lungs, the Spearman's correlation was run to determine the relationship between 101 values of *effective diameter*, D_w, and D_{wa}. There was a strong positive linear correlation among all three size metrics with the smallest r value of 0.89 and $p<0.0001$ between regional *effective diameter* and $D_{W,LowAtt}$. Despite this strong linear correlation (89% correlation) between effective diameter and $D_{W,LowAtt}$, a statistically significant improvement in correlation between normalized lung dose by $CTDI_{vol,LowAtt}$ and $D_{W,LowAtt}$ was observed compared to *effective diameter*.

A scatter plot with identity line demonstrating regional effective diameter versus $D_{W,LowAtt}$ was used to understand the relationship between these size metrics and the importance of the low attenuating region within thorax (Figure 9-24). As illustrated, effective diameter overestimates water equivalent diameter across all patients. However, there seem to be a varying degree of overestimation with respect to patient size. Smaller patients and larger, obese patients seem to be closer to the identity line than average sized patients with average body habitus. In Figure 9-24, the obese patient, patient number 188, has a larger ratio of fat/muscle to lung tissue and effective diameter overestimates $D_{W,LowAtt}$ only by 5 cm. For the more average looking patient, patient 210, effective diameter overestimates $D_{W,LowAtt}$ by 13 cm. For the pediatric patient, patient 228, the overestimation is only by 4.5 cm. This varying degree of difference between effective diameter and D_W is more profound once the D_W is averaged over the low attenuating region compared to the global average, which decreases the difference between effective diameter and water equivalent diameter. Figure 9-25 shows the difference between effective diameter and D_W for these three patients, nicely illustrating the large difference in these size metrics for patient 210, while demonstrating a smaller difference for the pediatric and obese patient. It is also evident that a regionally measured D_W will enhance the difference between effective diameter and D_W. Figure 9-26 shows the difference between global, regional and lung-specific measures of

effective diameter and D_W, with the largest difference observed between regional effective diameter and regional D_W.

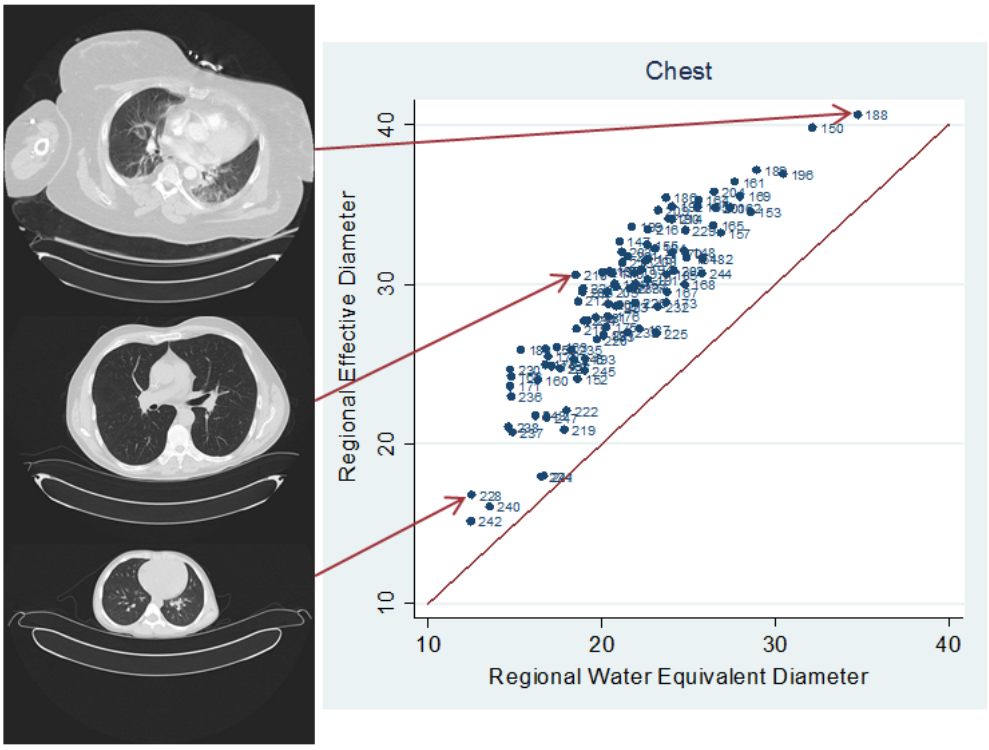

Figure 9-2 Scatter plot of Regional ED versus Regional WED in chest along with the identity line illustrates ED overestimating wed.

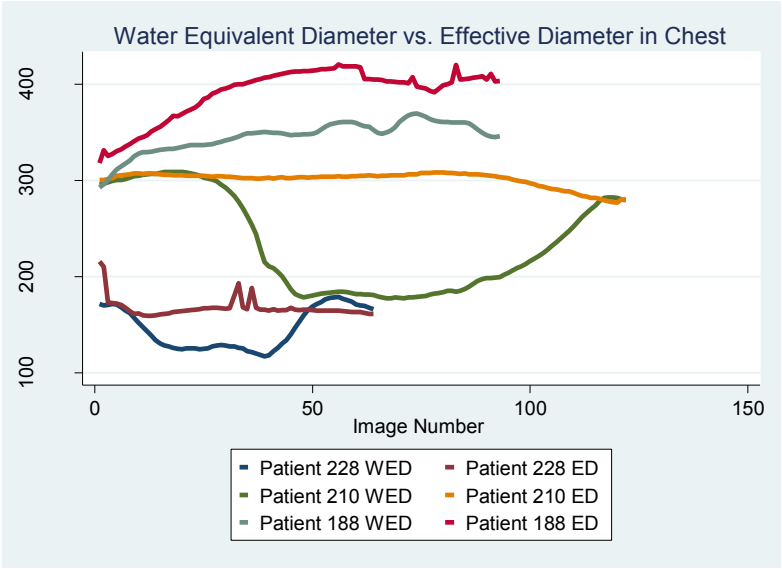

Figure 9-25 Differences between ED and WED in chest shown for three different patients: pediatric, average and obese.

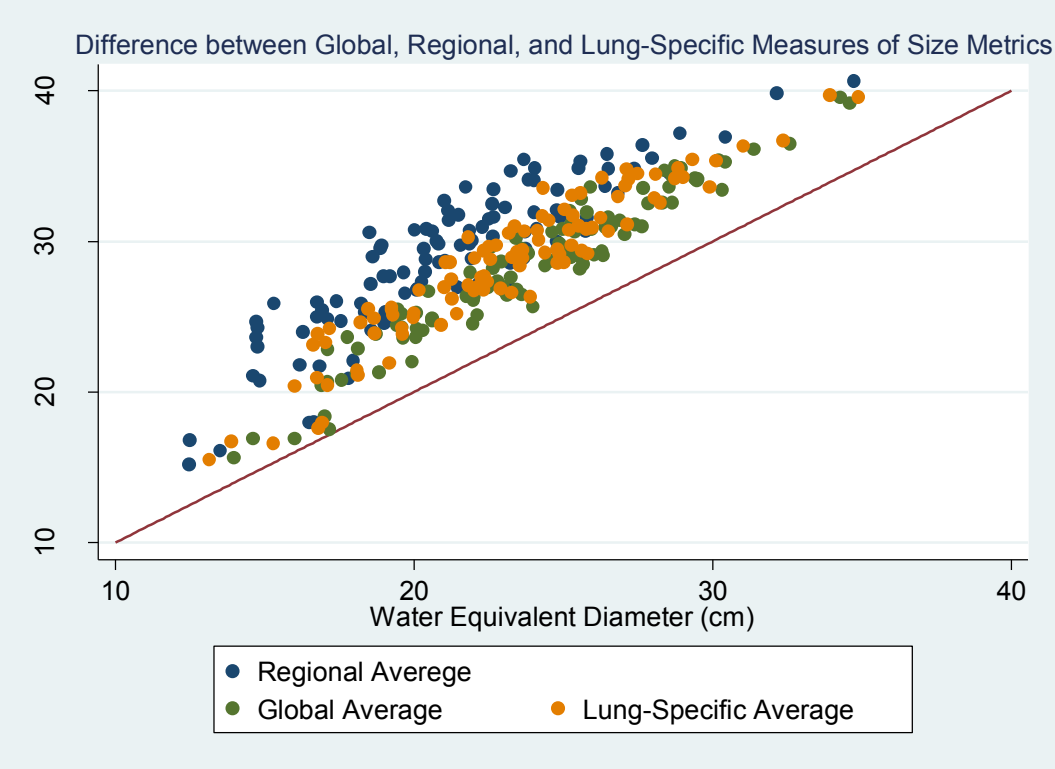

Figure 9-26 Differences between ED and WED in chest shown for three differently average size metrics, global average, regional average and lung-specific average.

To understand the relationship between effective diameter and D_W in the abdominal regions, similar plots were generated and examined. Figure 9-27 shows a scatter plot with identity line for effective diameter and D_W in the abdomen region. Each data point is very close to the identity line, indicating minor differences between effective diameter and D_W. Additionally, Figure 9-28 shows effective diameter and D_W as a function of image number for three different patient sizes, from pediatric to obese, illustrating once again minor differences between effective diameter and D_W. Figure 9-29 demonstrates the scatter plot with identity line for global, regional, and in this case, kidney-specific effective diameter and D_W, with minor differences between different regions.

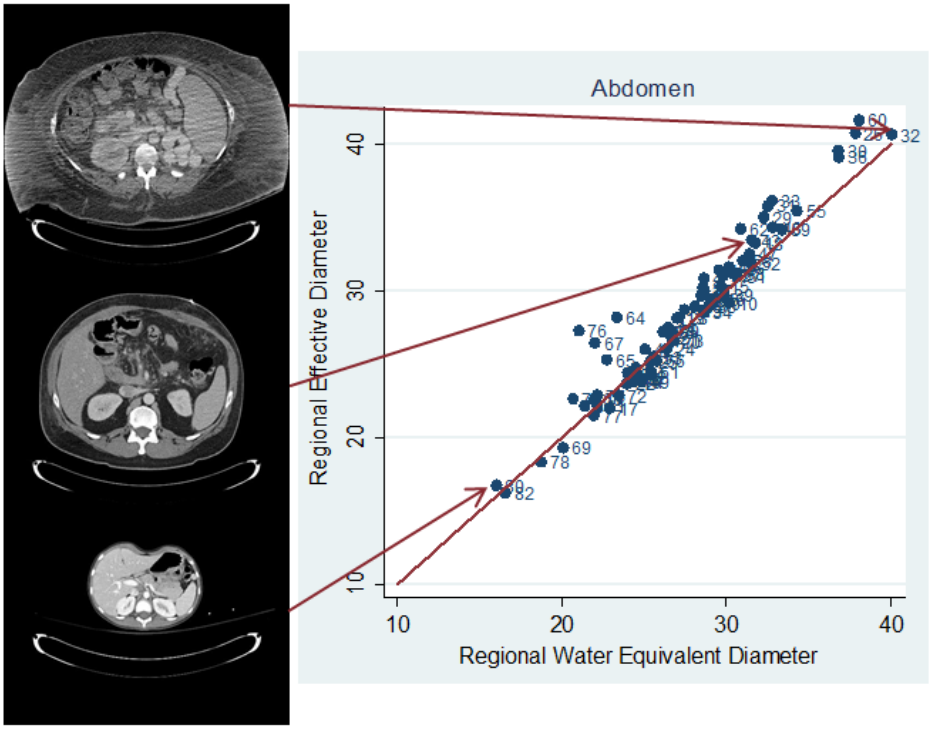

Figure 9-27 Scatter plot of Regional ED versus Regional WED in abdomen along with the identity line illustrates ED overestimating wed.

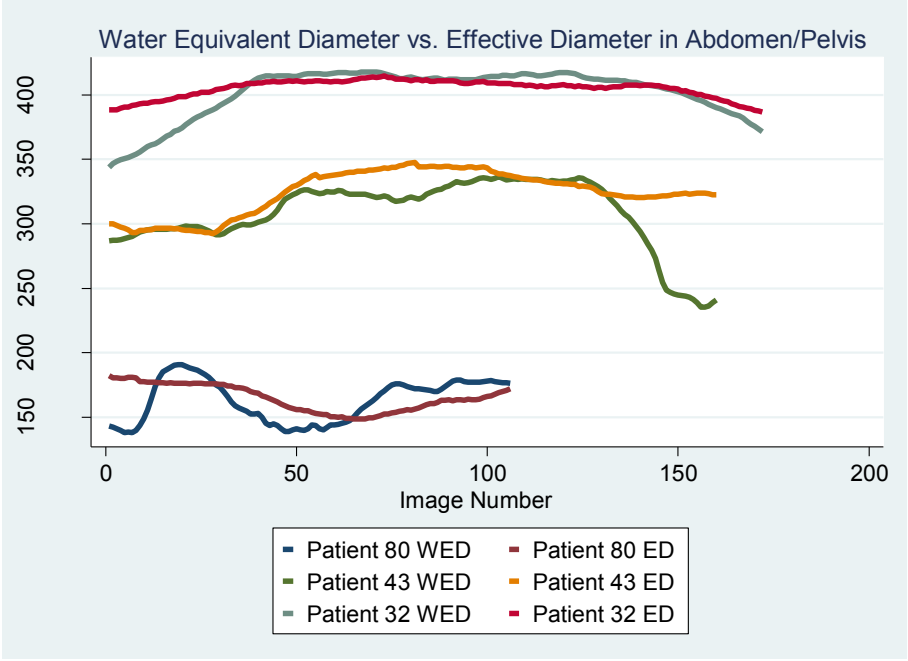

Figure 9-28 Differences between ED and WED in abdomen shown for three different patients: pediatric, average and obese.

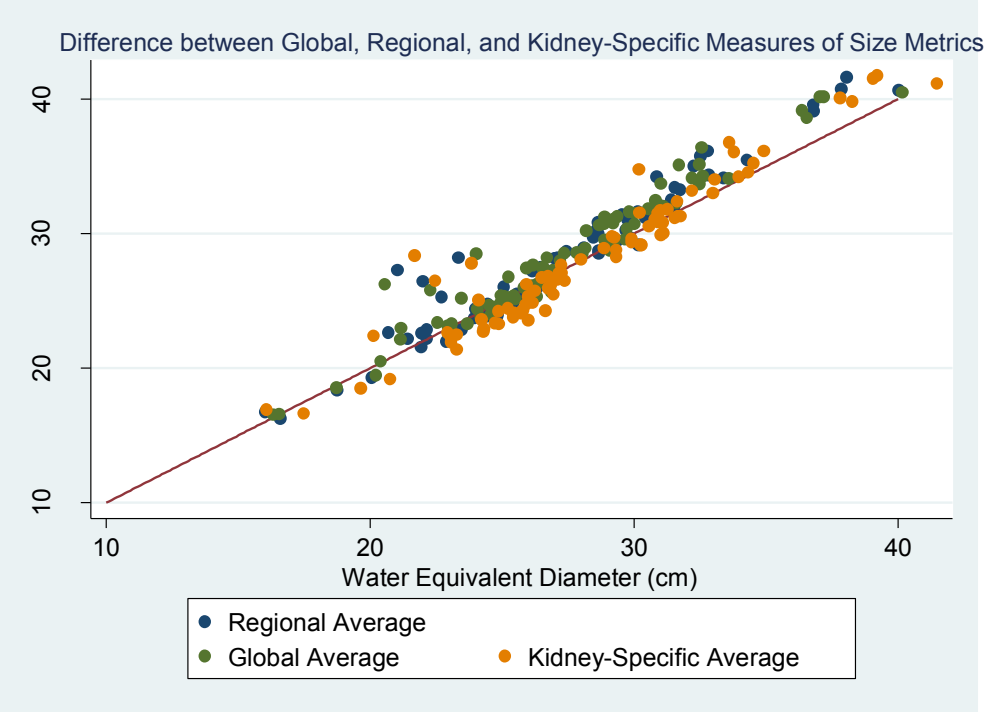

Figure 9-29 Differences between ED and WED in abdomen shown for three differently average size metrics, global average, regional average and kidney-specific average.

For approximated water equivalent diameter, D_{Wa}, no statistically significant difference was observed compared to effective diameter and waster equivalent diameter D_W. Figures 9-30 and 9-31 show the difference between D_{Wa} and D_W in the thorax and abdomen, respectively. In the thorax D_{Wa}, overestimates D_{Wa} in a linear fashion, while in abdomen the overestimation is not as drastic as it is in thorax. These results are expected due to D_{Wa} originating from all pixel values within the image including air, table, and any other objects within the scan field of view.

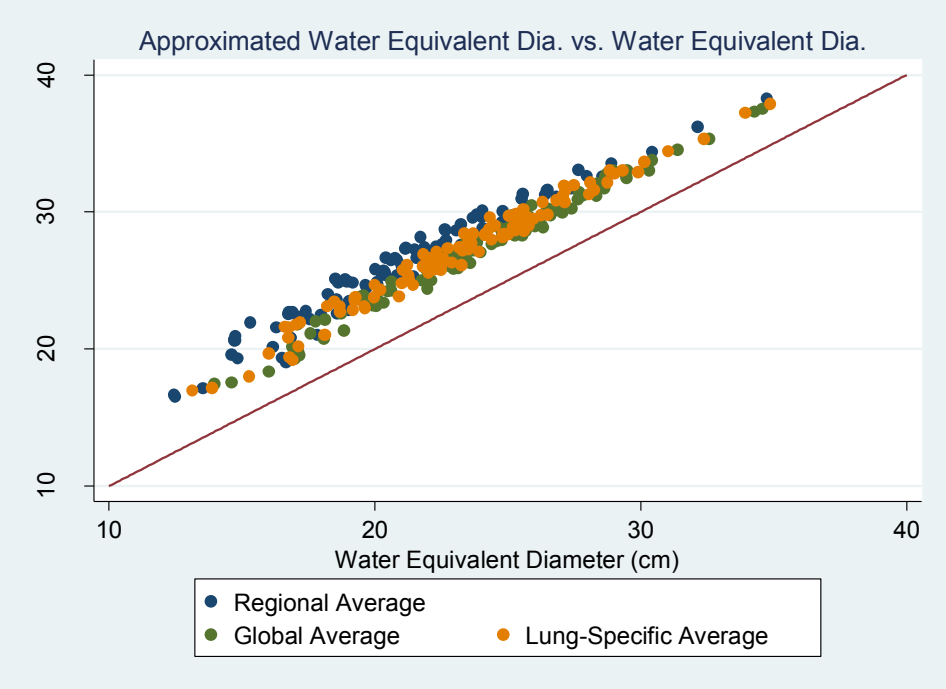

Figure 9-30 Differences between AWED and WED shown for three differently average size metrics, global average, regional average and lung-specific average.

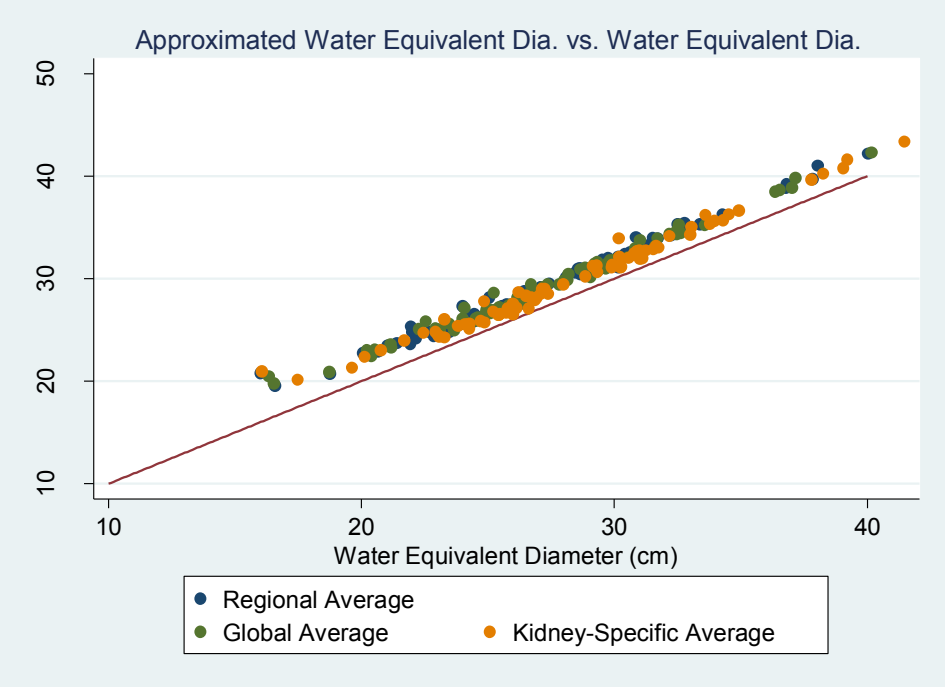

Figure 9-31 Differences between ED and WED shown for three differently average size metrics, global average, regional average and kidney-specific average.

9.5 CONCLUSION

As previously observed, in tube current modulated CT scans organ dose increases with patient size. However, for larger patients a transition between TCM and FTC occurs once the peak exposure exceeds system's limit. This transition from TCM to FTC results in a decrease in dose with increased patient size, which is observed in FTC CT scans. This behavior of organ dose was observed for all five investigated organs and size metrics. As shown in the discussion, this transition can be avoided by adjusting scan parameters such as rotation time and pitch. In Siemens Sensation 64, in case of a maxed out tube current, the operator is informed and suggested to adjust kVp, rotation time or pitch. However, the option of performing the exam without adjusting the suggested parameters is also available. Even though a decrease in dose is always preferred, in this case the decrease in dose can result in images with no diagnostic capabilities, especially for larger patients, and therefore result in repetition of the scan.

Although the value of R^2 increased for almost all five organs once D_W and D_{Wa} were used, no statistically significant difference was observed between effective diameter and attenuation-based size metric in the abdomen. The only statistically significant improvement was observed for normalized lung dose by regional $CTDI_{vol,LowAtt}$ and regional $D_{W,LowAtt}$ compared to effective diameter; 70% of the variation of size is explained by D_W, while only 43% is explained by *effective diameter*.

Overall, for abdominal organs, any of the size metrics discussed in this chapter (*effective diameter,* D_w*, and* D_{wa}) can be used as a predictor of dose. However, water equivalent diameter D_w showed improved statistically significant correlations with normalized lung dose by regional $CTDI_{vol}$ compared to D_{wa} and *effective diameter*. As a single size metric robust enough to be

used in any anatomical region, i.e. chest, abdomen, and pelvis, D_w is recommended. As shown in this study, the value of D_w varies significantly along the patient's long axis. Hence, if an averaged value of D_w is used as a size descriptor, it needs to reflect the averaged value of the region for which organ dose is estimated.

As the results show, the correlation between D_w and normalized organ dose is not perfect but improved compared to the previously used metric, effective diameter. Attenuation-based size metrics are capable of not only describing a patient's attenuation but also represent size in some fashion, hence the linear relationship between effective diameter and D_w.

However, these metrics are not capable of representing a patient's shape, which significantly affects the x-y modulation of the TCM function. Specifically, the x-y modulation for a patient with a very circular shape would be very different from one with a very elliptical shape. A possible improvement to an attenuation-based size metric in representing the patient's shape could be an angular-based attenuation metric in addition to the longitudinal-based attenuation metric used in this study. Additionally, instead of trying to find a correlation between organ dose and size from a CT examination using average dose to an identified organ and averaged D_w from a section of similar attenuating properties, detailed information about the variation of dose based on D_w at every single table location and gantry angle can be used to assess dose to not only directly exposed, but also partially exposed organs within a scan.

CHAPTER 10: GENERALIZED LINEAR MODEL FOR ESTIMATING ORGAN DOSE FROM TUBE CURRENT MODULATED CT SCANS

The purpose of this chapter is to generate and evaluate dose predictive models based on a generalized linear model to estimate organ dose from tube current modulated CT scans. Two different approaches will be investigated in generating dose predictive models: a) using the conventional exponential relationship between *normalized organ dose* and *size*, for which size and regional information of TCM, explored in chapters 8 and 9, are essential components, and b) using the exponential relationship between *actual organ dose* and *size* while using $CTDI_{vol}$ as a predictor rather than a normalization quantity. Additionally, the significance of using *categorical variables* such as scanner model, organ, and patient cohort (adults vs. pediatrics), will be investigated as possible predictors of organ dose.

10.1 INTRODUCTION

There has been a tremendous effort in estimating organ dose from fixed tube current CT scans with positive outcomes such as the CT Dosimetry package ImPACT [38] and Size-Specific Dose Estimates (SSDE), published by AAPM Task Group 204 [49]. However, there has been little to no work on dose estimation from tube current modulated CT scans, which in fact are the majority of all performed CT examinations in the clinic. As an example, every single body protocol (chest, abdomen, and pelvic) at the UCLA medical center makes use of Siemens Tube Current Modulation feature, Care Dose 4D, except for CT neuro-perfusion scans. With TCM widely implemented and used as a dose reduction technique, it is very important to be able to quantify and assess dose from these types of scans.

Currently used dose metrics to assess dose from TCM exams are the conventional $CTDI_{vol}$, ImPACT, and recently published coefficients by TG 204, the Size Specific Dose Estimates (SSDE) which are scanner-independent. As also described by Turner et al. [50, 51], in fixed tube current CT scans, $CTDI_{vol}$ can be used to normalize out differences among scanners, such as spectra and filtration. This capability was used in TG 204 report to generate scanner-independent and patient size-dependent dose coefficients for estimating dose from fixed tube current CT exam. This was possible because of the original assumption of constant tube current across fixed tube current CT scans. In TCM scans, this assumption no longer holds because of varying tube current across the scan length. Additionally, the algorithm by which tube current is modulated, in terms of implementation and optimization variables, is not constant across CT manufacturers and models. That is, due to differences in TCM algorithms, the same patient scanned under two CT scanners from different manufacturers will be subject to different modulating tube currents and hence different TCM functions. A normalization factor which can take into account varying tube current along a single scan was introduced in Chapter 8. Figure 10-1 shows examples of fixed and modulated tube current exams in 64 slice Siemens Sensation scanners.

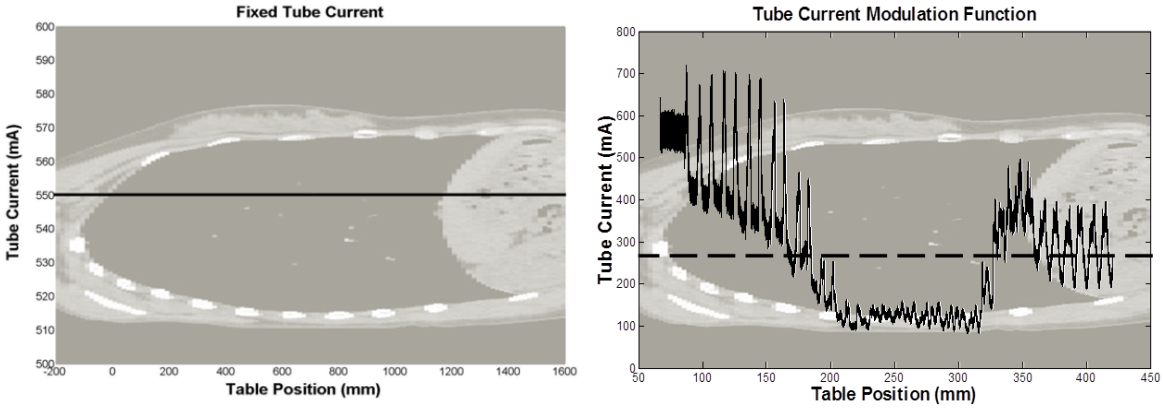

Figure 10-1 Left image illustrates an example of fixed tube current exam with constant mA throughout the entire exam length. Right, demonstrates a chest-specific tube current modulated exam with varying tube current across the scan length.

As shown in Chapter 8, regional tube current information, shown in Figure 10-2, can be used to account for varying tube current in TCM scans when the conventional exponential relationship between normalized organ dose and size is used (Eq. 10-1). Regional and organ-specific $CTDI_{vol}$ were demonstrated to be appropriate normalization factors for TCM scans compared to scanner-reported global $CTDI_{vol}$; i.e. they can be used (along with an appropriate size metric) to generate organ-specific regression equations for organ dose estimation in TCM.

However, this utility of regional and organ-specific $CTDI_{vol}$ was only validated for Siemens data. As described in Chapter 3, TCM algorithms across CT manufacturers are different from each other in not only implementation, but also optimization variables used to achieve similar image quality across a single scan and across patients. Therefore, the utility of regional $CTDI_{vol}$ needs to be confirmed across other CT manufacturers with different TCM algorithms.

$$Normalized\ organ\ dose\ Dose = Organ\ Dose/CTDI_{vol} = Ae^{-B \times Size} \qquad \textbf{Eq. 10-1}$$

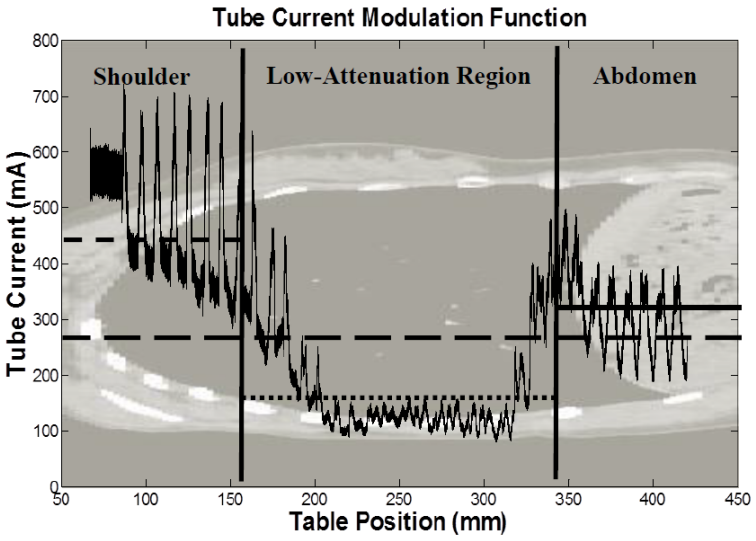

Figure 10-2 Variation of tube current along thorax, illustrating three differently attenuating regions, which results in differently modulating tube current.

The purpose of this chapter is to utilize results from Chapters 8 and 9 regarding normalization factors and size metrics for TCM scans to develop a dose predictive model capable of estimating organ dose from tube current modulated CT scans. This is done using a) the conventional relationship between *normalized organ dose* and size metric as described in Eq. 10-1, and b) using $CTDI_{vol}$ as a predictor within the constructed model rather than a normalization quantity and explore a possible predictive model with actual organ dose as the response variable. Rewriting Eq. 10-1 with respect to organ dose results in Eq. 10-2, which can be used to build a model to predict the actual unknown quantity, which is organ dose.

$$Organ\ Dose = CTDI_{vol} \times Ae^{-B \times Size} \qquad \textbf{Eq. 10-2}$$

In this chapter we will explore the utility of each model as well as exploring the level of specificity or generality used to develop each model. That is, the utility of models that are scanner-specific vs. scanner-independent as well as organ-specific vs. organ-independent and combinations (scanner-and organ-specific vs. scanner-and organ-independent) will be evaluated. This will be done by constructing different models based on scanners and organs and then testing these models against each other to determine the level of accuracy from each approach.

10.2 METHODS

10.2.1 Voxelized Models

As described in Chapter 5, voxelized models were generated from axial CT images acquired on three different CT scanner manufacturers at four different institutions, UCLA, MD Anderson in Houston, TX, UT Southwestern Medical Center, and Arkansas Children's Hospital. The Institutional Review Board (IRB) at each institution approved the collection of the images and raw projection data. The latter data, raw projections, was only available from scans acquired at

UCLA and so only those scans (from Siemens scanners) were used to extract detailed tube current information from raw projection data. Along with patient images, patient dose reports were also collected. Table 10-1 summarizes collected patient images from different CT scanner manufacturer, CT protocols, and genders. A total of 331 patients were collected for use in this study.

Patient Cohort	Siemens (Sensation 64)		GE (LightSpeed VCT)		Toshiba (Aquilion 64)	
	Abdomen/Pelvis	Thorax	Abdomen/Pelvis	Thorax	Abdomen/Pelvis	Thorax
Male	30	29	10	10	15	17
Female	32	42	9	9	11	24
Pediatric	20	29	5	9	13	18
Total	181		52		98	

Table 10-1 An overview of collected chest and abdomen/pelvic patient studies from different scanners.

Patients scanned on Siemens and GE scanners were reconstructed with 500 mm field of view to ensure body coverage throughout the entire scan. All adult patients scanned on Toshiba scanner from UT Southwestern Medical Center were either reconstructed at 500 or 400 mm FOV only minimal or no cutoff of anatomy. All pediatric patients scanned on Toshiba at Arkansas Children's Hospital were collected retrospectively and with no possibility of reconstructing with a larger FOV. These pediatric patient images were reconstructed using 200 mm to 400 mm FOV which resulted in some cases having some missing anatomy (mostly fat and tissue) but none had cutoffs on regions of interest, i.e. organs for which dose simulations were performed.

Liver, spleen, and kidneys were identified and countered in all abdomen/pelvis studies. Lungs and glandular breasts tissues were contoured in all thorax studies, with the latter organ being segmented only in female patients. Segmented images were used to generate voxelized models as

described in Chapter 5. Overall, 331 voxelized models, including abdomen/pelvis and chest models, were created for this study.

10.2.2 Monte Carlo Simulations

For all voxelized models acquired on Siemens Sensation 64, raw projection data were used to extract detailed TCM information for TCM simulations. For all the other models, tube current information extracted from image data, which represents the z-axis-only modulation part of the TCM function, was used for TCM simulations. This approximation method of TCM was described in details in Chapter 7.

The Monte Carlo simulation package described in Chapter 4 and validated in Chapter 6 was used to simulate dose to segmented organs from tube current modulated CT scans using collected detailed TCM functions for Siemens models and approximated TCM functions for GE and Toshiba generated models.

10.2.3 Size Metrics

Collected axial CT images were used to generate global and regional size metrics, effective diameter and water equivalent diameter on a slice basis. As shown in Chapter 9, in abdominal regions there is no significant difference between effective diameter and attenuation-based metrics. However, a statistically significant difference between these metrics was observed in the thoracic regions, especially for estimation of dose to low attenuating lungs. In particular, regional water equivalent diameter showed a statistically significant improvement over effective diameter for estimating dose to lungs. Hence, regional water equivalent diameter was used for creating predictive models in this chapter.

10.2.4 Statistical Analysis

Monte Carlo simulations were performed on all 331 patients and overall 714 organ doses were estimated. Patients were stratified by organ, gender, and scanner using their calculated water equivalent diameter into a training set of 60% (200 patients and 433 observations) and test set of 40% (131 patients and 281 observations) of all patients. The stratification was performed using size metric, water equivalent diameter, to ensure a distribution of different sizes within each training and test set.

The 40/60 division of the data is entirely empirical; however, as a rule of thumb, for every predictor in the model, at least 10 patients are recommended for good statistics. That said, the smallest number of patients within the training set are GE models with 30 independent data points and 67 observations, i.e., maximum of three predictors can be utilized in building a predictive dose model for this specific scanner.

The statistical method used for creating models is the Generalized Linear Model, which as the name suggests, is a generalization of linear regression models. One of the assumptions of linear regression is the normal distribution of the response variable. however, under Generalized Linear Models, the normality assumption can be violated using a *link function*, which relates the linear model to the response variable. The link function serves as a surrogate for the actual response variable (e.g organ dose) and is a function of the response variable (such as log (organ dose) or a multivariate function predicting organ dose), which varies linearly with the predictors rather than the assumption that the response variable itself varies linearly.

In a linear model, the response variable Y can be described using continuous predictor variables x's, coefficients β's, constant α, and independent errors ε:

$$Y_i = \alpha + \beta_1 x_{1i} + \beta_1 x_{1i} + \cdots + \varepsilon_i \qquad \textbf{Eq. 10-3}$$

$$\varepsilon_i \sim \mathcal{N}(0, \sigma^2) \qquad \textbf{Eq. 10-4}$$

Using Generalized Linear Models, the response variable Y can have a distribution other than normal, known as *exponential family of distributions*. Hence, the relationship between response variable and predictors does not need to be linear as shown in Eq. 10-3. Instead, transformation using *link functions* are used to describe the relationship:

$$g(Y_i) = \alpha + \beta_1 x_{1i} + \beta_1 x_{1i} + \cdots + \varepsilon_i \qquad \textbf{Eq. 10-5}$$

where g is the *link function*. In the exponential relationship between organ dose and size, the link function is the logarithm of the response variable, i.e. normalized organ dose or absolute dose.

10.2.4.a Normalized Organ Dose as the Response Variable

With regards to this work, the response variable is the organ dose normalized by $CTDI_{vol}$ (either regional or global) and the predictors are size metric and several categorical variables, also known as "dummy" variables, such as scanner manufacturers (Siemens, Toshiba or GE), exam type (Chest or Abd/Pel), organs (lung, breast, liver, kidney, spleen), and patient categories (adults versus pediatrics). Categorical variables are variables that can only take one of a limited number of values. For instance, exam type abdomen/pelvis can either take on the value 1 for indicating the exam type to be abdomen/pelvis or it can be 0 for being something else, e.g. a chest exam.

As previously known and shown by TG 204, the relationship between normalized dose and size is an exponential relationship:

$$Normalized\ organ\ dose\ Dose = Organ\ Dose/CTDI_{vol} = Ae^{-B \times Size} \quad \textbf{Eq. 10-6}$$

The link function used in this case to transform the response variable (normalized dose) to generate a linear relationship between the link function and the predictors, is the natural log (Ln) of the response function:

$$Ln(Normalized\ Dose) = Ln(A) - (B \times Size) \quad \textbf{Eq. 10-7}$$

By adding categorical variables, "dummy" variables, Eq. 10-7 can be rewritten as:

$$Ln(Normalized\ Dose) = \alpha + \{(\beta_1 \times Size) + (\beta_2 \times Scanner) + (\beta_3 \times Organ) + \cdots\} \quad \textbf{Eq. 10-8}$$

In case any of the categorical variables, which are all binary, take on the value zero, the variable is eliminated from the model.

10.2.4.b Organ Dose as the Response Variable

In the second section of this study, the response variable will be changed to the actual organ dose rather than its normalized version and $CTDI_{vol}$ will be used as a predictor in the model rather than used to normalize organ doses before model creation. The investigated predictive model will take the form:

$$Ln(Organ\ Dose) = \alpha + \{(\beta_1 \times CTDI_{vol}) + (\beta_2 \times Size)\} \quad \textbf{Eq. 10-9}$$

In case of additional predictors such as categorical variables Eq. 10-9 will change to:

$$Ln(Organ\ Dose) = \alpha + \{(\beta_1 \times CTDI_{vol}) + (\beta_2 \times Size) + (\beta_2 \times Scanner) + (\beta_2 \times Organ) + \cdots\} \quad \textbf{Eq. 10-10}$$

Created predictive models will be evaluated based on F-statistic and the p-value associated with it, R^2 (the coefficient of determination), and adjusted R^2.

It is reasonable to assume that both methods, one using $CTDI_{vol}$ as the normalization factor and the other as the predictor, will result in very similar outcomes in terms of their performance on estimating dose to the test set; however, in the latter approach only one variable, the dependent variable (organ dose), is estimated while $CTDI_{vol}$ is used in the prediction process, whereas in the first approach, $CTDI_{vol}$ is predicted along with organ dose. Very similar results are expected with both approaches.

10.2.4.c Selection of Predictors

Selection of predictors in building a model is an important step towards building a reliable predictive model. If too many variables are included in the model, including those unrelated to the response variable, the model is said to be *overfitted*; this results in the underestimation of the prediction errors when the model is used on a new data set. On the other hand, if too few variables are included in the model, including those able to explain the response variable, the model is said to be *underfitted*; this results in a biased prediction of new data set.

One way to decide which predictors to include in the model is to investigate the correlations and significance of correlations among independent and dependent variables, in this case, the response and the predictors. When generating a model using statistical software such as STATA, the regression analysis includes two-tailed p-values used in testing the null hypothesis that the coefficient predicted for a predictor is 0. This p-value can be used to decide if a predictor is statistically significant in predicting the response variable.

10.2.5 Outline of the Statistical Analysis

In the first section, the analysis will start with exploring the conventional relationship between normalized organ dose and size metric using two combinations of normalizing values and size metrics: (a) a regional combination ($CTDI_{vol,regional}$ and regional water equivalent diameter) and (b) a global combination ($CTDI_{vol,Global}$ and average effective diameter). For each combination, the predictive functions will be built using organ- and scanner-specific models, organ-specific models across scanners, scanner-specific models across organs, and pooled data across scanners and organs. After exploring the relationship between normalized organ dose and size, regional and attenuation information will be used along with appropriate categorical predictors to improve upon each model. Next, each model will be tested using the test set consisting of 40% of all collected 331 patients and compared to actual Monte Carlo simulated organ doses and to each other using mean and standard deviation percentages along with a t-test to test the null hypothesis that methods are indeed different from Monte Carlo simulated organ doses.

In the second section, the relationship between organ dose as response variable and size and $CTDI_{vol}$ as predictors will be explored using both regional and global information. Generated models will be once again tested using the test set and compared to each other and to the models from the previous section using normalized dose as the response variable. The most accurate model will be determined and compared to other existing CT dose metrics in Chapter 11. Table 10-2 highlights the main models, their definitions, and their response variables. All data in this chapter are analyzed using Stata 12.0 (StataCorp; College Station, TX).

Model		Definition	Response Variable	Size Metric	Predictors
Section I	Organ- and Scanner-Specific	Built for each organ and scanner, i.e. Liver-specific, Siemens-specific model	Normalized dose by $CTDI_{vol,Global}$	Effective Diameter	None
			Normalized dose by $CTDI_{vol,Regional}$	Water Equivalent Diameter	Dummy Variables, i.e. Gender, Exam Type, Interaction term
	Organ-Specific	Built for each organ across all scanners, i.e. liver-specific model	Normalized dose by $CTDI_{vol,Global}$	Effective Diameter	None
			Normalized dose by $CTDI_{vol,Regional}$	Water Equivalent Diameter	Dummy Variables, i.e. Scanner, Gender, Interaction term
	Scanner-Specific	Built for each scanner across all organs, i.e. Siemens-specific model	Normalized dose by $CTDI_{vol,Global}$	Effective Diameter	None
			Normalized dose by $CTDI_{vol,Regional}$	Water Equivalent Diameter	Dummy Variables, i.e. Organ, Gender, Interaction term
	Pooled	Built across all organs and all scanners	Normalized dose by $CTDI_{vol,Global}$	Effective Diameter	None
			Normalized dose by $CTDI_{vol,Regional}$	Water Equivalent Diameter	Dummy Variables, i.e. Organ, Scanner, Gender, Exam Type, Interaction term
Section II	Organ Dose-Regional	Built across all organs and all scanners	Organ Dose	Water Equivalent Diameter	$CTDI_{vol,Regional}$ + Dummy Variables, i.e. Organ, Scanner, Gender, Exam Type
	Organ Dose-Global	Built across all organs and all scanners		Water Equivalent Diameter	$CTDI_{vol,Global}$ + Dummy Variables, i.e. Organ, Scanner, Gender, Exam Type

Table 10-2 Overview of the generated models along with their definitions and response variables.

10.3 RESULTS

As mentioned in the methods, stratification based on size was used to separate data into training and test sets. The normality of regional water equivalent diameter was tested in both training and test sets. Figures 10-3 shows the histograms of size for both data sets. Patients are relatively normally distributed in both sets.

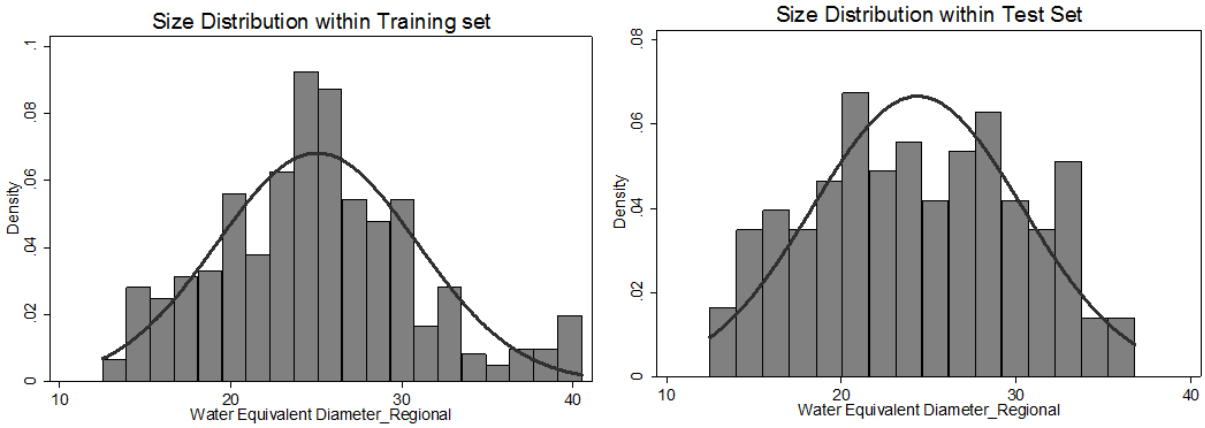

Figure 10-3 Normal distribution of size within the training and test set as a result of the stratification of data.

Next, the normality of the response variable has to be tested and in case of skewness in either extreme, a link function has to be identified, which can be used to relate the transformed response variable to predictors in a linear fashion. Figure 10-4 illustrates the normal distribution of the response variable for both normalized organ dose by global and regional $CTDI_{vol}$ values as well as their transformation using natural logarithm as the link function.

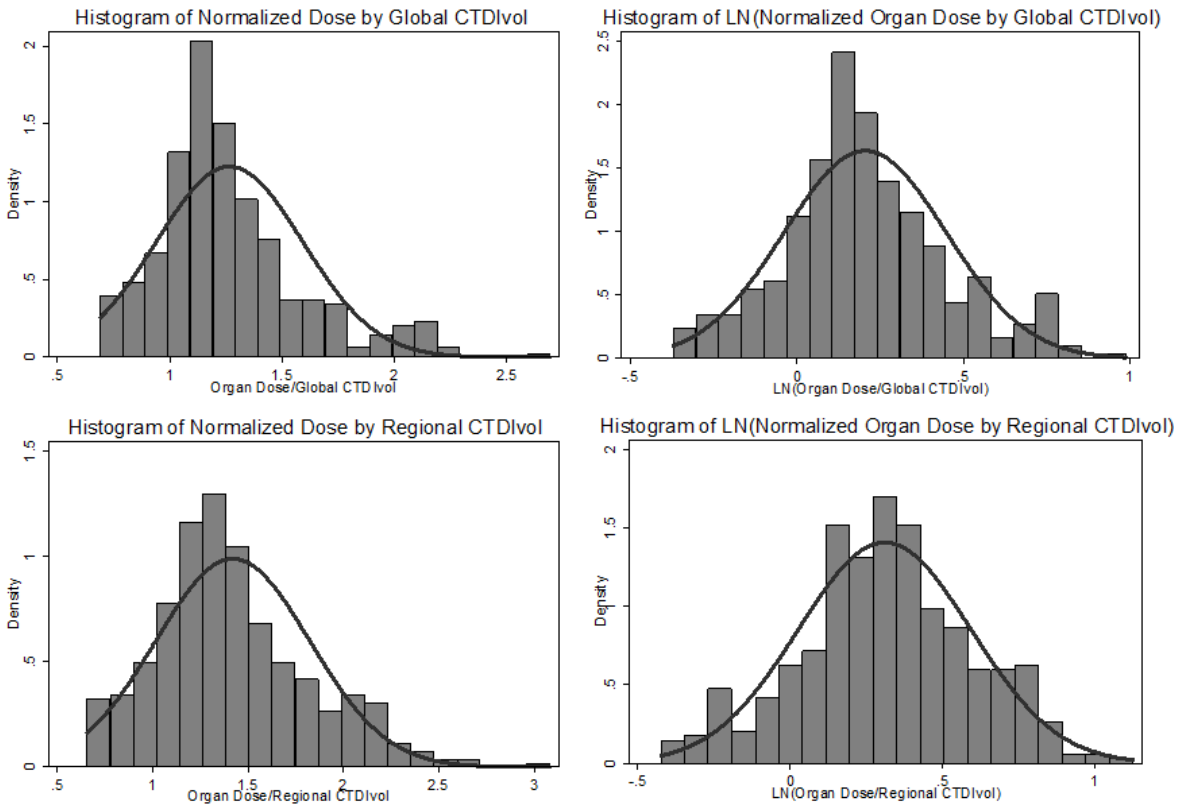

Figure 10-4 Transformation of the response variable, normalized organ dose, using natural logarithm to achieve normal distribution. Left charts both show the skewness of the data to the right and once transformed to ln(normalized dose) shown by the two right charts.

Once the normality of the response variable is confirmed, regression analysis can be performed to explore the relationship between the dependent and independent variables.

10.3.1 Normalized Organ Dose as the Response Variable

Following the normality test, the conventional relationship between normalized organ dose and size metric, as shown by Eq. 10-7, was investigated for global $CTDI_{vol,Global}$ and effective diameter versus regional $CTDI_{vol,Regional}$ and regional water equivalent diameter. Models, as described in the previous section, were created independently for each CT scanner manufacturer and organ and also for the entire training set, pooled data across scanners and organs. These scanner and organ-specific models along with the pooled data model are not using any categorical predictors as described in the previous section. The conventional relationship (Eq. 10-9) was first investigated before using "dummy" variables in the model (Eq. 10-10).

Table 10-3 summarizes the results for scanner and organ-specific models along with results for pooled data analysis. The table shows the R^2 values, usually used as a measure of the goodness of the fit and, the adjusted R^2 values, which penalizes the addition of the extraneous predictors to the model, the RMSE (Root Mean Square Error), which is the standard deviation of the error, and finally the A and B coefficients as described by Eq. 10-7. In addition to these parameters, attention was also paid to the F-statistics and its associated p-value which is used in testing the null hypothesis that all of the model coefficients, β's, are zero. The F-statistics is the mean square of regression divided by the mean square of residuals. In case the p-value is greater than 0.05, the null hypothesis that model's coefficients are zero is accepted. If this is the case in any of the models shown in Table 10-3 an asterisk is added to the R^2 value.

Table 10-3 Statistical measure of goodness of the linear fit for both forms of the predictive equations ($CTDI_{vol,\ regional}$ along with water equivalent diameter (WED) and global $CTDI_{vol}$ with effective diameter (ED)) for each scanner and for each organ as well as pooled combinations.

Organ		$Organ\ Dose/CTDI_{vol,Regional} = Ae^{-B\times WED}$				$Organ\ Dose/CTDI_{vol,Global} = Ae^{-B\times ED}$			
		Siemens	GE	Toshiba	Pooled	Siemens	GE	Toshiba	Pooled
Breasts	R^2	0.74	0.67	0.83	0.69	0.01*	0.85	0.83	0.35
	Adj. R^2	0.73	0.62	0.82	0.68	-0.02	0.82	0.82	0.34
	RMSE	0.12	0.15	0.12	0.14	0.15	0.12	0.11	0.19
	A	1.16	1.10	1.59	1.24	0.12	1.44	1.51	0.93
	B	-0.04	-0.03	-0.06	-0.04	0.00	-0.04	-0.05	-0.03
Lungs	R^2	0.74	0.81	0.79	0.70	0.53	0.90	0.74	0.59
	Adj. R^2	0.74	0.79	0.78	0.70	0.52	0.89	0.73	0.59
	RMSE	0.14	0.11	0.11	0.14	0.09	0.09	0.11	0.12
	A	1.69	1.39	1.44	1.50	0.79	1.68	1.16	1.05
	B	-0.05	-0.04	-0.05	-0.05	-0.02	-0.04	-0.03	-0.03
Liver	R^2	0.92	0.95	0.90	0.88	0.80	0.90	0.84	0.76
	Adj. R^2	0.92	0.95	0.89	0.88	0.79	0.90	0.83	0.76
	RMSE	0.06	0.08	0.10	0.09	0.10	0.10	0.12	0.13
	A	1.41	1.63	1.69	1.50	1.01	1.35	1.48	1.24
	B	-0.04	-0.05	-0.05	-0.05	-0.03	-0.04	-0.05	-0.04
Spleen	R^2	0.83	0.96	0.87	0.83	0.62	0.85	0.83	0.67
	Adj. R^2	0.82	0.96	0.86	0.83	0.61	0.83	0.83	0.67
	RMSE	0.07	0.06	0.11	0.10	0.09	0.11	0.13	0.14
	A	1.10	1.44	1.68	1.36	0.75	1.15	1.51	1.13
	B	-0.03	-0.04	-0.05	-0.04	-0.02	-0.03	-0.05	-0.03
Kidneys	R^2	0.84	0.96	0.90	0.86	0.70	0.90	0.89	0.75
	Adj. R^2	0.83	0.96	0.89	0.86	0.69	0.89	0.88	0.75
	RMSE	0.08	0.07	0.10	0.10	0.09	0.10	0.10	0.13
	A	1.23	1.61	1.68	1.44	0.86	1.31	1.50	1.20
	B	-0.04	-0.05	-0.05	-0.04	-0.03	-0.04	-0.05	-0.04
Pooled	R^2	0.77	0.90	0.81	0.79	0.46	0.84	0.79	0.62
	Adj. R^2	0.77	0.90	0.80	0.79	0.46	0.83	0.79	0.62
	RMSE	0.13	0.10	0.13	0.13	0.13	0.12	0.12	0.15
	A	1.37	1.46	1.48	1.39	0.78	1.35	1.40	1.13
	B	-0.04	-0.05	-0.05	-0.04	-0.02	-0.04	-0.04	-0.03

The R^2 values show improvement when using regional $CTDI_{vol}$ with water equivalent diameter versus global $CTDI_{vol}$ with conventional effective diameter. This improvement is almost seen across all organs and all three scanners. The increase in R^2 from using regional versus global information is more extreme for Siemens scanner as it is for GE and Toshiba. Similar analyses were performed for global $CTDI_{vol}$ with average water equivalent diameter, which resulted in

minor improvements over the global $CTDI_{vol}$ with effective diameter. Table 10-4 shows part of these results for breasts and kidneys and across organs, scanners and across both.

Table 10-4 Statistical measure of goodness of the liner fit for regional $CTDI_{vol}$ with water equivalent diameter (WED) versus global $CTDI_{vol}$ with water equivalent diameter (WED).

Organ		$Organ\ Dose/CTDI_{vol,Regional} = Ae^{-B \times WED}$				$Organ\ Dose/CTDI_{vol,Global} = Ae^{-B \times WED}$			
		Siemens	**GE**	**Toshiba**	**Pooled**	**Siemens**	**GE**	**Toshiba**	**Pooled**
Breasts	R^2	0.74	0.67	0.83	0.69	0.0001*	0.88	0.68	0.22
Kidney	R^2	0.84	0.96	0.90	0.86	0.69	0.94	0.85	0.72
Pooled	R^2	0.77	0.90	0.81	0.79	0.45	0.89	0.75	0.57

As confirmed in Chapters 8 and 9 and from Tables 10-3 and 10-4, it is evident that regional $CTDI_{vol}$ and water equivalent diameter perform better as normalization factor and size metric, respectively, across most scanners and organs. In only one case (GE scanner, breast dose), this combination performed worse.

To understand differences between scanners and organs, results from Table 10-3 are graphically represented using plots of fitted (predicted) values and actual normalized organ doses versus size metric. Figures 10-5 through 10-8 show fitted values versus actual values across scanners and organs.

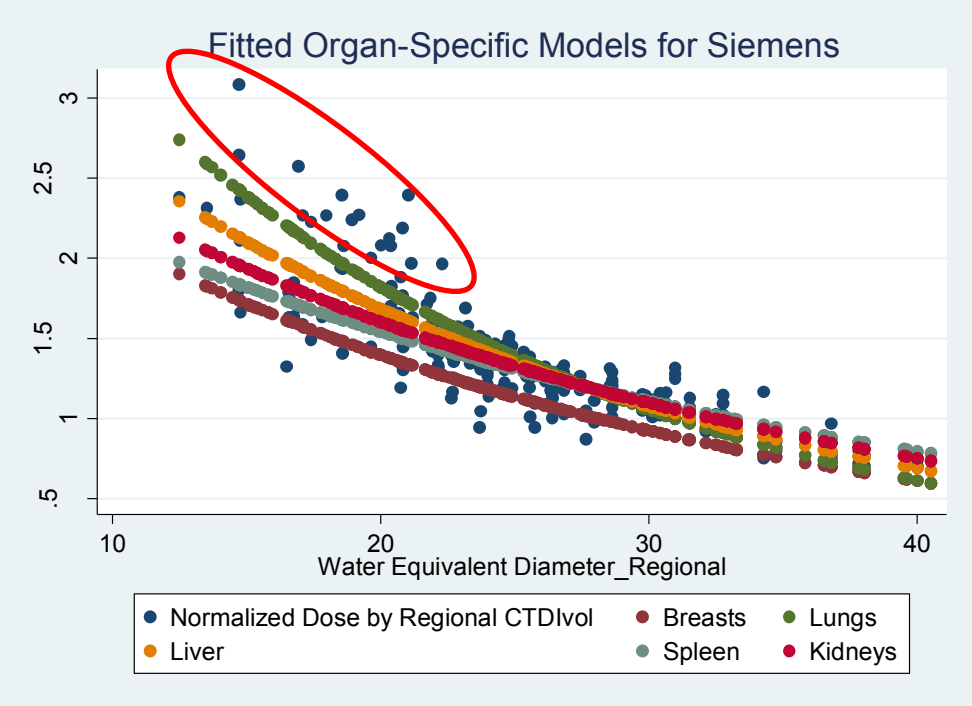

Figure 10-5 Siemens-specific, organ-specific fits shown along actual normalized organ doses by regional $CTDI_{vol}$ versus WED.

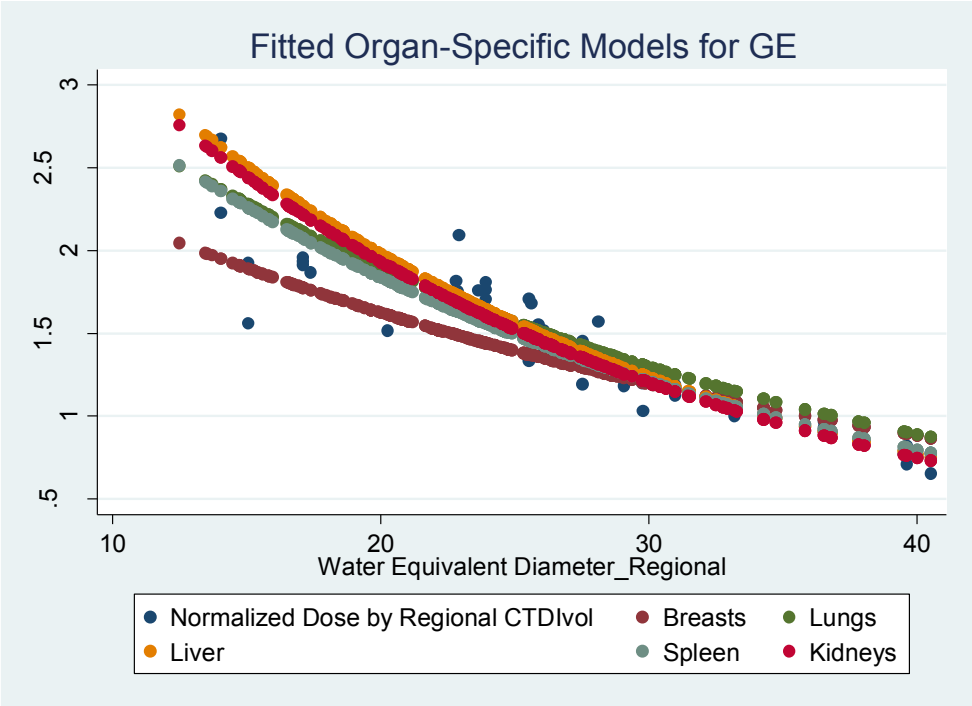

Figure 10-6 GE-specific, organ-specific fits shown along actual normalized organ doses by regional $CTDI_{vol}$ versus WED.

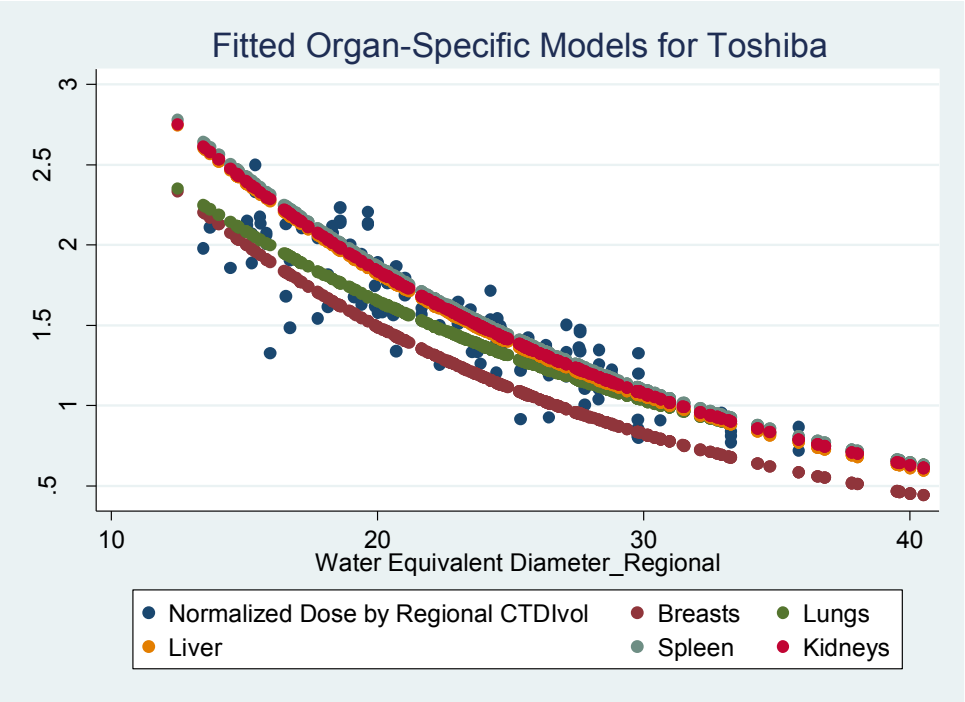

Figure 10-7 Toshiba-specific, organ-specific fits shown along actual normalized organ doses by regional $CTDI_{vol}$ versus WED.

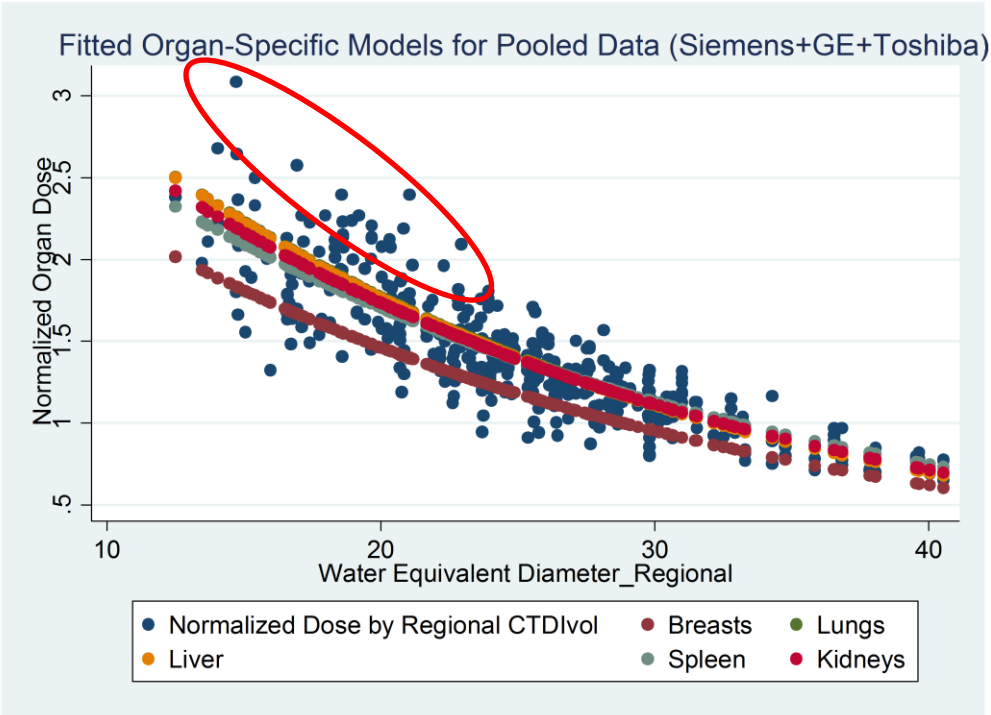

Figure 10-8 Organ-specific fits across all three scanners shown along actual normalized organ doses by regional $CTDI_{vol}$ versus WED.

Figures 10-5 through Figure 10-8 illustrate all organ-specific models for each individual scanner and also organ-specific fitted models for all three scanners combined. It is apparent that normalized breast dose behaves similarly across individual scanners. A similar observation is made for the abdominal organs. However, it is difficult to establish a single pattern for normalized lung dose across scanners. In the pooled data, there seem to be a distinct difference between normalized breast dose and all other normalized organ doses, which nicely overlap. This could be due to differences in position and location of these organs within human anatomy; breasts are smaller and more peripherally positioned organs than liver, kidneys, spleen and lungs, which are larger, more in-depth organs.

Within individual scanners, the difference between normalized organ doses is small for larger patients, but it diverges with decreasing size. These differences among normalized organ doses are more profound for Siemens than for GE and Toshiba. This spread of data seen for smaller patients could at least partially be due to patient positioning. Ideally a consistent positioning across all patients would reduce variability of individual organ doses; however patient positioning within the gantry is a variable that is hard to control and to keep constant. The positioning of patients has a larger impact on organ dose among smaller patients than larger patients, since the variability of positioning for larger patients is limited.

There seems to be outliers from the Siemens data, shown in Figure 10-5, which are also evident in the pooled model across scanners shown in Figure 10-8. Taking a closer look at these patients, nothing abnormal is observed. These are Siemens patients and a combination of males and females and some pediatrics. However, when the plot is observed for lungs only, as seen in Figure 10-9, there is a single outlier which seems to be forcing the fit downward.

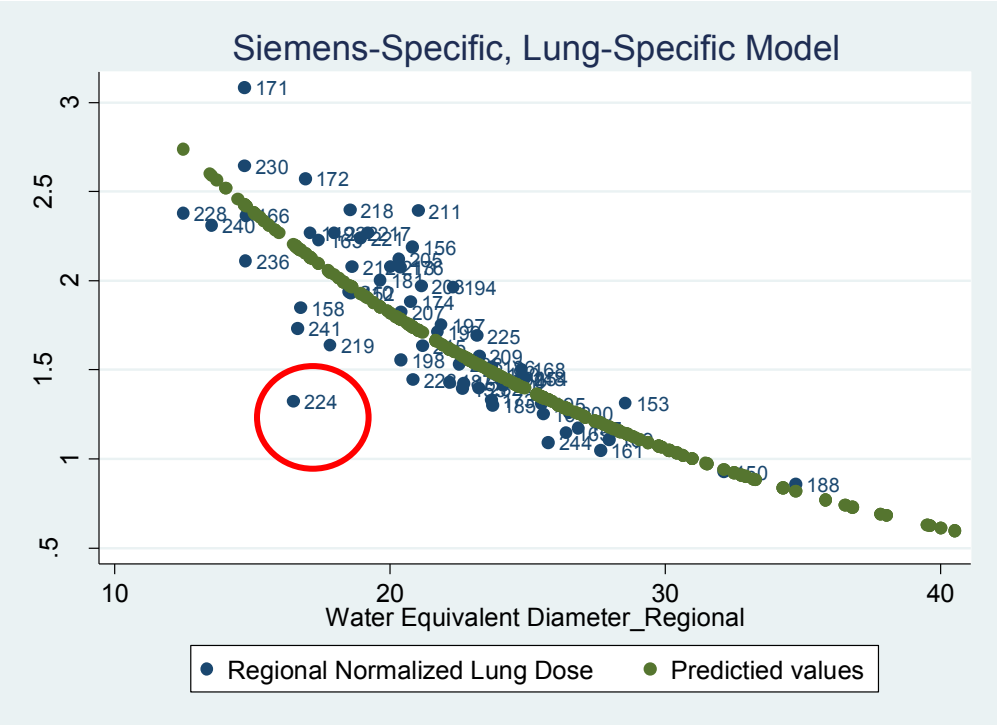

Figure 10-9 Siemens-specific, lung-specific fitted values versus Monte Carlo normalized lung doses using regional $CTDI_{vol}$.

Taking a closer look at this pediatric patient, as shown in Figure 10-10, this patient is suffering from some interstitial lung disease resulting in abnormal lung density.

Because lungs are typically less dense than, for instance abdominal tissue, lungs will attenuate fewer x-ray photons than other tissue types. Therefore lungs will have higher absorbed dose than other tissue types subject to the same photon fluence. Hence, this patient received lower lung dose than usually observed with lungs due to different (higher) attenuation caused by interstitial lung disease.

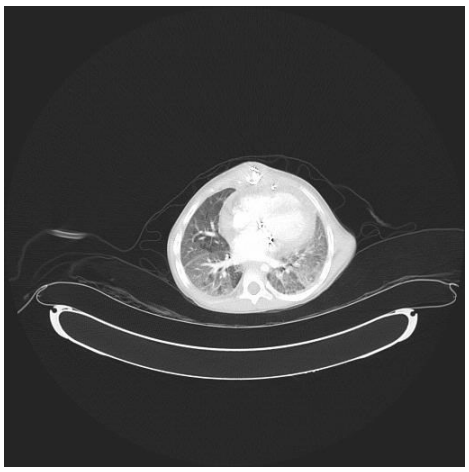

Figure 10-10 Single axial CT image of patient 224, indicating interstitial lung disease.

Removing this patient from the dataset improves the R_2 value of the Siemens-specific and lung-specific model from 0.74 to 0.80, while the lung-specific model across all three scanners improved from 0.70 to 0.76.

Next, organ-specific models were observed for different scanners to explore differences among individual organs from different CT scanners manufacturers. Figures 10-11 through 10-16 illustrate these models for all five organs, while the last chart demonstrates fitted scanner-specific models across all organs.

While most abdominal organs seem to be behaving similarly across scanners, breasts and lungs behave interchangeably and not similar. For all the abdominal organs, there is a divergence of predicted values towards smaller sizes while for larger sizes, the fit converge with minimal differences among them. As mentioned above, this could be due to patient positioning and its effect of organ dose, which is more extreme for smaller patients than it is for larger patients. For abdominal organs, Siemens (orange fit) is falling below other scanners, while for breasts and lungs, the lower fits are Siemens and Toshiba interchangeably from smaller to larger patients.

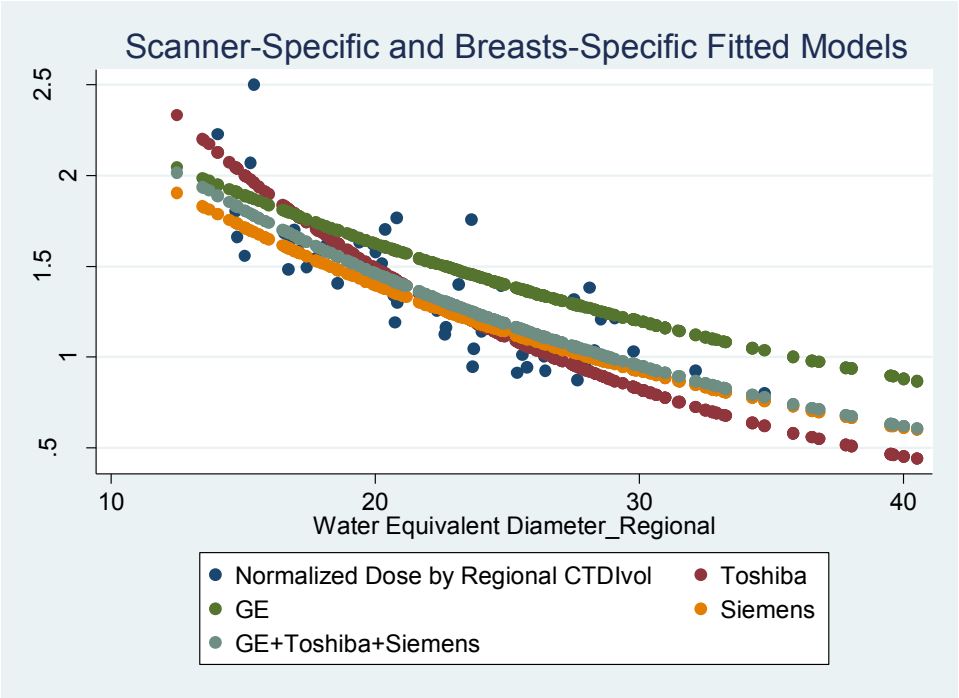

Figure 10-11 Breasts-specific models for individual scanners and across all three scanners plotted along actual normalized breast doses versus WED.

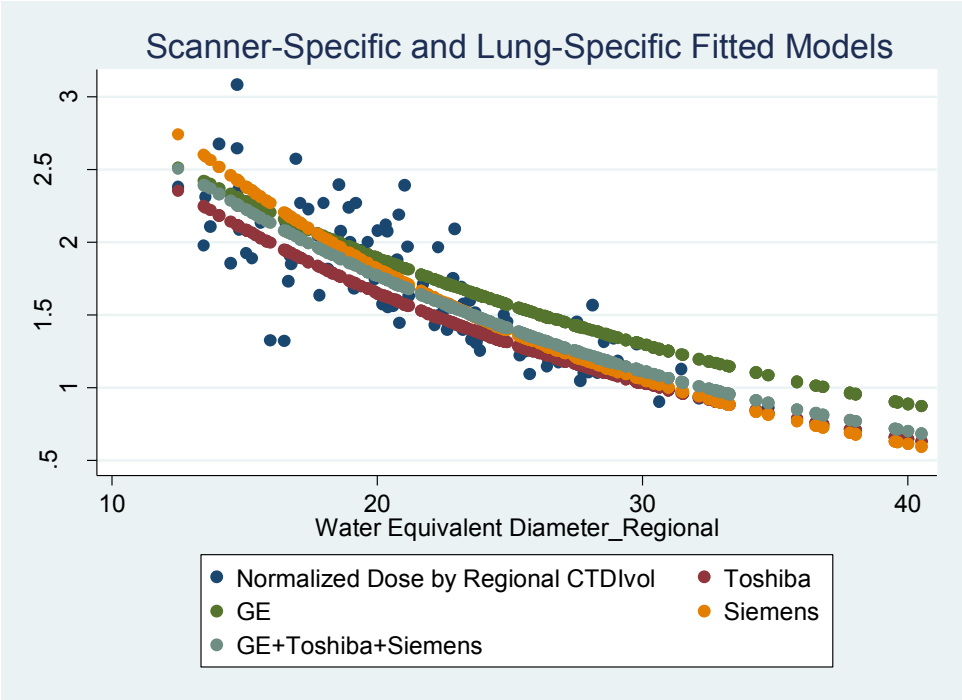

Figure 10-12 Lung-specific models for individual scanners and across all three scanners plotted along actual normalized lung doses versus WED.

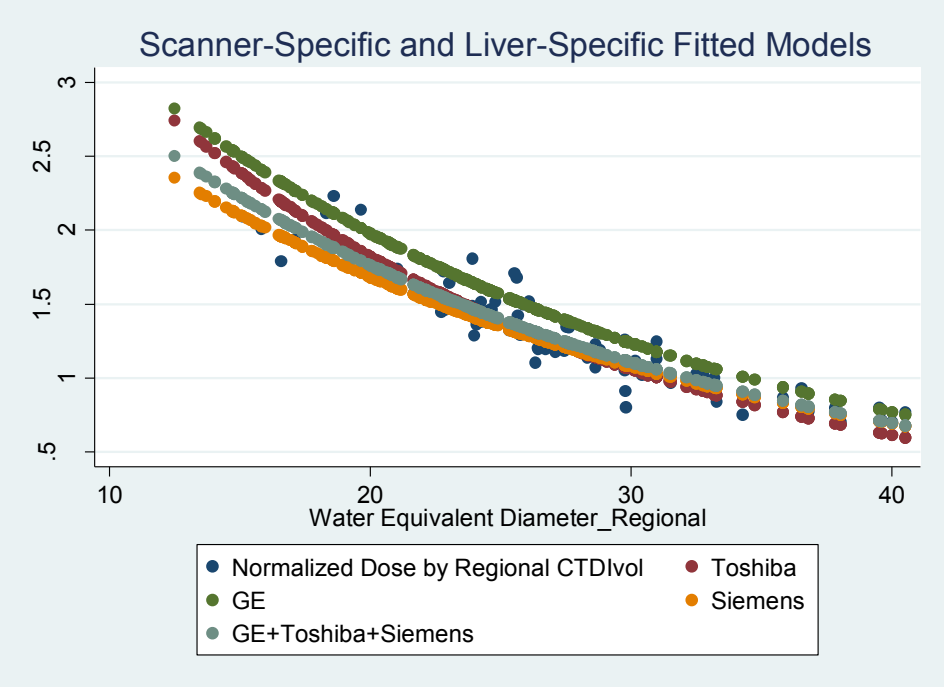

Figure 10-13 Liver-specific models for individual scanners and across all three scanners plotted along actual normalized Liver doses versus WED.

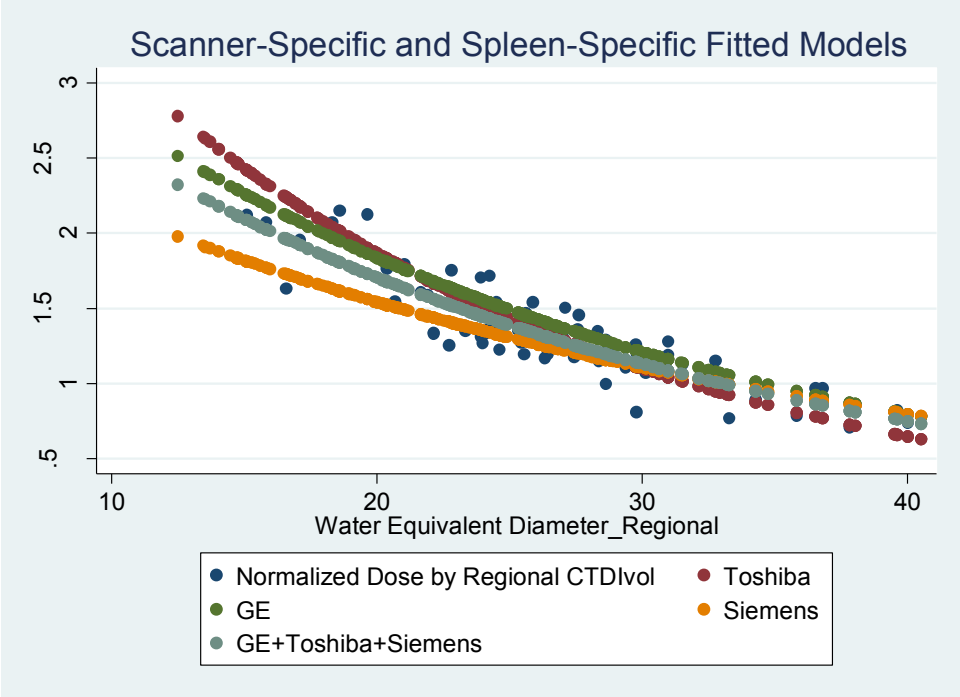

Figure 10-14 Spleen-specific models for individual scanners and across all three scanners plotted along actual normalized spleen doses versus WED.

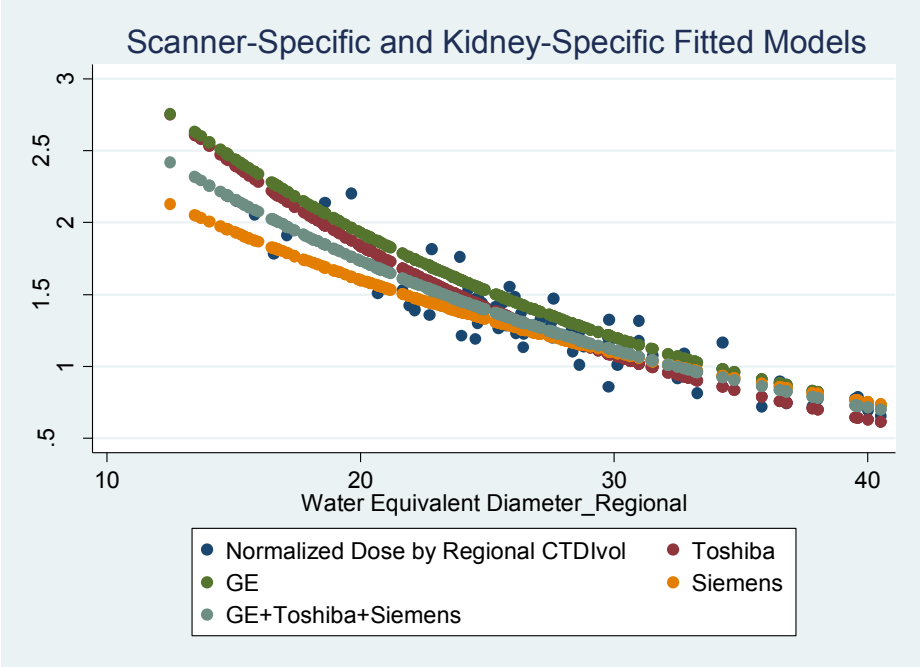

Figure 10-15 Kidneys-specific models for individual scanners and across all three scanners plotted along actual normalized kidney doses versus WED.

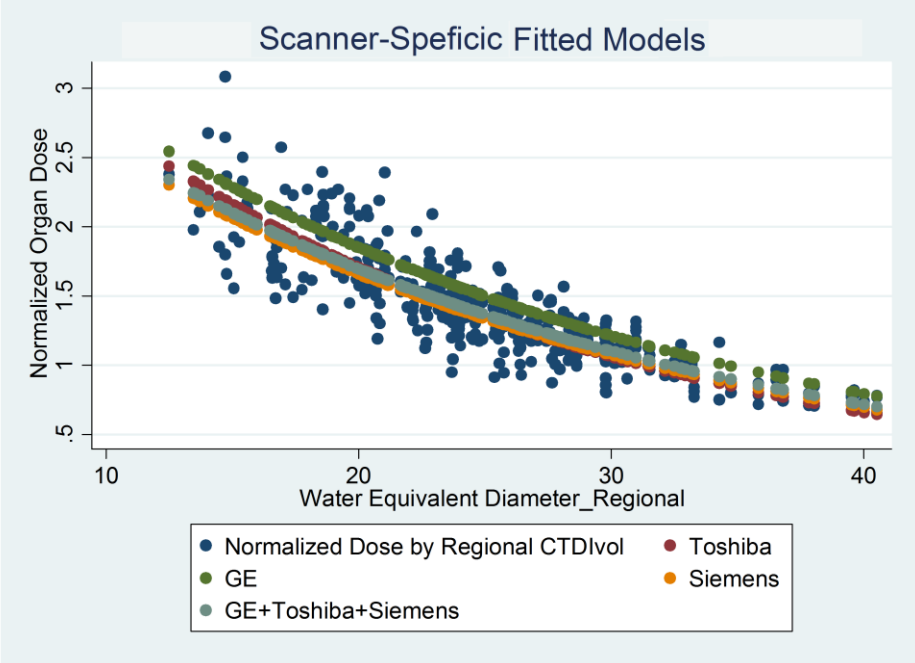

Figure 10-16 Scanner-specific models across all organs along with pooled model across all scanners and organs.

Until now, categorical variables discussed in the previous section were not used. The regression analysis will be improved by adding appropriate categorical predictors to the model. First, a simple example will be illustrated to explain the role of categorical predictors.

Toshiba-specific model generated with A and B coefficients, shown in Table 10-3, was created using the conventional Eq. 10-5 without any categorical predictors. Taking another look at the Toshiba-specific and organ-specific models shown in Figure 10-7, it is apparent that thoracic organs stand out, indicating possible categorical predictors to be breast, lung and/or chest exam. The difference between abdominal and thoracic exams for Toshiba models becomes even more evident when looking at predictive models generated for Toshiba Abdomen/Pelvis scans versus chest exams (Figure 10-17). Similar behavior is seen for GE and Siemens (Figures 10-18 and 10-19).

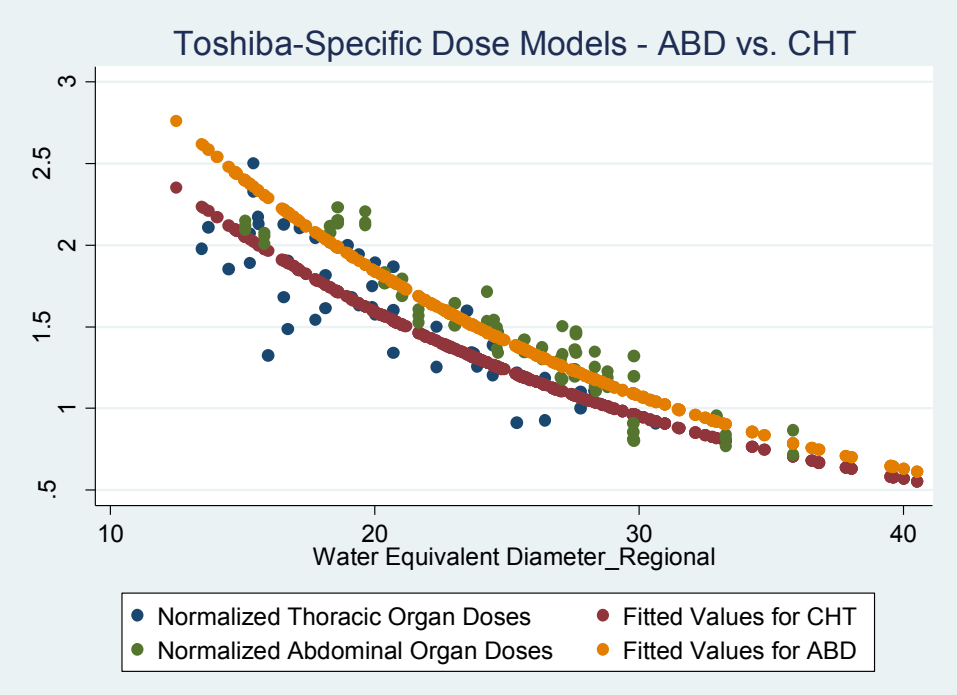

Figure 10-17 Exam-specific models for chest and abdomen/pelvis for Toshiba scanner.

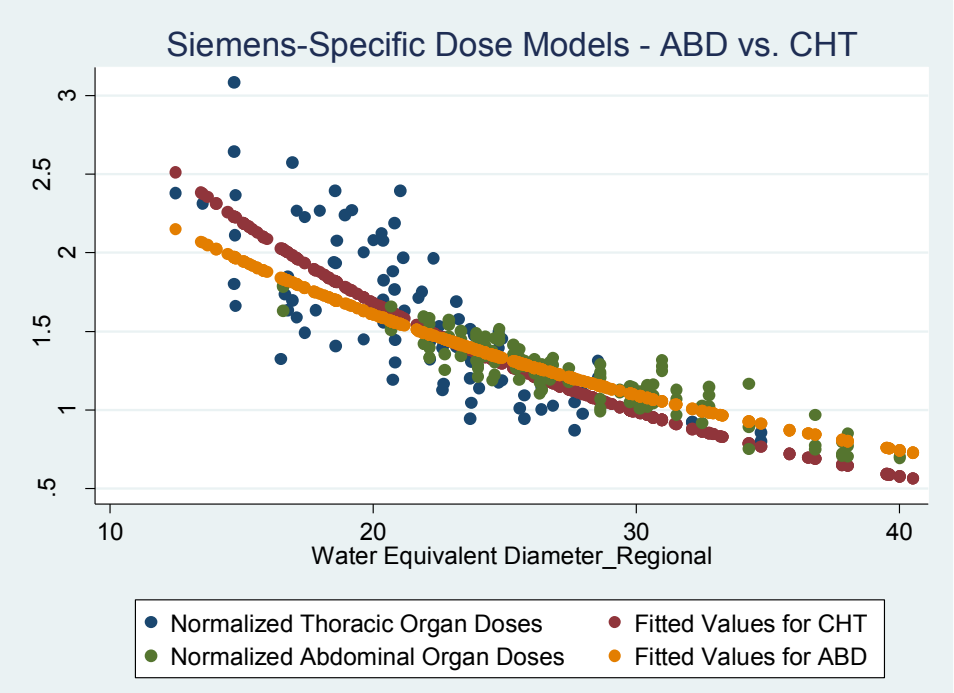

Figure 10-18 Chest- and abdomen/pelvis-specific models generated using Siemens data and plotted versus actual data points,

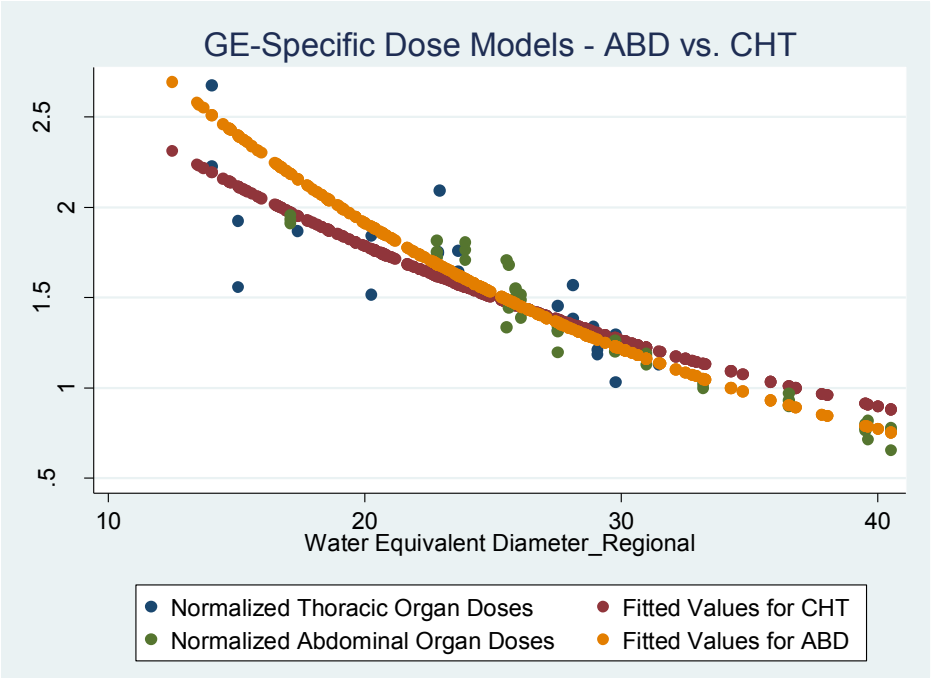

Figure 10-19 Exam type-specific fitted values versus actual normalized organ doses shown for GE data.

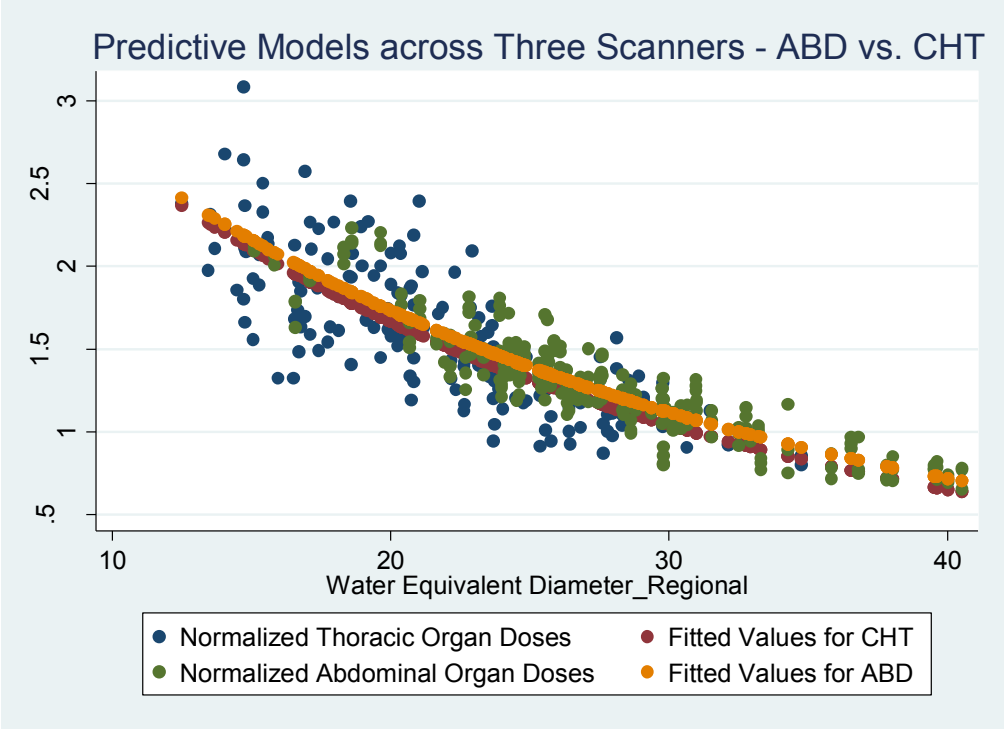

Figure 10-20 Chest- and abdomen/pelvis-specific fitted values across all three scanners versus actual normalized organ doses.

Once exam type-specific models are generated across scanners, the differences seem to be minimized, resulting in two closely exponential fits (Figure 10-20).

A modified model will be generated using the Categorical variables "Breasts" and either "Lung" or "CHT" for chest. The equation of the predictive model is as follows:

$$Ln(Normalized\ Dose) = \alpha - \{(\beta_1 \times WED) + (\beta_2 \times Breasts) + (\beta_3 \times Lungs(CHT))\}\} \qquad \textbf{Eq. 10-11}$$

In case dose is estimated for another organ, for instance liver, the last two terms in the predictive model drop out and the model simplifies to the original form:

$$Ln(Normalized\ Dose) = \alpha - (\beta \times WED) \qquad \textbf{Eq. 10-12}$$

Figure 10-21 shows the STATA output for the simple model without any categorical variables, followed by models with categorical predictors. As illustrated, the R^2 increased from 83% to 89% once categorical predictors were added to the model. As predicted, all three predictors, Breasts, Lung, and CHT are contributing towards increasing the coefficient of determination, R^2, of the model. Since there is a co-linearity between these variables, i.e. lung dose and breast dose result from chest exams; a combination (a pair) of either two of these three predictors is enough to increase the R^2. Indeed, the R^2 does not change depending on which pair is chosen for the model. Additionally, the adjusted R^2 also increases once categorical predictors are added to the model, indicating appropriateness of the model over the previous one.

```
. reg lnorgandose_regional waterequivalentdiameter_regional  if Toshiba==1

      Source |       SS       df       MS              Number of obs =     133
-------------+------------------------------           F(  1,   131) =  628.48
       Model |  9.01060442     1  9.01060442            Prob > F      =  0.0000
    Residual |  1.87815713   131  .014337077           R-squared     =  0.8275
-------------+------------------------------           Adj R-squared =  0.8262
       Total |  10.8887615   132  .082490618           Root MSE      =  .11974

------------------------------------------------------------------------------
lnorgandose_regional |      Coef.   Std. Err.      t    P>|t|     [95% Conf. Interval]
---------------------+--------------------------------------------------------
waterequivalentdiame~l |  -.0484133   .0019312   -25.07   0.000    -.0522335    -.044593
               _cons |   1.509709    .046173    32.70   0.000     1.418368     1.60105
------------------------------------------------------------------------------

. reg lnorgandose_regional waterequivalentdiameter_regional Lung Breasts  if Toshiba==1

      Source |       SS       df       MS              Number of obs =     133
-------------+------------------------------           F(  3,   129) =  332.23
       Model |  9.64094302     3  3.21364767            Prob > F      =  0.0000
    Residual |  1.24781852   129  .009673012           R-squared     =  0.8854
-------------+------------------------------           Adj R-squared =  0.8827
       Total |  10.8887615   132  .082490618           Root MSE      =  .09835

------------------------------------------------------------------------------
lnorgandose_regional |      Coef.   Std. Err.      t    P>|t|     [95% Conf. Interval]
---------------------+--------------------------------------------------------
waterequivalentdiame~l |  -.0534645   .0017683   -30.24   0.000     -.056963    -.0499659
                Lung |  -.0928429   .0218273    -4.25   0.000    -.1360287    -.0496571
            Breasts |   -.214882    .027358    -7.85   0.000    -.2690104    -.1607536
               _cons |   1.679287   .0458696    36.61   0.000     1.588533     1.770041
------------------------------------------------------------------------------

. reg lnorgandose_regional waterequivalentdiameter_regional Lung CHT  if Toshiba==1

      Source |       SS       df       MS              Number of obs =     133
-------------+------------------------------           F(  3,   129) =  332.23
       Model |  9.64094302     3  3.21364767            Prob > F      =  0.0000
    Residual |  1.24781852   129  .009673012           R-squared     =  0.8854
-------------+------------------------------           Adj R-squared =  0.8827
       Total |  10.8887615   132  .082490618           Root MSE      =  .09835

------------------------------------------------------------------------------
lnorgandose_regional |      Coef.   Std. Err.      t    P>|t|     [95% Conf. Interval]
---------------------+--------------------------------------------------------
waterequivalentdiame~l |  -.0534645   .0017683   -30.24   0.000     -.056963    -.0499659
                Lung |   .122039   .0291014     4.19   0.000     .0644613     .1796168
                 CHT |   -.214882    .027358    -7.85   0.000    -.2690104    -.1607536
               _cons |   1.679287   .0458696    36.61   0.000     1.588533     1.770041
------------------------------------------------------------------------------

. reg lnorgandose_regional waterequivalentdiameter_regional Breasts CHT  if Toshiba==1

      Source |       SS       df       MS              Number of obs =     133
-------------+------------------------------           F(  3,   129) =  332.23
       Model |  9.64094302     3  3.21364767            Prob > F      =  0.0000
    Residual |  1.24781852   129  .009673012           R-squared     =  0.8854
-------------+------------------------------           Adj R-squared =  0.8827
       Total |  10.8887615   132  .082490618           Root MSE      =  .09835

------------------------------------------------------------------------------
lnorgandose_regional |      Coef.   Std. Err.      t    P>|t|     [95% Conf. Interval]
---------------------+--------------------------------------------------------
waterequivalentdiame~l |  -.0534645   .0017683   -30.24   0.000     -.056963    -.0499659
            Breasts |   -.122039   .0291014    -4.19   0.000    -.1796168    -.0644613
                 CHT |  -.0928429   .0218273    -4.25   0.000    -.1360287    -.0496571
               _cons |   1.679287   .0458696    36.61   0.000     1.588533     1.770041
------------------------------------------------------------------------------
```

Figure 10-21 STATA output showing models with and without categorical predictors.

Once all categorical variables are added, the predicted values do not simply fall along the same line. Figure 10-22 illustrates the predicted values for the Toshiba-specific model using Breasts and Lungs as the categorical predictors. As mentioned before, categorical variables are binary; with two categorical predictors, there are four different possibilities: (a) both Breasts and Lung can be zero, i.e. the model is predicting liver, kidneys or spleen dose, (b) both can be one, i.e. the model is predicting dose from chest exam to both female and males, and (c) lung can take on the value one while Breasts is zero, i.e. model is predicting dose from chest exam to male patients which overlaps with the option Breasts=1 and Lungs=1. The last possibility, (d) Lungs=0 and Breasts=1 does not exist within our dataset, i.e. there are no patients with just breasts dose. Figure 10-22 shows the different stages of adding each possibility to the model.

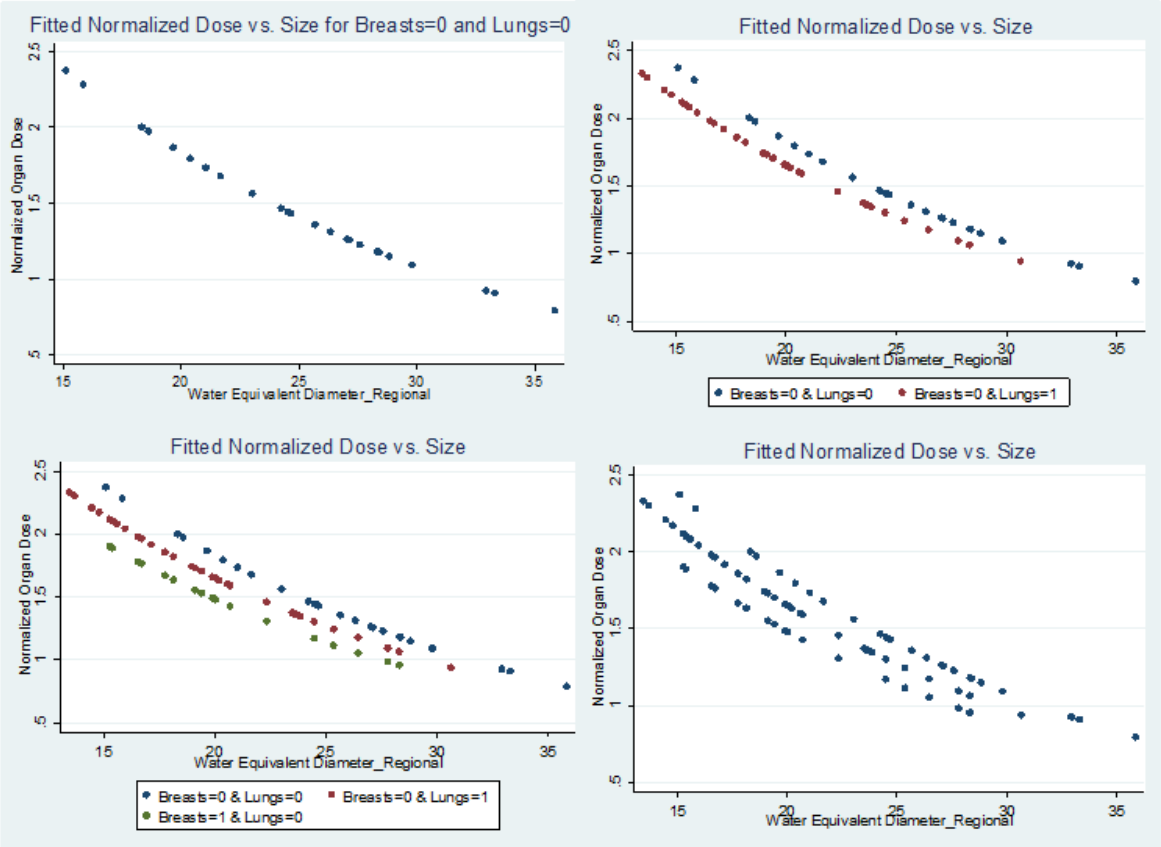

Figure 10-22 Fitted predicted values shown for one possibility at a time. Bottom right shows fitted values for all different possibilities.

Another improvement to the predictive model can be accomplished by identifying possible interaction between variables, which can further be used as a predictor in the model. In TCM the tube current changes, i.e. modulates, based on patient attenuation. And $CTDI_{vol}$ is proportional to tube current, therefore it is plausible to expect an interaction between $CTDI_{vol}$ and water equivalent diameter. The example above is repeated using another predictor which is the interaction between regional size metric and the regional normalization factor, $CTDI_{vol}$.

Source	SS	df	MS
Model	9.70138545	4	2.42534636
Residual	1.1873761	128	.009276376
Total	10.8887615	132	.082490618

Number of obs	= 133
F(4, 128)	= 261.45
Prob > F	= 0.0000
R-squared	= 0.8910
Adj R-squared	= 0.8875
Root MSE	= .09631

lnorgandose_regional	Coef.	Std. Err.	t	P>|t|	[95% Conf.	Interval]
waterequivalentdiameter_regional	-.0453262	.0036281	-12.49	0.000	-.0525051	-.0381474
interaction	-.0001184	.0000464	-2.55	0.012	-.0002102	-.0000266
Breasts	-.1161618	.0285913	-4.06	0.000	-.1727347	-.059589
CHT	-.0553234	.0259411	-2.13	0.035	-.1066524	-.0039945
_cons	1.524247	.0755438	20.18	0.000	1.37477	1.673723

Figure 10-23 STATA output showing a predictive model with the interaction term between WED and $CTDI_{vol,\ Regional}$.

As seen in the STAT output shown in Figure 10-23, the interaction term between size and $CTDI_{vol,Regional}$ has a minor improvement on the R^2, nevertheless the p-value is <0.05, indicating a statistically significant improvement in explaining the response variable. The small improvement is also translated into the β coefficient of the interaction term; it is a very small value, but this could also be due to the interaction term being a large value, which is the product of regional WED and $CTDI_{vol,Regional}$. It is interesting to see the change in t and p-value of the predictor chest, "CHT", once the interaction term is added to the regression. This suggests that the interaction term and "CHT" are somehow correlated. Co-linearity and, hence, elimination of one of these variables, can result from high correlations. However, in this case the correlation

was not strong enough to cause co-linearity and therefore both variables are still significant predictors.

Next, differences between genders and pediatric versus adult patients is explored in another example using Siemens data. Both pediatric and female patients are significant predictors in Siemens-specific model, as shown by STATA output in Figure 10-24. Looking at gender-specific models for Siemens scanners, shown in Figure 10-25, distinct differences between males and females are visible. A similar difference, but reverse, was observed in Chapter 8, in which the fitted line for males was below the fitted data for females. This could be due to a limited number of patient models used in Chapter 8. Additionally, it was observed that there are no differences between males and females in the abdominal regions, while the difference is only arising from thoracic models. Figures 10-26 and 10-27 illustrate this for Siemens abdominal and thoracic models, respectively. While for Toshiba data, similar differences between males and females is observed (Figure 10-28), for GE both fit overlap (Figure 10-29). Looking at gender-specific models across all three scanners (Figure 10-30), these differences are still noticeable. Similarly, there are some differences between pediatric and adult patients within Siemens data, as shown by Figure 10-31, which results in "Peds" being a significant predicator in predicting dose from Siemens scanners.

Source	SS	df	MS
Model	14.4494341	5	2.88988681
Residual	2.23493781	226	.009889105
Total	16.6843719	231	.072226718

Number of obs = 232
F(5, 226) = 292.23
Prob > F = 0.0000
R-squared = 0.8660
Adj R-squared = 0.8631
Root MSE = .09944

lnorgandose_regional	Coef.	Std. Err.	t	P>|t|	[95% Conf.	Interval]
waterequivalentdiameter_regional	-.0456131	.0015604	-29.23	0.000	-.0486879	-.0425382
Breasts	-.2320295	.0226678	-10.24	0.000	-.2766969	-.1873622
CHT	.0673038	.0178016	3.78	0.000	.0322255	.1023822
Female	-.0481528	.014238	-3.38	0.001	-.0762089	-.0200967
Peds	-.0643913	.018372	-3.50	0.001	-.1005936	-.028189
_cons	1.477834	.0468221	31.56	0.000	1.38557	1.570098

Figure 10-24 STATA output showing Siemens-specific model with categorical predictors.

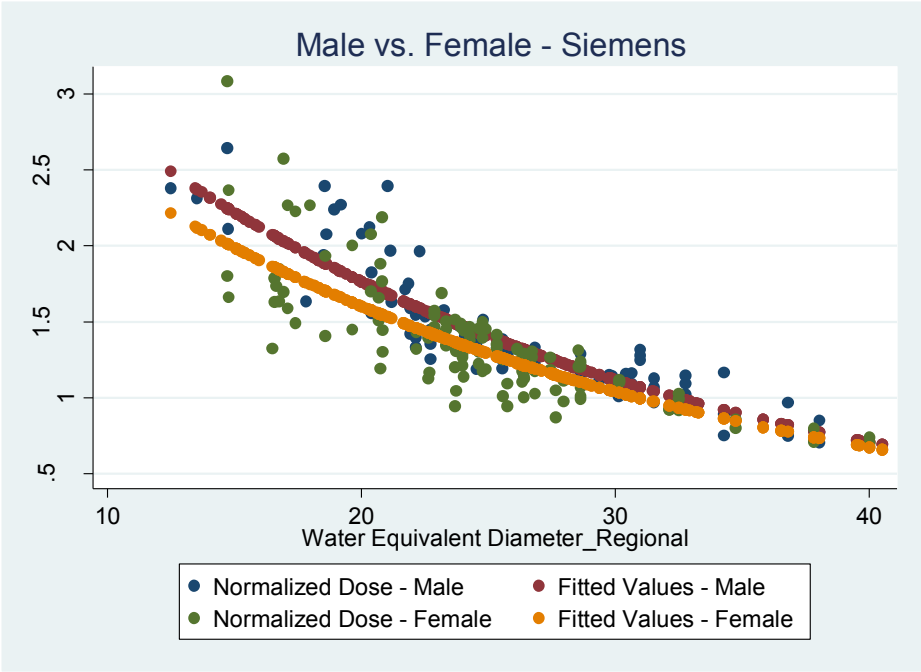

Figure 10-25 Male versus female-specific models for Siemens data.

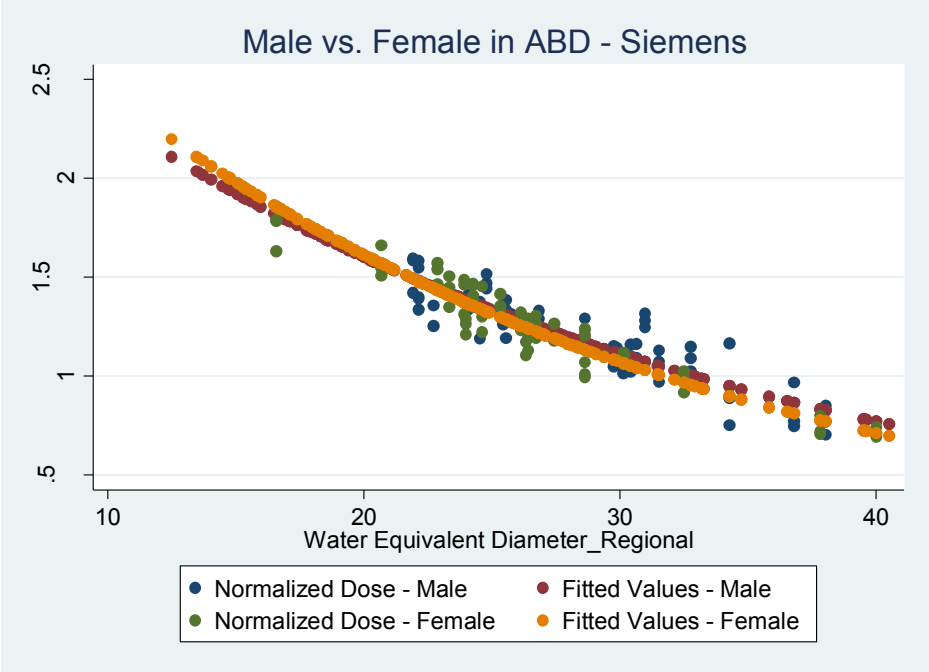

Figure 10-26 Male versus female-specific models for Siemens abdomen/pelvis data.

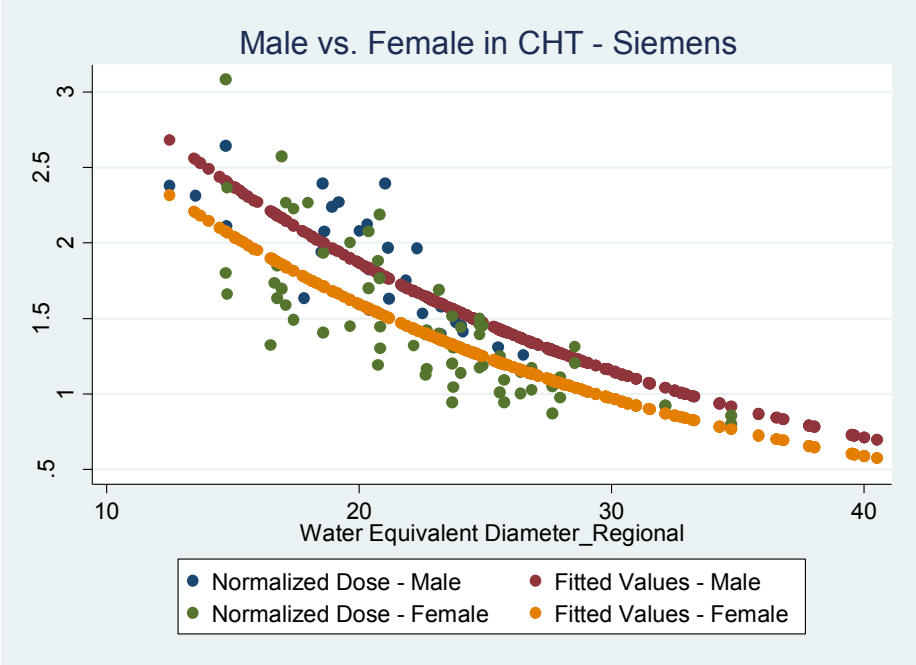

Figure 10-27 Male versus female-specific models for Siemens thoracic data.

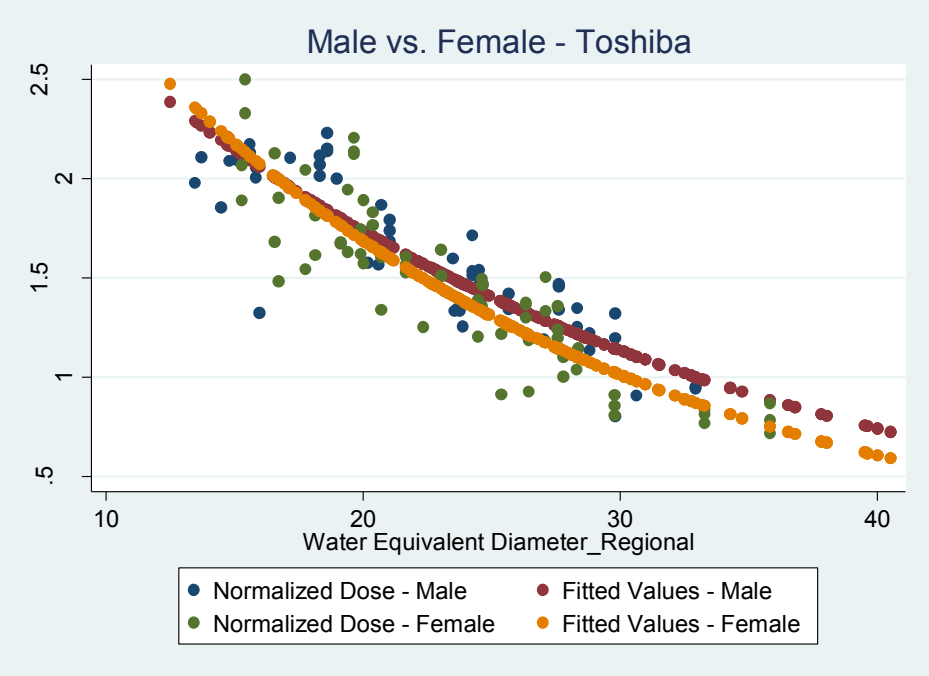

Figure 10-28 Male versus female-specific models for Toshiba data.

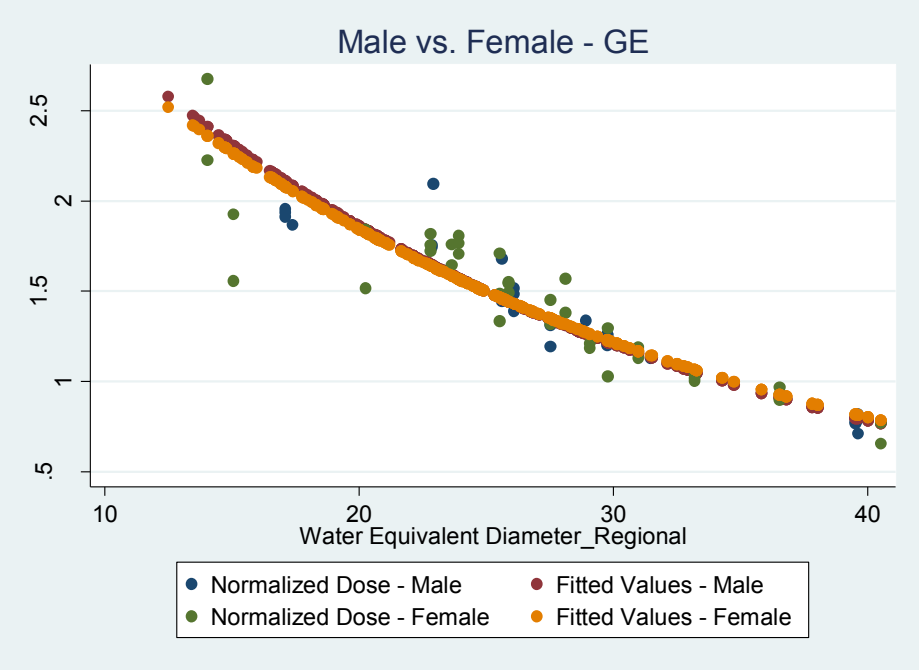

Figure 10-29 Male versus female-specific models for GE data.

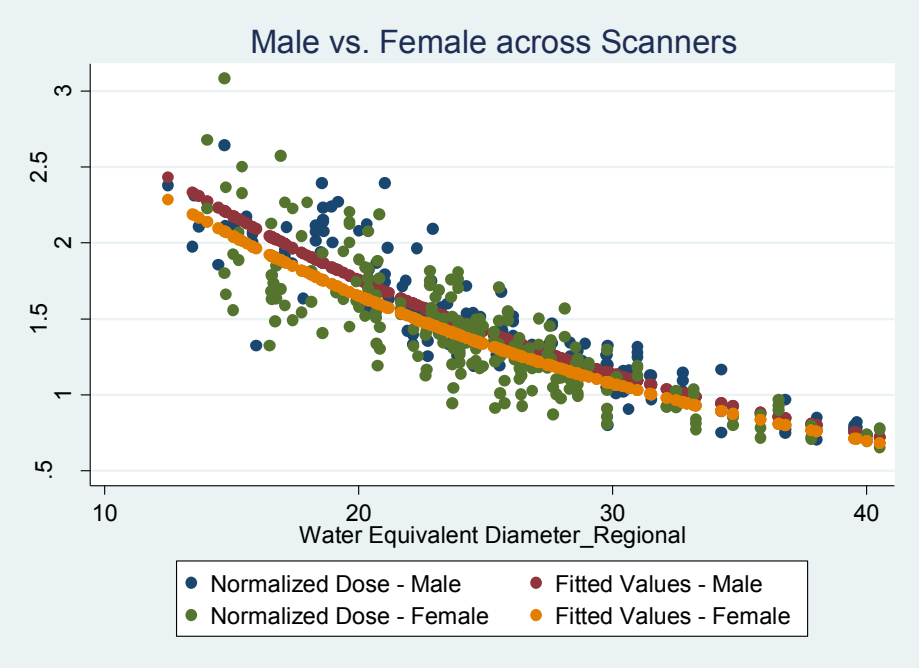

Figure 10-30 Male versus female-specific models for pooled data across scanners and organs.

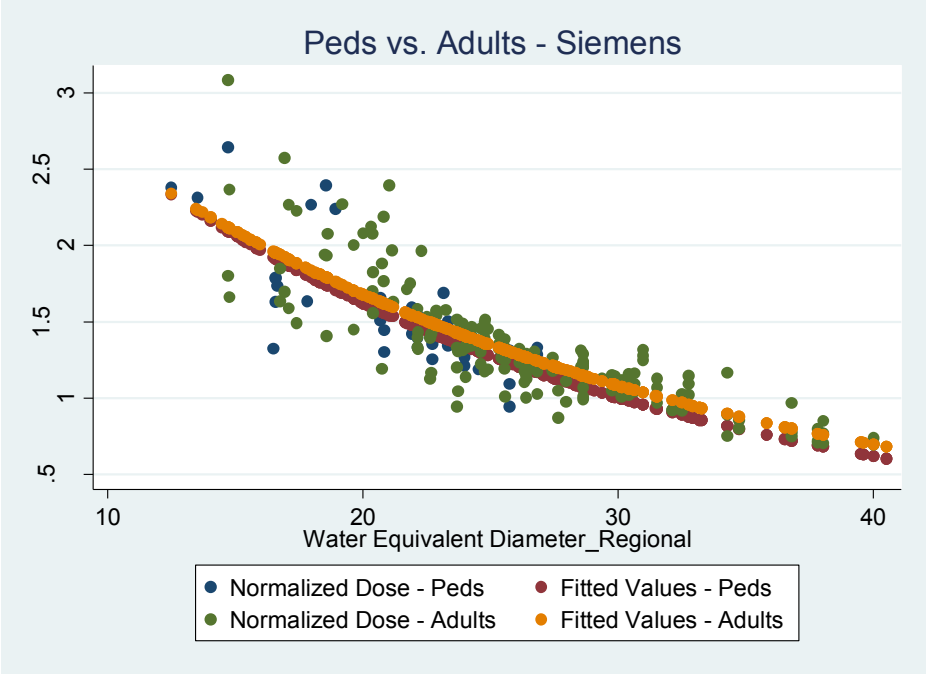

Figure 10-31 Pediatric versus adult-specific models for Siemens data.

Now that categorical predictors proved to improve dose predictive models, the models in Table 10-3 were repeated using appropriate categorical predictors and the interaction term ($WED*CTDI_{vol,Regional}$). Generated plots on scanner- and organ-specific models can help in determining these predictors. As previously mentioned, the significance of each added predictor can be determined using the p-value reported for the regression analysis. P-values greater than 0.05 indicate that an added predictor is not statistically significant in explaining the response variable. Table 10-4 illustrates all organ-specific models with added predictors and interaction term, while Table 10-5 displays scanner-specific models across all organs. The grayed out areas indicate no significant improvement with added categorical or the interaction term, hence the model would be the same as that found in Table 10-3.

Once Tables 10-4 and 10-5 were completed, the resulting models were tested using the test set cases. The percent mean, standard deviation, minimum, and maximum differences between

predicted organ doses and those obtained from the detailed Monte Carlo simulations were reported for each predictive model. Finally, the results of the predictive models and detailed Monte Carlo estimates for the test set were compared using a one-sample t-test. This will help determine the level of accuracy achieved from each model, which can be used to assist in choosing the most accurate model for organ dose estimation.

It is worthwhile to mention that the more detailed a model is, for instance a breast-specific and Siemens-specific model, the less possible it is to find other predictors than size simply due to the low variation of the response variable in a highly specific model. Figure 10-32 shows the STATA output for this specific example without and with the added categorical predictor.

Source	SS	df	MS		
Model	1.16627724	1	1.16627724	Number of obs	= 32
Residual	.415483291	30	.013849443	F(1, 30)	= 84.21
				Prob > F	= 0.0000
				R-squared	= 0.7373
				Adj R-squared	= 0.7286
Total	1.58176053	31	.051024533	Root MSE	= .11768

lnorgandose_regional	Coef.	Std. Err.	t	P>|t|	[95% Conf.	Interval]
waterequivalentdiameter_regional	-.0413173	.0045024	-9.18	0.000	-.0505124	-.0321221
_cons	1.160301	.1054342	11.00	0.000	.9449753	1.375626

Source	SS	df	MS		
Model	1.16754431	2	.583772156	Number of obs	= 32
Residual	.414216217	29	.014283318	F(2, 29)	= 40.87
				Prob > F	= 0.0000
				R-squared	= 0.7381
				Adj R-squared	= 0.7201
Total	1.58176053	31	.051024533	Root MSE	= .11951

lnorgandose_regional	Coef.	Std. Err.	t	P>|t|	[95% Conf.	Interval]
waterequivalentdiameter_regional	-.0412894	.0045734	-9.03	0.000	-.050643	-.0319358
PedsxSiemens	-.0215927	.0724971	-0.30	0.768	-.169866	.1266806
_cons	1.161685	.1071739	10.84	0.000	.9424902	1.38088

Figure 10-32 STATA output showing without and with added categorical predictor "Peds".

As shown in Figure 10-32 the adjusted R^2 decreased once the categorical predictor was added into the model, this value penalizes the addition of an insignificant predictor by decreasing from 0.7286 to 0.7201. This measure can further help in choosing appropriate predictors.

Table 10-4 Statistical measure of goodness of the liner fit for regional $CTDI_{vol}$ along with water equivalent diameter (WED) with improved statistics using categorical predictors and interaction term between $WED*CTDI_{vol,Regional}$ for scanner- and organ-specific models. Grayed out areas represent combinations where no improvement over the results of Table 10-3 is found by adding categorical predictors.

Organ	Siemens			GE			Toshiba			Pooled (GE+Toshoba+Siemens)		
	Predictors	Statistics		Predictors	Statistics		Predictors	Statistics		Predictors	Statistics	
Breasts	WED	R^2	0.7900	WED	R^2	0.753	WED	R^2	0.9008	WED	R^2	0.8114
		Adj. R^2	0.7700		Adj. R^2	0.654		Adj. R^2	0.8780		Adj. R^2	0.8007
	Interaction	α	0.6257		α	0.749	Interaction	α	1.1733	Interaction	α	1.0384
		β1	-0.0015	Interaction	β1	-0.007		β1	-0.0366		β1	-0.0004
	Peds	β2	-0.0010		β2	-0.001	Peds	β2	-0.0002	Siemen	β2	-0.1444
		β3	-0.2415					β3	0.1400		β3	0.1400
Lungs	WED	R^2	0.8604	WED	R^2	0.821	WED	R^2	0.9174	WED	R^2	0.8332
		Adj. R^2	0.8532		Adj. R^2	0.789		Adj. R^2	0.9094		Adj. R^2	0.8285
	Interaction	α	1.4165		α	0.749	Interaction	α	1.4523	Interaction	α	1.4932
		β1	-0.0282	Interaction	β1	-0.028		β1	-0.0407		β1	-0.0389
	Peds	β2	-0.0009		β2	0.000	Peds	β2	-0.0002	Peds	β2	-0.0004
		β3	-0.1859					β3	-0.1210		β3	-0.1386
Liver										WED	R^2	0.9175
											Adj. R^2	0.9155
											α	1.5266
										GE	β1	-0.0485
											β2	0.1378
Spleen										WED	R^2	0.8558
											Adj. R^2	0.8525
											α	1.3856
										Siemens	β1	-0.0406
											β2	-0.0836
Kidneys	WED	R^2	0.8532							WED	R^2	0.8836
		Adj. R^2	0.8464								Adj. R^2	0.8794
		α	1.3347							Toshiba	α	1.5369
	Peds	β1	-0.0411								β1	-0.0451
		β2	-0.0742							Siemens	β2	-0.0713
											β3	-0.1103

Table 10- Statistical measure of goodness of the liner fit for regional $CTDI_{vol}$ along with water equivalent diameter (WED) with improved statistics using categorical predictors and the interaction term for scanner-specific model across all organs.

Model	Siemens			GE			Toshiba			Pooled (GE+Toshoba+Siemens)		
	Predictors	Statistics		Predictors	Statistics		Predictors	Statistics		Predictors	Statistics	
Pooled (Breasts+Lungs+Liver+Spleen+Kidneys)	WED	R^2	0.8666	WED	R^2	0.9211	WED	R^2	0.8910	WED	R^2	0.8708
		Adj. R^2	0.8631		Adj. R^2	0.9173		Adj. R^2	0.8875		Adj. R^2	0.8687
	Interaction	α	1.4289		α	1.3967	Interaction	α	1.5242	Interaction	α	1.5871
		β1	-0.0427	Interaction		-0.0379		β1	-0.0453	Toshiba	β1	-0.0436
	Breasts	β2	-0.0001		β1		Breasts	β2	-0.0001		β2	-0.0001
		β3	-0.2312		β2	-0.0001		β3	-0.1162	Siemens	β3	-0.1043
	CHT	β4	0.0734				CHT	β4	-0.0553	Female	β4	-0.1257
	Female	β5	-0.0499	Breasts	β3	-0.1064				Peds	β5	-0.0258
	Peds	β6	-0.0731							Breasts	β6	-0.0413
											β7	-0.1673

As shown in Table 10-4, there were no improvements for liver and spleen-specific models for all three scanners once categorical predictors were used in the model. However, there were improvements (in terms of R^2 and adjusted R^2) for lung and breast-specific models for all three scanners and Siemens kidney-specific model.

Another observation that can be made from this table is the frequency of using the interaction term. The interaction of WED and $CTDI_{vol,Regional}$ seems to be only of significance for lung-specific and breast-specific models for individual scanners and across scanners. However, it is not used for any of the abdominal organs. Only once the models are generated based on pooled

organs, shown in Table 10-5, does the interaction term becomes a significant predictor for individual scanners and across scanners.

Figure 10-33 illustrates predicted values versus actual organ doses for the pooled scanner, pooled organs model. Figure 10-34 shows the more familiar plot of normalized dose versus size (WED) for both predicted and actual normalized organ doses. As shown in this plot, the categorical predictors allowed for a more broad fit of the data which can cover the spread of this dataset and relate it to differences among scanners, organs, and patients. Figure 10-35 shows predicted values versus actual organ doses as a scatter plot along with the identify line showing data points falling under and over the line.

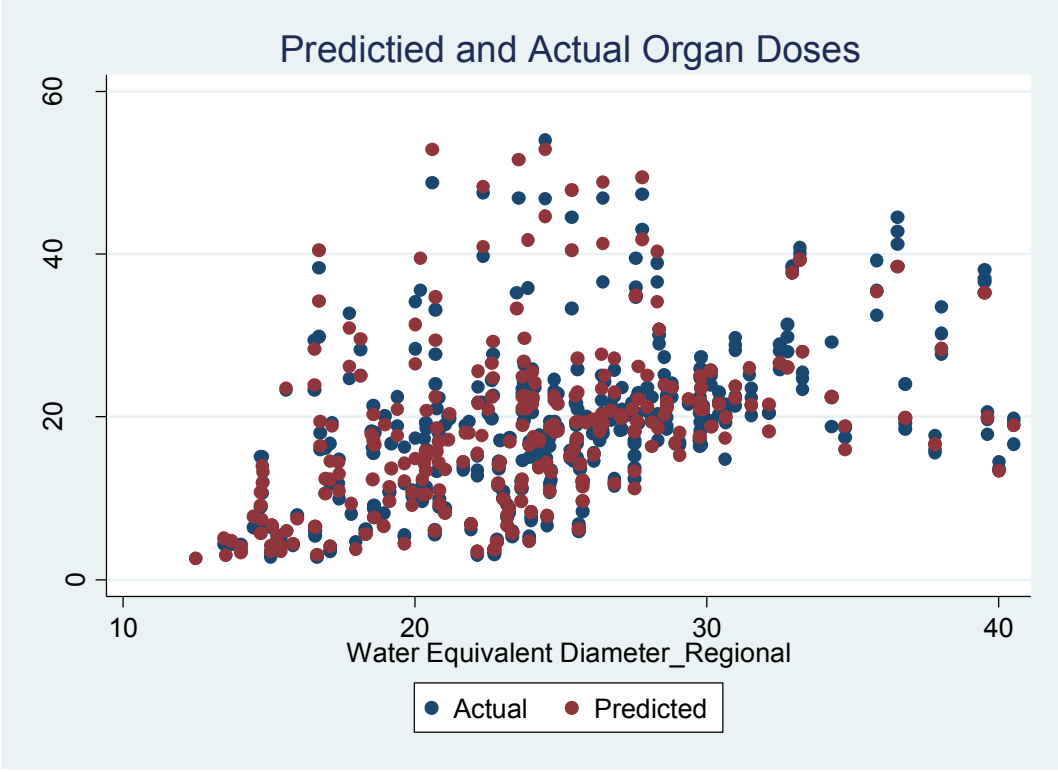

Figure 10-33 Predicted organ doses versus actual simulated organ doses shown for the entire training set using categorical predictors. Adding the categorical predictors increased R^2 and adjusted R^2 from 0.79 to 0.87.

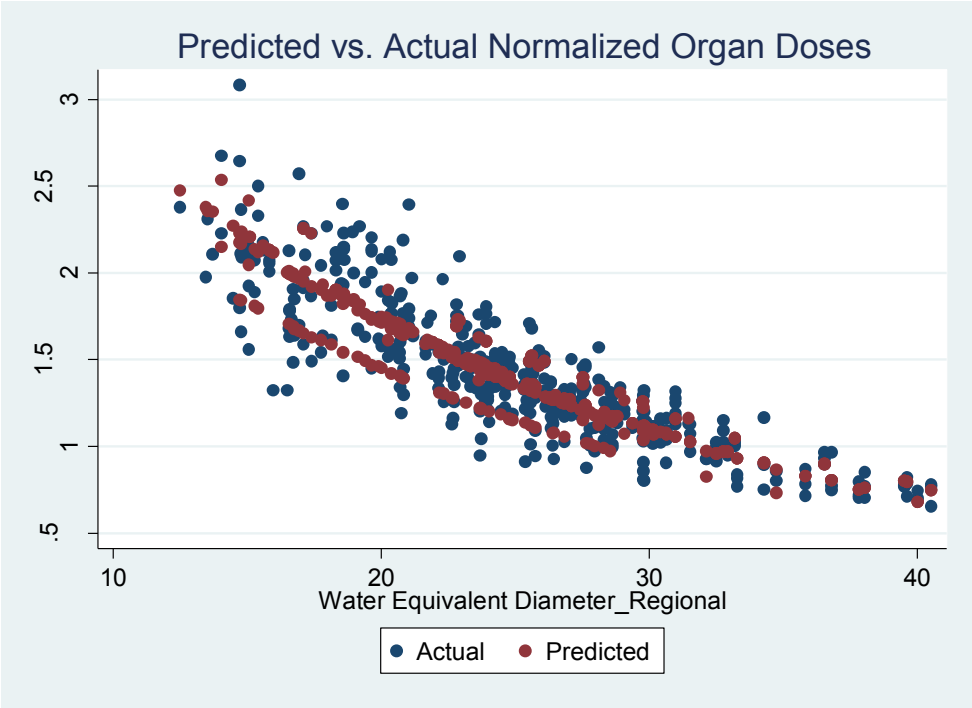

Figure 10-34 Predicted normalized organ doses by regional $CTDI_{vol}$ versus actual normalized organ doses for the entire training set using categorical predictors. Adding the categorical predictors increased R^2 and adjusted R^2 from 0.79 to 0.87.

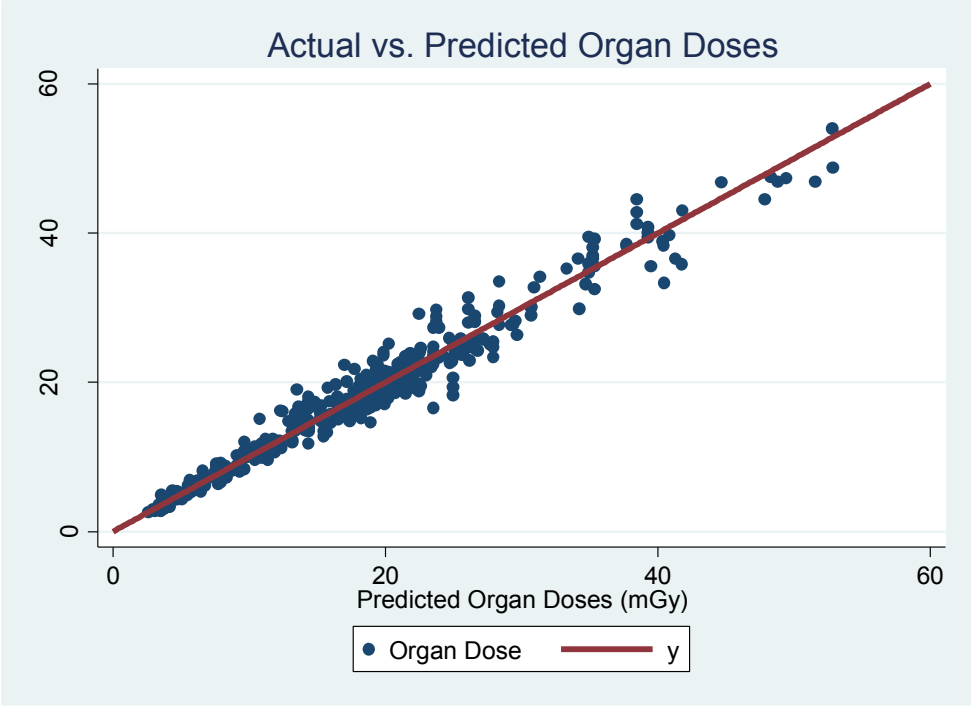

Figure 10-35 Predicted values versus actual organ doses falling along the identity line.

Now that appropriate models are generated, their performance can be tested using the test set. Each model was applied on the test set and compared to the true values (Monte Carlo simulated values of organ doses); by calculating percent differences for each model and then calculating the mean, minimum, maximum and standard deviation for the test set. Additionally, estimated organ doses from each model were compared to Monte Carlo simulated organ doses using t-test analysis. Tables 10-6 through 10-8 summarize the results for each scanner and organ.

Table 10-6 Mean, standard deviation, maximum, and minimum percent difference for each organ and each model when compared to detailed Monte Carlo estimates for each case in the test set from a Siemens Scanner. The asterisk represents p-values <0.05, indicating statistically significant difference between the estimates calculated using the model and the reference method, Monte Carlo simulations.

Siemens				
Breast				
Model Description	**% Mean**	**% SD**	**% Max**	**%Min**
Organ & Scanner Specific	4.48	17.81	48.27	-28.29
Organ-Specific	6.79	14.59	33.05	-15.43
Scanner-Specific	9.13*	14.69	36.26	-12.81
Pooled Data	8.81*	14.57	35.65	-14.66
Lung				
Organ & Scanner Specific	2.30	13.06	34.09	-26.83
Organ-Specific	1.74	14.52	33.94	-29.57
Scanner-Specific	6.47*	17.04	43.20	-24.22
Pooled Data	-2.13	14.98	28.79	-29.57
Liver				
Organ & Scanner Specific	2.91*	7.09	23.69	-8.66
Organ-Specific	3.72*	7.90	30.19	-9.54
Scanner-Specific	-1.91	7.78	14.76	-12.96
Pooled Data	1.94	7.80	23.11	-8.79
Spleen				
Organ & Scanner Specific	2.74	7.65	25.50	-10.23
Organ-Specific	3.08	8.70	24.05	-11.15
Scanner-Specific	2.82	8.54	20.83	-12.98
Pooled Data	2.50	11.38	26.76	-14.90
Kidney				
Organ & Scanner Specific	2.55	8.55	19.81	-13.05
Organ-Specific	2.93	12.34	30.05	-14.31
Scanner-Specific	2.25	9.80	21.18	-12.58
Pooled Data	2.03	13.38	29.00	-14.52

Table 10-7 Mean, standard deviation, maximum, and minimum percentages for each organ and each model from a GE Scanner. The asterisk represents p-values <0.05, indicating statistically significant difference between the estimates calculated using the model and the reference method, Monte Carlo simulations.

GE				
Breast				
Model Description	**% Mean**	**% SD**	**% Max**	**% Min**
Organ & Scanner Specific	2.29	16.06	33.61	-19.25
Organ-Specific	4.62	13.33	28.51	-11.86
Scanner-Specific	5.90	13.09	22.48	-11.02
Pooled Data	2.96	13.57	21.50	-16.81
Lung				
Organ & Scanner Specific	0.85	15.29	22.38	-29.58
Organ-Specific	2.24	13.21	23.03	-21.01
Scanner-Specific	-0.92	13.63	17.39	-27.03
Pooled Data	2.76	12.83	19.44	-23.29
Liver				
Organ & Scanner Specific	1.29	6.08	7.76	-12.45
Organ-Specific	0.87	6.12	7.60	-12.88
Scanner-Specific	2.30	6.35	8.70	-12.10
Pooled Data	2.06	6.14	8.01	-11.74
Spleen				
Organ & Scanner Specific	-6.62	8.32	2.51	-19.98
Organ-Specific	-8.45*	8.03	0.24	-21.48
Scanner-Specific	-4.72	8.89	5.38	-19.11
Pooled Data	-4.92	9.13	7.62	-18.79
Kidney				
Organ & Scanner Specific	-4.29	7.89	4.87	-19.22
Organ-Specific	-4.05	7.80	4.87	-18.71
Scanner-Specific	-0.65	8.10	8.68	-16.62
Pooled Data	-0.91	7.72	7.99	-16.29

In addition to the descriptive tables, the analysis is also graphically represented in Figures 10-36 through 10-39, with the latter showing the analysis for all three scanners combined. Overall, it seems the model created based on all data (pooled analysis) yields the worst performance among the models across scanners and organs. All the other organ and scanner-specific models seem to be performing equally across organs and scanner.

Table 10-8 Mean, standard deviation, maximum, and minimum percentages for each organ and each model from a Toshiba Scanner The asterisk represents p-values <0.05, indicating statistically significant difference between the estimates calculated using the model and the reference method, Monte Carlo simulations.

Toshiba				
Breast				
Model Description	**% Mean**	**% SD**	**% Max**	**% Min**
Organ & Scanner Specific	7.72	18.19	52.08	-14.86
Organ-Specific	6.51	13.93	38.45	-10.92
Scanner-Specific	6.85	12.83	31.81	-11.40
Pooled Data	4.32	10.49	22.60	-10.47
Lung				
Organ & Scanner Specific	3.04	6.91	15.60	-12.97
Organ-Specific	3.64*	8.18	21.00	-8.88
Scanner-Specific	3.58	8.85	23.09	-14.48
Pooled Data	7.07*	8.13	20.50	-9.38
Liver				
Organ & Scanner Specific	0.91	7.58	18.97	-9.36
Organ-Specific	-0.87	5.82	11.56	-10.46
Scanner-Specific	1.72	6.78	16.49	-8.75
Pooled Data	0.54	4.89	7.71	-6.31
Spleen				
Organ & Scanner Specific	-1.23	10.13	23.86	-17.05
Organ-Specific	-1.11	8.36	12.59	-11.57
Scanner-Specific	-3.49	9.70	18.94	-20.07
Pooled Data	-4.67	7.70	9.98	-18.08
Kidney				
Organ & Scanner Specific	0.23	10.39	28.54	-11.33
Organ-Specific	-0.87	8.14	19.04	-16.82
Scanner-Specific	-0.34	10.28	24.98	-19.18
Pooled Data	-1.53	8.39	15.56	-14.75

In both tables and the charts, the asterisk and the plus signs, respectively, represent p-values <0.05, indicating that the predictive model resulted in significantly different organ doses compared to Monte Carlo simulated organ dose estimates. Overall, the models appear to be predicting significantly different dose estimates compared to Monte Carlo simulations for breasts and liver, as also graphically illustrated in Figure 10-39.

Figure 10-40 shows the difference across models with categorical variables versus pooled data without the addition of any significant categorical variables.

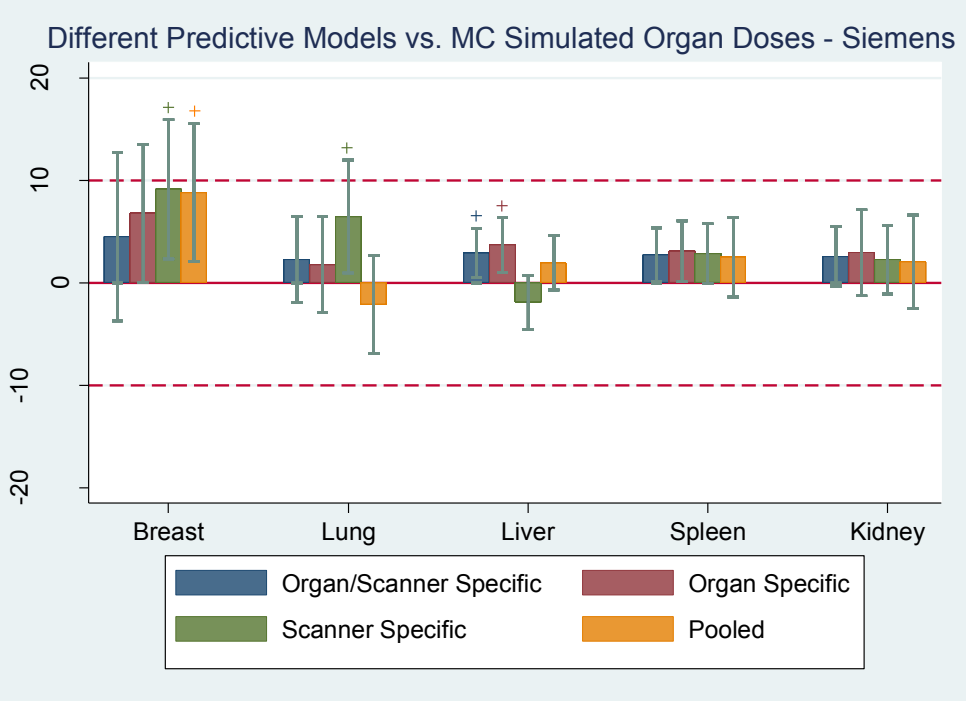

Figure 10-36 Mean percent difference, including error bars, between the reference method (Monte Carlo simulations) and each predictive model for Siemens data and for each organ. The plus signs represent p-values <0.05.

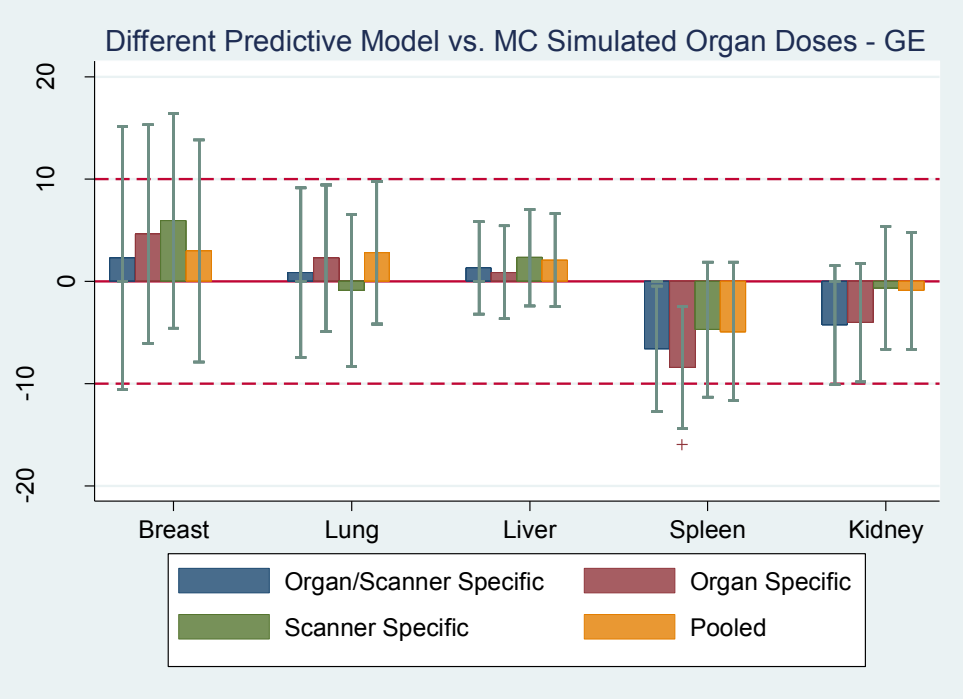

Figure 10-37 Mean percent difference, including error bars, between the reference method (Monte Carlo simulations) and each predictive model for GE data and for each organ. The plus signs represent p-values <0.05.

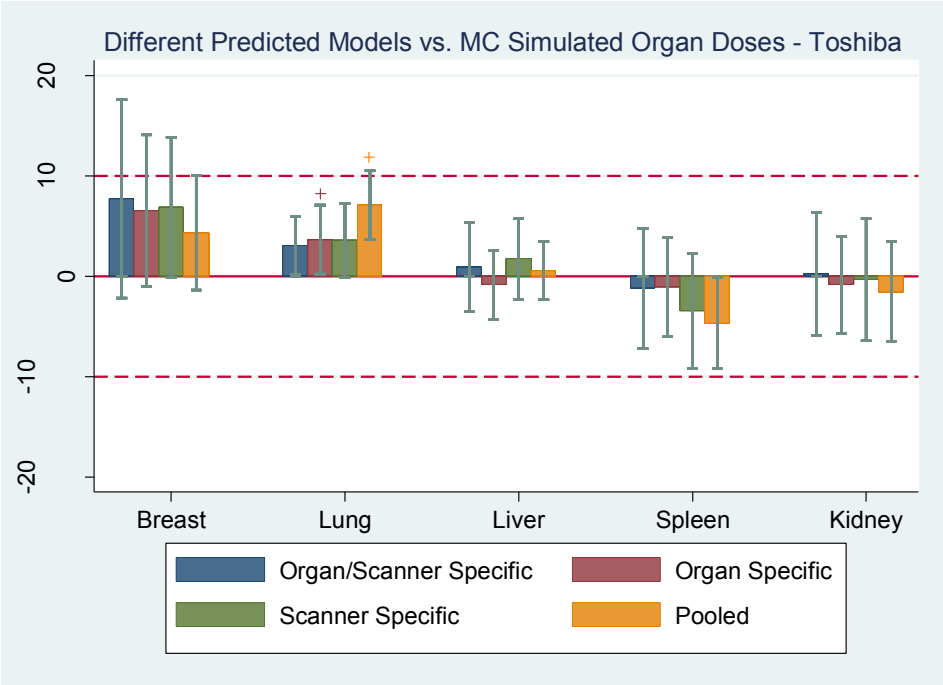

Figure 10-38 Mean percent difference, including error bars, between the reference method (Monte Carlo simulations) and each predictive model for Toshiba data and for each organ. The plus signs represent p-values <0.05.

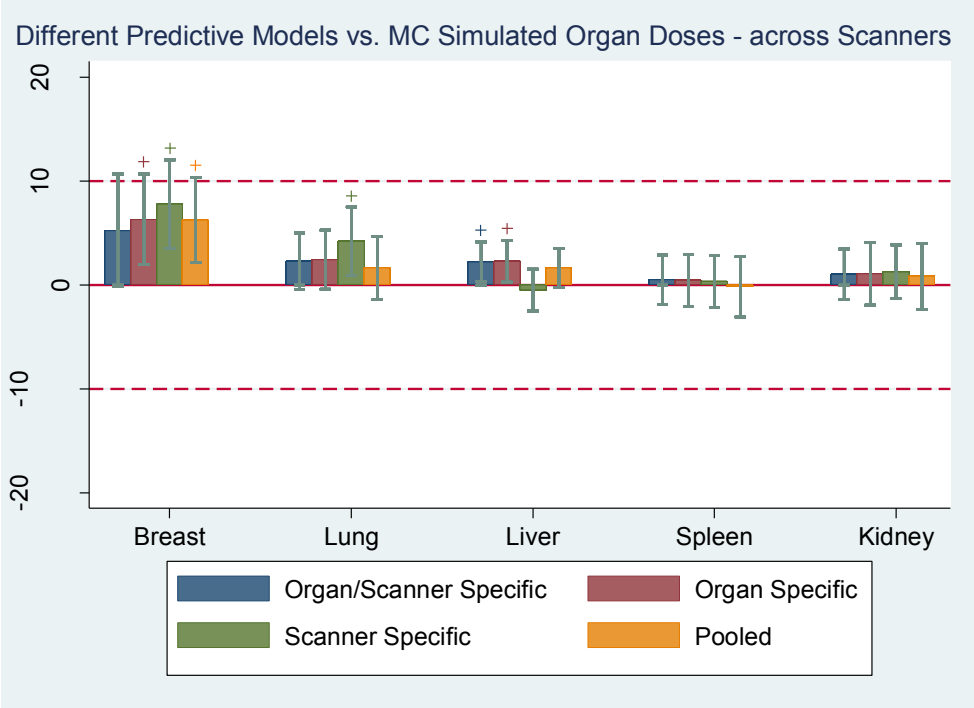

Figure 10-39 Mean percent difference, including error bars, between the reference method (Monte Carlo simulations) and each predictive model for all three scanners and for each organ. The plus signs represent p-values <0.05.

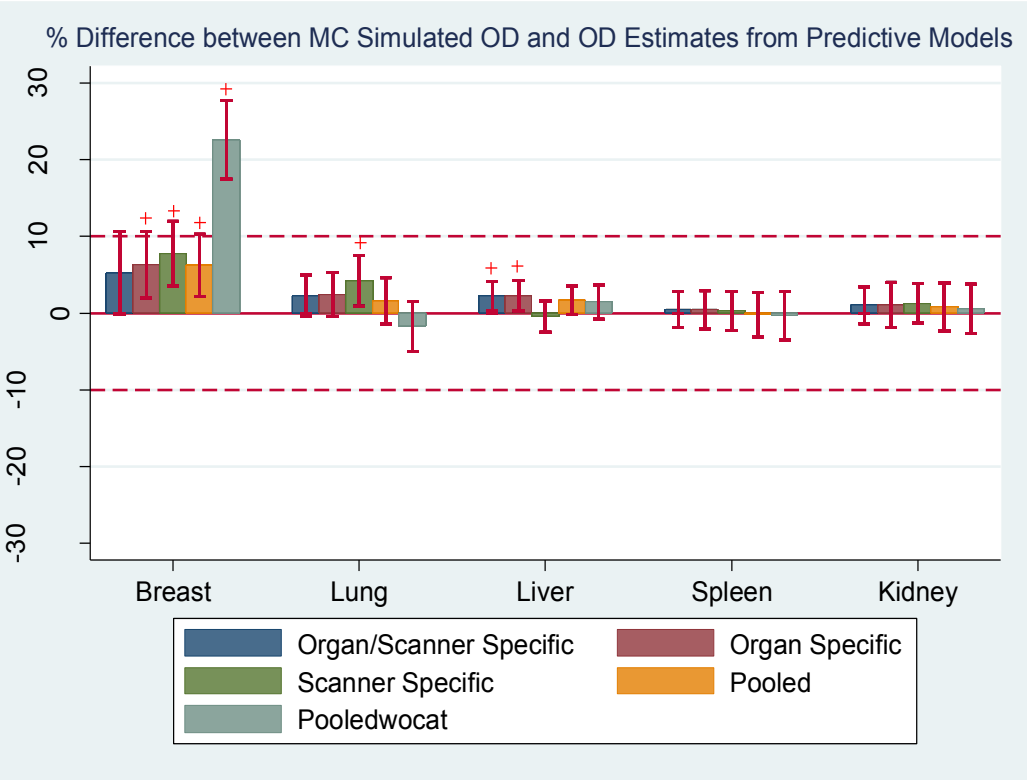

Figure 10-40 Mean percent difference, including error bars, between the reference method (Monte Carlo simulations) and each predictive model with categorical variables along with pooled model without addition of any categorical variables denoted as Pooledwocat. The plus signs represent p-values <0.05.

As seen in Figure 10-40, categorical variables, which were mostly significant for lung and breast dose, seem to be improving dose estimates compared to Monte Carlo simulated organ doses for only lungs and breasts.

10.3.2 Organ Dose as the Response Variable

As previously mentioned, instead of using $CTDI_{vol}$ as a normalization factor it can also be used as a predictor in the predictive model. First, a similar table as in the previous section was generated only for selected organs and scanners to look at differences between regional and global $CTDI_{vol}$ values as *predictors* in this case.

Table 10-9 Statistical measure of goodness of the liner fit for regional $CTDI_{vol}$ versus global $CTDI_{vol}$ as predictors for organ dose. β1 is the coefficient for water equivalent diameter and β2 is the coefficient for $CTDI_{vol}$.

Organ		$Organ\ Dose = CTDI_{vol,Regional}Ae^{-B\times WED}$				$Organ\ Dose = CTDI_{vol,Global}Ae^{-B\times WED}$			
		Siemens	**GE**	**Toshiba**	**Pooled**	**Siemens**	**GE**	**Toshiba**	**Pooled**
Breasts	**R^2**	0.90	0.97	0.99	0.96	0.82	0.98	0.99	0.91
	Adj. R^2	0.89	0.96	0.99	0.95	0.81	0.97	0.98	0.91
	RMSE	0.11	0.16	0.08	0.12	0.15	0.13	0.09	0.18
	A	1.23	0.91	1.47	1.26	0.15	1.04	1.08	0.76
	β1	-0.032	-0.013	-0.034	-0.03	0.005	-0.02	-0.010	-0.004
	β2	0.89	0.88	0.85	0.88	0.91	0.87	0.78	0.79
Kidneys	**R^2**	0.98	0.98	0.97	0.97	0.97	0.99	0.97	0.95
	Adj. R^2	0.98	0.99	0.97	0.97	0.97	0.99	0.96	0.95
	RMSE	0.08	0.09	0.10	0.11	0.09	0.07	0.11	0.13
	A	1.32	1.56	1.37	1.39	0.95	1.45	1.55	1.24
	β1	-0.05	-0.05	-0.02	-0.04	-0.03	-0.042	-0.04	-0.03
	β2	1.07	1.00	0.82	0.96	1.03	1.00	0.95	0.94
Pooled	**R^2**				0.94				0.94
	Adj. R^2				0.94				0.94
	RMSE				0.15				0.15
	A				1.46				1.08
	β1				-0.04				-0.02
	β2				0.94				0.89

In contrast to the previous results with response variable being the normalized organ dose, for the new response variable (organ dose) there is little to no improvement with regional $CTDI_{vol}$, while R^2 values are surprisingly high. Only a few selected possibilities are shown in Table 10-9, but an overall similar pattern and R^2 values were observed with other combination of organs and scanners. The higher R^2 in this table should not be compared to R^2 in Table 10-3 due to different

units of the response variable for each approach. To further understand the results, Figure 10-41 will illustrate the fit of some of these models.

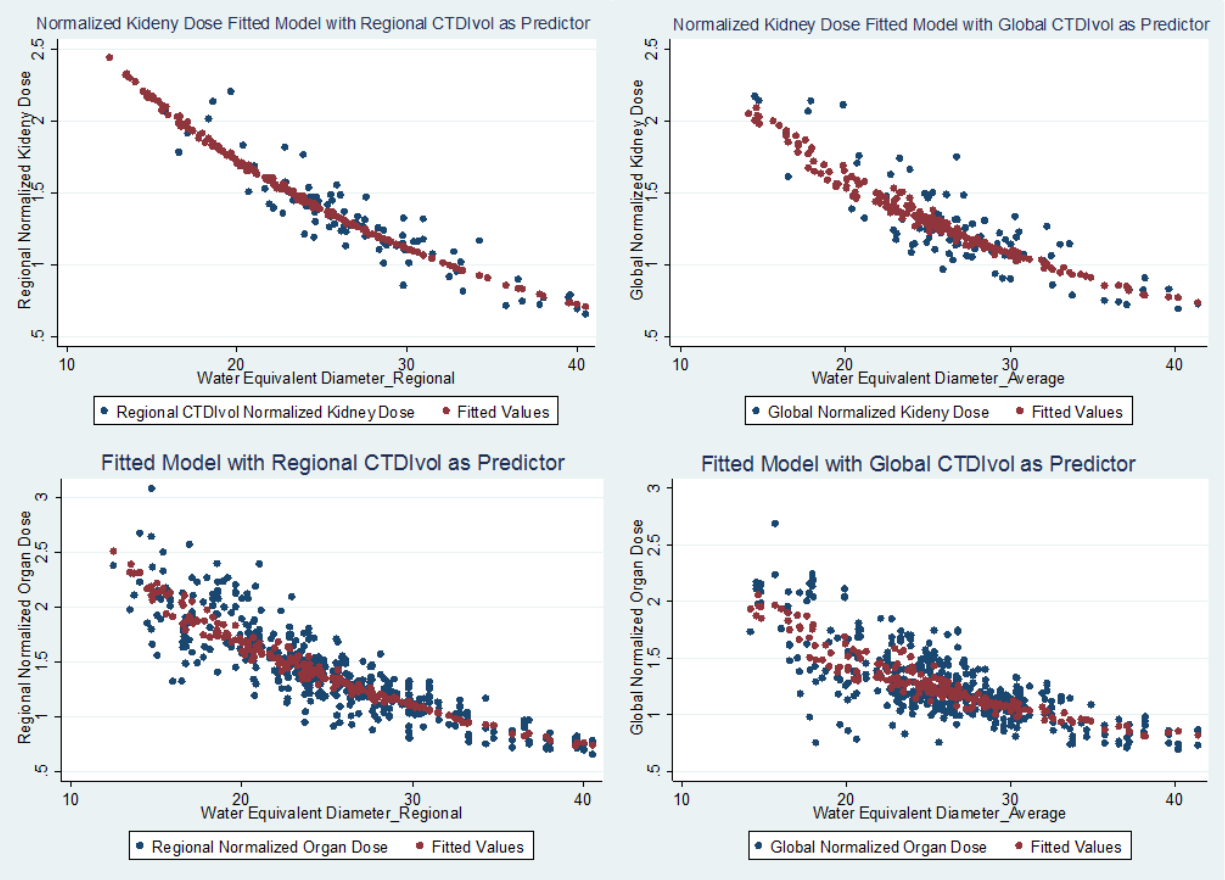

Figure 10-41 The top row charts illustrate fitted normalized kidney doses (red) versus actual normalized doses (blue) by regional $CTDI_{vol}$ (left) and global $CTDI_{vol}$ (right). Bottom row charts show fitted versus actual normalized organ doses (pooled data) using regional $CTDI_{vol}$ (left) and global $CTDI_{vol}$ (right) as the predictor in the model. None of the shown fits includes any categorical variables.

Comparing these results with the results from the previous section, a wider range of the data can be fitted using the predictive model once $CTDI_{vol}$ is used as a predictor (Figure 10-41). Using $CTDI_{vol}$ as a predictor allows for a wider fit without the categorical variables. In the previous section the fitted values fell on a single exponential line while using normalized dose as the

response variable and only size metric as the predictor. The more improved fit including a wider range of the data was achieved only after categorical variables were used in the model. While in the former approach, $CTDI_{vol}$ was predicted to be a linearly increasing variable with patient size, in this approach it's actual value, which is not only dependent on patient size/average tube current value, but also changes with other factors not simple to be modeled such as patient positioning, is made use of as a predictor. Hence in the latter approach fitted values show some variability caused by $CTDI_{vol}$ values used as predictors.

The two fits shown in the bottom row of Figure 10-41 used all data across scanners and organs without any categorical variables in the model. These fits were extended by adding significant categorical variables. The results of these fits are shown in Figures 10-42 and 10-43 for global $CTDI_{vol}$ and regional $CTDI_{vol}$, respectively. Table 10-10 shows these models with significant categorical variables. For both regional and global $CTDI_{vol}$, the interaction term (WED * $CTDI_{vol,Regional}$), which was a significant predictor in the previous section with normalized organ dose as the response variable, was not a significant predictor and therefore removed from the model.

$CTDI_{vol,\ Global}$

logorgandose	Coef.	Std. Err.	t	P>|t|	[95% Conf.	Interval]
waterequivalentdiameter_average	-.027753	.001936	-14.34	0.000	-.0315583	-.0239476
logctdivol_average	.9278163	.0127025	73.04	0.000	.9028483	.9527843
Toshiba	-.0458869	.0197529	-2.32	0.021	-.0847129	-.0070609
Siemens	-.1895625	.0174398	-10.87	0.000	-.2238421	-.155283
Liver	.1392893	.0206445	6.75	0.000	.0987108	.1798679
Spleen	.1446639	.0206445	7.01	0.000	.1040854	.1852425
Kidneys	.139272	.0206445	6.75	0.000	.0986935	.1798506
Lung	.1527905	.0188167	8.12	0.000	.1158045	.1897764
_cons	1.104163	.0380065	29.05	0.000	1.029458	1.178868

$CTDI_{vol,\ Regional}$

logorgandose	Coef.	Std. Err.	t	P>|t|	[95% Conf.	Interval]
waterequivalentdiameter_regional	-.038299	.0019406	-19.74	0.000	-.0421134	-.0344846
logctdivol_regional	.9002081	.0170934	52.66	0.000	.8666094	.9338069
Toshiba	-.0608185	.018755	-3.24	0.001	-.0976833	-.0239536
Siemens	-.0950613	.0153723	-6.18	0.000	-.1252772	-.0648455
Liver	.1445996	.0198136	7.30	0.000	.105654	.1835452
Spleen	.1499742	.0198136	7.57	0.000	.1110286	.1889198
Kidneys	.1445823	.0198136	7.30	0.000	.1056367	.1835279
Lung	.1843963	.0169464	10.88	0.000	.1510865	.217706
Peds	-.1173164	.0207008	-5.67	0.000	-.1580059	-.076627
_cons	1.475768	.0358445	41.17	0.000	1.405312	1.546224

Table 10-10 Significant predictors along with their coefficients for the predictive models based on pooled data using once $CTDI_{vol,Regional}$ as the predictor and once using $CTDI_{vol,Global}$ as the predictor.

Equation 10-13 shows the model based on the regional $CTDI_{vol}$ and water equivalent diameter.

$$Ln(Organ\ Dose) = \alpha + \{(\beta_1 \times Ln(CTDI_{vol,Regional})) + (\beta_2 \times WED) + (\beta_3 \times Toshiba) + (\beta_4 \times Siemens) + (\beta_5 \times Liver) + (\beta_6 \times Spleen) + (\beta_7 \times Kidney) + (\beta_8 \times Lung) + (\beta_9 \times Peds)\} \quad \textbf{Eq. 10-13}$$

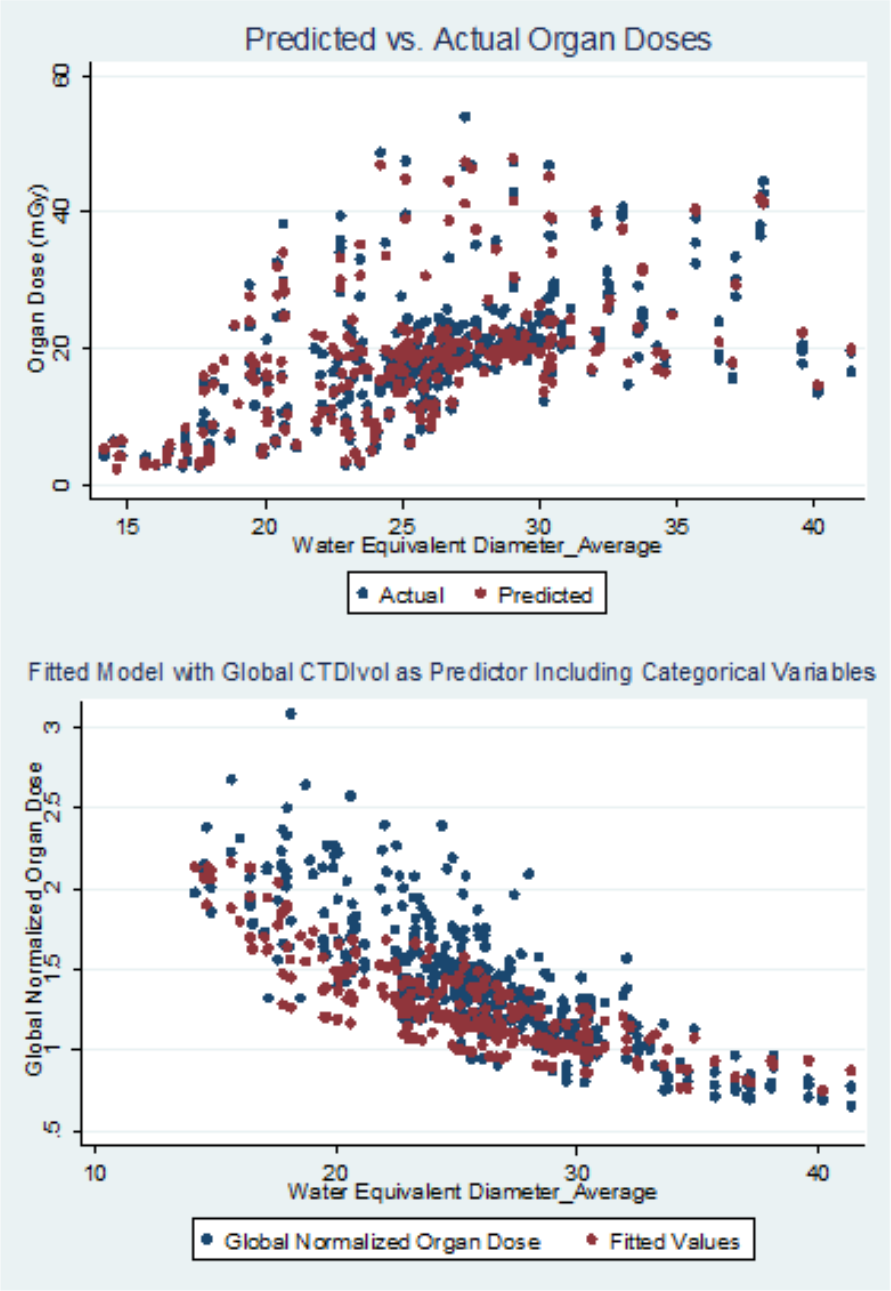

Figure 10-42 Top chart illustrate fitted absolute organ doses (red) versus actual Monte Carlo simulated doses (blue) using global $CTDI_{vol}$ as the predictor, while bottom chart shows predicted normalized doses (red) and actual simulated normalized doses (blue) using global $CTDI_{vol}$ as the normalization factor.

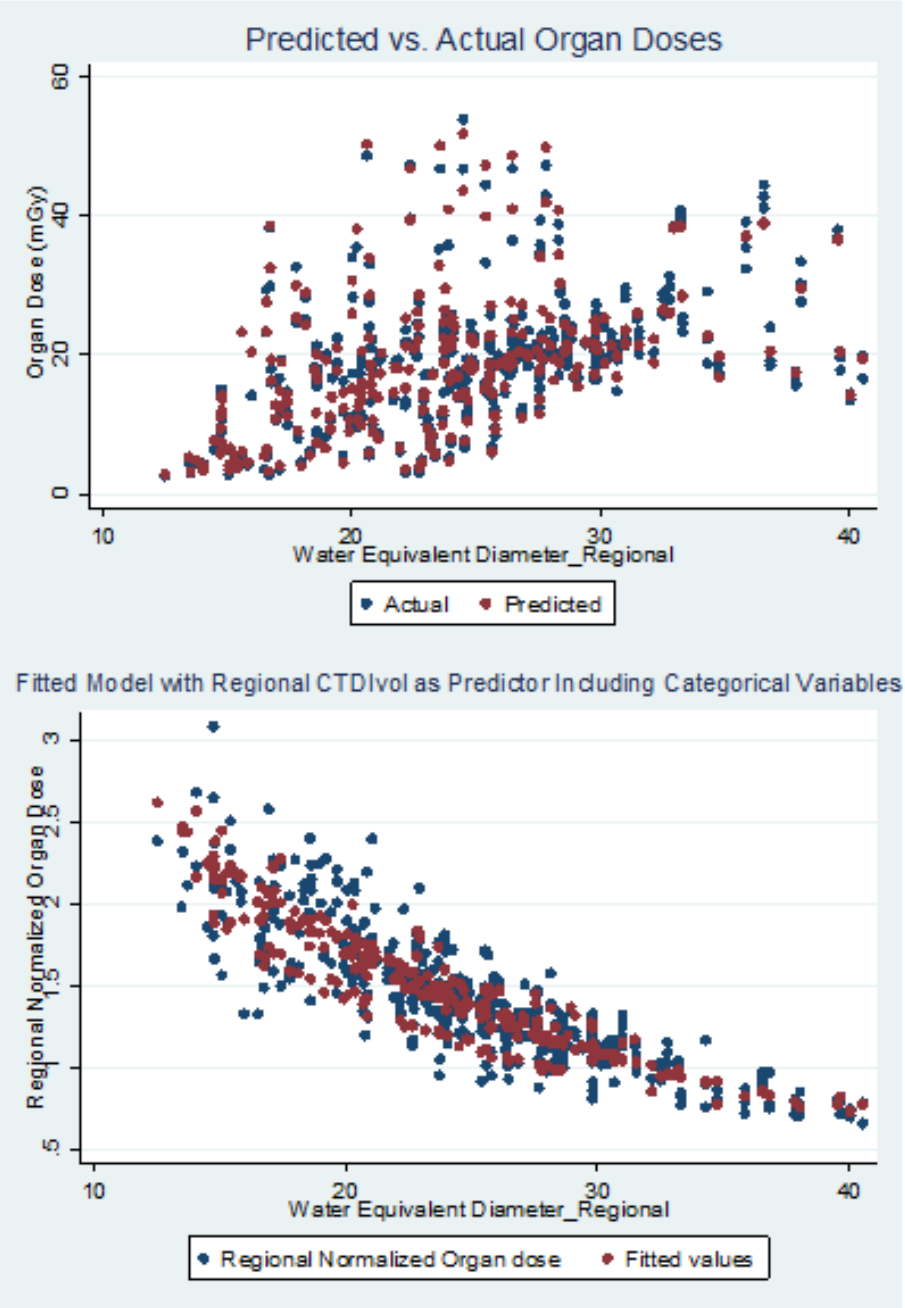

Figure 10-43 Top chart illustrate fitted absolute organ doses (red) versus actual Monte Carlo simulated doses (blue) using regional $CTDI_{vol}$ as the predictor, while bottom chart shows predicted normalized doses (red) and actual simulated normalized doses (blue) using regional $CTDI_{vol}$ as the normalization factor.

From the normalized fit, it is evident that regional $CTDI_{vol}$ performs as a better predictor than global $CTDI_{vol}$ (Figure 10-43). With the global $CTDI_{vol}$, the fit seems to be underestimating actual organ doses (Figure 10-42). When compared to actual organ doses by calculating percent mean, standard deviation, minimum, and maximum difference with respect to Monte Carlo simulated organ doses, the results indeed show an underestimation of dose when using global $CTDI_{vol}$ as a predictor compared to regional. Table 10-11 shows the statistical measures for individual organs.

Table 10-11 Mean, standard deviation, maximum, and minimum percentages for each organ and each model compared to Monte Carlo simulated organ doses. The asterisk represents p-values <0.05, indicating statistically significant difference between the estimates calculated using the model and the reference method, Monte Carlo simulations. Both models were generated using pooled data across both organ and scanners.

Across Scanners				
Breast				
Model Description	**% Mean**	**% SD**	**% Max**	**% Min**
Organ Dose-Global	-2.72*	18.37	77.48	-21.71
Organ Dose-Regional	6.60*	12.99	41.65	-16.03
Lung				
Organ Dose-Global	-8.65*	7.73	7.94	-37.41
Organ Dose-Regional	2.43	13.55	28.51	-31.03
Liver				
Organ Dose-Global	-8.49*	8.86	11.19	-28.68
Organ Dose-Regional	2.11	7.02	26.81	-14.68
Spleen				
Predictor Global $CTDI_{vol}$	-9.77*	10.51	13.76	-34.02
Predictor Regional $CTDI_{vol}$	0.69	9.65	23.71	-20.61
Kidney				
Organ Dose-Global	-9.43*	10.49	13.23	-32.36
Organ Dose-Regional	1.11	10.11	29.47	-18.60

As shown in Table 10-11, global $CTDI_{vol}$ is consistently underestimating dose across all five organs. Additionally, the results of the t-test indicate that there is statistically significant difference between estimated doses using global $CTDI_{vol}$ and actual Monte Carlo simulated

organ doses, as shown with the p-value <0.05. The results in Table 10-11 are also graphically represented using bar graphs. Plus signs indicate p-values <0.05 (Figure 10-44).

Finally, estimated organ doses using all predictive models are compared to Monte Carlo simulated organ doses and to each other. Figure 10-45 shows all models with in a plot showing mean percentage and standard deviation from the reference method.

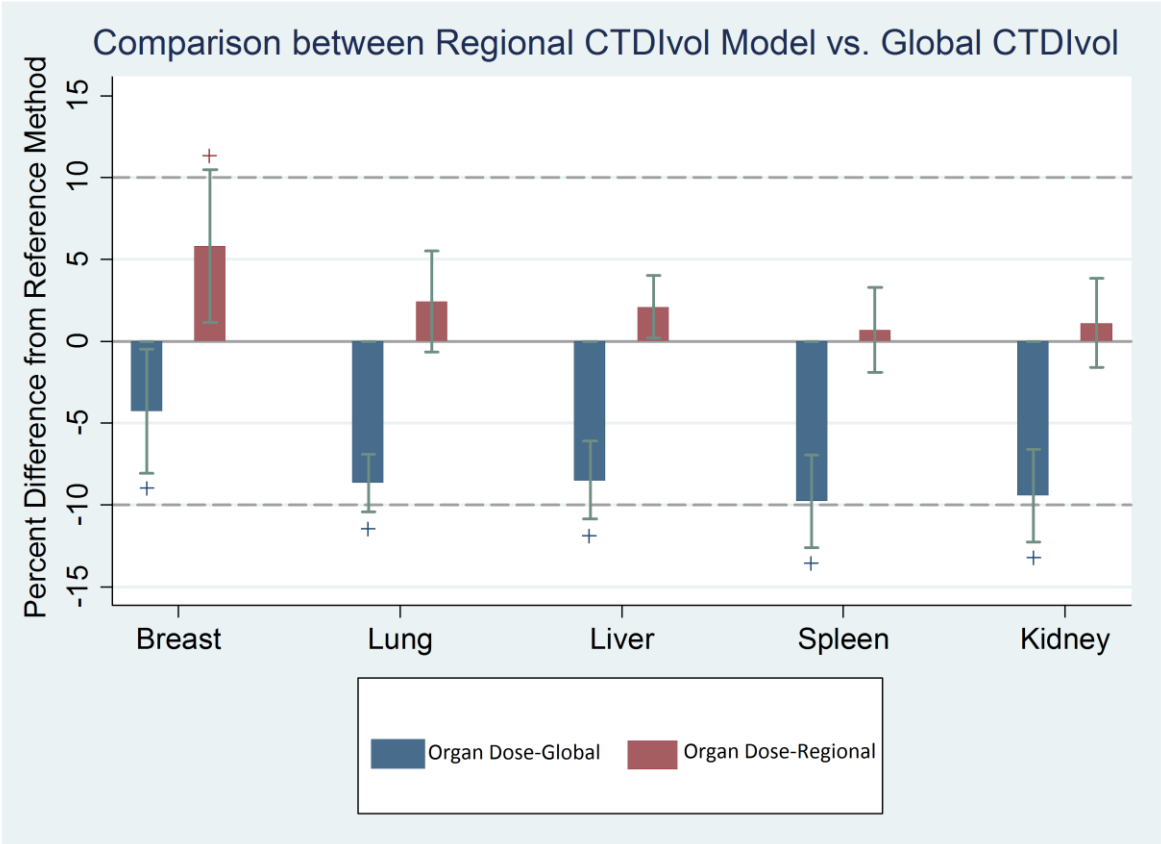

Figure 10-44 Mean percent difference between the reference method (Monte Carlo simulated organ doses) and estimates calculated using generated predictive methods. Plus sign indicates p-values <0.05.

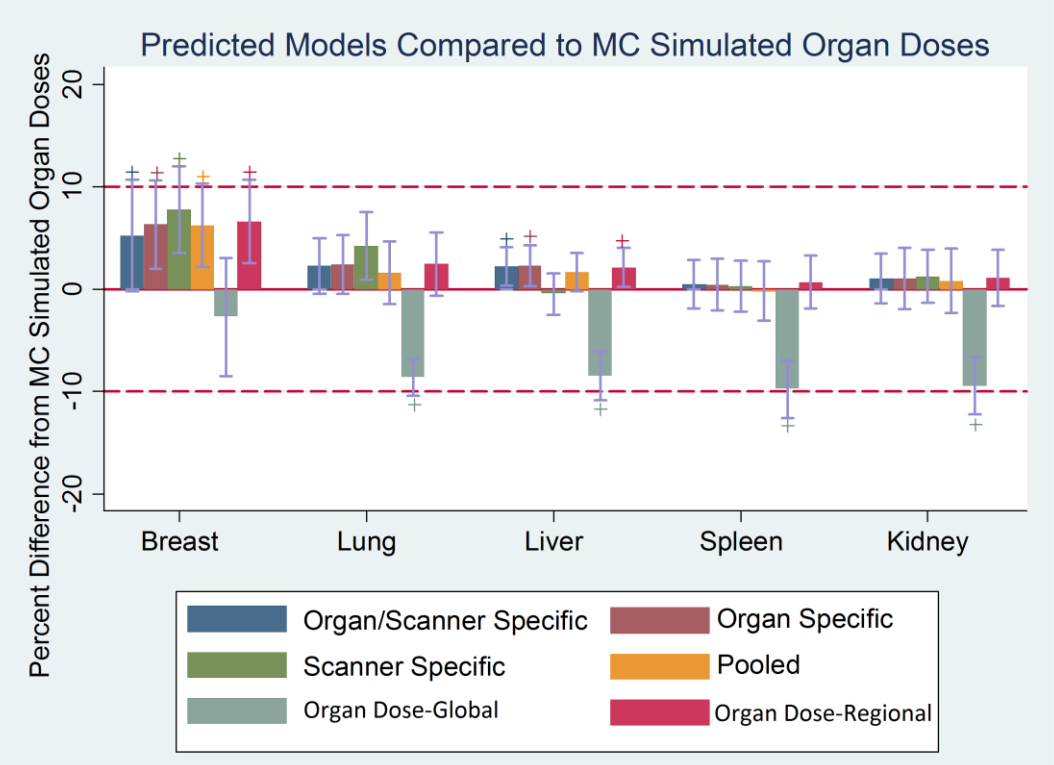

Figure 10-45 Mean percent difference between the reference method (Monte Carlo simulated organ doses) and organ dose estimates calculated using each predictive method.

Regardless of either regional $CTDI_{vol}$ used as normalization factor or as a predictor within the model, it is confirmed that regional information provides more accurate dose estimates for tube current modulated CT examinations compared to global $CTDI_{vol}$. Besides pooled model (denoted as Global) with global $CTDI_{vol}$ as predictor, all other models seem to be performing very similarly across organs, overall estimating organ doses within less than 10% of the actual Monte Carlo simulated organ doses.

10.4 Discussion and Conclusion

Computed Tomography Dose Index is a simple robust measure of CT dose output and while it is not patient dose, its usefulness as organ dose predictor is undeniable. As mentioned in the introduction, $CTDI_{vol}$ was used to normalize organ doses from fixed tube current CT exams resulting from different scanners to eliminate differences among scanners. However, its usefulness in TCM exams degenerates due to varying tube current which is a function of patient attenuation, hence very patient-specific. Additionally, across scanners there are differences in implementation and optimization of TCM, which further complicates the general relationship between tube output and patient attenuation. Regional $CTDI_{vol}$ was observed to take into account varying tube current by concentrating on regions of similar attenuation properties.

Once regional $CTDI_{vol}$ was used to generate organ-specific models across scanners and pooled organs and scanner models, scanners were significant categorical predictors in explaining the response variable, i.e. normalized dose. This indicates that, across individual scanners, regional $CTDI_{vol}$ is capable of eliminating differences among different TCM outputs resulting from different patient sizes, as shown in Chapter 8; however, when explored across different scanners, it is not capable of completely eliminating differences across scanners, due to differences in TCM algorithms. That said, regional $CTDI_{vol}$ is still a good predictor within individual scanners, just not across all scanners due to differences in TCM algorithms. This is also evident from results shown in Table 10-3. The improvement of using regional $CTDI_{vol}$ over global $CTDI_{vol}$ was more severe for Siemens scanner than it was for GE and Toshiba, which could be another indication for differences in TCM algorithms. Taking a closer look at TCM functions from all three scanners, a more consistent pattern and more extreme modulation of the tube current is observed for Siemens scanner compared to GE and Toshiba. Figures 10-46 and 10-47 show

different TCM functions from different CT scanners separated for chest and abdomen/pelvis, respectively. In addition to these typical TCM functions with minor z-axis modulation shown for GE and Toshiba, there were several patients with almost no modulation at all. As seen in these Figures, minor modulation of the TCM implies small differences between regional and global $CTDI_{vol}$ values; hence the reason for the small improvement of the R^2 with regional $CTDI_{vol}$ compared to global $CTDI_{vol}$ for these two scanners could be their moderate modulation of tube current along the z-axis. This claim certainly needs further evaluations and experiments to be confirmed; such as scanning of the same anthropomorphic phantom with each of these scanners and observation of the detailed TCM function (x-y and z modulation of the tube current) rather than just the z-axis-only modulation, which was the only available TCM information for GE and Toshiba, which was extracted from the DICOM header of axial CT images.

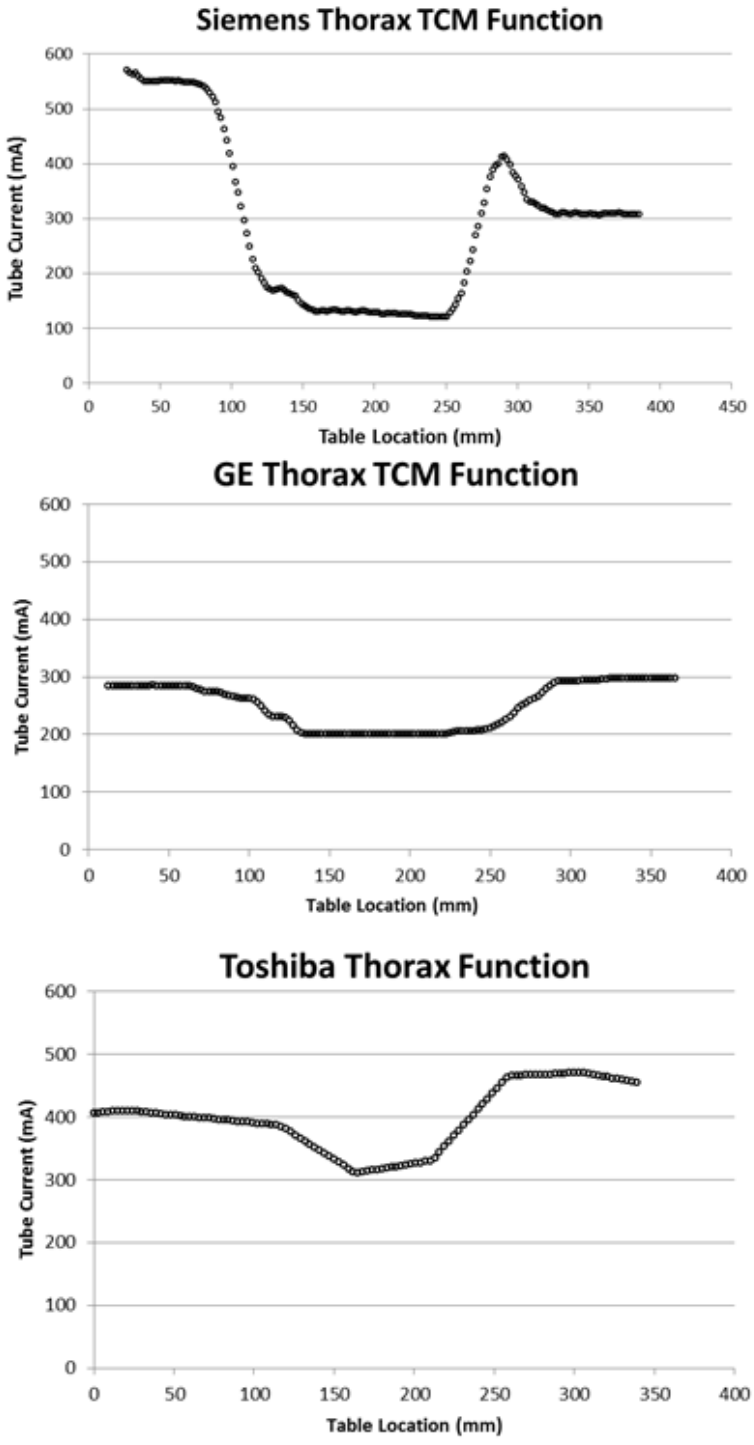

Figure 10-46 Typical z-axis-only TCM functions of thorax shown for each CT scanner manufacturer used in this dissertation.

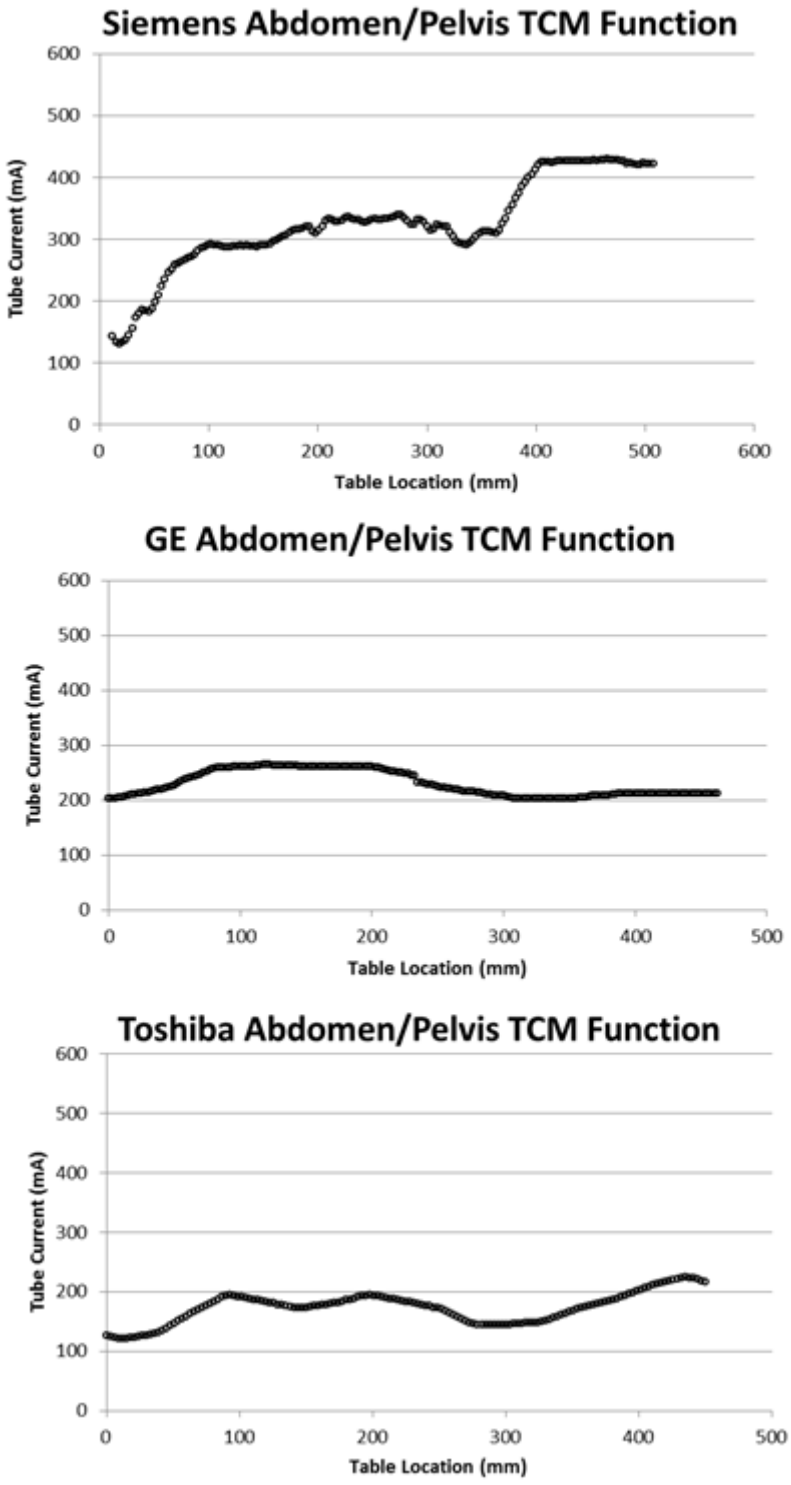

Figure 10-47 Typical z-axis-only TCM functions of abdomen/pelvis shown for each CT scanner manufacturer used in this dissertation.

As shown in Figures 10-46 and 10-47, for both GE and Toshiba the maximum tube current does not seem to be reaching 500 mA or higher for chest and 300 mA or higher for abdomen pelvis. As mentioned in Chapter 3, both of these scanners require the user to set both a maximum and minimum the tube current, along with a noise value using standard deviation of pixels. The minimum and maximum mA are acting as boundaries for the modulated tube current and it seems the output of the TCM function is heavily dependent on these specific settings. This would suggest that the profile of the TCM function in GE and Toshiba scanners is highly dependent on the used protocol, specifically on set minimum and maximum tube current values. Protocols are not consistent across hospitals, with the implication that the outcome of TCM algorithms in GE and Toshiba scanners is site-specific, i.e. different sites using the same scanner models may have different TCM functions. GE and Toshiba site-specific TCM algorithms suggests that predictive models based on data from GE and Toshiba may not be generalizable across other GE and Toshiba scanners from other sites.

However, the results of this study do indicate that there is some uniformity across sites, the patient models generated using Toshiba data consists of images received from two different institutions. All adult patient images were collected at UT Southwestern Medical Center, while pediatric images were obtained from Arkansas Children's Hospital. As illustrated in Figure 10-48 top, absolute doses from these two institutions stand out as two distinct populations of datasets. However, after normalizing these organ doses with regional $CTDI_{vol}$, all data points fall nicely along the same line, eliminating difference in scan parameters including differences in set minimum and maximum tube current. Additionally, when Toshiba-specific pooled-organs model was constructed, categorical predictor "Peds" resulted in a statistically insignificant predictor of

organ dose. This suggests that, normalization of pediatric and adult doses eliminates differences in imaging protocols including set minimum and maximum tube current values.

Similar plots are shown for GE data in Figure 10-49. Both pediatric and adult patient models were obtained from UT-MD Anderson and as shown in Figure 10-49 top, the absolute organ doses from both populations fall along the same along line when data shown in red box is eliminated. These data points belong to obese patients with “maxed-out” tube current, which results in doses comparable to a fixed tube current scan.

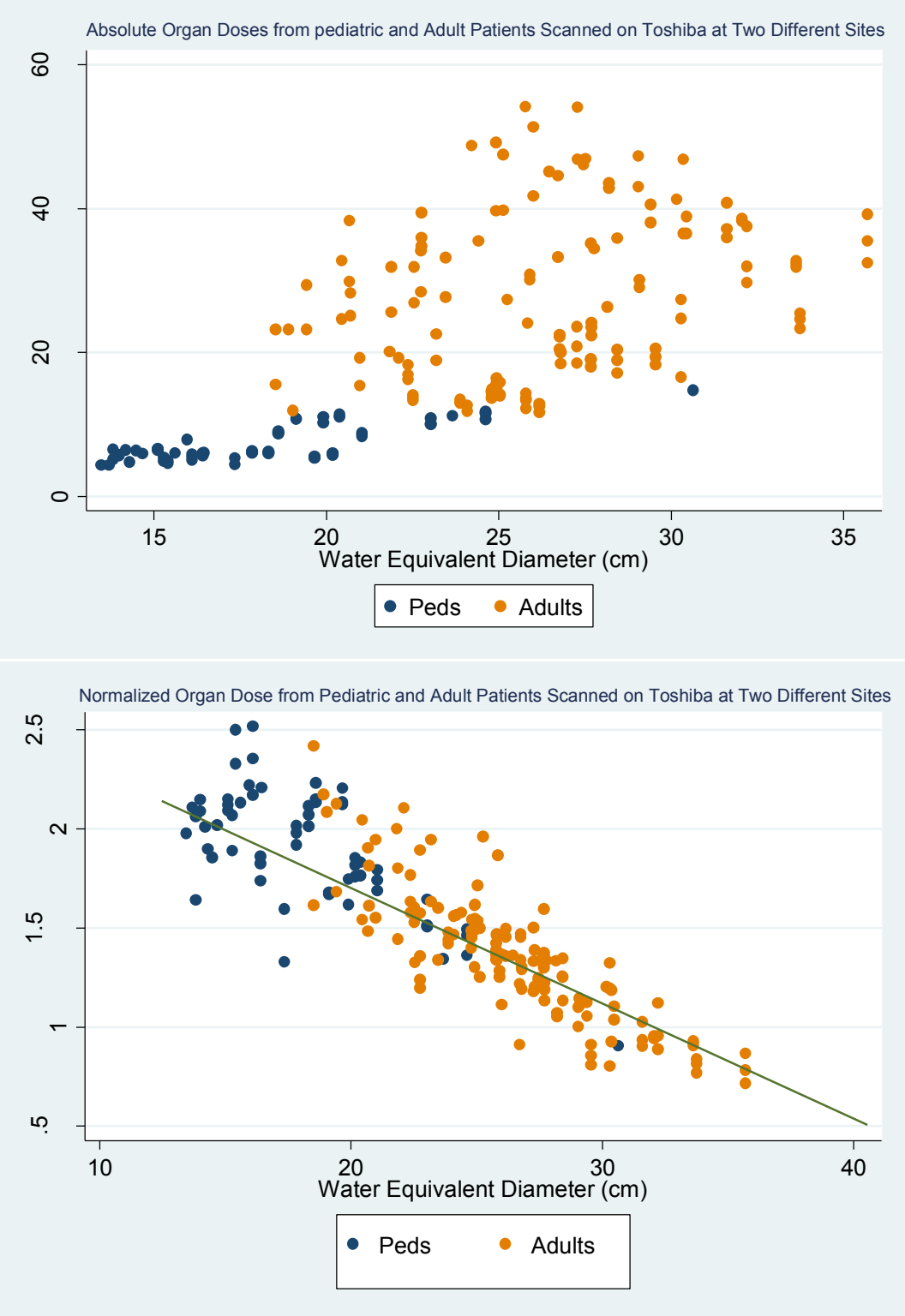

Figure 10-48 Top, absolute organ doses for pediatric and adult patients scanned on Toshiba scanner at different sites versus water equivalent diameter. Bottom, doses normalized by $CTDI_{vol,Regional}$ and shown as a function of water equivalent diameter.

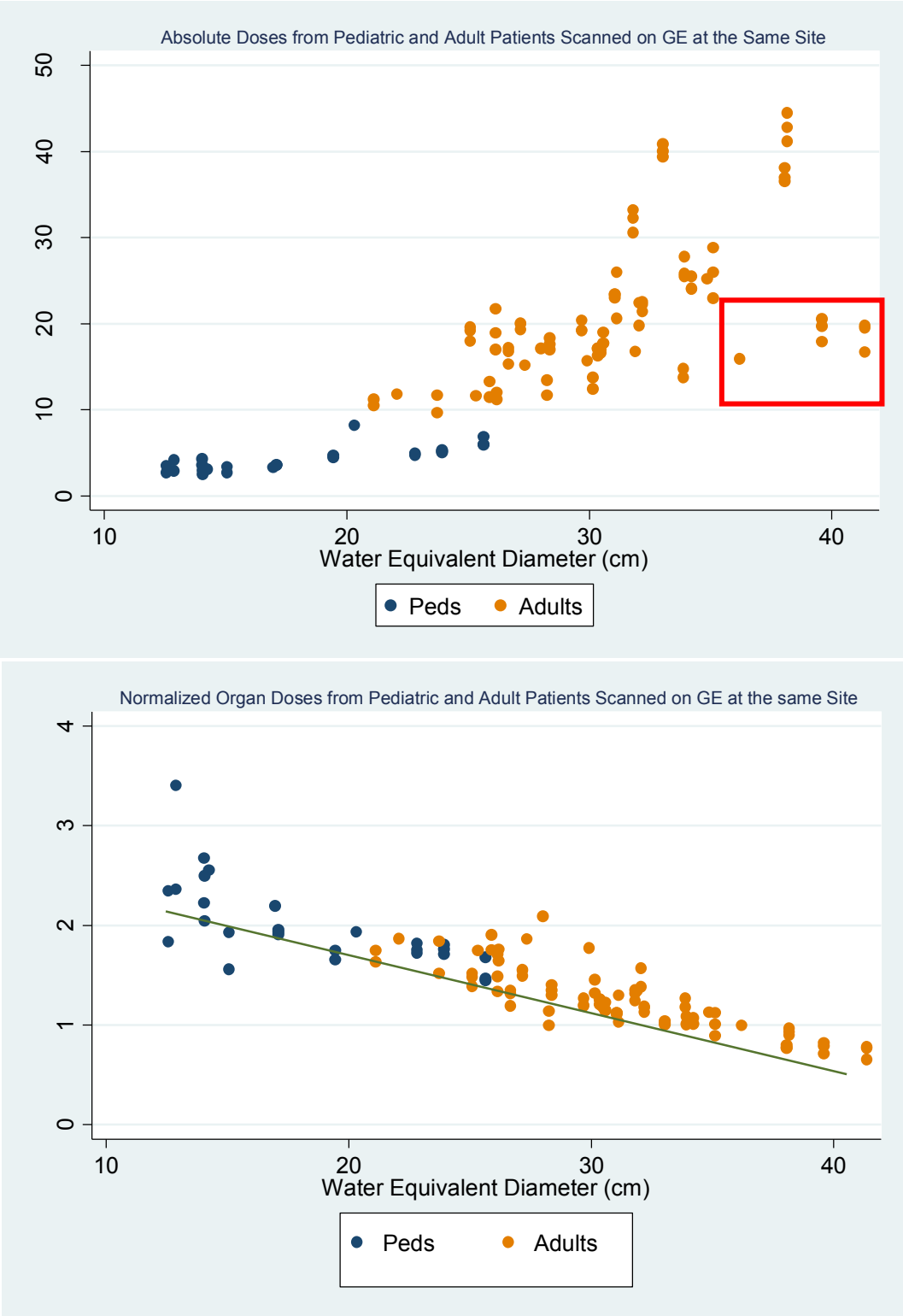

Figure 10-49 Top, absolute organ doses for pediatric and adult patients scanned on GE scanner at the same site versus water equivalent diameter. Bottom, doses normalized by $CTDI_{vol,Regional}$ and shown as a function of water equivalent diameter.

Although the interaction between size and $CTDI_{vol}$ was significant for almost all pooled data models (except for regional and global models using $CTDI_{vol}$ as predictor in Section II of the analyses) the contribution towards explaining the response variable was statistically insignificant. Figure 10-50 shows all models compared to Monte Carlo simulated organ dose. The top bar graph shows models without the interaction term, while the bottom chart shows results from models with the interaction term added. As evident by these two charts, there is minor difference between results when the interaction term is used versus when it is not utilized in creating the predictive dose model.

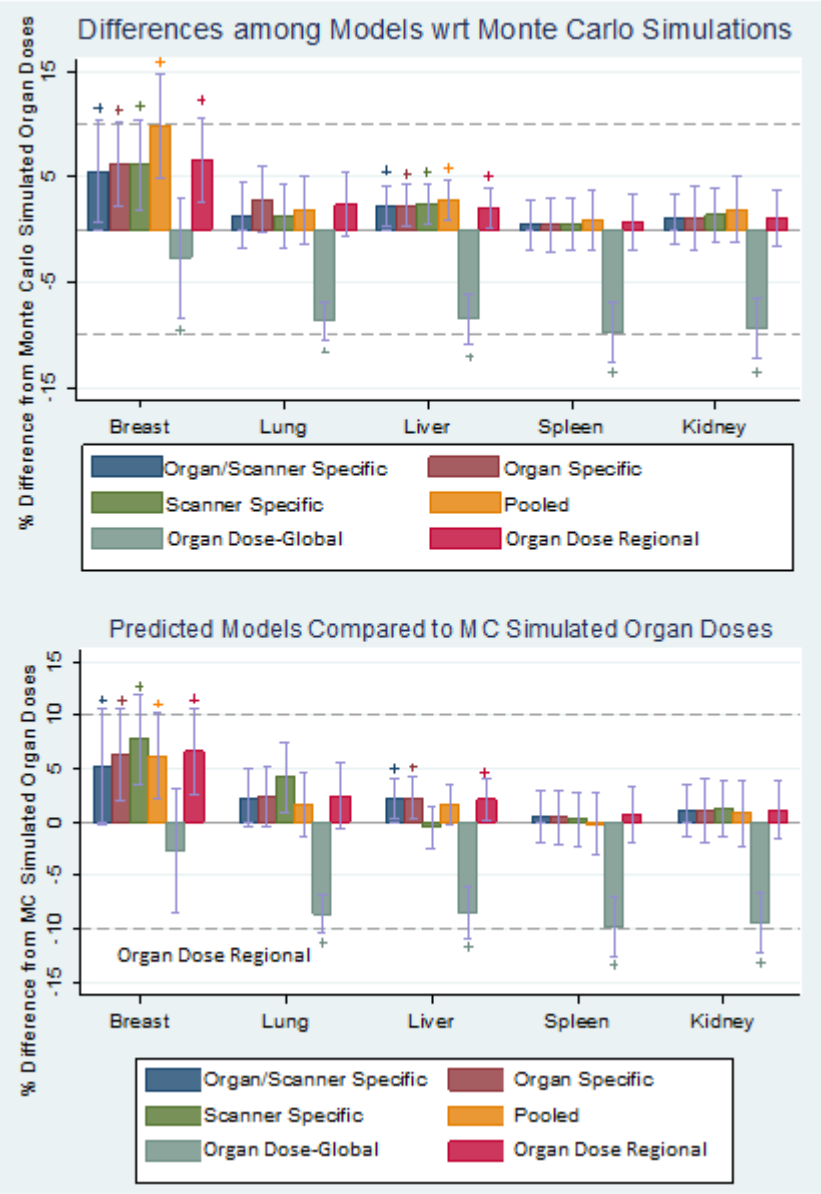

Figure 10-50 Top chart illustrates comparisons between individual models and Monte Carlo simulated organ doses without the interaction between size and $CTDI_{vol}$ as an additional predictor, while bottom chart demonstrates same comparisons with adding interaction of size and $CTDI_{vol}$ as a predictor.

To summarize, predictive models with different levels of detail were constructed using global and regional $CTDI_{vol}$ and an attenuation-based metric, the water equivalent diameter. All models were tested using a separate test set and compared to actual Monte Carlo simulated organ doses.

Overall the predicted values based on regional $CTDI_{vol}$ were within less than 10% from actual Monte Carlo simulated organ doses across all organs and all scanners. Table 10-12 summarizes different models and their accuracy of estimating organ dose as compared to Monte Carlo simulated organ doses along with a description of the actual model for assessing each model's complexity in terms of computational burden. Gray areas indicate the model with worse performance.

Table 10-12 Summary of the accuracy and complexity of each constructed dose predictive model.

Model		Definition	Accuracy of Dose Estimates across all Organs and Scanners			Multiple Equations	Multiple Coefficients
			Max. Mean % Diff	Max. % STD	Max. % Diff		
Section I	Organ- and Scanner-Specific	Built for each organ and scanner, i.e. Liver-specific, Siemens-specific model – requires regional $CTDI_{vol}$	7.7	18.2	52.0	Yes	Yes
	Organ-Specific	Built for each organ across all scanners, i.e. liver-specific model – requires regional $CTDI_{vol}$	8.5	14.6	38.3	Yes	Yes
	Scanner-Specific	Built for each scanner across all organs, i.e. Siemens-specific model – requires regional $CTDI_{vol}$	9.0	17.04	43.2	Yes	Yes
	Pooled	Built across all organs and all scanners – requires regional $CTDI_{vol}$	8.8	15.0	35.6	No	Yes
	Pooled w/o Categorical Variables	Built across all organs and all scanners w/o categorical variables – requires regional $CTDI_{vol}$	23.0	29.0	98.0	No	Yes
Section II	Organ Dose-Regional	Built across all organs and all scanners – requires regional $CTDI_{vol}$	6.6	13.6	41.7	No	Yes
	Organ Dose-Global	Built across all organs and all scanners – Does not required regional $CTDI_{vol}$	9.8	18.4	77.5	No	Yes

A global model based on global $CTDI_{vol}$ value provided the worst estimates compared to Monte Carlo simulated organ doses across organs and scanners. As also suggested by the predictive fit of this model, the estimates consistently underestimated actual simulated organ doses across all organs. All the other models seem to be performing equally in estimating organ doses. While more specific models to organs and scanner performed slightly better compared to the pooled-data models "Organ Dose-Regional" and "Pooled", the differences are negligible. In terms of complexity, while "Organ Dose-Regional" and "Pooled" models each provide a single predictive equation for organ dose estimations which applies to all organs and scanners using organs and scanners as predictors, organ and scanner-specific models result in multiple predictive equations. Hence, the "Pooled" model provides reasonable estimates and is simple enough to be used as a single predictive dose equation to estimate organ dose from different CT scanners. In terms of accuracy and ability to estimate simulated organ doses within reasonable ranges, all models based on regional $CTDI_{vol}$ are performing equally and could be used; however in terms of simplicity the "Pooled" model, which provides a single equation to account for different scanner manufacturers and organs, is recommended over scanner and organ specific models, which provide multiple equations for individual scanners and organs.

CHAPTER 11: CT DOSE ESTIMATES FROM PREDICTIVE MODELS: HOW CLOSELY DO THEY APPROXIMATE DETAILED MONTE CARLO BASED ORGAN DOSE ESTIMATES AND OTHER DOSE ESTIMATION METHODS?

The purpose of this chapter is to evaluate the generated and tested predictive model from the previous chapter against currently used CT dose metrics, including $CTDI_{vol}$, the SSDE metric from AAPM TG 204, and estimates from the ImPACT

CT dose calculator spreadsheet (which are based on NRPB report 250) as well as detailed Monte Carlo based organ dose estimates provided for each patient

11.1 INTRODUCTION

The results from Chapter 10 demonstrated the feasibility of estimating organ doses from TCM CT examinations using predictive models based on regional information on the output of the scanner and patient attenuation. The purpose of this chapter was to evaluate this model's improved capabilities to estimate organ dose by comparing its results against other, currently used CT dose metrics. From all currently used metrics, only the ImPACT dose spreadsheet provides estimates of organ doses and those are limited to fixed tube current exams. The Size Specific Dose Estimates (SSDE) is dose to the center of the scan volume adjusted for size, which is based on a physical measure of patients' dimensions - the effective diameter. Finally, as often noted, $CTDI_{vol}$ is simply dose to a standard homogenous PMMA phantom and not patient dose.

The ImPACT CT Dosimetry package is a widely used spreadsheet calculator which is based on the NRPB R250 conversion factors published in 1991 [38]. These conversion factors were approximated from single detector geometries and continuous axial scans using the geometric MIRD phantom patient model. The simple Excel sheet allows the user to choose the scan length

using a display of the MIRD phantom, along with the scanner, scanner model, kVp, mAs pitch, and collimation. The output provided for the set of selected parameters is a list of organ dose estimates which are based on conversion factors generated using Monte Carlo simulations. These conversion factors are based on CT scanners available in the 1990s and to be able to estimate dose from currently used multi-detector CT scanners, another set of conversion factors are used to match modern scanners with older versions on CT scanner available two decades ago.

As mentioned before, the mathematical hermaphrodite phantom, MIRD, is used as the standard man for all the calculations. Besides providing only estimates for currently used multi-detector scanners, another major drawback of ImPACT is that unless results are adjusted for size, with the MIRD phantom, doses are either an underestimation for smaller patients or an overestimation for larger patients.

Besides not being able to estimate dose to individual patients using patient-specific habitus, ImPACT does not adjust for TCM and therefore is only capable of estimating dose from fixed tube current exams. Nevertheless, ImPACT is used frequently in the clinic by physicists to report dose to concerned patients. On the other hand, ImPACT is the only method capable of providing organ doses necessary for calculating risk from a procedure.

A recently developed metric, mostly motivated by the pediatric community, is the Size Specific Dose Estimates (SSDE). While CT manufacturers are required to report $CTDI_{vol}$ from each exam, until recently there were no standards on what size phantom to be used to consider patient size, which resulted in significant confusion as different manufacturers used different reporting schemes. Some manufacturers report $CTDI_{vol}$ based on the 32cm phantom for all body examinations without considering patient population, i.e. adults versus pediatrics; others used the

32 cm phantom for reporting adult body scans and the 16 cm diameter phantom for pediatric body scans. The 16 cm phantom is consistently used for all head scans. This was concerning to the pediatric community since the reported dose based on the 32 cm phantom is an underestimation for small children. Clearly, there was a need for adjusting $CTDI_{vol}$ based on patient size and so AAPM Task Group 204 was assigned the task of improving upon $CTDI_{vol}$ to account for patient size. SSDE is based on Monte Carlo simulations and actual measurements of fixed tube current scan. Simulated and measured doses in different size phantoms and patient models were normalized by $CTDI_{vol}$ in order to eliminate differences between scanners and enhance the size dependency of dose. The outcomes of this Task Group are the so called f-factors as a function of effective diameter, which are multiplied by scanner-reported $CTDI_{vol}$ to adjust for patient size.

This was a huge step towards patient-specific dosimetry; however, SSDE fails to take into account TCM exams. In addition, all the measurements and simulations were performed on homogenous phantoms and abdomen simulations of patient models, respectively. Additionally, SSDE has been speculated to underestimate dose to thoracic scans due to the effective diameter's inability to account for patient attenuation. This issue was described in detail in Chapter 9.

Another major limitation of SSDE is its inability to report organ dose. It is said that SSDE is dose to the center of the scan volume without the capability of being used to estimate risk from CT examinations.

The Computed Tomography Dose Index was described in detail in Chapter 1. Despite not being patient dose, let alone organ dose, this index has proven to be a tremendously useful measure of

CT output, used to normalize out spectra and filtration differences among scanners, and as shown in Chapter 10, as a predictor for organ dose.

In this chapter, these different dose metrics will be generated for a set of 131 actual patient CT examinations including abdomen/pelvis and chest exams. In addition to these dose estimates, the models generated and evaluated in the previous chapter will be used to estimate organ doses to these 131 patients. All dose estimates methods will be compared to detailed Monte Carlo simulated organ doses, which were estimated using the Monte Carlo package described in Chapter 4 and validated in Chapter 6, using actual patients TCM information and patient images used to generate voxelized models as described in Chapter 5.

11.2 METHODS

11.2.1 $CTDI_{vol}$

For all 131 collected patients, $CTDI_{vol}$ values were either collected from patient dose reports or estimated based on kVp and collimation dependent mGy/mAs ratios. Figure 11-1 through 11-3 shows patient dose reports from three different CT scanners, Siemens, GE, and Toshiba, respectively. For all the Toshiba patient models, $CTDI_{vol}$ values were calculated using kVp and Collimation dependent mGy/mAs ratios; this was necessary because for the version of software in use at the time of the scans, Toshiba dose reports utilized the maximum tube current (mA) rather than the average mA to calculate $CTDI_{vol}$ for an exam. Patient images DICOM headers were used to automatically extract average mA values and calculate an average mA for the exam, which was then utilized to calculate a $CTDI_{vol}$ value.

Total mAs 7570 Total DLP 1082

	Scan	kV	mAs / ref.	CTDIvol	DLP	TI	cSL
Patient Position F-SP							
Abd/PelTopo	1	120				5.3	0.6
Abd w/o	2	120	125 / 180	9.57	244	0.5	0.6
Abd/Pel w/c	3	120	226 / 275	17.31	838	0.5	0.6

Figure 11-1 Siemens generated patient dose report for an abdomen without contrast and abdomen/pelvis with contrast CT examinations. Along with $CTDI_{vol}$ for each exam (17.31 mGy for the abdomen/pelvis exam which was used in this study) some scan parameters are also reported on this report. Newer version of Siemens dose reports indicates which phantom size is used to report $CTDI_{vol}$.

Dose Report

Series	Type	Scan Range (mm)	CTDIvol (mGy)	DLP (mGy-cm)	Phantom cm
1	Scout	-	-	-	-
200	Axial	I296.750-I296.750	16.88	8.44	Body 32
2	Helical	S12.250-I290.250	7.47	260.89	Body 32
2	Helical	I179.500-I414.500	12.87	361.63	Body 32
2	Helical	I417.000-I614.500	12.87	313.38	Body 32
2	Helical	I231.500-I369.000	12.87	236.19	Body 32
2	Helical	I467.250-I554.750	12.87	171.86	Body 32
			Total Exam DLP:	1352.38	

Figure 11-2 Dose report from a GE scanner demonstrating scan length, $CTDI_{vol}$, DLP and the phantom size used to report $CTDI_{vol}$.

<< Dose Information >>

CTDIvol(mGy)	(Head) : -	(Body) : 11.00
DLP(mGycm)	(Head) : -	(Body) : 461.50

Figure 11-3 "Dose Information" section of Toshiba's patient dose report. Along with the reported $CTDI_{vol}$, the report indicates which CTDI phantom the $CTDI_{vol}$ value is based off of. While other scanners use the average tube current value to calculate a $CTDI_{vol}$ value for TCM CT scan, the software version for these Toshiba scans used the maximum mA value to calculate CTDIvol. In the newer version of their software, an average tube current value is used to calculate $CTDI_{vol}$.

11.2.2 Calculation of SSDE

For all 131 patient scans, effective diameters were calculated using semi-automatically generated measurements of lateral and anterior-posterior measurements performed on axial CT images.

These measurements were done on a single slice basis; i.e. the middle slice (image) of each image series was identified to calculate an effective diameter based on the definition provided by TG 204 report and previously shown in Chapter 9:

$$effective\ Diameter = \sqrt{LAT \times AP} \qquad \textbf{Eq. 11-1}$$

For each patient, table 1 from TG 204 report was used to assign an f-factor based on their calculated effective diameter and multiplied by their collected $CTDI_{vol}$ values.

Table 1A

Lat+AP Dim (cm)	Effective Dia (cm)	Conversion Factor
16	7.7	2.79
18	8.7	2.69
20	9.7	2.59
22	10.7	2.50
24	11.7	2.41

Table 1B

Lateral Dim (cm)	Effective Dia (cm)	Conversion Factor
8	9.2	2.65
9	9.7	2.60
10	10.2	2.55
11	10.7	2.50
12	11.3	2.45

Table 1C

AP Dim (cm)	Effective Dia (cm)	Conversion Factor
8	8.8	2.68
9	10.2	2.55
10	11.6	2.42
11	13.0	2.30
12	14.4	2.18

Table 1D

Effective Dia (cm)	Conversion Factor
8	2.76
9	2.66
10	2.57
11	2.47
12	2.38

Figure 11-4 Partially shows TG 204 table with conversion coefficients used to obtain an SSDE for each patient. In this case, patient f-factors shown in table 1D were used based on calculated effective diameter.

11.2.3 Organ Dose Calculation Using ImPACT

Organ doses were calculated using ImPACT (version 1.0.3) and using each patient's specific scanning parameters. Depending on the exam type, the scan ranges were specified on the MIRD phantom as shown in Figure 11-5 for abdomen and Figure11-6 for thoracic exams. For the mA (tube current) value, the average tube current through the entire scan length was utilized. For each patient, the parameters and exam length were selected and doses to liver, spleen, and kidneys for all the abdomen/pelvis exams, and breasts and lungs from thoracic exams were recorded. A screen shot of the spread sheet (Figure 11-7) illustrates the section for imaging parameters and the output as organ doses in mGy and the corresponding weighting factors from ICRP report 103, along with the last column calculating the corresponding effective dose in mSv.

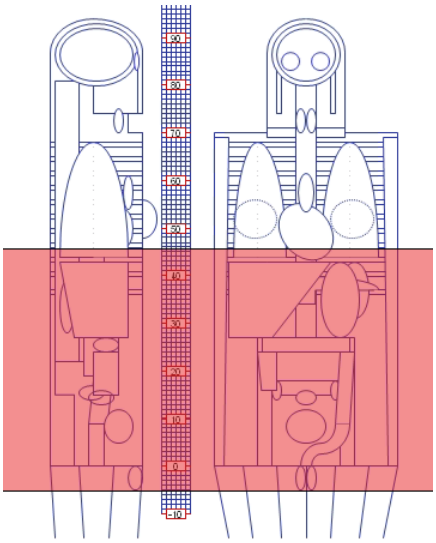

Figure 11-5 A diagram of MIRD phantom used in ImPACT to indicate the range of the scan. In this case all doses from abdomen/pelvis scans were estimated using the scan range shown by the pink box.

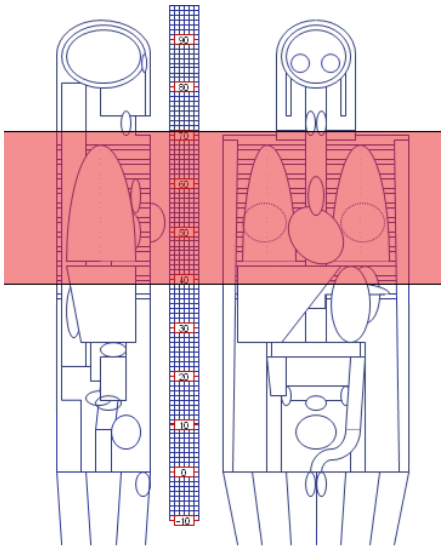

Figure 11-6 A diagram of MIRD phantom used in ImPACT to indicate the range of the scan. In this case all doses from chest scans were estimated using the scan range shown by the pink box.

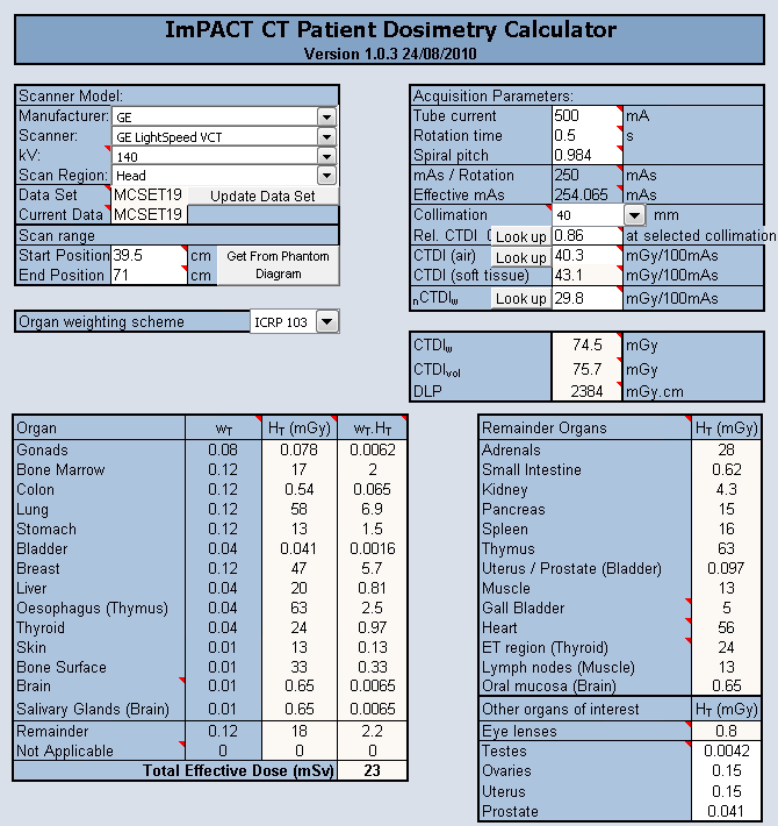

ImPACT CT Patient Dosimetry Calculator
Version 1.0.3 24/08/2010

Scanner Model:			
Manufacturer:	GE		
Scanner:	GE LightSpeed VCT		
kV:	140		
Scan Region:	Head		
Data Set	MCSET19	Update Data Set	
Current Data	MCSET19		
Scan range			
Start Position	39.5	cm	Get From Phantom Diagram
End Position	71	cm	

Organ weighting scheme	ICRP 103

Acquisition Parameters:			
Tube current	500	mA	
Rotation time	0.5	s	
Spiral pitch	0.984		
mAs / Rotation	250	mAs	
Effective mAs	254.065	mAs	
Collimation	40	mm	
Rel. CTDI	Look up	0.86	at selected collimation
CTDI (air)	Look up	40.3	mGy/100mAs
CTDI (soft tissue)		43.1	mGy/100mAs
$_nCTDI_w$	Look up	29.8	mGy/100mAs

$CTDI_w$	74.5	mGy
$CTDI_{vol}$	75.7	mGy
DLP	2384	mGy.cm

Organ	w_T	H_T (mGy)	$w_T.H_T$
Gonads	0.08	0.078	0.0062
Bone Marrow	0.12	17	2
Colon	0.12	0.54	0.065
Lung	0.12	58	6.9
Stomach	0.12	13	1.5
Bladder	0.04	0.041	0.0016
Breast	0.12	47	5.7
Liver	0.04	20	0.81
Oesophagus (Thymus)	0.04	63	2.5
Thyroid	0.04	24	0.97
Skin	0.01	13	0.13
Bone Surface	0.01	33	0.33
Brain	0.01	0.65	0.0065
Salivary Glands (Brain)	0.01	0.65	0.0065
Remainder	0.12	18	2.2
Not Applicable	0	0	0
Total Effective Dose (mSv)			**23**

Remainder Organs	H_T (mGy)
Adrenals	28
Small Intestine	0.62
Kidney	4.3
Pancreas	15
Spleen	16
Thymus	63
Uterus / Prostate (Bladder)	0.097
Muscle	13
Gall Bladder	5
Heart	56
ET region (Thyroid)	24
Lymph nodes (Muscle)	13
Oral mucosa (Brain)	0.65
Other organs of interest	**H_T (mGy)**
Eye lenses	0.8
Testes	0.0042
Ovaries	0.15
Uterus	0.15
Prostate	0.041

Figure 11-7 An example of the ImPACT spreadsheet with scan parameters and scanner specific models entered in the top two tables, while the output in terms of organ dose in mGy and effective dose in mSv are shown in the bottom two tables.

11.2.4 Predictive Organ Dose Models (from Chapter 10)

Organ doses were estimated using models generated in the previous chapter. As an example of one of these models, Table 11-1 illustrates the predictors, including some categorical ones, along with their coefficients generated for regional $CTDI_{vol}$ model using pooled data. As mentioned before, categorical predictors are binary variables with the possibility of taking on either 1 or 0 depending on the scanner, organ, or patient of interest. To calculate dose to a specific organ, for instance for liver, all other organs take on the value 0 and are eliminated from Eq. 11-2.

Similarly, for calculating dose to breasts from a Siemens scanner, all organs take on the value zero including the categorical variable Toshiba.

$CTDI_{vol,\ Regional}$

logorgandose	Coef.	Std. Err.	t	P>|t|	[95% Conf.	Interval]
waterequivalentdiameter_regional	-.038299	.0019406	-19.74	0.000	-.0421134	-.0344846
logctdivol_regional	.9002081	.0170934	52.66	0.000	.8666094	.9338069
Toshiba	-.0608185	.018755	-3.24	0.001	-.0976833	-.0239536
Siemens	-.0950613	.0153723	-6.18	0.000	-.1252772	-.0648455
Liver	.1445996	.0198136	7.30	0.000	.105654	.1835452
Spleen	.1499742	.0198136	7.57	0.000	.1110286	.1889198
Kidneys	.1445823	.0198136	7.30	0.000	.1056367	.1835279
Lung	.1843963	.0169464	10.88	0.000	.1510865	.217706
Peds	-.1173164	.0207008	-5.67	0.000	-.1580059	-.076627
_cons	1.475768	.0358445	41.17	0.000	1.405312	1.546224

Table 11-1 Demonstration of significant predictors along with their coefficients for the predictive model based on pooled data using once $CTDI_{vol,Regional}$ as the predictor.

$$\mathrm{L}n(Organ\ Dose) = \alpha + \{(\beta_1 \times Ln(CTDI_{vol,Regional})) + (\beta_2 \times WED) + (\beta_3 \times Toshiba) + (\beta_4 \times Siemens) + (\beta_5 \times Liver) + (\beta_6 \times Spleen) + (\beta_7 \times Kidney) + (\beta_8 \times Lung) + (\beta_9 \times Peds)\} \quad \textbf{Eq. 11-2}$$

All other models will have a similar form as described above with a smaller number of predictors for more specified models, such as organ-specific models, and more predictors for more generalized models, such as models based on pooled data across scanner and organs as shown by Eq. 11-2. Figure 11-8 illustrates an outline of newly developed dose estimation method for an example to obtaining pediatric lung dose.

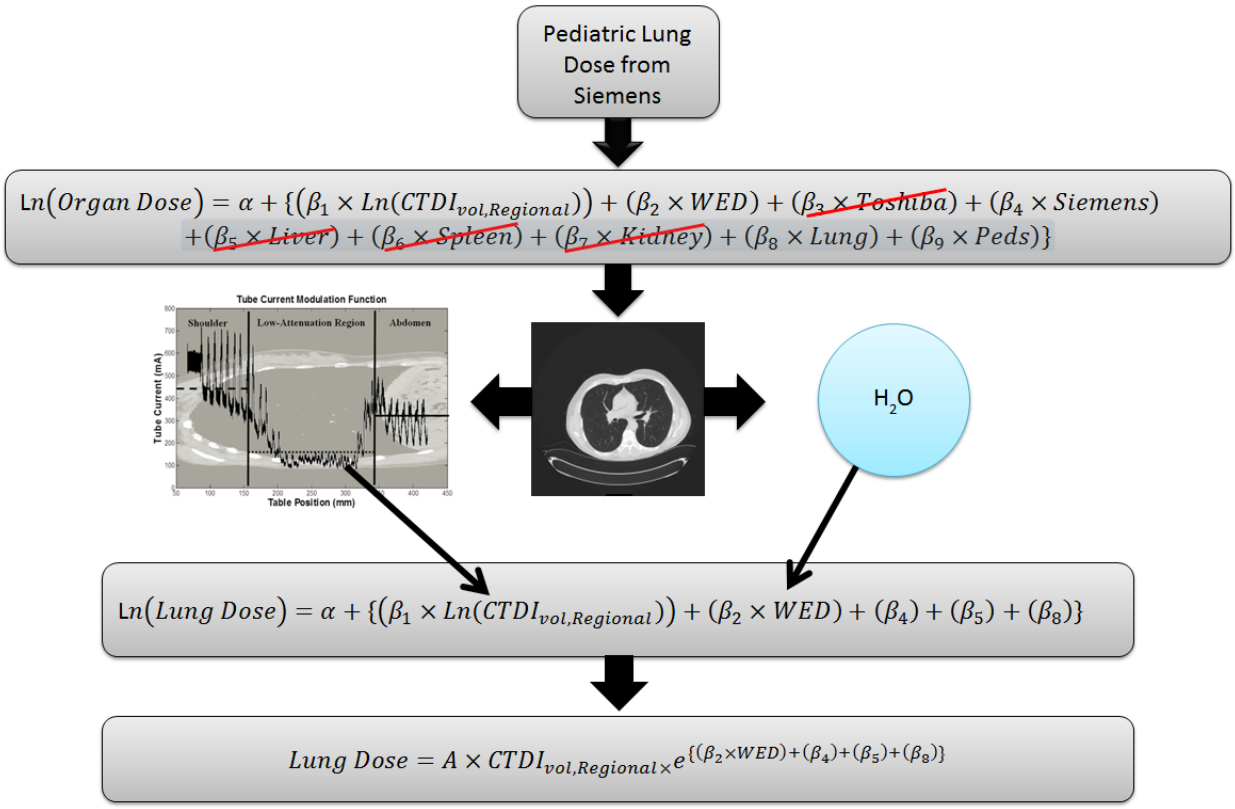

Figure 11-8 A diagram of calculating organ dose using the predictive model developed in this dissertation using regional $CTDI_{vol}$ and regional water equivalent diameter.

11.2.5 Statistical Analysis

For each of the different dose estimation methods, $CTDI_{vol}$, SSDE, ImPACT, and predictive models generated in Chapter 10, the dose estimate is compared to the organ dose values obtained using detailed Monte Carlo simulations performed for each patient, which will serve as the reference method. From the resulting comparisons of each method to the reference method, the percent difference mean, standard deviation, minimum, and maximum across all patients were calculated.

Additionally, one sample t-test was used for each method to test the null hypothesis that the estimation method is different from detailed Monte Carlo simulated organ doses. All data were analyzed using Stata 12.0 (StataCorp; College Station, TX).

11.3 RESULTS

The following organ-specific tables (Tables 11-2 through 11-6) summarize the descriptive analysis for each individual method compared to Monte Carlo simulated organ doses.

Breast				
Model Description	**% Mean**	**% SD**	**% Max**	**% Min**
CTDIvol	-10.86	24.09	77.15	-56.25
SSDE	19.97	28.90	143.06	-15.02
ImPACT	13.83	40.38	167.49	-46.43
Global	-2.72	18.38	77.45	-21.71
Regional	6.60	13.00	41.63	-16.04
Pooled	6.21	13.02	35.65	-16.81
Scanner-Specific	7.77	13.52	36.26	-12.81
Organ-Specific	6.31	13.82	38.45	-15.43
Scanner and Organ Specific	5.23	17.33	52.08	-28.29

Table 11-2 Illustrates percent mean, standard deviation, maximum, and minimum calculated for each method compared to Monte Carlo simulated breast dose.

Lung				
Model Description	**% Mean**	**% SD**	**% Max**	**% Min**
CTDIvol	-26.86	15.27	3.84	-69.64
SSDE	-3.74	14.45	43.20	-27.03
ImPACT	18.94	34.26	176.09	-32.38
Global	-8.64	7.74	8.14	-37.41
Regional	2.44	13.56	28.62	-31.05
Pooled	1.61	13.32	28.79	-29.57
Scanner-Specific	4.20	14.45	43.20	-27.03
Organ-Specific	2.41	12.51	33.94	-29.57
Scanner and Organ Specific	2.25	11.88	34.09	-29.58

Table 11-3 Illustrates percent mean, standard deviation, maximum, and minimum calculated for each method compared to Monte Carlo simulated lung dose.

Liver				
Model Description	**% Mean**	**% SD**	**% Max**	**% Min**
CTDIvol	-13.82	18.92	35.19	-50.95
SSDE	11.65	21.02	100.82	-31.55
ImPACT	10.67	25.75	69.79	-36.47
Global	-8.48	8.87	11.20	-28.68
Regional	2.11	7.04	26.99	-14.68
Pooled	1.64	6.94	23.11	-11.74
Scanner-Specific	-0.48	7.49	16.49	-12.96
Organ-Specific	2.27	7.39	30.19	-12.88
Scanner and Organ Specific	2.22	6.99	23.69	-12.45

Table 11-4 Illustrates percent mean, standard deviation, maximum, and minimum calculated for each method compared to Monte Carlo simulated liver dose.

Spleen				
Model Description	**% Mean**	**% SD**	**% Max**	**% Min**
CTDIvol	-15.84	17.41	25.25	-54.55
SSDE	8.06	20.27	55.65	-37.02
ImPACT	5.30	23.83	43.39	-45.74
Global	-9.77	10.52	13.76	-34.02
Regional	0.69	9.65	23.81	-20.61
Pooled	-0.19	10.80	26.76	-18.79
Scanner-Specific	0.30	9.30	20.83	-20.07
Organ-Specific	0.44	9.34	24.05	-21.48
Scanner and Organ Specific	0.47	8.86	25.50	-19.98

Table 11-5 Illustrates percent mean, standard deviation, maximum, and minimum calculated for each method compared to Monte Carlo simulated spleen dose.

Kidney				
Model Description	**Mean**	**SD**	**Max**	**Min**
CTDIvol	-15.27	16.51	32.80	-57.57
SSDE	8.86	19.75	58.86	-35.08
ImPACT	28.74	27.29	86.41	-29.08
Global	-9.43	10.49	13.23	-32.36
Regional	1.10	10.11	29.35	-18.60
Pooled	0.80	11.69	29.00	-19.18
Scanner-Specific	1.24	9.60	24.98	-16.62
Organ-Specific	1.05	11.12	30.05	-18.71
Scanner and Organ Specific	1.02	9.06	28.54	-19.22

Table 11-6 Illustrates percent mean, standard deviation, maximum, and minimum calculated for each method compared to Monte Carlo simulated kidney dose.

Data displayed in the above tables are also graphically illustrated using bar graphs in Figure 11-9. The plus sign on top of bars indicate p-values <0.05, indicating that there is a statistically significant difference between the organ dose from specified method and Monte Carlo simulated organ doses.

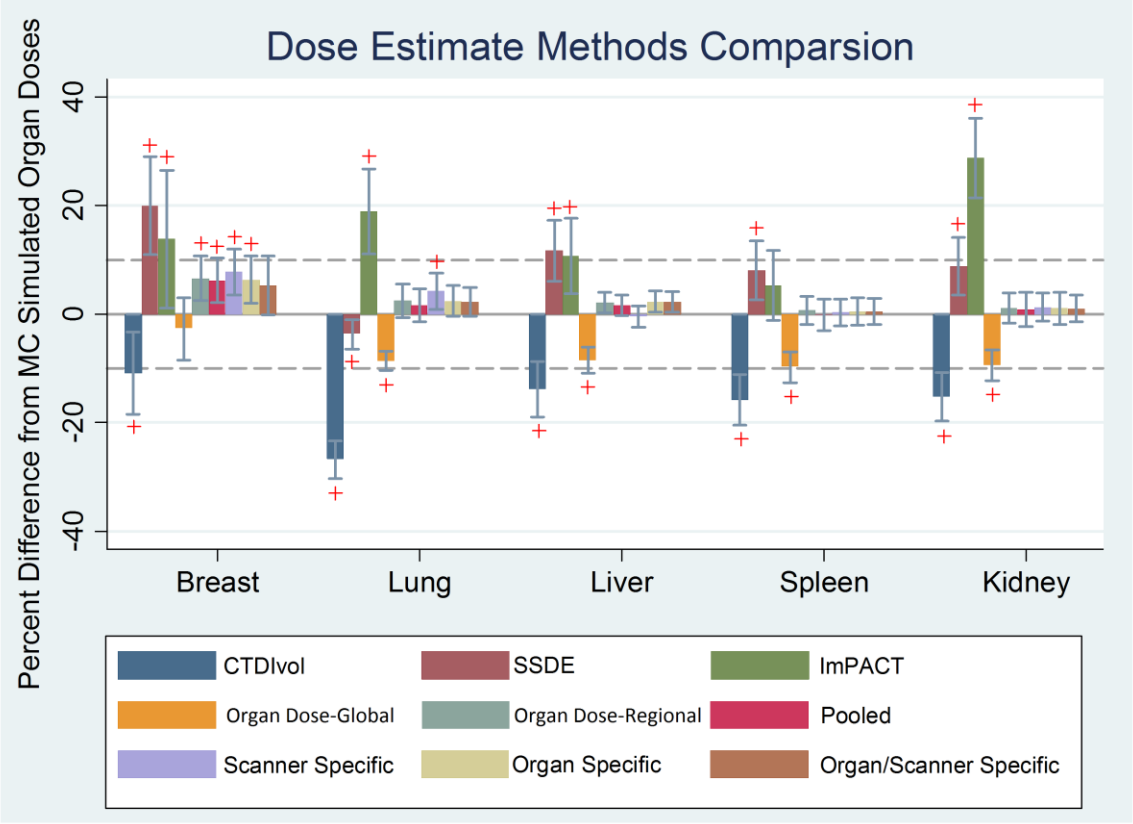

Figure 11-9 Percent difference mean, standard deviation, maximum, and minimum calculated for each method compared to Monte Carlo simulated kidney dose.

As shown by these results, models from previous chapter estimate organ doses within less than 10% from actual Monte Carlo simulated organ doses. Additionally, for all organs except for breasts, the null hypothesis is rejected, indicating no statistically significant difference between predictive models and Monte Carlo simulated organ doses. However, for the conventional CT

dose metrics, CTDIvol, SSDE, and ImPACT, p-values are <0.05, showing a statistically significant difference between these metrics and actual simulated organ doses.

11.4 Discussion and Conclusion

This work showed that conventional methods of estimating dose from TCM exams differ from actual Monte Carlo simulated organ doses by almost 30% on average, and even more in individual cases, while regional $CTDI_{vol}$ and water equivalent size metric can provide estimates to within less than 10% of actual simulated organ doses.

Although the usefulness and advantage of regional $CTDI_{vol}$ and water equivalent diameter in TCM exams over global $CTDI_{vol}$ and effective diameter was shown and evaluated in this chapter, these parameters are not easily obtainable. The process of gathering this information for an individual patient is not yet automated and can be time consuming and impractical. Regions of interest, for which regional $CTDI_{vol}$ and water equivalent diameter had to be calculated, were manually identified by viewing axial CT images. For calculating water equivalent diameter, although a segmentation method was developed, it was only semi-automated and still labor-intensive.

Although impractical at the time, both of these key pieces of information can be obtained in a more automated fashion, with a little effort. As it was recently showed by Sodickson et al. [142], it is possible to identify anatomical regions given a series of CT images, hence it is feasible to be able to extract regional anatomy within a series of images. In point of fact, in collaboration with Brigham and women's Hospital at Boston, regional information based on slice by slice information on attenuation or CT numbers can be obtained using a previous knowledge base on attenuation properties of specific landmarks such as start of the diaphragm within a series or iliac

crest. Figure 11-7 shows the mean CT number of a thoracic and abdomen/pelvis exam versus slice number, which looks a lot like what is expected, knowing the different attenuating sections along the z-axis of human anatomy. This information can be used to extract image numbers corresponding to a region of interest.

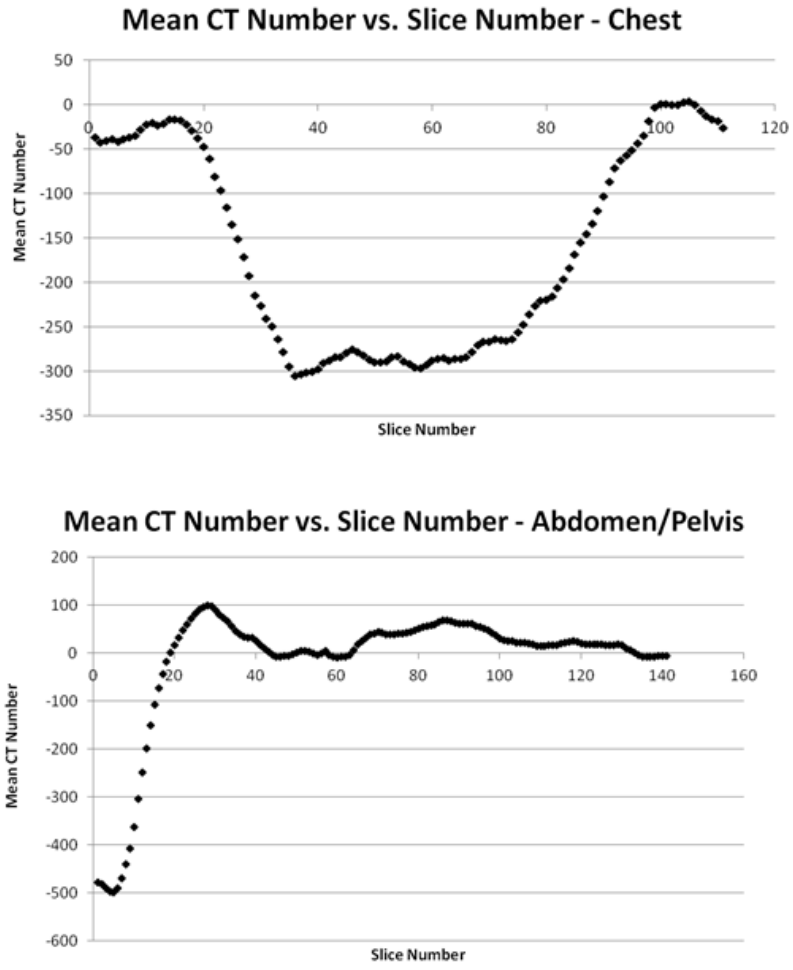

Figure 11-7 Illustrates mean CT number versus slice number for a chest and abdomen/pelvic exam, which can be used to extract slice numbers corresponding to a region of interest.

Once the slice numbers are automatically identified for a region of interest, it is simple to automatically calculate an average tube current value which can be used to calculate a regional $CTDI_{vol}$ value.

As mentioned previously, the segmentation method developed for this study to contour out the body from the surrounding air and table is still semi-automated and needs some user interaction for a clean contour. However, it is feasible to improve this method by adding constraints using a previous knowledge of table attenuation properties.

Overall results presented in this chapter are encouraging that regional $CTDI_{vol}$ and water equivalent diameter are extremely valuable parameters in estimating dose from TCM exams, and hence, efforts put towards making these parameters easily accessible are worthwhile. While comparing different predictive models based on their performance and complexity, they all seem to be performing equally across organs except for the "Organ Dose-Global" model, which was based on global $CTDI_{vol}$ as the dose predictor. Global model underestimates organ dose across all organs and scanners and is significantly different than actual simulated organ doses. Organ-specific and scanner-specific models resulted in lowest mean percent differences across all organs and scanners and, therefore, represent the best models for estimating organ doses. However, the difference between organ- and scanner-specific models and more generalized pooled-data models (Regional and Pooled) in terms of their performance in estimating actual organ doses is minimal. In terms of complexity, "Organ dose-Regional" and "Pooled", which are based on pooled data across organs and scanners, each provide a single model applicable to all three scanners despite using scanners as predictors, while the organ- and scanner-specific models results in multiple models, i.e. predictive functions. Both "Organ Dose-Regional" and "Pooled" models can be used for estimating dose from TCM CT scans to be within less than 10% of the

actual Monte Carlo simulated organ doses, while conventional methods provide estimates within 30% of the actual simulated organ dose.

CHAPTER 12: DISSERTATION SUMMARY AND CONCLUSION

The purpose of this dissertation was to develop predictive models capable of quantifying radiation dose to organs from tube current modulated CT examinations, which are the majority of scans performed in current clinical practice. While there are estimation methods available to approximate dose from fixed tube current CT exams, there are no such dose approximation methods for tube current modulated CT examinations. Although nearly all body CT examinations make use of TCM, current dose metrics are entirely developed from fixed tube current information. These dose estimation methods are shown to be statistically significantly different from actual Monte Carlo simulated organ doses from TCM exams. Hence, the development of a new model was necessary and a valuable contribution to the field of diagnostic medical imaging.

For creating a model capable of estimating dose from TCM procedures, a validated Monte Carlo method, in particular validated to provide accurate dose values from TCM examinations, was a requirement. Therefore, Chapter 6 was dedicated to validating a previously developed and modified MCNPX platform to simulate CT source, pathway, and variable output. The validation of the TCM included simple geometry such as the CTDI phantom, and more complex geometry such as the anthropomorphic phantom, which resulted in very similar TCM function as an actual patient. With a validated Monte Carlo simulation package, TCM simulations could be performed with high confidence in the accuracy of results.

Although TCM is used in almost every CT exam, it is not as easily accessible as patient images are. TCM is mostly extracted from raw projection data, for which special programs are needed and can only be made available by the manufacturer. Hence, approximation methods had to be

implemented for patients whose TCM functions were not available. This problem was discussed and possible approximations, along with their accuracy of estimating dose from TCM, were proposed in Chapter 7. Most TCM functions from different CT manufacturers consist of two types of modulations: the in-plane (x-y) modulation of the tube current and the z-axis-only modulation, which is along a patient's longitudinal direction. The dose reduction effect of TCM is mostly contributed by the z-axis modulation and, therefore, as shown in Chapter 7, it is sufficient to estimate dose from the z-axis-only modulation of the tube current. Most importantly, this modulation of the tube current is embedded in the DICOM header of patient images and therefore easily accessible without the need of having access to raw projection data.

Once organ doses from TCM examinations can successfully be simulated using either patients' detailed TCM function extracted from raw projection data, or the approximated version extracted from patient images, predictors of dose were required for creation of a predictive model, capable of estimating dose from TCM exams.

In chapter 8, one of these predictors was introduced as the regional $CTDI_{vol}$. $CTDI_{vol}$ has been proven to be a valuable index in measuring a scanner's output and, as shown by TG 204, it can be used to normalize differences among CT scanner manufacturers. However, its utility is highly dependent on the assumption of a constant tube current across the entire scan length, which, of course, is violated in TCM mode. Hence, there was a need for a better scanner output metric which can take into account the varying tube current across an examination in TCM mode. The feasibility of regional $CTDI_{vol}$ as a normalization factor in TCM mode was investigated in Chapter 8 using Siemens data and it demonstrated high potential as a predictor of organ dose in TCM mode.

In addition to a modified normalization factor, there was a need for an improved size metric which is capable of accounting for varying attenuation properties within different exam types and patients. The work by TG 204 was criticized for its size metric (effective diameter) not being able to account for the low attenuating lungs in a chest exam and, hence, an underestimation of dose from chest CT scans. Therefore, it has been suggested that an attenuation based metric would be a more appropriate metric over the currently use effective diameter, which is a physical measure of patients dimensions. In Chapter 9, water equivalent diameter, which is the diameter of a water cylinder with the same attenuation as the patient, was investigated and compared to effective diameter. Results showed that there is almost no difference between effective diameter and water equivalent diameter in abdominal areas. However, in the thorax, the difference was only statistically significant when water equivalent diameter was reported for the region of interest, which was the low attenuating region of lungs without any contaminations of higher attenuations from shoulders and abdomen. Hence, not only is there a need for regional tube output, but also regional size metric, especially for dose estimation to lungs.

With an improved dose metric capable of accounting for TCM and an improved size metric able to account for attenuation differences between different body regions, different predictive models were investigated in Chapter 10. A Generalized Linear Model was used to develop a predictive model using a training set of 200 patients from three major CT manufacturers for which detailed Monte Carlo simulations were performed to estimate dose to organs of interest. Models were generated for specific scanners and specific organs along with pooled-data models across scanners, across organs or across both. Models that pooled scanners and pooled organs resulted in scanner and organ-specific coefficients, indicating TCM differences among scanners, which cannot be normalized out with only regional $CTDI_{vol}$ values. However, although regional

$CTDI_{vol}$ is still a reasonable dose predictor for individual scanners, it is not sufficient to eliminate differences in TCM among CT manufacturers.

The models developed in Chapter 10 were compared to conventional dose metrics currently used to report dose from TCM exams. These methods include scanner-reported $CTDI_{vol}$, SSDE, and ImPACT. These methods proved to be statistically significantly different from actual Monte Carlo simulated organ doses and, on average, were different from actual organ doses by almost 30%. Organ doses estimated from models developed in Chapter 10 were within 10% of actual organ doses and were not significantly different from detailed Monte Carlo simulation estimates of organ doses. Hence, regional $CTDI_{vol}$ and size metric are extremely valuable parameters for estimating dose to TCM CT examinations.

Although the usefulness of regional $CTID_{vol}$ and water equivalent diameter has been demonstrated, these two parameters are still not easily obtainable. Therefore, future work will focus on automated identification and extraction of regional information on tube current and calculation of regional $CTDI_{vol}$. Identification of regions within the anatomy could be made possible using previous knowledge of attenuation properties of anatomical landmarks of interest, which are easily accessible from axial CT images. Other possibilities are atlas-based recognition of regional landmarks.

Other easy improvements to the current state of CT dosimetry can be achieved by extracting regional tube current and water equivalent diameter from a CT localizer to be able to report dose prospectively. Considering the fact that CT manufacturers are required to report an approximated $CTDI_{vol}$ value before the actual examination, the knowledge of regional $CTDI_{vol}$ before the actual exam should be very feasible.

Being able to estimate risk from CT examinations is the ultimate goal of this presented work and similar works cited. As previously mentioned, currently available risk estimates are limited and large uncertainties are associated with them. Effective dose is the currently used predictor of radiation risk. However, effective dose represents a generic estimate of risk from an x-ray involved procedure for a generic model of actual human anatomy. Because effective dose was designed to reflect overall risk averaged over all ages and both sexes for a reference patient, it should not be calculated for individual patients or used for epidemiologic studies and representation of risk to any one individual. Additionally, to be able to calculate effective dose, the dose to every individual radiosensitive organ has to be known. Therefore, the current results of this dissertation cannot be used to calculate effective dose, because dose was only quantified in five organs.

For individual risk estimates or epidemiologic studies, estimation of individual organ doses accounting for patient's body size and attenuation properties, along with data from BEIR VII, [18] can be used to estimate risk to specific patients. Results from this dissertation can provide patient-specific dose estimates for a handful of radiosensitive organs, for which lifetime risk of cancer incidence and risk of cancer mortality can be estimated using BEIR VII [18]. As previously mentioned, perhaps the biggest limitation of BEIR VII [18] is that there are not enough numbers of exposed people to investigate reliably the small increases in the incidence of cancer that small exposures to radiation may cause.

In the end, there is no satisfactory solution to estimating risk from ionizing radiation. But what is certain is that dose to individual organs can eventually be used to improve and enhance risk models and, hence, should not only be accurately quantified, but also used as the most appropriate metric to track dose from individual CT examinations.

The ultimate extension of this work is to be able to accurately estimate organ dose from CT in order to keep and update patient-specific dose reports. Accurate CT dosimetry is not only helpful for patient dose management purposes, but future epidemiological work and risk assessment of CT examinations may be greatly enhanced by improved patient-specific CT dosimetry.

REFERENCES

1. Adam, J., Changes in the computed tomography patient population. European Radiology Supplements, 2006. **16**(4).
2. Goldman, L.W., Principles of CT and CT Technology. Journal of Nuclear Medicine Technology, 2007. **35**(3): p. 115-128.
3. Fahimian, B.P., et al., Radiation dose reduction in medical x-ray CT via Fourier-based iterative reconstruction. Medical Physics, 2013. **40**(3): p. 031914-10.
4. Prakash, P., et al., Radiation Dose Reduction With Chest Computed Tomography Using Adaptive Statistical Iterative Reconstruction Technique: Initial Experience. Journal of Computer Assisted Tomography, 2010. **34**(1): p. 40-45
5. Shrimpton, P.C., et al., National survey of doses from CT in the UK: 2003. Br J Radiol, 2006. **79**(948): p. 968-80.
6. Mettler, F.A., Jr., et al., Medical radiation exposure in the U.S. in 2006: preliminary results. Health Phys, 2008. **95**(5): p. 502-7.
7. Greess, H., et al., Dose reduction in computed tomography by attenuation-based on-line modulation of tube current: evaluation of six anatomical regions. European Radiology, 2000. **10**(2): p. 391-394.
8. Raff, Gl., et al., RAdiation dose from cardiac computed tomography before and after implementation of radiation dose–reduction techniques. JAMA, 2009. **301**(22): p. 2340-2348.
9. Hidajat, N., et al., Radiation Exposure in Spiral Computed Tomography: Dose Distribution and Dose Reduction. Investigative Radiology, 1999. **34**(1): p. 51-57.

10. Hundt, W., et al., Dose Reduction in Multislice Computed Tomography. Journal of Computer Assisted Tomography, 2005. **29**(1): p. 140-147.

11. Smith-Bindman, R., et al., RAdiation dose associated with common computed tomography examinations and the associated lifetime attributable risk of cancer. Archives of Internal Medicine, 2009. **169**(22): p. 2078-2086.

12. Berrington de González, A., et al., PRojected cancer risks from computed tomographic scans performed in the united states in 2007. Archives of Internal Medicine, 2009. **169**(22): p. 2071-2077.

13. Redberg, R.F., Cancer risks and radiation exposure from computed tomographic scans: How can we be sure that the benefits outweigh the risks? Archives of Internal Medicine, 2009. **169**(22): p. 2049-2050.

14. Brenner, D. and E. Hall, Computed tomography - An increasing source of radiation exposure. New England Journal of Medicine, 2007. **357**(22).

15. Hall, P., et al., Effect of low doses of ionising radiation in infancy on cognitive function in adulthood: Swedish population based cohort study. Bmj, 2004. **328**(7430): p. 19.

16. FDA, Computed Tomography (CT). Food and Drug Administration, 2010.

17. Relative biological effectiveness (RBE), quality factor (Q), and radiation weighting factor (w(R)). A report of the International Commission on Radiological Protection. Ann ICRP, 2003. **33**(4): p. 1-117.

18. National Research Council. Health Risks from Exposure to Low Levels of Ionizing Radiation: BEIR VII Phase 2 2005, The National Academies Press: Washington DC.

19. The Measurement, Reporting, and Management of Radiation Dose in CT. AAPM Report Number 96 Report of AAPM Task Group 23 of the Diagnostic Imaging Council CT Committee. 2008.

20. The 1990 Recommendations of the International Commission on Radiological Protection. ICRP publication 60. Ann ICRP, 1991. **21**: p. 1-32.

21. The 2007 Recommendations of the International Commission on Radiological Protection. ICRP publication 103. Ann ICRP, 2007. **37**(2-4): p. 1-332.

22. AB-510 Radiation control: health facilities and clinics: records. 2011-2012.

23. 1237, C.S.B., California Health and Safety Code, Radiation control: health facilities and clinics: records, (Chapter 521, Sections 115111, 115112, and 115113).

24. FDA, FDA Unveils Initiative to Reduce Unnecessary Radiation Exposure from Medical Imaging. February 9, 2010.

25. Neumann, R.D. and D.A. Bluemke, Tracking Radiation Exposure From Diagnostic Imaging Devices at the NIH. Journal of the American College of Radiology, 2010. **7**(2): p. 87-89.

26. Rehani, M.M. and D.P. Frush, Patient exposure tracking: the IAEA smart card project. Radiation Protection Dosimetry, 2011. **147**(1-2): p. 314-316.

27. Loftus, M.L., et al., Radiation Exposure from Medical Imaging.

28. Zondervan, R.L., et al., Body CT Scanning in Young Adults: Examination Indications, Patient Outcomes, and Risk of Radiation-induced Cancer. Radiology, 2013.

29. Shope, T.B., R.M. Gagne, and G.C. Johnson, A method for describing the doses delivered by transmission x-ray computed tomography. Med Phys, 1981. **8**(4): p. 488-95.

30. McNitt-Gray, M.F., AAPM/RSNA Physics Tutorial for Residents: Topics in CT. Radiation dose in CT. Radiographics, 2002. **22**(6): p. 1541-53.

31. Jucius, R.A. and G.X. Kambic, Radiation Dosimetry In Computed Tomography (CT). 1977: p. 286-295.

32. McCollough, C.H., CT dose: how to measure, how to reduce. Health Phys, 2008. **95**(5): p. 508-17.

33. Dixon, R.L., A new look at CT dose measurement: beyond CTDI. Med Phys, 2003. **30**(6): p. 1272-80.

34. Boone, J.M., The trouble with CTDI[sub 100]. Medical physics, 2007. **34**(4): p. 1364-1371.

35. McCollough, C.H., It is time to retire the computed tomography dose index (CTDI) for CT quality assurance and dose optimization. Against the proposition. Med Phys, 2006. **33**(5): p. 1190-1.

36. McCollough, C.H., et al., CT Dose Index and Patient Dose: They Are Not the Same Thing. Radiology, 2011. **259**(2): p. 311-316.

37. Commission., I.E., Medical electrical equipment, part 2-44: particular requirements for the safety of x-ray equipment for computed tomography. IEC publication no. 60601-2-44. Ed 2.1, 2002.

38. Jones, D., Shrimpton, P.C., Survey of the practice in the UK. Part 3: Normalized organ doses calculated using Monte Carlo techniques. 1991, National Radiological Protection Board (NRPB). p. NRPB R-250.

39. Zankl, M., Drexler, G., The calculation of dose from external photon exposures using reference human phantoms and Monte Carlo methods part VI: Organ doses from

computed tomographic examinations. GSF report 30/91. 1991, Oberschleisheim: GSF-Forschungszentrum.

40. Jessen, K.A., et al. , EUR 16262: European Guidelines on Quality Criteria for Computed Tomography. 2000.

41. Shrimpton, P.C., et al., Effective dose and dose-length product in CT. Radiology, 2009. **250**(2): p. 604-5.

42. Hurwitz, L.M., et al., Radiation dose from contemporary cardiothoracic multidetector CT protocols with an anthropomorphic female phantom: implications for cancer induction. Radiology, 2007. **245**(3): p. 742-50.

43. Hurwitz, L.M., et al., Radiation dose to the fetus from body MDCT during early gestation. AJR Am J Roentgenol, 2006. **186**(3): p. 871-6.

44. Hurwitz, L.M., et al., Effective dose determination using an anthropomorphic phantom and metal oxide semiconductor field effect transistor technology for clinical adult body multidetector array computed tomography protocols. J Comput Assist Tomogr, 2007. **31**(4): p. 544-9.

45. Hurwitz, L.M., et al., Radiation dose savings for adult pulmonary embolus 64-MDCT using bismuth breast shields, lower peak kilovoltage, and automatic tube current modulation. AJR Am J Roentgenol, 2009. **192**(1): p. 244-53.

46. Hurwitz, L.M., et al., Radiation dose to the female breast from 16-MDCT body protocols. AJR Am J Roentgenol, 2006. **186**(6): p. 1718-22.

47. Price, R., et al., Dose reduction during CT scanning in an anthropomorphic phantom by the use of a male gonad shield. Br J Radiol, 1999. **72**(857): p. 489-94.

48. Cody, D.D., et al., Strategies for formulating appropriate MDCT techniques when imaging the chest, abdomen, and pelvis in pediatric patients. AJR Am J Roentgenol, 2004. **182**(4): p. 849-59.

49. Boone, J.M., et al., Size-Specific Dose Estimates (SSDE) in Pediatric and Adul Body CT Examinations. AAPM Report No 204, 2011.

50. Turner, A.C., et al., The Feasibility of Patient Size-Corrected, Scanner-Independent Organ Dose Estimates for Abdominal CT Exams. Med Phys, 2011.

51. Turner, A.C., et al., The feasibility of a scanner-independent technique to estimate organ dose from MDCT scans: Using CTDI[sub vol] to account for differences between scanners. Medical Physics, 2010. **37**(4): p. 1816.

52. Kalender, W.A., et al., Dose reduction in CT by anatomically adapted tube current modulation. II. Phantom measurements. Med Phys, 1999. **26**(11): p. 2248-53.

53. Kalender, W.A., et al., Dose reduction in CT by on-line tube current control: principles and validation on phantoms and cadavers. Eur Radiol, 1999. **9**(2): p. 323-28.

54. Gies, M., et al., Dose reduction in CT by anatomically adapted tube current modulation. I. Simulation studies. Med Phys, 1999. **26**(11): p. 2235-47.

55. McCollough, C.H., M.R. Bruesewitz, and J.M. Kofler, Jr., CT dose reduction and dose management tools: overview of available options. Radiographics, 2006. **26**(2): p. 503-12.

56. Kalra, M.K., et al., Techniques and applications of automatic tube current modulation for CT. Radiology, 2004. **233**(3): p. 649-57.

57. Greess, H., et al., Dose reduction in computed tomography by attenuation-based on-line modulation of tube current: evaluation of six anatomical regions. Eur Radiol, 2000. **10**(2): p. 391-4.

58. Lee, C.H., et al., Radiation Dose Modulation Techniques in the Multidetector CT Era: From Basics to Practice1. Radiographics, 2008. **28**(5): p. 1451-1459.

59. Kalra, M.K., et al., Computed tomography radiation dose optimization: scanning protocols and clinical applications of automatic exposure control. Curr Probl Diagn Radiol, 2005. **34**(5): p. 171-81.

60. Söderberg, M. and M. Gunnarsson, The effect of different adaptation strengths on image quality and radiation dose using Siemens Care Dose 4D. Radiation Protection Dosimetry, 2010. **139**(1-3): p. 173-179.

61. Kalra, M., S.R. Rizzo, and R. Novelline, Reducing radiation dose in emergency computed tomography with automatic exposure control techniques. Emergency Radiology, 2005. **11**(5): p. 267-274.

62. Khatonabadi, M., et al., A comparison of methods to estimate organ doses in CT when utilizing approximations to the tube current modulation function. Medical physics, 2012. **39**(8): p. 5212-5228.

63. Kalra, M.K., et al., Computed Tomography Radiation Dose Optimization: Scanning Protocols and Clinical Applications of Automatic Exposure Control. Current Problems in Diagnostic Radiology, 2005. **34**(5): p. 171-181.

64. Rogers, D.W.O., Fifty years of Monte Carlo simulations for medical physics. Physics in Medicine and Biology, 2006. **51**(13): p. R287.

65. Rogers, D. and A. Bielajew, Monte Carlo techniques of electron and photon transport for radiation dosimetry. The dosimetry of ionizing radiation, 1990. **3**: p. 427-539.

66. Salvat, F., et al., PENELOPE, and algorithm and computer code for Monte Carlo simulation of electron-photon showers. 1996.

67. Décombaz, M., J.-J. Gostely, and J.-P. Laedermann, Coincidence-summing corrections for extended sources in gamma-ray spectrometry using Monte Carlo simulation. Nuclear Instruments and Methods in Physics Research Section A: Accelerators, Spectrometers, Detectors and Associated Equipment, 1992. **312**(1): p. 152-159.

68. Beck, J.W., W.L. Dunn, and F. O'Foghludha, A Monte Carlo model for absorbed dose calculations in computed tomography. Medical Physics, 1983. **10**(3): p. 314-320.

69. ImPACT CTDosimetry. Imaging performance assessment of CT Scanners: a medical devices agency evaluation group. CT scanner matching data, tables of CTDI values in air, CTDIw, and phantom factor values. 2003, ImPACT Internet home page (http://www.ImPACTscan.org).

70. Atherton, J.V. and W. Huda, CT doses in cylindrical phantoms. Phys Med Biol, 1995. **40**(5): p. 891-911.

71. Huda, W. and J.V. Atherton, Energy imparted in computed tomography. Med Phys, 1995. **22**(8): p. 1263-9.

72. Boone, J.M., et al., Monte Carlo assessment of computed tomography dose to tissue adjacent to the scanned volume. Medical Physics, 2000. **27**(10): p. 2393-2407.

73. Caon, M., G. Bibbo, and J. Pattison, An EGS4-ready tomographic computational model of a 14-year-old female torso for calculating organ doses from CT examinations. Phys Med Biol, 1999. **44**(9): p. 2213-25.

74. Caon, M., G. Bibbo, and J. Pattison, Monte Carlo calculated effective dose to teenage girls from computed tomography examinations. Radiation protection dosimetry, 2000. **90**(4): p. 445-448.

75. Martin, C., B. Giovanni, and P. John, A comparison of radiation dose measured in CT dosimetry phantoms with calculations using EGS4 and voxel-based computational models. Physics in Medicine and Biology, 1997. **42**(1): p. 219.

76. Jarry, G., et al., A Monte Carlo-based method to estimate radiation dose from spiral CT: from phantom testing to patient-specific models. Phys Med Biol, 2003. **48**(16): p. 2645-63.

77. DeMarco, J.J., et al., Estimating radiation doses from multidetector CT using Monte Carlo simulations: effects of different size voxelized patient models on magnitudes of organ and effective dose. Phys Med Biol, 2007. **52**(9): p. 2583-97.

78. DeMarco, J.J., et al., A Monte Carlo based method to estimate radiation dose from multidetector CT (MDCT): cylindrical and anthropomorphic phantoms. Phys Med Biol, 2005. **50**(17): p. 3989-4004.

79. Petoussi-Henss, N., et al., The GSF family of voxel phantoms. Phys Med Biol, 2002. **47**(1): p. 89-106.

80. Angel, E., et al., Radiation dose to the fetus for pregnant patients undergoing multidetector CT imaging: Monte Carlo simulations estimating fetal dose for a range of gestational age and patient size. Radiology, 2008. **249**(1): p. 220-7.

81. Angel, E., et al., Monte Carlo simulations to assess the effects of tube current modulation on breast dose for multidetector CT. Phys Med Biol, 2009. **54**(3): p. 497-512.

82. Angel, E., et al., Radiation Dose to the Fetus for Pregnant Patients Undergoing Multidetector CT Imaging: Monte Carlo Simulations Estimating Fetal Dose for a Range of Gestational Age and Patient Size1. Radiology, 2008. **249**(1): p. 220-227.

83. Li, X., et al., Patient-specific radiation dose and cancer risk estimation in CT: Part I. Development and validation of a Monte Carlo program. Medical Physics, 2011. **38**(1): p. 397-407.

84. Li, X., et al., Patient-specific radiation dose and cancer risk estimation in CT: Part II. Application to patients. Medical Physics, 2011. **38**(1): p. 408-419.

85. Li, X., et al., Patient-specific Radiation Dose and Cancer Risk for Pediatric Chest CT. Radiology, 2011. **259**(3): p. 862-874.

86. Gu, J., et al., The development, validation and application of a multi-detector CT (MDCT) scanner model for assessing organ doses to the pregnant patient and the fetus using Monte Carlo simulations. Physics in Medicine and Biology, 2009. **54**(9): p. 2699.

87. Gu, J., et al., Assessment of patient organ doses and effective doses using the VIP-Man adult male phantom for selected cone-beam CT imaging procedures during image guided radiation therapy. Radiation Protection Dosimetry, 2008. **131**(4): p. 431-443.

88. Lee, C., et al., Organ doses for reference adult male and female undergoing computed tomography estimated by Monte Carlo simulations. Medical Physics, 2011. **38**(3): p. 1196-1206.

89. Lee, C., et al., Organ doses for reference pediatric and adolescent patients undergoing computed tomography estimated by Monte Carlo simulation. Medical Physics, 2012. **39**(4): p. 2129-2146.

90. Long, D.J., et al., Monte Carlo simulations of adult and pediatric computed tomography exams: Validation studies of organ doses with physical phantoms. Medical Physics, 2013. **40**(1): p. 013901-10.

91. Kalender, W.A., et al., A PC program for estimating organ dose and effective dose values in computed tomography. Eur Radiol, 1999. **9**(3): p. 555-62.

92. Schmidt, B., Kalender, W A A fast voxel-based Monte Carlo method for scanner- and patient-specific dose calculations in computed tomography. Phys. Med. , 2002. **18** p. 43–53.

93. Deak, P., et al., Validation of a Monte Carlo tool for patient-specific dose simulations in multi-slice computed tomography. European Radiology, 2008. **18**(4): p. 759-772.

94. Chen, W., et al., Fast on-site Monte Carlo tool for dose calculations in CT applications. Medical Physics, 2012. **39**(6): p. 2985-2996.

95. Turner, A., A method to generate equivalent energy spectra and filtration models based on measurement for multidetector CT Monte Carlo dosimetry simulations. Medical Physics, 2009. **36**(6): p. 2154-2164.

96. ICRU, Phantoms and computational models in therapy, diagnosis and protection. The International Commission on Radiation Units and Measurements, Report No. 48, ICRU, Bethesda, MD, 1992.

97. Fisher HL, S.W., Distribution of dose in the body from a source of gamma rays distributed uniformly in an organ. Proceedings of the First International Congress on Radiation Protection. , Oxford, England: Pergamon 1968: p. 1473-1486.

98. WS Snyder, M.R.F., GG Warner, HL Fisher, Jr., Estimates of Absorbed Fractions for Monoenergetic Photon Sources Uniformly Distributed in Various Organs of a Heterogeneous Phantom. J Nucl Med Suppl Number 3 August 1969.

99. ICRP, Reference man: anatomical, physiological and metabolic characteristics ICRP Publication 23. Ann ICRP, Oxford: Pregamon,1975.

100. Gibbs, S.J., et al., Patient risk from interproximal radiography. Oral Surgery, Oral Medicine, Oral Pathology, 1984. **58**(3): p. 347-354.

101. Williams, G., et al., The calculations of dose from external photon exposures using reference and realistic human phantoms and Monte Carlo methods. Physics in Medicine and Biology, 1986. **31**(4): p. 449.

102. Zankl, M., et al., The construction of computer tomographic phantoms and their application in radiology and radiation protection. Radiat Environ Biophys, 1988. **27**(2): p. 153-64.

103. Yong Hum, N., et al., Deformable adult human phantoms for radiation protection dosimetry: anthropometric data representing size distributions of adult worker populations and software algorithms. Physics in Medicine and Biology, 2010. **55**(13): p. 3789.

104. Gu, J., et al., FETAL DOSES TO PREGNANT PATIENTS FROM CT WITH TUBE CURRENT MODULATION CALCULATED USING MONTE CARLO SIMULATIONS AND REALISTIC PHANTOMS. Radiation Protection Dosimetry, 2012.

105. Xu, X.G., et al., A boundary-representation method for designing whole-body radiation dosimetry models: pregnant females at the ends of three gestational periods—RPI-P3, -P6 and -P9. Physics in Medicine and Biology, 2007. **52**(23): p. 7023.

106. Xu, X.G. and C. Shi. Preliminary development of a 4D anatomical model for Monte Carlo simulations. in Monte Carlo 2005 Topical Meeting. The Monte Carlo method: versatility unbounded in a dynamic computing world [CD-ROM]. Chattanooga (TN): American Nuclear Society, LaGrange Park (IL). 2005.

107. Zhang, J., et al., Development of a geometry-based respiratory motion–simulating patient model for radiation treatment dosimetry. Journal of applied clinical medical physics/American College of Medical Physics, 2008. **9**(1): p. 2700.

108. Lee, C., et al., Hybrid computational phantoms of the male and female newborn patient: NURBS-based whole-body models. Physics in medicine and biology, 2007. **52**(12): p. 3309.

109. Lee, C., et al., Hybrid computational phantoms of the 15-year male and female adolescent: applications to CT organ dosimetry for patients of variable morphometry. Medical physics, 2008. **35**: p. 2366.

110. Bolch, W., et al., Hybrid computational phantoms for medical dose reconstruction. Radiation and Environmental Biophysics, 2010. **49**(2): p. 155-168.

111. He, W., et al., X-ray tube current modulation and patient doses in chest CT. Radiation Protection Dosimetry, 2011. **143**(1): p. 81-87.

112. Tran, L., et al., Comparison of treatment response classifications between unidimensional, bidimensional, and volumetric measurements of metastatic lung lesions on chest CT. Acad Radiol, 2004. **11**(12).

113. ICRU, Tissue Substitutes in Radiation Dosimetry and Measurement The International Commission on Radiation Units and Measurements, Report No. 44, ICRU, Bethesda, MD, 1989.

114. DeMarco, J.J., T.D. Solberg, and J.B. Smathers, A CT-based Monte Carlo simulation tool for dosimetry planning and analysis. Med Phys, 1998. **25**(1): p. 1-11.

115. Lee, C., et al., Organ and effective doses in pediatric patients undergoing helical multislice computed tomography examination. Med Phys, 2007. **34**(5): p. 1858-73.

116. Khursheed, A., et al., Influence of patient age on normalized effective doses calculated for CT examinations. Br J Radiol, 2002. **75**(898): p. 819-30.

117. Deak, P., et al., Validation of a Monte Carlo tool for patient-specific dose simulations in multi-slice computed tomography. Eur Radiol, 2008. **18**(4): p. 759-72.

118. Schmidt, R., et al., Monte Carlo based calculation of patient exposure in X-ray CT-examinations, in 4th European Conference of the International Federation for Medical and Biological Engineering, J. Sloten, et al., Editors. 2009, Springer Berlin Heidelberg. p. 2487-2490.

119. Fearon, T., et al., Patient-specific CT dosimetry calculation: a feasibility study. J Appl Clin Med Phys, 2011. **12**(4): p. 3589.

120. Ackerman, M.J., The visible human project. Proceedings of the IEEE, 1998. **86**(3): p. 504-511.

121. Vining DJ, G.D., Bechtold RE, Scharling ES, Grishaw EK, Shifrin RY, Technical feasibility of colon imaging with helical CT and virtual reality. AJR AM J Roentgenol, 1994. **62 (Suppl.)**.

122. DeMarco, J.J., T.D. Solberg, and J.B. Smathers, A CT-based Monte Carlo simulation tool for dosimetry planning and analysis. Medical Physics, 1998. **25**(1): p. 1-11.

123. Zhang, D., Savandi, AS, DeMarco, JJ, Cagnon, CH, Angel E et al. , Variability of surface and center position radiation dose in MDCT: Monte Carlo simulations using CTDI and anthropomorphic phantoms. Med Phys, 2009. **36**(3): p. 1025-1038.

124. Israel, G.M., et al., Patient Size and Radiation Exposure in Thoracic, Pelvic, and Abdominal CT Examinations Performed With Automatic Exposure Control. American journal of roentgenology, 2010. **195**(6): p. 1342-1346.

125. Tsalafoutas, I.A. and S. Metallidis, A method for calculating the dose length product from CT DICOM images. Br J Radiol, 2010: p. 37630380.

126. Lin, P.-J.P., T. Kubo, and R. Krishnapillai, Extraction of tube current values from DICOM CT images for patient dose estimation. Medical Physics, 2010. **37**(6): p. 2951.

127. Waters, E., MCNPX User's Manual, Version 2.4.0 Los Alamos National Laboratory report LA-CP-02-408, 2002.

128. Waters, E., MCNPX Version 2.5.C Los Alamos National Laboratory report LA-UR-03-2202 2003.

129. ICRU, Tissue substitutes in radiation dosimetry and measurement. The International Commission on Radiation Units and Measurements, Report No. 44, ICRU, Bethesda, MD, 1989.

130. Cribbie, R.A., J.A. Gruman, and C.A. Arpin-Cribbie, Recommendations for applying tests of equivalence. Journal of Clinical Psychology, 2004. **60**(1): p. 1-10.

131. Schuirmann, D.J., A comparison of the Two One-Sided Tests Procedure and the Power Approach for assessing the equivalence of average bioavailability. Journal of Pharmacokinetics and Pharmacodynamics, 1987. **15**(6): p. 657-680.

132. Zhang, D., Reducing radiation dose to selected organs by selecting the tube start angle in MDCT helical scans: A Monte Carlo based study. Med. Phys., 2009. **36**(12): p. 5654.

133. NCRP Report No. 160: Ionizing Radiation Exposure of the Population of the United States. Journal of Radiological Protection, 2009. **29**(3): p. 465.

134. FDA, FDA Unveils Initiative to Reduce Unnecessary Radiation Exposure from Medical Imaging. 2010.

135. Schlattl, H., et al., Dose conversion coefficients for CT examinations of adults with automatic tube current modulation Physics in Medicine and Biology 2010. **55**: p. 6243.

136. Schlattl, H., et al., Dose conversion coefficients for paediatric CT examinations with automatic tube current modulation. Physics in Medicine and Biology, 2012. **57**(20): p. 6309.

137. Turner, A.C., et al., A method to generate equivalent energy spectra and filtration models based on measurement for multidetector CT Monte Carlo dosimetry simulations. Medical Physics, 2009. **36**(6): p. 2154-2164.

138. Li, B., R.H. Behrman, and A.M. Norbash, Comparison of topogram-based body size indices for CT dose consideration and scan protocol optimization. Medical Physics, 2012. **39**(6): p. 3456-3465.

139. Wang, J., et al., Attenuation-based estimation of patient size for the purpose of size specific dose estimation in CT. Part I. Development and validation of methods using the CT image. Medical Physics, 2012. **39**(11): p. 6764-6771.

140. Wang, J., et al., Attenuation-based estimation of patient size for the purpose of size specific dose estimation in CT. Part II. Implementation on abdomen and thorax phantoms using cross sectional CT images and scanned projection radiograph images. Medical Physics, 2012. **39**(11): p. 6772-6778.

141. Menke, J., Comparison of Different Body Size Parameters for Individual Dose Adaptation in Body CT of Adults1. Radiology, 2005. **236**(2): p. 565-571.

142. Sodickson, A., et al., Exposing Exposure: Automated Anatomy-specific CT Radiation Exposure Extraction for Quality Assurance and Radiation Monitoring. Radiology, 2012. **264**(2): p. 397-405.

143. Xun, J., et al., GPU-based fast Monte Carlo simulation for radiotherapy dose calculation. Physics in Medicine and Biology, 2011. **56**(22): p. 7017.

144. Jia, X., et al., A GPU tool for efficient, accurate, and realistic simulation of cone beam CT projections. Medical Physics, 2012. **39**(12): p. 7368-7378.

145. Huda, W., et al., An approach for the estimation of effective radiation dose at CT in pediatric patients. Radiology, 1997. **203**(2): p. 417-22.

146. Huda, W., E.M. Scalzetti, and M. Roskopf, Effective doses to patients undergoing thoracic computed tomography examinations. Med Phys, 2000. **27**(5): p. 838-44.

147. Toth, T., Z. Ge, and M.P. Daly, The influence of patient centering on CT dose and image noise. Medical physics, 2007. **34**(7): p. 3093-3101.

148. Khatonabadi, M., et al., The feasibility of a regional CTDI[sub vol] to estimate organ dose from tube current modulated CT exams. Medical Physics, 2013. **40**(5): p. 051903-11.